ISSN 1983-4195

IBRACON

IBRACON Structures and Materials Journal

Revista IBRACON de Estruturas e Materiais

Volume 16, Number 6
December 2023

ISSN 1983-4195
Volume 16, Number 6
December 2023

IBRACON Structures and Materials Journal
Revista IBRACON de Estruturas e Materiais

Contents

Cover: Parametric Tower

Courtesy: Marcela Noronha P. de O. e Sousa

IBRACON

Ibracon Structures and Materials Journal is published bimonthly. (February, April, June, August, October, and December) by IBRACON.

IBRACON
Instituto Brasileiro do Concreto Founded in 1972

Av. Queiroz Filho, nº 1700 — sala 407/408
Torre D — Villa Lobos Office Park
CEP 05319-000 — São Paulo, SP — Brazil
Phone: +55 11 3735-0202
Fax: +55 11 3733-2190
E-mail: riem@ibracon.org.br
Website: http://www.ibracon.org.br

Cover design & Layout: Editora Cubo www.editoracubo.com.br

Support: Wallison Angelim Medeiros

Aims and Scope

Aims and Scope

The IBRACON Structures and Materials Journal (in Portuguese: Revista IBRACON de Estruturas e Materiais) is a technical and scientific divulgation vehicle of IBRACON (Brazilian Concrete Institute), published every two months. Each issue has 12 to 15 articles and, possibly, a technical note and/or a technical discussion regarding a previously published paper. All contributions are reviewed and approved by professionals with recognized scientific competence in the area. The IBRACON Structures and Materials Journal is an open access Journal, free of charges for authors and readers.

Objectives

The IBRACON Structures and Materials Journal´s main objectives are:

- Present current developments and advances in concrete structures and materials.
- Make possible the better understanding of structural concrete behavior, supplying subsidies for a continuous interaction among researchers, producers, and users.
- Stimulate the development of scientific and technological research in the areas of concrete structures and materials, through papers peer-reviewed by a qualified Editorial Board.
- Promote the interaction among researchers, constructors and users of concrete structures and materials and the development of Civil Construction.
- Provide a vehicle of communication of high technical level for researchers and designers in the areas of concrete structures and materials.

Submission Procedure

The procedure to submit and revise the contributions, as well as the formats, are detailed in the Journal Website (ismj.org).

The papers and the technical notes are revised by at least two reviewers indicated by the editors. Discussions and replies are accepted for publication after a review by the editors and at least one member of the Editorial Board. In case of disagreement between the reviewer and the authors, the contribution will be sent to a specialist in the area, not necessarily linked to the Editorial Board. Conflict of interests is carefully handled by the Editors.

Contribution Types

The Journal will publish original papers, short technical notes, and paper discussions. Original papers will be accepted if they are in accordance with the objectives of the Journal and present quality of information and presentation. A technical note is a brief manuscript. It may present a new feature of research, development, or technological application in the areas of Concrete Structures and Materials, and Civil Construction. This is an opportunity to be used by industries, companies, universities, institutions of research, researchers, and professionals willing to promote their works and products under development.

A discussion is received no later than 3 months after the publication of the paper or technical note. The discussion must be limited to the topic addressed in the published paper and must not be offensive. The right of reply is granted to the Authors. The discussions and the replies are published in the subsequent issues of the Journal.

The submission file should be in accordance with the paper template available at the Journal Website. It is recommended that the length of the papers does not exceed 25 pages. Where available, URLs for the references should be provided.

The IBRACON Structures and Materials Journal will conduct the review process for manuscripts submitted in English. Titles, abstracts, and keywords are presented in English, and in Portuguese or Spanish. Articles and technical notes are peer-reviewed and only published after approval of the reviewers and the Editorial Board.

Once accepted, an article is typeset according to the journal layout. The author will be required to review and approve the galleys before publishing. At this stage only typesetting errors will be considered.

Internet Access

The IBRACON Structures and Materials Journal Webpage is available at http://ismj.org.

Sponsors

The funds for the maintenance of the Journal are currently obtained from the IBRACON. The Journal is not supposed to be maintained with funds from private sponsorship, which could diminish the credit of the publications.

Photocopying

Photocopying in Brazil. Brazilian Copyright Law is applicable to users in Brazil. IBRACON holds the copyright of contributions in the journal unless stated otherwise at the bottom of the first page of any contribution. Where IBRACON holds the copyright, authorization to photocopy items for internal or personal use, or the internal or personal use of specific clients, is granted for libraries and other users registered at IBRACON.

Copyright

IBRACON

Av. Queiroz Filho, 1700 – sala 407/408 – Torre D
Villa Lobos Office Park
05319-000 – Vila Hamburguesa
São Paulo – SP
Phone: +55 (11) 3735-0202
E-mail: riem@ibracon.org.br

Disclaimer

Papers and other contributions and the statements made, or opinions expressed therein are published on the understanding that the authors of the contribution are the only responsible for the opinions expressed in them and that their publication does not necessarily reflect the views of IBRACON or of the Journal Editorial Board.

Editorial Board

Editorial Board

Direction

Board of Direction 2021/2023 Biennium

President
Paulo Helene

1st Vice-President Director
Júlio Timerman

2nd Vice-President Director
Enio José Pazini Figueiredo

Presidency Advisors
Arnaldo Forti Battagin
Eduardo Antonio Serrano
Gilberto Antonio Giuzio
Iria Lícia Oliva Doniak
Jaques Pinto
João Luis Casagrande
Jorge Batlouni Neto
José Marques Filho
Mario William Esper
Ronaldo Tartuce
Rubens Machado Bittencourt
Selmo Chapira Kuperman
Simão Priszkulnik
Túlio Nogueira Bittencourt
Wagner Roberto Lopes

1st Director-Secretary
Cláudio Sbrighi Neto

2nd Director-Secretary
Carlos José Massucato

1st Treasurer Director
Júlio Timerman

2nd Treasurer Director
Hugo S. Armelin

Marketing Director
Alexandre Britez

Marketing Director Advisor
Guilherme Covas

Publications Director
Guilherme Parsekian

Publications Director Advisor
Túlio Nogueira Bittencourt

Event Director
Rafael Timerman

Event Director Advisor
Luis César De Luca

Technical Director
Carlos Britez

Technical Director Advisor
Emílio Takagi

Institutional Relations Director
César Henrique Daher

Institutional Relations Director Advisor
José Vanderley de Abreu

Course Director
Jéssica Pacheco

Course Director Advisor
André Mendes

Student Activities Director
Jéssica Andrade Dantas

Student Activities Director Advisor
Patrícia Bauer

Personnel Certification Director
Adriano Damásio Soterio

Personnel Certification Director Advisor
Paula Baillot

Research and Development Director
Bernardo Tutikian

Research and Development Director Advisor
Roberto Christ

Council 2021/2023 Biennium

Individual Members
Alio Ernesto Kimura
Antônio Carlos dos Santos
Antônio Domingues de Figueiredo
Arnaldo Forti Battagin
Bernardo Fonseca Tutikian
Carlos José Massucato
César Henrique Sato Daher
Claudio Sbrighi Neto
Enio José Pazini Figueiredo
Geraldo Cechella Isaia
Iberê Martins da Silva
Inês Laranjeira da Silva Battagin
Iria Lícia Oliva Doniak
Jéssika Mariana Pacheco Misko
José Tadeu Balbo
Leandro Mouta Trautwein
Luiz Prado Vieira Júnior (*in memoriam*)
Mário William Esper
Rafael Timerman
Rubens Curti
Vladimir Antonio Paulon

Past President Members
Eduardo Antônio Serrano
José Marques Filho
Júlio Timerman
Paulo Roberto do Lago Helene
Ronaldo Tartuce
Rubens Machado Bittencourt
Selmo Chapira Kuperman
Simão Priszkulnik
Túlio Nogueira Bittencourt

Corporate Members

ABCIC - Associação Brasileira da Construção Industrializada de Concreto – Iria Lícia Oliva Doniak

ABCP - Associação Brasileira de Cimento Portland – Paulo Camilo Penna

ABECE - Associação Brasileira de Engenharia e Consultoria Estrutural – João Alberto de Abreu Vendramini

ABESC - Associação Brasileira das Empresas de Serviços de Concretagem – Wagner Roberto Lopes

EPUSP - Escola Politécnica da Universidade de São Paulo – Túlio Nogueira Bittencourt

IPT - Instituto de Pesquisas Tecnológicas do Estado de São Paulo – José Maria de Camargo Barros

MC-BAUCHEMIE BRASIL INDÚSTRIA E COMÉRCIO LTDA – Jaques Pinto

PhD Engenharia Ltda – Douglas de Andreza Couto

TQS Informática Ltda – Nelson Covas

VOTORANTIM Cimentos S/A – Mauricio Bianchi

Reviewers List: Aug, 2021 – Jul, 2023

Abdalla Filho, João Elias
Aguiar, Cásssio
Aguilar, Maria Teresa
Albuquerque, Arthur
Albuquerque, Gabriela
Almeida Filho, Fernando
Almeida, Fernando C.R.
Almeida, Luiz
Almeida, Saulo José de Castro
Almeida, Sylvia
Alva, Gerson
Alves, Antonio
Alves, Elcio
Alves, Vinícius Nicchio
Andrade, Jairo José de Oliveira
Ângulo, Sérgio
Antunes, Elaine Guglielmi Pavei
Araújo, Daniel
Araujo, Francisco Celio de
Araújo, Tereza
Ashish, Deepankar
Azadeh, Arash
Balbo, José
Balestra, Carlos
Barboza, Aline
Barros, Rodrigo
Baságlia, Cilmar
Beck, André
Bernardin, Adriano
Bernardo, Luís
Bianco, Vincenzo
Bittencourt Jr., Luis
Bittencourt, Eduardo
Bolina, Fabricio
Bompa, Dan
Botte, Wouter
Britez, Carlos
Brito, Jorge de
Brito, José
Bueno, Cristiane
Buttignol, Thomaz
Caldas, Rodrigo Barreto
Caldentey, Alejandro Perez
Calixto, José Marcio
Calmon, Joao Luiz
Camarini, Gladis
Campos Filho, Américo
Campos, Heloisa
Capuzzo, Valdirene Maria Silva
Cardoso, Daniel Carlos Taissum
Carneiro, Arnaldo Manoel Pereira
Carrazedo, Ricardo
Carrazedo, Rogério
Carvalho, Eliene Pires
Carvalho, Hermes
Casali, Juliana
Castro, Alessandra Lorenzetti de
Cervenka, Jan
Cheung, Andrés
Christ, Roberto
Christoforo, André
Cincotto, Maria
Cordeiro, Luciana
Costa, Carla Neves
Costa, Fernanda Bianchi Pereira da
Costa, Leonardo
Couto, Douglas
Dalfré, Gláucia
Daminelli, Bruno Luis
De Nardim, Silvana
Delalibera, Rodrigo Gustavo
Désir, Jean Marie
Diniz, Sofia Carrato
Dominguez, Joel
Durand, Raúl
Etse, Guillermo
Fairbairn, Eduardo
Fakury, Ricardo
Farage, Michèle
Feldmann, Markus
Felix, Emerson
Ferreira, Fernanda
Ferreira, Gisleiva Cristina dos Santos
Ferreira, Gonçalo
Ferreira, Maurício de Pina
Ferreira, Walnorio
Flórez-López, Julio
Folino, Paula
Fonseca, Ana
Fonseca, Regis da
Formagini, Sidiclei
Freitas, Marcílio Sousa da Rocha
Frizon, Tiago
Furtado, Andre
Futai, Marcos
Galdino, André Gustavo de Sousa
Garcez, Monica Regina
Garcia, Maria da Luz
Gaspar, Cássio
Giuseppe, Guimarães
Golaszewski, Jacek
Gomes, Carlos Marmorato
Gomes, Francisco Augusto Aparecido
Gomes, Paulo
Gomes, Wyllerson
Gumieri, Adriana
Gusmão, Alexandre Duarte Gusmão
Haach, Vladimir
Hamdia, Khader M.
Haselbach, Liv
Henriques, António Abel
Horowitz, Bernardo
Hosen, Md. Akter
Hotza, Dachamir
Irassar, Edgardo F.
Iskander, Mina
Isoldi, Liércio André
Isufi, Brisid
Izquierdo, Indara
Jacintho, Ana
Jacinto, Luciano
Joshaghani, Alireza
Justino Filho, Manoel Rodrigues
Kadhim, Majid M. A.
Karayannis, Chris G.
Kazmierczak, Cláudio
Kempka, Mariane
Kenai, S.
Khatib, Jamal
Khazanovich, Lev
Khoshnazar, Rahil
Kleina, Mariana
Krahl, Pablo Augusto
Kripka, Moacir
Kroetz, Henrique Machado
Lameiras, Rodrigo
Lantsoght, Eva O. L.
Lazzari, Bruna
Lazzari, Paula
Lemes, Igor
Lemonge, Afonso
Li, Hui
Liberati, Elyson
Lima, Flávio
Lima, Luciano R. O. de
Linn, Renato
Liu, Yi
Lopes, Dario
Lübeck, André
Ludvig, Péter
Luz, Caroline Angulski da
Machado, Roberto
Maciel, Geraldo
Maedo, Michael
Magalhães, Aldo de
Magalhães, Fábio
Makul, Natt
Malomo, Daniele
Manzoli, Osvaldo
Marfil, Silvina
Marques Filho, Jose
Marques, Marília
Marques, Severino
Martirena, Fernando
Masuero, João Ricardo
Matos, Ana Mafalda
Matos, Paulo de
Matoski, Adalberto
Mazer, Wellington
Medeiros, Arthur
Medeiros, Marcelo
Medeiros, Ronaldo
Medeiros, Wallison Angelim
Melges, José Luiz Pinheiro
Melo Neto, Antônio Acácio
Melo, Antônio
Mendes, Júlia Castro
Meneghetti, Leila Cristina
Menendez, E.
Menezes, Ivan
Menezes, Ruy
Mennucci, Marina Martins
Mesacasa Jr., Enio
Mesquita, Esequiel
Miguel, Leandro Fleck Fadel
Milanesi, Carlos
Milani, Margot Pereira
Moahmed, Hoda
Modolo, Regina
Monte, Renata
Montes-Garcia, Pedro
Moreira, Rodrigo Falcão
Morsch, Inácio
Motta, Leila Aparecida de Castro
Munaiar Neto, Jorge
Muñoz-Rojas, Pablo
Neves Jr., Alex
Nicolaides, Demetris
Nóbrega, Petrus
Nogueira, Caio
Nogueira, Fernando
Nunes, David
Oliveira, Cristina
Oliveira, Dênio Ramam Carvalho de

Reviewers List: Aug, 2021 – Jul, 2023

Oliveira, Leonardo Henrique
Oliveira, Luciane Marcela Filizola de
Oliveira, Mateus Antônio Nogueira
Oliveira, Romilde
Paccola, Rodrigo
Pacheco, Alexandre
Paes, José Luiz Rangel
Palermo Jr., Leandro
Paliari, José Carlos
Paliga, Charlei
Pantoja, João
Parente Jr., Evandro
Parsekian, Guilherme A.
Patil, Chetan
Pedroso, Cynthia
Pelisser, Fernando
Pereira, Danilo
Pereira, Eduardo
Pereira, Sebastião Salvador Real
Pfeil, Michèle
Pileggi, Rafael
Pimenta, Roberval
Pimentel, Lia Lorena
Pimentel, Mario
Pinto, Roberto Caldas de Andrade
Pinto, Silas
Pitangueira, Roque
Pituba, José Julio de Cerqueira
Pontes, Helder
Positieri, Maria ajosefina
Possan, Edna
Prado, Lisiane
Pravia, Zacarias M. C.
Punhagui, Katia
Quaranta, Giuseppe
Quinino, Uziel
Rashad, Alaa
Real, Mauro
Reales, Oscar Aurélio Mendoza
Rêgo, João da Silva
Rezende, Mariana Felicetti
Ribeiro, Daniel
Ribeiro, Diogo
Rigobello, Ronaldo
Rocha, Marcelo
Rodrigues, Eduardo
Rodrigues, Monique
Rojas, Rosangel
Rossignolo, João Adriano
Saisi, Antonella
Sakata, Rafael Dors
Sandoval, Gersson Fernando Barreto
Santos, Ana Carolina Parapinski dos
Santos, Daniel
Santos, Sérgio Hampshire C.
Santos, White
Sarker, Prabir K.
Savaris, Gustavo
Schulz, Mauro
Sciarretta, Francesca
Serafini, Ramoel
Shishegaran, Aydin
Silva Filho, José
Silva, André da
Silva, Andrea
Silva, António Santos
Silva, Bruno do Vale
Silva, Fernando Marques da
Silva, Guilherme Jorge Brigolini
Silva, Gustavo Ribeiro
Silva, Jordlly
Silva, José Guilherme Santos da
Silva, Maria Cecília Teixeira da
Silva, Wellington Andrade da
Silvestro, Laura
Simonetti, Camila
Siqueira, Gustavo
Snoeck, Didier
Sotiriadis, Konstantinos
Soto, Orieta
Sousa, Adla
Sousa, Carlos
Souza, Luiz Antonio Farani de
Souza, Rafael Alves
Stucchi, Fernando Rebouças
Takagi, Emilio Minoru
Tamayo, Jorge
Tambara, Luís
Tarabia, Ahmed
Tavares, Maria Elizabeth
Thomas, Carlos
Trautwein, Leandro
Trigo, Ana Paula Moreno
Trindade, Ana Carolina Constâncio
Tutikian, Bernardo
Valença, Jonatas
Varela, Wendell
Venancio, Rogerio
Veríssimo, Gustavo de Souza
Vianna, Savio S. V.
Vieira, Geilma
Vieira, Manuel
Wang, Wen-Wei
Wardeh, George
Welter, Nathanaell Vinícius de Camargos
Yang, Shangtong
Yu, Runqing
Yuchen, Song
Zhang, Dong

IBRACON Structures and Materials Journal
Revista IBRACON de Estruturas e Materiais
ISSN 1983-4195 ismj.org

ORIGINAL ARTICLE

Moving mass/load speed influence on the structural dynamic response of a bridge

Influência da velocidade da massa/carga móvel na resposta dinâmica da estrutura de uma ponte

Rafael Costa da Hora[a]
Silvio de Souza Lima[a]
Sergio Hampshire de Carvalho Santos[a]

[a]Universidade Federal do Rio de Janeiro – UFRJ, Department of Structures, Rio de Janeiro, RJ, Brasil

Received 13 July 2022
Accepted 17 January 2023

Abstract: The increasing technological advance in the structural engineering field allows not only the design of better structures, but also the development of new methods. When it comes to bridges, more specifically, railway bridges, a special kind of attention is necessary since the dynamic nature of some external loads must be taken into account. In this study, the inertial effect caused on the structure by the moving vehicle is quantified and taken into consideration in the analyses, through the coupling of the vehicle mass matrix with the global mass matrix of the structure at each integration time step. The numerical dynamic analysis was performed by the LOADYN software, a computer program developed by the authors. The influence of the train speed on the structural dynamic response is analyzed. Comparisons between the structural responses with and without the vehicle inertial effect are made. The results show the importance of the inertial forces generated by the vehicle. Those forces must be taken into account, especially at higher speeds and mass ratios since they play an important role on the response magnitude and critical velocities.

Keywords: structural dynamics, railway bridges, moving mass, numerical solution, LOADYN.

Resumo: O crescente avanço tecnológico permite não só a concepção de estruturas cada vez mais sofisticadas e esbeltas, mas também a criação de novos métodos. No caso de pontes, uma análise mais robusta se faz necessária tendo em vista a complexidade dos carregamentos atuantes de natureza dinâmica. No presente trabalho, as forças inerciais geradas pelas massas dos veículos na estrutura são levadas em consideração, e seus efeitos quantificados, através do acoplamento das matrizes de massas dos veículos à matriz de massa global da estrutura a cada intervalo de integração. A análise dinâmica em questão foi realizada pelo programa LOADYN, ferramenta computacional desenvolvida pelos autores. A influência da velocidade de passagem do veículo na resposta dinâmica da estrutura é analisada. São feitas comparações entre as respostas estruturais com e sem a consideração das forças inerciais geradas pelo veículo. Tais forças não devem ser negligenciadas, especialmente a grandes velocidades e altas relações entre as massas do veículo e estrutura já que têm um papel imprescindível na magnitude da resposta e nas velocidades críticas.

Palavras-chave: análise dinâmica, massas móveis, pontes ferroviárias, solução numérica, LOADYN.

How to cite: R. C. Hora, S. de Souza Lima, and S. H. C. Santos, "Moving mass/load speed influence on the structural dynamic response of a bridge," *Rev. IBRACON Estrut. Mater.*, vol. 16, no. 6, e16601, 2023, https://doi.org/10.1590/S1983-41952023000600001

1 INTRODUCTION

The growing development of high-speed trains makes the inertial effects generated by the vehicle masses on the structure extremely relevant to the analyses. The consideration of such effect simply as static loads amplification coefficients leads to conservative results when it comes to design safety. On the other hand, for a more specific analysis

Corresponding author: Rafael Costa da Hora. E-mail: rafaelcostadahora@poli.ufrj.br
Financial support: None.
Conflict of interest: Nothing to declare.
Data Availability: The data that support the findings of this study are available from the corresponding author, [RCH], upon reasonable request.

of the dynamic problem, the accounting of these effects is crucial and may even lead to more economical projects [1]. This conservative approach of the problem neglects the influence of vital structural properties that play important roles in the dynamic analysis, such as, the geometry of the structural system itself, natural frequencies of vibration, vibration modes, vehicle speed and vehicle mass. When dealing with specific cases, for instance, a structure subjected to high-speed trains, these properties become relevant as the vehicle speed increases and the ratio between the vehicle mass and the structure mass increases [2].

In the case of multiple vehicles [3], the dynamic loading induced by the travelling vehicles on the structure is sequential and repetitive by nature, which implies the existence of some forced external frequency of excitation [4]–[6]. When the induced load frequency is close to some natural frequency of the structure, the resonance phenomena may occur. This external frequency can be predicted, basically, by the vehicle speed and the length between consecutive axels of the vehicle [7]. This study divides the problem in two groups with different approaches to the solution, the moving load problem and the moving mass problem. The first one treats the vehicle as a concentrated moving load with speed *v* acting on the structure through time. In the case of a simply supported beam, the aforementioned approach allows closed form solutions. The other way of dealing with the problem is by treating the vehicle as a concentrated moving mass. In addition to the effect of the moving load problem, this approach includes the inertial effects generated by the moving mass on the structure [5]. Evidently, in order to deal with more complex structural geometry, boundary conditions and loads, a numerical approach of the problem is essential in both cases [8], [9]. More complex models may be formulated and implemented. For instance, the consideration of the rail irregularities which may be numerically generated by random noise functions. The train can also be modeled as a sub dynamic system of any complexity limited only by the available computational resources [10]. However, these approaches play a major role when the primary concern is focused on the vehicle response itself regarding, for instance, passenger comfort, vehicle vertical acceleration and fatigue analysis. A more complex vehicle does not, necessarily, affect the overall structural response in terms of displacement as seen in [7] and [11]. For those reasons only the moving load and moving mass models were addressed in this paper. Figure 1 illustrates the moving load model.

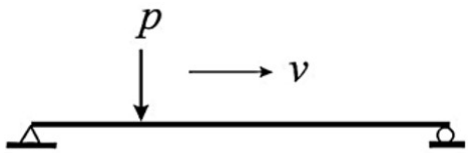

Figure 1. The moving load model.

As previously mentioned, this simplified model allows closed form solutions and is fundamentally governed by the Euler-Bernoulli differential equation, which constitutes the dynamic equilibrium of a beam (Equation 1).

$$m_b \frac{\partial^2 w(x,t)}{\partial t^2} + c \frac{\partial w(x,t)}{\partial t} + EI \frac{\partial^4 w(x,t)}{\partial x^4} = f(x,t) \tag{1}$$

Where, m_b is the linear mass, c the viscous damping coefficient, EI the flexural stiffness of the beam, $f(x,t)$ and $w(x,t)$ the externally applied loads and the deflection on the x coordinate on the instant t, respectively. When the vehicle inertial effects are considered, it is represented by a concentrated mass as shown in Figure 2.

Figure 2. The moving mass model.

2 DESCRIPTION OF THE PROBLEM

This work aims to determine the influence of the vehicle speed on the structural dynamic response. More specifically, it aims to determine, quantify and compare the influence of the vehicle speed on the structure in the case of the moving load and the moving mass problem. Therefore, time history analyses are iteratively performed varying incrementally the vehicle travelling speed on each analysis. The maximum response values for each time history are stored. This process is called critical speed analysis [12]. The critical speeds are the ones that generate higher response magnitudes. The response comparison is achieved by plotting the relation between the structure and vehicle mass ratio against the vehicle speed on a 3D chart. The aforementioned process is used both for the moving load and moving mass problem.

3 METHODOLOGY

In order to perform the required analysis and solution visualization of the already described problems, a specific computational tool was entirely developed by the authors. The LOADYN software was built to solve the dynamic moving mass / load problem using 3D frame elements [13], [14]. Its capability was extended to perform modal analysis [15], [16], critical speed analysis and static analysis [17]. It uses a skyline storage scheme to efficiently manage memory resources when storing the system matrices [13] and a sparse solver to take advantage of the high level of sparsity of the system of equations. Therefore, a better performance is achieved by reducing the factorization time when solving the algebraic linear system of equations and by reducing the required memory for storage [18].

The unconditionally stable Newmark method was implemented to numerically solve the differential dynamic equilibrium equations of the problem [19], [20]. The inertial effects of the vehicle are taken into account by deriving a local mass matrix that represents the concentrated mass contributions at the element nodes and coupling it with the structure global mass matrix. This derived local matrix is called vehicle mass matrix [7]. As can be inferred by the nature of the problem, the vehicle mass matrix is not constant since it is a function of the vehicle position within the element domain. This can be regarded as a concentrated mass element as shown in Figure 3. This numerical approach allows the quantification of the vehicle inertial influence on the response for any structural geometry configuration and is not adopted by the available commercial softwares known by the authors.

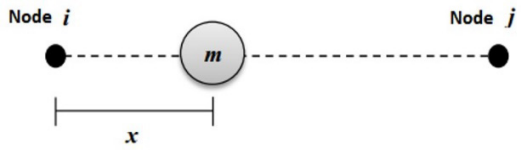

Figure 3. The concentrated mass element.

In Figure 3, x is the distance from the concentrated mass to the initial node of the element and m is the concentrated mass. The distance x increases in $\boldsymbol{v} * \Delta t$ on each integration time step, where $\boldsymbol{v}$ is the vehicle speed and Δt is the chosen time step. Therefore, the vehicle mass matrix needs to be assembled on each solution time step since x is not constant. The derivation of the vehicle local mass matrix is given by the use of the element shape functions. There is no distributed mass within the concentrated mass element domain, which means there is no need for the usual integration process. Equation 2 synthesizes what was described.

$$[M] = [M_e] + \sum_{i=1}^{j} [N(x)]^T [m_i][N(x)] \tag{2}$$

Where, $[M]$ is the sum of the element mass matrix with the vehicle mass matrix, $[M_e]$ is the element mass matrix, $[N(x)]$ is the element shape functions in matrix form, $[m_i]$ is vehicle mass matrix and j is the number of vehicles within the element at time t.

3.1 THE SYSTEM MATRICES

The 3D uniform frame element stiffness matrix [k] used by the program is shown in Figure 4. The shear deformation is taken into account by the factors $Ö_y$ *e* $Ö_z$. The complete formulation of the stiffness matrix is presented in [21].

$$
K = \begin{bmatrix}
\frac{EA}{l} & & & & & & & & & & & \\
0 & \frac{12EI_z}{l^3(1+\Phi_y)} & & & & & & & & & & \\
0 & 0 & \frac{12EI_y}{l^3(1+\Phi_z)} & & & & & & & & & \\
0 & 0 & 0 & \frac{GJ}{l} & & & & & & & & \\
0 & 0 & \frac{-6EI_y}{l^2(1+\Phi_z)} & 0 & \frac{(4+\Phi_z)EI_y}{l(1+\Phi_z)} & & & & & & & \\
0 & \frac{6EI_z}{l^2(1+\Phi_y)} & 0 & 0 & 0 & \frac{(4+\Phi_y)EI_z}{l(1+\Phi_y)} & & & & & & \\
\frac{-EA}{l} & 0 & 0 & 0 & 0 & 0 & \frac{AE}{l} & & & & & \\
0 & \frac{-12EI_z}{l^3(1+\Phi_y)} & 0 & 0 & 0 & \frac{-6EI_z}{l^2(1+\Phi_y)} & 0 & \frac{12EI_z}{l^3(1+\Phi_y)} & & & & \\
0 & 0 & \frac{-12EI_y}{l^3(1+\Phi_z)} & 0 & \frac{6EI_y}{l^2(1+\Phi_z)} & 0 & 0 & 0 & \frac{12EI_y}{l^3(1+\Phi_z)} & & & \\
0 & 0 & 0 & \frac{-GJ}{l} & 0 & 0 & 0 & 0 & 0 & \frac{GJ}{l} & & \\
0 & 0 & \frac{-6EI_y}{l^2(1+\Phi_z)} & 0 & \frac{(2-\Phi_z)EI_y}{l(1+\Phi_z)} & 0 & 0 & 0 & \frac{6EI_y}{l^2(1+\Phi_z)} & 0 & \frac{(4+\Phi_z)EI_y}{l(1+\Phi_z)} & \\
0 & \frac{6EI_z}{l^2(1+\Phi_y)} & 0 & 0 & 0 & \frac{(2-\Phi_y)EI_z}{l(1+\Phi_y)} & 0 & \frac{-6EI_z}{l^2(1+\Phi_y)} & 0 & 0 & 0 & \frac{(4+\Phi_y)EI_z}{l(1+\Phi_y)}
\end{bmatrix}
$$

Symmetric

Figure 4. Element stiffness matrix.

The consistent element mass matrix $[M_e]$ with rotational inertia is used by the software instead of the lumped one. The 3D uniform frame element mass matrix is shown in Figure 5. Its complete formulation is also presented in [21].

$$
\mathbf{m} = \rho A l \begin{bmatrix}
\frac{1}{3} & & & & & & & & & & & \\
0 & \frac{13}{35}+\frac{6I_z}{5Al^2} & & & & & & & & & & \\
0 & 0 & \frac{13}{35}+\frac{6I_y}{5Al^2} & & & & & & & & & \\
0 & 0 & 0 & \frac{J_x}{3A} & & & & & & & & \\
0 & 0 & -\frac{11l}{210}-\frac{I_y}{10Al} & 0 & \frac{l^2}{105}+\frac{2I_y}{15A} & & & & & & & \\
0 & \frac{11l}{210}+\frac{I_z}{10Al} & 0 & 0 & 0 & \frac{l^2}{105}+\frac{2I_z}{15A} & & & & & & \\
\frac{1}{6} & 0 & 0 & 0 & 0 & 0 & \frac{1}{3} & & & & & \\
0 & \frac{9}{70}-\frac{6I_z}{5Al^2} & 0 & 0 & 0 & \frac{13l}{420}-\frac{I_z}{10Al} & 0 & \frac{13}{35}+\frac{6I_z}{5Al^2} & & & & \\
0 & 0 & \frac{9}{70}-\frac{6I_y}{5Al^2} & 0 & -\frac{13l}{420}+\frac{I_y}{10Al} & 0 & 0 & 0 & \frac{13}{35}+\frac{6I_y}{5Al^2} & & & \\
0 & 0 & 0 & \frac{J_x}{6A} & 0 & 0 & 0 & 0 & 0 & \frac{J_x}{3A} & & \\
0 & 0 & \frac{13l}{420}-\frac{I_y}{10Al} & 0 & -\frac{l^2}{140}-\frac{I_y}{30A} & 0 & 0 & 0 & \frac{11l}{210}+\frac{I_y}{10Al} & 0 & \frac{l^2}{105}+\frac{2I_y}{15A} & \\
0 & -\frac{13l}{420}+\frac{I_z}{10Al} & 0 & 0 & 0 & -\frac{l^2}{140}-\frac{I_z}{30A} & 0 & -\frac{11l}{210}-\frac{I_z}{10Al} & 0 & 0 & 0 & \frac{l^2}{105}+\frac{2I_z}{15A}
\end{bmatrix}
$$

Symmetric

Figure 5. Element mass matrix.

The Rayleigh formulation was adopted for the system damping, which means that [C], the global damping matrix, is a linear combination of [K] and [M], the global stiffness and mass matrix, respectively.

$$[C] = \alpha[M] + \beta[K] \tag{3}$$

where,

$$\alpha = 2\omega_k \frac{\xi_k \omega_i{}^2 - \xi_i \omega_i \omega_k}{\omega_i{}^2 - \omega_k{}^2} \tag{4}$$

$$\beta = \frac{2\xi_i \omega_i - 2\xi_k \omega_k}{\omega_i{}^2 - \omega_i \omega_k} \tag{5}$$

In this case, ω_i *and* ω_k are the frequency range limits relevant to the analysis. They may or may not match some of the structure's natural frequencies. ξ_i and ξ_k represent the damping ratios of the structure for *i* and *k* frequencies A diagram of the Rayleigh damping is shown in Figure 6.

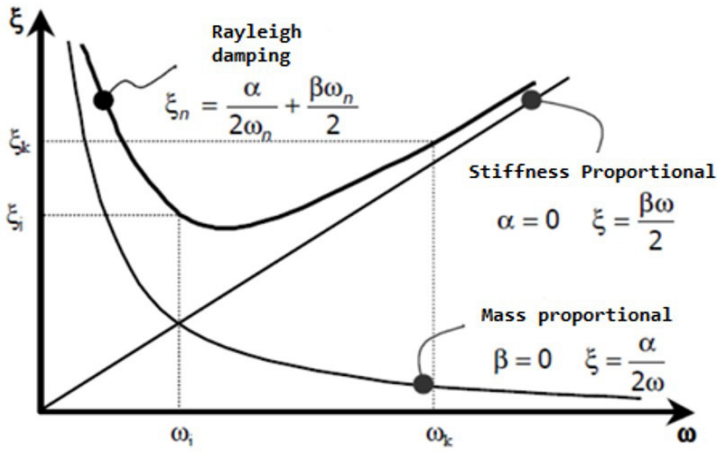

Figure 6. Rayleigh damping.

3.2 DYNAMIC INTERACTION MODELING

The dynamic interaction was taken into account through the contact points between vehicle and structure. Despite the vehicle is not treated as a dynamic system in this work, the following approach of the problem allows the implementation of the vehicle matrices if desired. In other words, the vehicle representation can vary from a single moving load to a complex chain of multiple coupled dynamic systems. The contact points cause the coupling of the differential equations in the problem. The assembled matrices are time dependent and must be updated as the contact points change position. It defines an incremental time history analysis. [19] explains the Newmark method for linear systems, a consolidated, implicit and unconditionally stable numerical method used to direct integrate the dynamic equilibrium equations.

The vehicle may be divided into two parts: the upper or noncontact part consists of the car body, suspension systems and bogies which DOF's are indicated by the vector $\{d_u\}$. The wheel or contact part consists of the wheelsets. Assuming that each wheelset is represented by one vertical DOF, the wheel part can be denoted as $\{d_w\}$. The vehicle equilibrium equation:

$$[m_v]\{\ddot{d}_v\} + [c_v]\{\dot{d}_v\} + [k_v]\{d_v\} = \{f_v\} \tag{6}$$

Where the force vector $\{f_v\}$ may be split as follows:

$$\{f_v\} = \{f_e\} + [l]\{f_c\} \tag{7}$$

The vector $\{f_e\}$ represents the external forces except the contact ones, which are represented by the vector $\{f_c\}$. $[l]$ is a transformation matrix. The displacement vector $\{d_v\}$ is composed by $\langle\{d_u\}\{d_w\}\rangle^T$, which represent the displacements in the direction of the degrees of freedom without and with contact with the structure, respectively. The wheels displacements $\{d_w\}$ are connected to the contact points displacements $\{d_c\}$ through the following relation:

$$\{d_w\} = [\tilde{A}]\{d_c\} + \{r\} \tag{8}$$

The $[\tilde{A}]$ matrix represents the vehicle jumping conditions and assumes unitary value if no jumps exist in the analysis. $\{r\}$ vector accounts for the rail irregularities. When those are not considered, the wheels displacements and the contact points displacements are the same. Only the contact forces acting towards gravity direction are taken into account within the context of this work. Horizontal forces generated by breaking are not studied.

The analysis takes into consideration that all the information of the system on time *t* are known. A small integration time step value Δt is assigned. The analysis interest lies on obtaining the system responses for time $t + \Delta t$. Equation 6 can be rewritten in matrix form for the new integration time step separating the vehicle degrees of freedom and the wheels (contact) degrees of freedom as follows:

$$\begin{bmatrix}[m_{uu}] & [m_{uw}]\\ [m_{wu}] & [m_{ww}]\end{bmatrix}\begin{Bmatrix}\{\ddot{d}_u\}\\ \{\ddot{d}_w\}\end{Bmatrix}_{t+\Delta t} + \begin{bmatrix}[c_{uu}] & [c_{uw}]\\ [c_{wu}] & [c_{ww}]\end{bmatrix}\begin{Bmatrix}\{\dot{d}_u\}\\ \{\dot{d}_w\}\end{Bmatrix}_{t+\Delta t} + \begin{bmatrix}[k_{uu}] & [k_{uw}]\\ [k_{wu}] & [k_{ww}]\end{bmatrix}\begin{Bmatrix}\{d_u\}\\ \{d_w\}\end{Bmatrix}_{t+\Delta t} = \begin{Bmatrix}\{f_{ue}\}\\ \{f_{we}\}\end{Bmatrix}_{t+\Delta t} + \begin{bmatrix}[l_u]\\ [l_w]\end{bmatrix}\{f_c\}_{t+\Delta t} \tag{9}$$

Expanding equation's 9 first line:

$$[m_{uu}]\{\ddot{d}_u\}_{t+\Delta t} + [c_{uu}]\{\dot{d}_u\}_{t+\Delta t} + [k_{uu}]\{d_u\}_{t+\Delta t} = \{f_{ue}\}_{t+\Delta t} - \{q_{uc}\}_{t+\Delta t} \tag{10}$$

Where,

$$\{q_{uc}\}_{t+\Delta t} = [m_{uw}]\{\ddot{d}_w\}_{t+\Delta t} + [c_{uw}]\{\dot{d}_w\}_{t+\Delta t} + [k_{uw}]\{d_w\}_{t+\Delta t} \tag{11}$$

Applying the Newmark's method described in [19] and some algebraic transformation as shown in [7], part of the solution is obtained as follows:

$$\{\ddot{d}_u\}_{t+\Delta t} = b_0\{\Delta d_u\} - b_1\{\dot{d}_u\}_t - b_2\{\ddot{d}_u\}_t \text{ ;}$$

$$\{\dot{d}_u\}_{t+\Delta t} = \{\dot{d}_u\}_t + b_3\{\ddot{d}_u\}_t + b_4\{\ddot{d}_u\}_{t+\Delta t} \text{ ;} \tag{12}$$

$$\{d_u\}_{t+\Delta t} = \{d_u\}_t + \{\Delta d_u\} \text{ ;}$$

The parameters for the solution's numerical stability β *and* γ; and the coefficients above are:

$$
\begin{aligned}
&b_0 = \frac{1}{\beta \ddot{A}t^2}\ ;\ b_1 = \frac{1}{\beta \ddot{A}t}\ ;\ b_2 = \frac{1}{2\beta} - 1\ ;\\
&b_3 = (1-\gamma)\ddot{A}t\ ;\ b_4 = \gamma \ddot{A}t\ ;\ b_5 = \frac{\gamma}{\beta \ddot{A}t}\ ;\\
&b_6 = \frac{\gamma}{\beta} - 1\ ;\ b_7 = \frac{\ddot{A}t}{2}\left(\frac{\gamma}{\beta} - 2\right);\\
&\gamma = \frac{1}{2}\ ;\ \beta = \frac{1}{4}\ ;
\end{aligned}
\tag{13}
$$

Plugging in Equation 12 into Equation 9 with the necessary algebraic manipulation, the solution can proceed by solving a linear system of algebraic equation:

$$
[\emptyset_{uu}]\{\ddot{A}d_u\} = \left\{f_{ue}\right\}_{t+\ddot{A}t} - \left\{q_{uc}\right\}_{t+\ddot{A}t} + \left\{q_u\right\}_t \tag{14}
$$

Where,

$$
[\emptyset_{uu}]\ =\ b_0[m_{uu}] + b_5[c_{uu}] + [k_{uu}] \tag{15}
$$

And,

$$
\begin{aligned}
&\{q_u\}_t\ =\ [m_{uu}]\left(b_1\{\dot{d}_u\}_t + b_2\{\ddot{d}_u\}_t\right)\\
&+[c_{uu}]\left(b_6\{\dot{d}_u\}_t + b_7\{\ddot{d}_u\}_t\right) - [k_{uu}]\{d_u\}_t
\end{aligned}
\tag{16}
$$

The solution of the algebraic linear system represents the displacement increments $\{\ddot{A}d_u\}$ of the vehicle's degrees of freedom not in contact with the structure. Plugging in this vector in the Equation 12, the displacement vector $\{d_u\}_{t+\ddot{A}t}$ of the upper part is achieved. When these displacements are known for the $t + \ddot{A}t$ time step, the contact forces acting on the system are easily obtained by the substitution of these displacements in the governing Equation 9 of the problem. Expanding the second line terms of this equation as follows:

$$
\left\{f_c\right\}_{t+\ddot{A}t} = [m_c]\left\{\ddot{d}_w\right\}_{t+\ddot{A}t} + [c_c]\left\{\dot{d}_w\right\}_{t+\ddot{A}t} + [k_c]\{d_w\}_{t+\ddot{A}t} + \left\{p_c\right\}_{t+\ddot{A}t} + \left\{q_c\right\}_t \tag{17}
$$

Where the contact matrices are:

$$
\begin{aligned}
&[m_c] =\ [l_w]^{-1}([m_{ww}] - [\emptyset_{wu}][\emptyset_{uu}]^{-1}[m_{uw}])\ ;\\
&[c_c] =\ [l_w]^{-1}([c_{ww}] - [\emptyset_{wu}][\emptyset_{uu}]^{-1}[c_{uw}])\ ;\\
&[k_c] =\ [l_w]^{-1}([k_{ww}] - [\emptyset_{wu}][\emptyset_{uu}]^{-1}[k_{uw}])\ ;
\end{aligned}
\tag{18}
$$

The load vectors are:

$$
\begin{aligned}
&\{p_c\}_{t+\ddot{A}t} = [l_w]^{-1}([\emptyset_{wu}][\emptyset_{uu}]^{-1}\{f_{ue}\}_{t+\ddot{A}t} - \{f_{we}\}_{t+\ddot{A}t})\\
&\{q_c\}_t = [l_w]^{-1}([\emptyset_{wu}][\emptyset_{uu}]^{-1}\{q_u\}_t - \{q_w\}_t)
\end{aligned}
\tag{19}
$$

In addition,

$$[\emptyset_{wu}] = b_0[m_{wu}] + b_5[c_{wu}] + [k_{wu}] \tag{20}$$

$$\{q_w\}_t = [m_{wu}]\left(b_1\{\dot{d}_u\}_t + b_2\{\ddot{d}_u\}_t\right)$$

$$+[c_{wu}]\left(b_6\{\dot{d}_u\}_t + b_7\{\ddot{d}_u\}_t\right) - [k_{wu}]\{d_u\}_t \tag{21}$$

Since no jump conditions are allowed, the wheels displacements are treated as the contact displacements, which means $\{d_w\} \equiv \{d_c\}$. Therefore, Equation 17 may be rewritten as follows:

$$\{f_c\}_{t+\ddot{A}t} = [m_c]\{\ddot{d}_c\}_{t+\ddot{A}t} + [c_c]\{\dot{d}_c\}_{t+\ddot{A}t} + [k_c]\{d_c\}_{t+\ddot{A}t} + \{p_c\}_{t+\ddot{A}t} + \{q_c\}_t \tag{22}$$

3.2.1 THE NEWMARK METHOD

Newmark's direct integration process is widely used for numerical solution of systems of differential equations, mainly when it comes to structural dynamics and wave propagation, for instance. The numerical stability of its solution does not depend on the size of the chosen integration time step. That is why the method is unconditionally stable. This does not mean, however, that the mathematical solution accuracy does not depend on the numerical step size. It is an implicit method. In other words, it is mandatory to know the state of all variables of the problem on the previous step in order to achieve its equilibrium conditions. Generally speaking, implicit methods have lower computational costs and the solutions are more robust when compared to explicit methods [20]. The average acceleration method was implemented in the present work.

3.2.2 THE MOVING MASS ALGORITHM

The main analysis algorithm is synthetized and presented as a pseudocode in table 1. The user is able to opt for the account of the vehicle inertial effect in the analysis by simply setting the VEHICLE_INERTIAL_EFFECT key to *TRUE* [12]. The algorithm returns the degrees of freedom displacements, velocities and accelerations for all the integration time steps. The time history response solution may now be visualized and internal stresses calculated.

Table 1. Main algorithm pseudocode

```
ALGORITHM: MAIN ANALYSIS
1  PROGRAM MAIN
2  FOR I:= 1 TO NUMBER_OF_TIME_STEPS DO:
3    FOR W:= 1 TO NUMBER_OF_VEHICLE_LOADS DO:
4      X[W]:= UPDATE_LOAD_POSITION()
5      IF X[W] IS_ON_THE_STRUCTURE THEN:
6        E[W]:= CHECKS_CONTACT_ELEMENT_NUMBER()
7        F[W]:= ELEMENT_NODAL_FORCES_VECTOR()
8        ADD_TO_GLOBAL_FORCES_VECTOR(F[W])
9        IF VEHICLE_INERTIAL_EFFECT == TRUE THEN:
10         M:= ASSEMBLE_VEHICLE_LOAD_MASS_MATRIX(E[W],X[W])
11         UPDATE_GLOBAL_MASS_MATRIX(M)
12       END IF 9
13     END IF 5
14   END FOR 3
15   FL : = ASSEMBLE_NEWMARK_PSEUDOFORCE_VECTOR()
16   KL : = ASSEMBLE_NEWMARK_PSEUDOSTIFFNESS_MATRIX()
17   U[:, I]:= SOLVE_NEWMARK_PSEUDOSYSTEM_FOR_DISPLACEMENT(FL,KL)
18   V[:, I]:= CALCULATE_VELOCITY()
19   A[:, I]:= CALCULATE_ACCELERATION()
20 END FOR 2
21 RETURN(U,V,A)
22
23 END MAIN
```

4 CASE STUDY

4.1 SINGLE MOVING MASS

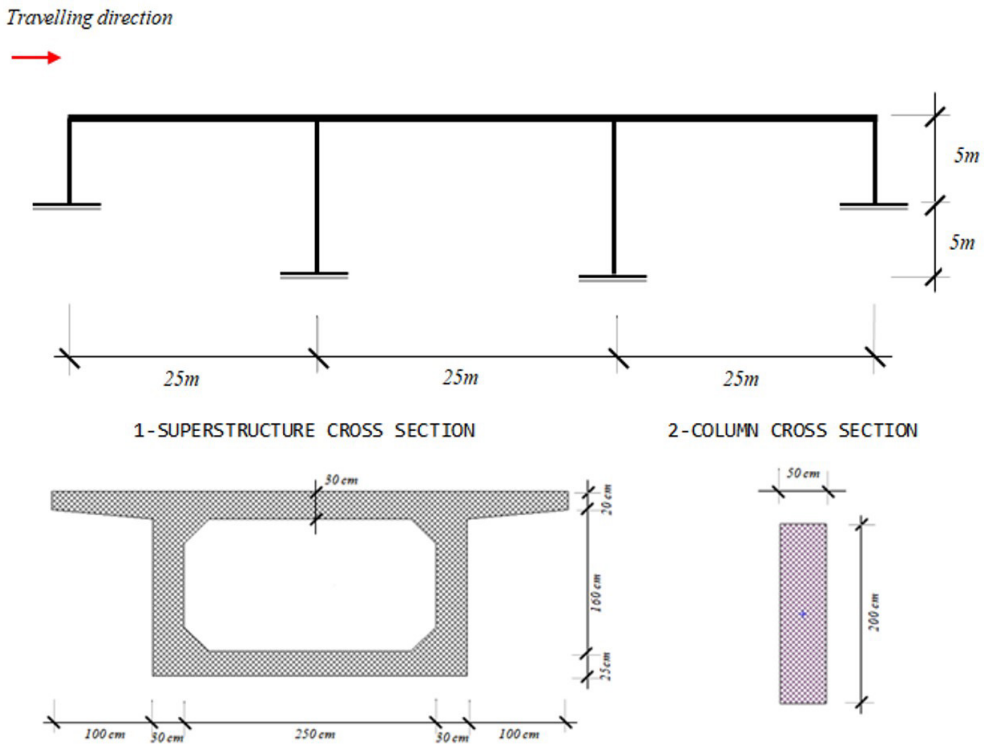

Figure 7. The structural model.

The structural model and the cross sections used in the analysis are shown in Figure 7. The material and properties of the structural model are presented in Table 2.

Table 2. Material and section properties [kN, m].

MATERIAL PROPERTIES						
Num	**E**	**Poisson**	**Alpha**	**Gamma**		
1	28E+06	0.2	1E+05	25.0		
SECTION PROPERTIES						
Num	**Ax**	**Ay**	**Az**	**Ix**	**Iy**	**Iz**
1	3.1	0.0	0.0	2.96	5.16	1.51
2	1	0.0	0.0	0.07	0.33	0.021

Where, E is the Young's modulus, Gamma is the specific weight of the material, A the cross-sectional area, I_y and I_z the second moment of area, I_x the torsional constant of the section, *Alpha* and *Gamma* are the material thermal expansion coefficient and the specific weight, respectively, A_y and A_z represent the shear areas (the effective area of the section participating in the shear deformation). The model is then pre-processed by the software as shown in Figure 8. The discrete model is represented by 20 elements and 126 degrees of freedom. The element consistent mass matrix was implemented in order to better represent the mass distribution within its domain. Figure 9 shows the moving mass analysis input data from the software's editor. The analysis properties shown were changed throughout the process.

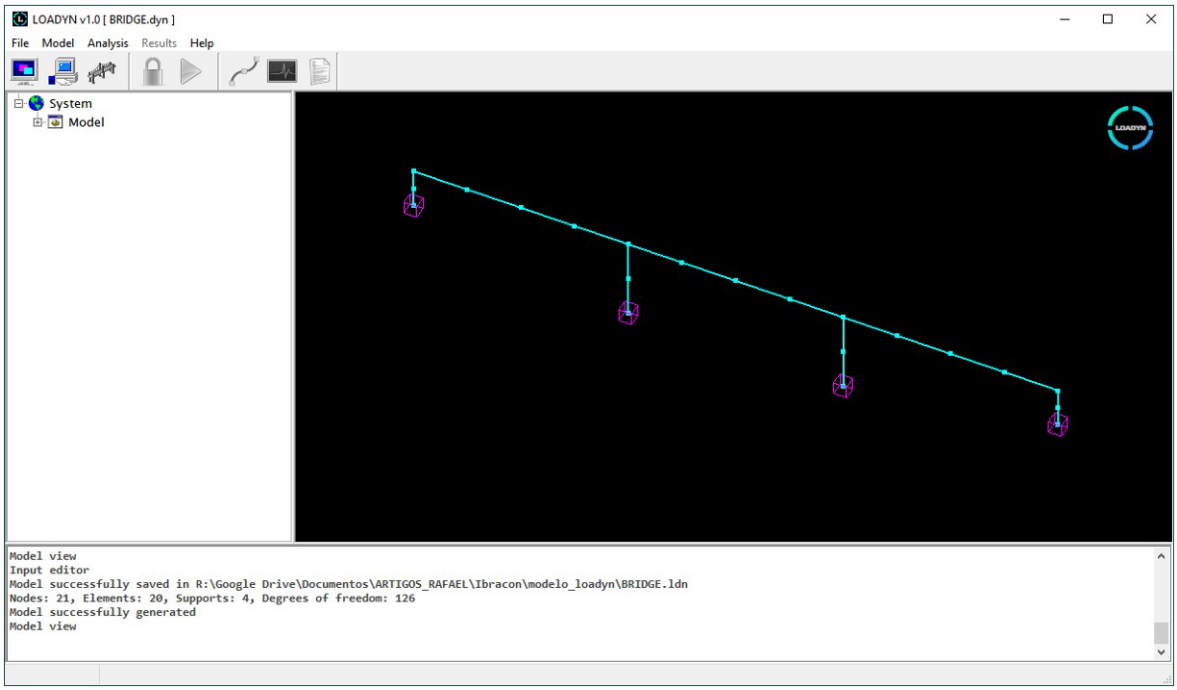

Figure 8. Pre-processed model.

```
RAYLEIGH DAMPING PROPERTIES
Omega i    Omega j    Damp. ratio
   13.9       37.3           0.05
0

TRAFFIC SEQUENCE
Elements
        1 2 3 4 5 6
Entry node
        1 1 1 1 1 1
0

VEHICLE PROPERTIES
Load magnitude    No of loads    Axle dist   Speed  Acceleration
         -4000              1            0      20             0
0

MOVING MASSES ANALYSIS DYNAMIC PROPERTIES
Iterations        Delta t        Inertial effect
       750           0.01                      1
0
```

Figure 9. Analysis input data.

The structure mass used to compute the mass ratio (vehicle/bridge) was the superstructure mass between columns (middle free span). In this section a single moving load/mass was considered.

4.2 MULTIPLE MOVING MASSES

This section prepares the analyses to compare the results of the critical speed analysis for the multiple moving loads and masses problems using the same structural model.

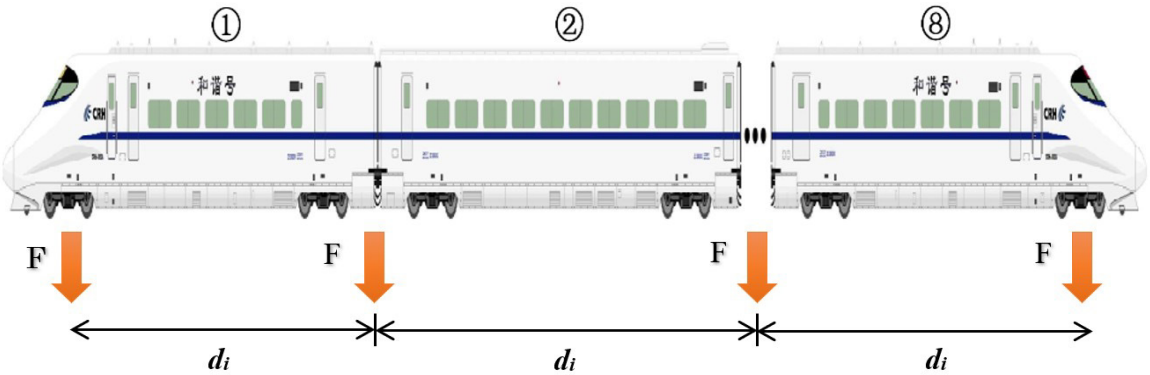

Figure 10. Axle arrangements of high speed train model.

Figure 10 shows a schematic representation of the vehicle. The train is modeled by multiple forces F (axles) equally spaced by d_i . It consists of 8 cars with the length of 25m each. In summary, the entire vehicle is modeled by 9 loads of 125 kN each. The critical speed analysis input data for vehicle speed was 10 m/s as starting speed to 150m/s as final speed. The vehicle speed was incremented 200 times between the defined speed limits. The critical speed analysis process was presented in section 2 of this study.

5 RESULTS AND DISCUSSIONS

5.1 SINGLE MOVING MASS CASE

The analyses are iteratively performed in order to gather enough data. For each performed analysis the bridge maximum absolute vertical displacement of the central node and the mass ratio are stored. The comparison results are presented in Figure 11. The first one compares the structure absolute maximum displacement values obtained by the moving mass and moving load analyses for different mass ratios. The second one compares the relative difference between the structure absolute maximum displacement values obtained by the moving mass and moving load analyses.

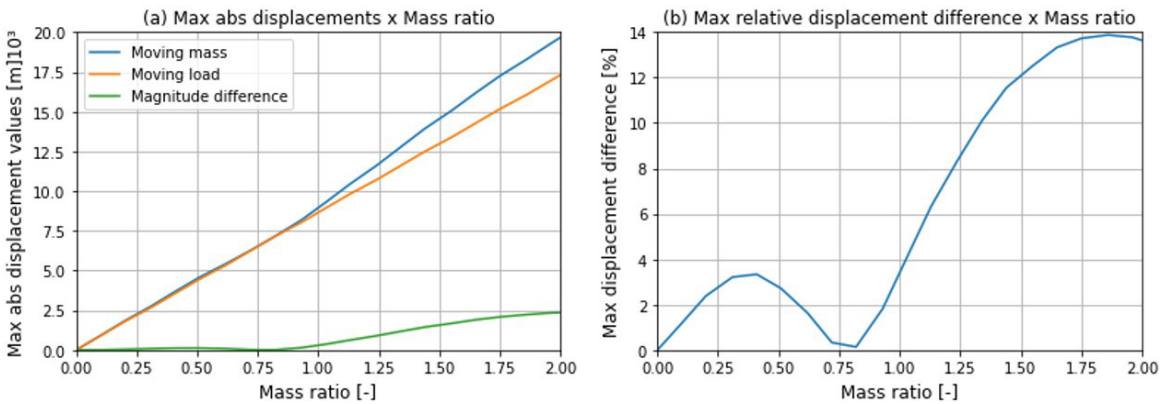

Figure 11. (a) Absolute and (b) relative difference between analysis max responses.

Figure 11 shows the difference between the moving mass analyses and the moving load analyses responses maximum absolute and relative values. For this case study, as shown, the responses difference only has significant

values when the mass ratio becomes greater than approximately one. In other words, the vehicle inertial effect plays a non-negligible role in the analysis when the vehicle mass is greater than the structure mass in terms of magnitude. Figure 12 shows and compares the time history responses of both moving mass and moving load analysis for different mass ratios.

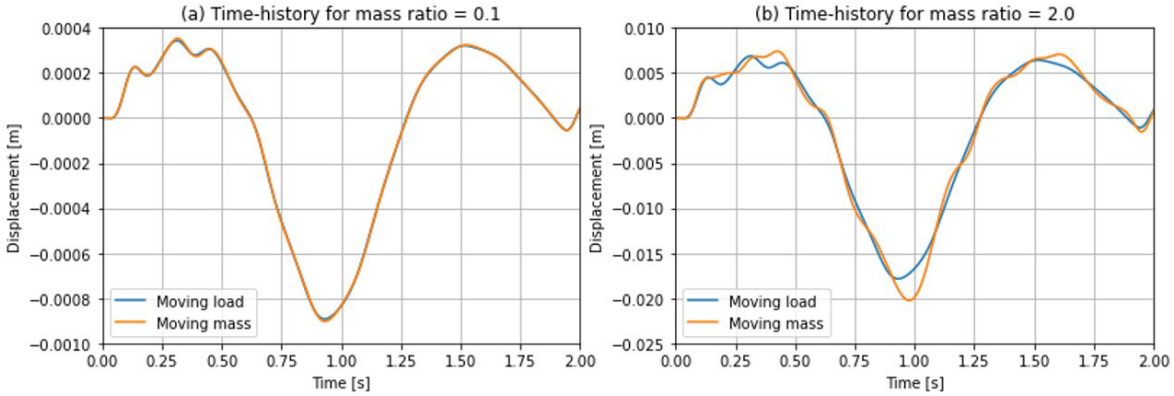

Figure 12. (a) Time-history for mass ratio = 0.1 (b) Time-history for mass ratio = 2.0.

From chart (a) on Figure 12, it is clear that the absolute displacement difference between analyses types is almost inexistent from an engineering point of view. Chart (b), visually shows clear absolute magnitude difference between responses. This magnitude difference is measured and presented on Figure 13 in absolute terms over time.

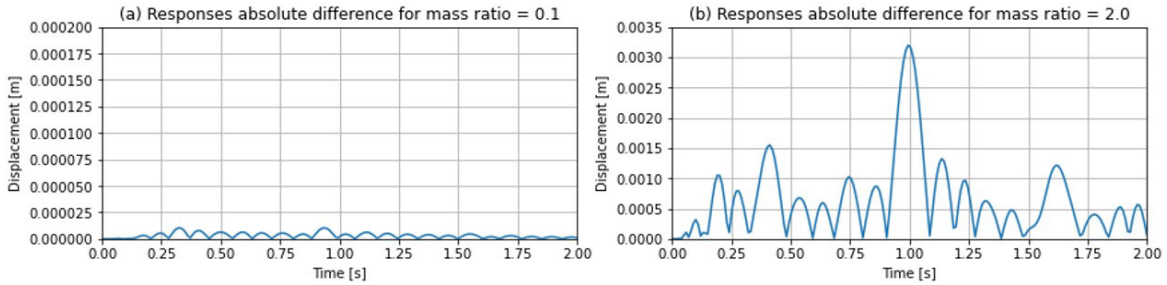

Figure 13. (a) Time-history absolute difference for mass ratio = 0.1 (b) Time-history absolute difference for mass ratio = 2.0.

The absolute magnitude time-history difference between analyses is not only visually, but quantitatively confirmed. As already discussed, for a low mass ratio the difference between analyses is negligible from an engineering perspective. Notice that Figure 13a and b do not share the same order of magnitude on the ordinate axis scale. In some cases, the relative difference is also important as shown next.

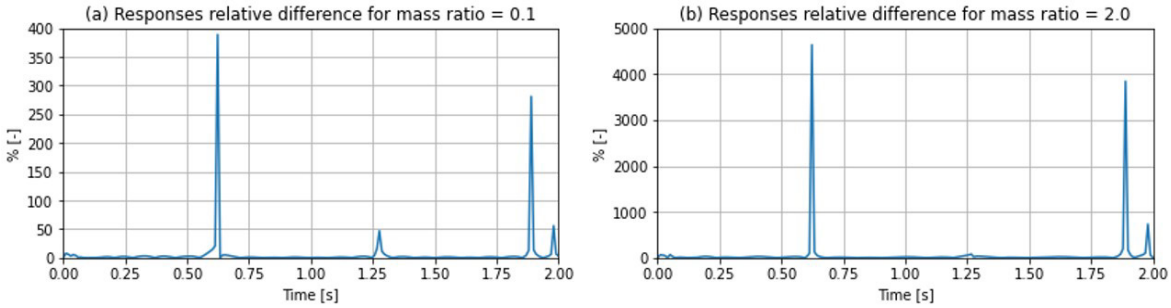

Figure 14. (a) Time-history relative difference for mass ratio = 0.1 (b) Time-history relative difference for mass ratio=2.0.

Figure 13 and 14 demonstrate that the greater relative differences do not necessarily occur at the same point in time where the biggest absolute differences occur. This in turn does not mean that the relative differences are necessarily bigger than the absolute ones. The relative differences peaks occur when time-history values get close to zero.

Ultimately, the relation between the structure and vehicle mass ratio and the vehicle speed is plotted against the maximum structural response on the same degree of freedom for the given moving load and the moving mass situation. Figures 15 and 16 show the structural response tendency across the analyzed dimensions for the moving load and moving mass problem, respectively. The former shows a linear variation of the response throughout the mass ratio axis for any given velocity. On the other hand, when observed from the velocity axis, the response assumes a specific shape which is entirely linearly amplified for any increasing mass ratio. The response peaks often indicate resonance condition and should be avoided. The latter shows an indirect behavior of the response across any analyzed dimension. In addition, for any increasing variation of mass ratio at any given velocity, a non-linear growth of the response can be noticed. Figures 17 and 18 feature the contour plots of the discussed situations in order to provide, perhaps, a better comprehension of the general behavior of the moving load/mass problem.

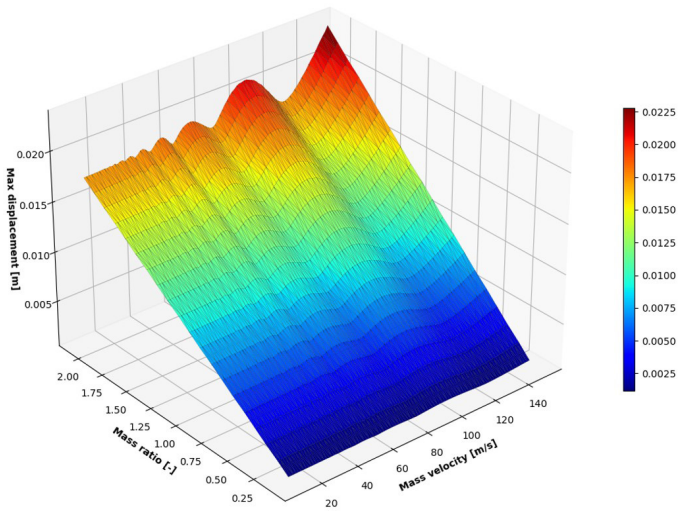

Figure 15. 3D Plot for the moving load problem.

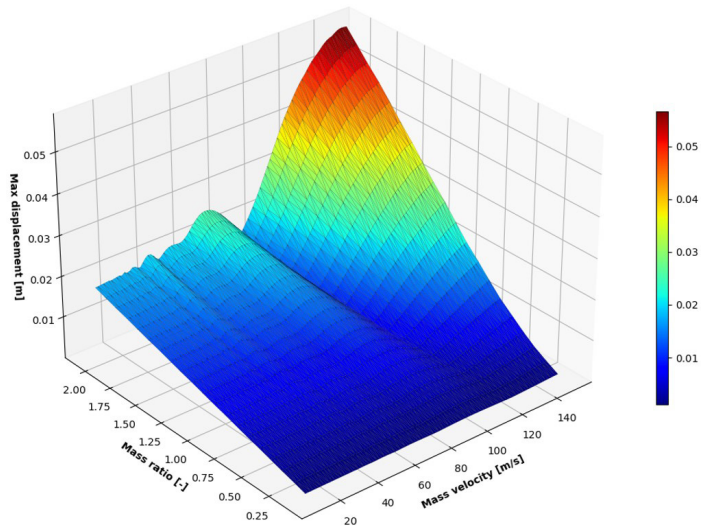

Figure 16. 3D Plot for the moving mass problem.

Figure 15 clearly shows the increasing direct response shape tendency across the mass ratio dimension as presented. In Figure 16, the response peaks appear to be left shifted as the mass ratio grows. This configures a decrease in resonance velocities as the mass ratio increases. In other words, the greater the mass present on the structure, the lower the dynamic natural frequency of the entire system. Consequently, a lower travelling vehicle velocity is required to generate critical structural responses. That justifies the left shifted response peaks.

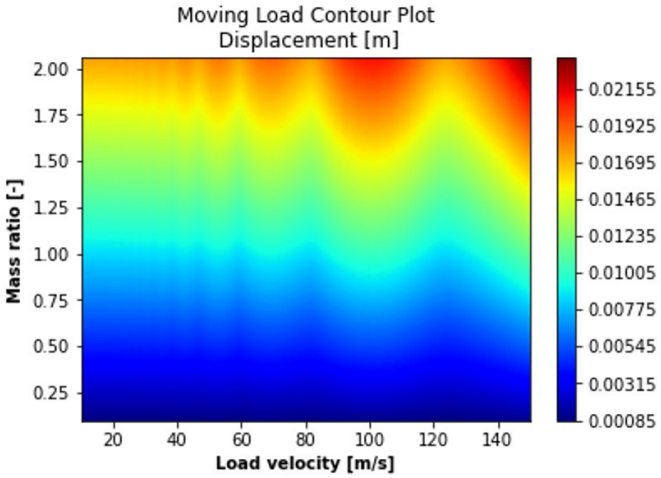

Figure 17. Contour Plot for the moving load problem.

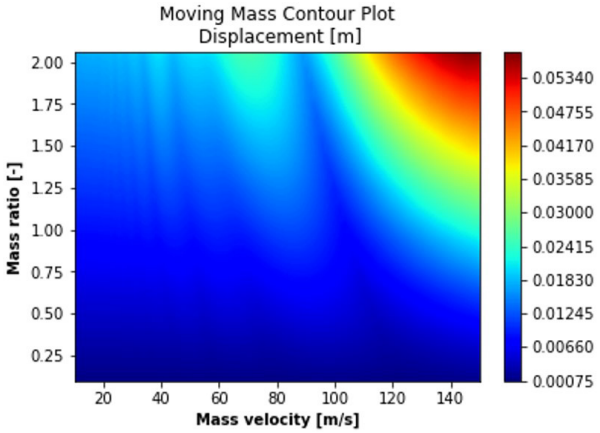

Figure 18. Contour Plot for the moving mass problem

5.2 MULTIPLE MOVING MASSES CASE

First, different time history responses are presented for the multiple moving masses scenario. Figure 19 shows the midpoint vertical displacements time-histories for a vehicle travelling speed of 10 m/s with an integration time step $\Delta t = 0.01s$ and a vehicle travelling speed of 150 m/s with an integration time step $\Delta t = 7 \, . \, 10^{-4} s$. Figure 20 shows the acceleration time-histories based on the same parameters mentioned for Figure 19.

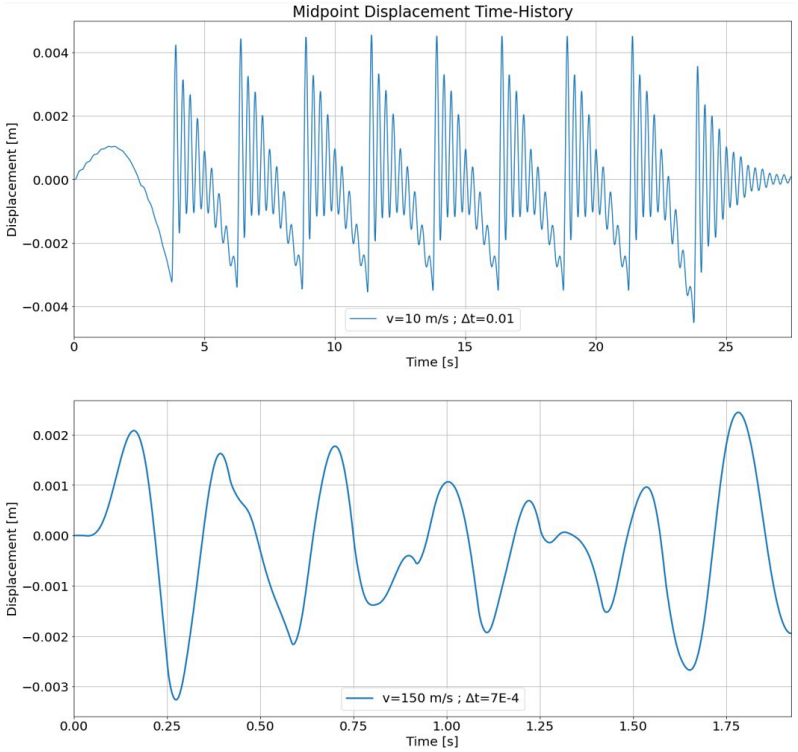

Figure 19. Displacement time-history

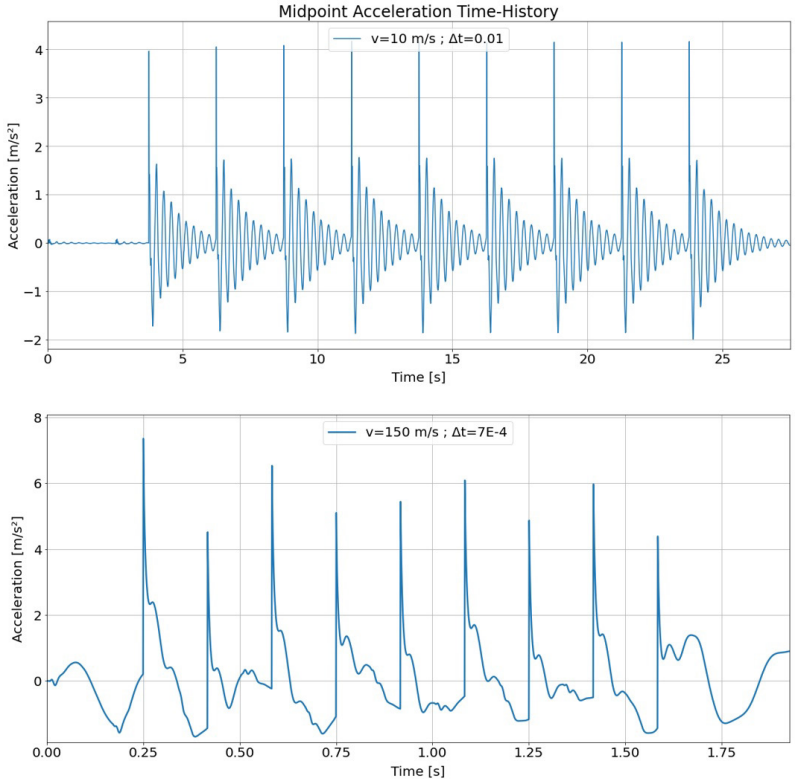

Figure 20. Acceleration time-history

These analyses were performed in order to better simulate real design situations with multiple moving masses acting simultaneously on the structure. Critical speed analysis for the multiple moving loads and multiple moving masses cases were also performed and compared as follows. Figure 21 shows that the greater response peak occurs at a vehicle travelling speed of approximately 90 m/s.

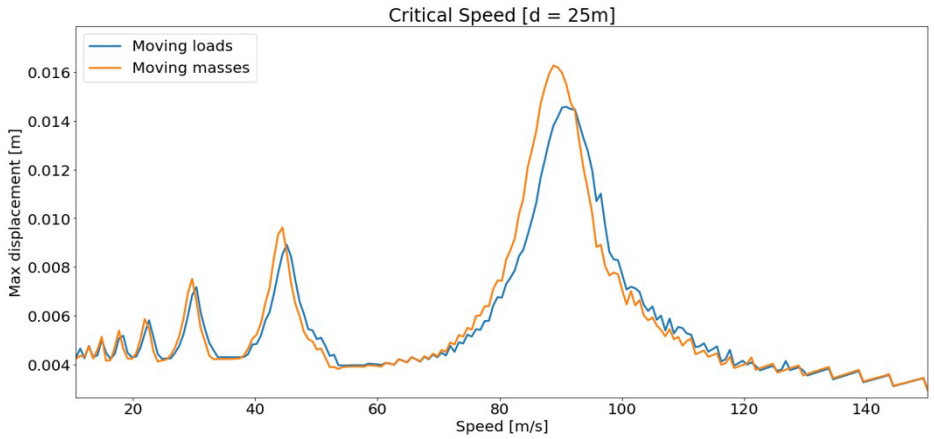

Figure 21. Critical speed analysis [d=25m]

The critical speeds (peaks) in Figure 21 seem to be shifted to the left when dealing with the moving masses analysis. This represents a decrease in critical speeds and can be coherently justified by the fact that the vehicle masses are being added to the system as a whole. Which in turn, evidently, decreases its natural frequencies and as a consequence, lower vehicle travelling (lower external frequency) speeds are able to generate maximum responses. The same train with a smaller distance *d* between axles would have generated a slightly greater left shift in the critical speeds, since the amount of masses that would have been present on the system at the same time would also have been greater as will be shown.

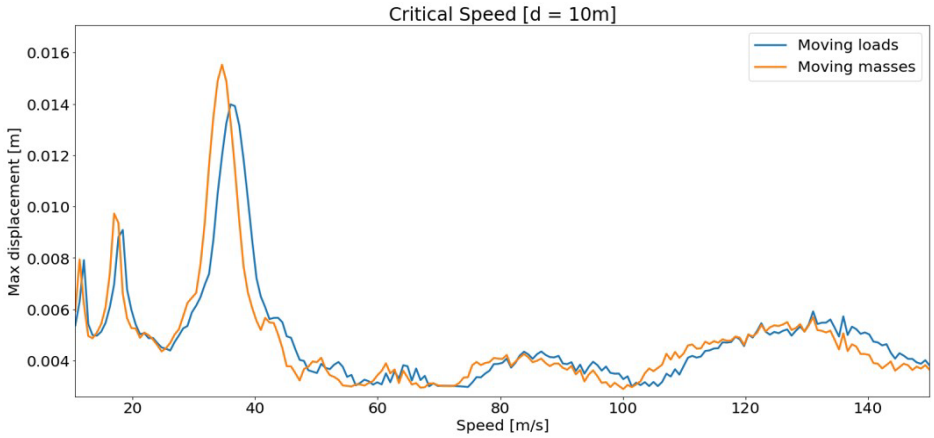

Figure 22. Critical speed analysis [d=10m]

Figure 22 shows that the main critical speed peak moved from 90 m/s in Figure 21 to approximately 40 m/s by simply changing the length of the vehicle. In both figures the moving mass analyses displacements show a greater value than the moving load analyses. Critical speeds are calculated for a specific set of vehicle and structure. Any change on the set leads to a completely different response behavior.

6 CONCLUSIONS

The bridge dynamic problem induced by moving bodies has been studied since the beginnings of engineering itself. Although it is common practice to adopt simplified and standardized methods to overcome these kinds of problem, the current technological development allows specific approaches to solve specific problems. This, in turn, may even generate more affordable solutions. One approach possibility is to include the inertial forces caused by the travelling vehicles in the analysis. Its relevance grows as the vehicle speed and/or the mass ratio grow.

The presented software solves the dynamic problem by coupling the vehicle mass matrix with the structure mass matrix at each integration time step. The problem formulation can be easily extended in order to account for two-dimensional finite elements, more complex vehicles, rail irregularities, jump conditions and so on.

As shown, for low mass ratios the responses difference magnitude between moving mass and load analyses stays negligible within engineering perspective. On the other hand, it was noticed that for mass ratios greater than one, the moving mass analysis should be chosen instead of the moving load one, since the absolute and the relative differences show values that cannot be treated as irrelevant any more. Additionally, the maximum relative and absolute difference do not occur at the same instant in the time-history analyses.

The consideration of the vehicle inertial forces in the analysis decreases the resonant speeds as the mass ratio increases in the overall scenario. This generates more precise and reliable results which tend to be closer to reality despite the inherent and necessary approximations.

Taking into account the technological resources currently available, the moving mass analysis might be more advantageous than the moving load analysis. In most cases, the amount of additional computational time and power required for the inertial analysis do not represent a major problem.

7 REFERENCES

[1] S. S. Lima, H. L. Soriano, and F. J. C. Reis, “Considerações quanto à determinação do coeficiente de impacto em pontes,” *Eng. Estud. Pesqui.*, vol. 5, p. 7, 2002.

[2] F. K. R. Cepeda and F. G. Castillo, *Análisis Dinámico de Estructuras Sometidas a Acciones de Trenes de Alta Velocidad*. Madrid: Grupo de Mecánica Computacional/Universidad Politécnica de Madrid, 2005.

[3] E. Savin, "Dynamic amplification factor and response spectrum for the evaluation of vibrations of beams under successive moving loads," *J. Sound Vibrat.*, vol. 248, no. 2, pp. 267–288, 2001.

[4] L. Frýba, *Vibration of Solids and Structures under Moving Loads*. The Netherlands: Springer, 1972.

[5] L. Frýba and T. Telford, *Dynamics of Railway Bridges*. República Tcheca: Thomas Telford Ltd., 1996, pp. 332.

[6] S. P. Timoshenko, D. H. Young, and W. Weaver, *Vibration Problems in Engineering*. Baltimore: John Wiley & Sons, 1974.

[7] Y. B. Yang, J. D. Yau, and Y. S. Wu, *Vehicle-Bridge Interaction Dynamics: With Applications to High-Speed Railways*. Singapore: World Scientific Publishing Co. Pte. Ltd., 2004.

[8] Y. Wang, Q. Wei, J. Shi, and X. Long, "Resonance characteristics of two-span continuous beam under moving high speed trains," *Lat. Am. J. Solids Struct.*, vol. 7, pp. 185–199, 2010.

[9] W. Suijiang, "Numerical calculation of bridge seismic response considering beam-block colligion effect," *J. Constr.,* pp. 111–122, 2019.

[10] P. Bucinskas and L. V. Andersen, "Dynamic response of vehicle-bridge-soil system using lumped-parameter models for structure-soil interaction," *Comput. Struc.*, vol. 238, pp. 106270, 2020.

[11] A. Pesterev, "On asymptotics of the solution of the moving oscillator problem," *J. Sound Vibrat.*, vol. 260, no. 3, pp. 519–536, 2003.

[12] R. C. Hora, S. S. Lima, and S. H. C. Santos, "Avaliação da resposta dinâmica de uma ponte sob ação de massas móveis," Dissertação de mestrado, Univ. Fed. Rio Jan., Rio de Janeiro, Brasil, 2021.

[13] K.-J. Bathe, *Finite Element Procedures*. USA: Prentice-Hall, 1996.

[14] C. A. Felippa, *Introduction to Finite Element Methods*. Colorado: Department of Aerospace Engineering Sciences and Center for Aerospace Structures, University of Colorado, 2004. p. 612.

[15] A. K. Chopra, *Dynamics of Structures. Theory and Application to Earthquake Engineering*, 4th ed. USA: Prentice-Hall.

[16] R. W. Clough and J. Penzien, *Dynamics of Structures*. Berkeley, CA, McGraw-Hill College, 2003.

[17] S. S. Lima and S. H. C. Santos, *Análise Dinâmica das Estruturas, vol. 1*. Rio de Janeiro: Ciência Moderna, 2008.

[18] S. S. Lima, *Análise de Estruturas com Computadores*. Rio de Janeiro: Ciência Moderna, 2017.

[19] N. M. Newmark and S. P. Chan, *A Comparison of Numerical Methods for Analyzing the Dynamic Response of Structures*. Urbana, Illinois: University of Illinois, 1952.

[20] G. Noh and K.-J. Bathe, "For direct time integrations: a comparison of the Newmark and Bathe schemes," *Comput. Struc.*, vol. 225, pp. 1–12, 2019.

[21] J. S. Przemieniecki, *Theory of Matrix Structural Analysis*. New York: McGraw-Hill, 1968.

Author's contributions: RCH: conceptualization, writing, data curation, formal analysis; SSL: conceptualization, supervision, data curation, formal analysis; SHCS: conceptualization, supervision, data curation, formal analysis.

Editors: Bernardo Horowitz, Guilherme Aris Parsekian.

IBRACON Structures and Materials Journal
Revista IBRACON de Estruturas e Materiais
ISSN 1983-4195 ismj.org

ORIGINAL ARTICLE

Effect of ultrasonication on carboxyl-functionalized multiwalled carbon nanotubes in fresh and hardened Portland cement pastes

Efeito da ultrassonicação em nanotubos de carbono de paredes múltiplas funcionalizados com grupo carboxílico no estado fresco e endurecido de pastas de cimento Portland

André Valmir Saugo Ribeiro[a]
Jéssyca Mendes da Silva[a]
Karyne Ferreira dos Santos[b]
Francine Padilha[a]
Philippe Jean Paul Gleize[a]

[a]Universidade Federal de Santa Catarina – UFSC, Departamento de Engenharia Civil, Florianópolis, SC, Brasil
[b]Universidade de Brasília – UnB, Engenharia Civil, Brasília, DF, Brasil

Received 03 June 2022
Accepted 18 January 2023

Abstract: The effects of chemical and physical methods on multiwalled carbon nanotube (MWCNT) dispersion in Portland cement pastes were investigated. Consistency, rheology, compressive strength, dynamic elastic modulus, flexural strength, water absorption, and void content tests were performed to evaluate these effects. Changes in the rheology of the cement pastes and surfactants resulted in a significant reduction in apparent viscosity and yield strength. Additionally, cement pastes containing carboxyl- functionalized MWCNTs (MWCNT-COOH) and surfactant showed higher compressive strengths at 28 d. However, the ultrasonic dispersion method did not significantly influence the properties of hardened Portland cement compared with Portland cement produced using the non-sonicated aqueous solution.

Keywords: physical and chemical dispersion, multiwalled carbon nanotube, cement paste, compressive strength.

Resumo: Foram investigados os efeitos dos métodos químicos e físicos na dispersão de nanotubos de carbono de paredes múltiplas (MWCNT) em pastas de cimento Portland. Para avaliar estes efeitos, foram realizados testes de consistência, reologia, resistência à compressão, módulo elástico dinâmico, resistência à flexão, absorção de água, e teor de vazio. As alterações na reologia das pastas de cimento e surfactantes resultaram numa redução significativa da viscosidade aparente e da resistência ao escoamento. Além disso, pastas de cimento contendo MWCNT funcionalizados com grupo carboxílicos (MWCNT-COOH) e surfactante mostraram maiores resistências à compressão a 28 d. No entanto, o método de dispersão ultrassônica não influenciou significativamente as propriedades do cimento Portland endurecido em comparação com o cimento Portland produzido utilizando a solução aquosa não sonicada.

Palavras-chave: dispersão física e química, nanotubo de carbono com múltiplas paredes, pasta de cimento, resistência à compressão.

How to cite: A. V. S. Ribeiro, J. M. Silva, K. F. Santos, F. Padilha, and P. J. P. Gleize, "Effect of ultrasonication on carboxyl-functionalized multiwalled carbon nanotubes in fresh and hardened Portland cement pastes," *Rev. IBRACON Estrut. Mater.*, vol. 16, no. 6, e16602, 2023, https://doi.org/10.1590/S1983-41952023000600002

Corresponding author: André Valmir Saugo Ribeiro. E-mail: andrecivilutfpr@gmail.com
Financial support: Coordenação de aperfeiçoamento de pessoal de nível superior (CAPES). Conselho nacional de desenvolvimento científico e tecnológico (CNPq).
Conflict of interest: Nothing to declare.
Data Availability: The data that support the findings of this study are available from the corresponding author, A.V.S. RIBEIRO, upon reasonable request.

1 INTRODUCTION

Recently, the incorporation of nanomaterials into Portland cement matrices has been the subject of numerous investigations [1]–[4]. These studies clearly indicated that the presence of nanomaterials in cement matrices improves both mechanical performance and durability, depending on their effective dispersion within the composites [5]–[8].

Carbon nanotubes (CNTs) are among the common nanomaterials used in cementitious matrices [9]. One way to classify them is based on the number of walls or layers present in their structure; multiwalled carbon nanotubes (MWCNTs) or single-walled carbon nanotubes (SWCNTs). It is noteworthy that MWCNTs are readily available owing to the low complexity of their production compared with SWCNTs, which provides a reduction in the final cost of the product.

Several studies [4], [10], [11] emphasized that the incorporation of MWCNTs, 0.10% relative to the mass of Portland cement (w.c.), creates connections that enhance stress distribution when sufficient adequate MWCNT-matrix adhesion is achieved. This effect was reported to control or mitigate the propagation of microcracks and reduce the porosity of Portland cement-based composites.

In addition to modifying the structure of the composite in its hardened state, the incorporation of CNT has been reported to promote variation in the rheological properties of cement pastes because it can increase the yield strength and viscosity of the mixtures. A reduction in mortar dispersion was achieved by incorporating MWCNTs (0.10% w.c.) and a fixed surfactant admixture content [8]. Notably, a reduction in the scattering diameter (slump test) by 30 mm was confirmed, which verified that the nanomaterial interacts with the mixture and promotes improved dispersion based on a mechanical response. Moreover, the amount of free surfactant in the system decreased, which reduced its lubricating capacity and, consequently, decreased dispersion.

The interaction of functionalized CNTs with water was capable of reducing the amount available for lubrication of the system [3]. Consequently, greater friction between the particles is generated owing to the higher solid content in the mixture. When comparing the dynamic yield strength and apparent viscosity of mortars without and with MWCNT (0.25% w.c.), an increase of 25 to 125 Pa and 1.6 to 2.25 Pa.s was observed, respectively. This behavior was attributed to the high specific surface area of the nanomaterial and the adsorption of the dispersant admixture on its surface.

However, studies have indicated that the main challenge regarding CNT utilization is their effective dispersion in the matrix. [12]–[14]. CNTs tend to agglomerate owing to Van der Waals forces of attraction, in addition to their high specific surface area and aspect ratio (length/diameter), which further contributes to agglomeration. Moreover, it is noteworthy that its hydrophobic character further complicates its dispersion in an aqueous medium.

A combination of physical and chemical methods can be used to promote the dispersion of these nanomaterials. Among the existing physical methods, ultrasonication is the most common because it provides high dispersion by applying ultrasonic pulses to the solution and disaggregating the nanotubes [15]–[17]. Two ultrasonication procedures are possible: probe (tip) or bath, the former is the most common and effective [4]. However, the time and energy applied requires careful consideration. When these factors are too low, efficient dispersion of the nanomaterial cannot be achieved. In contrast, when they are too high, damage such as shortening and reduction of the diameter of the nanomaterial may occur, which reduces its performance [10], [18].

Chemical methods involve the functionalization of nanomaterials and are divided into covalent and noncovalent modifications. The former refers to the treatment of nanotubes using acids that alter the surface of the CNTs, promoting the insertion of functional groups such as -OH or -COOH. Conversely, noncovalent functionalization utilizes surfactants that interact with CNTs, promoting their dispersion and preventing re-agglomeration, while preserving the structure and properties of the nanomaterial [19]–[21]. Based on these reports, MWCNTs dispersion techniques are complex and often applied in combination to improve the performance of the final product.

Although several studies have evaluated the addition of nanomaterials to cementitious matrices, the application of different dispersion methods (combined and separately) to MWCNTs in aqueous solutions and the probable existence of a synergistic effect, based on the mechanical and rheological properties, has not been reported thus far. This study aims to investigate the combined effect of the different dispersion methods of CNTs functionalized with carboxyl groups (-COOH) on their performance in Portland cement pastes. Thus, this study includes the characterization of compressive strength, flexural strength, Young's modulus, water absorption, and pore volume, in addition to rheological analysis by scattering and rheometry. The fresh and hardened states of the pastes are evaluated to determine the effect of mainly ultrasonication, in terms of its promotion of CNT dispersion.

2 MATERIALS AND EXPERIMENTAL PROGRAM

The CNTs used in this study were purchased from Nanostructured & Amorphous Materials Inc. (Figure 1). These CNTs, with a length of 10–30 μm, internal diameter of 5–10 nm, external diameter of 20–30 nm, and 95% purity, were

functionalized by the addition of carboxyl groups (-COOH) to their structure (1.9 to 2.1 wt%). The MWCNTs content used in the cement paste was 0.10% relative to the cement mass (c.w.) because it is the most commonly used nanomaterial content to achieve an improved mechanical response in literature [22]. A common Portland cement was used for the preparation of the pastes, and its physicochemical characterization is listed in Table 1. Notably, the C4AF content was determined based on the Bogue equation. Additionally, two types of surfactants (SA and SB), based on polycarboxylate, were used at a 1:1 ratio (nanotube:surfactant).

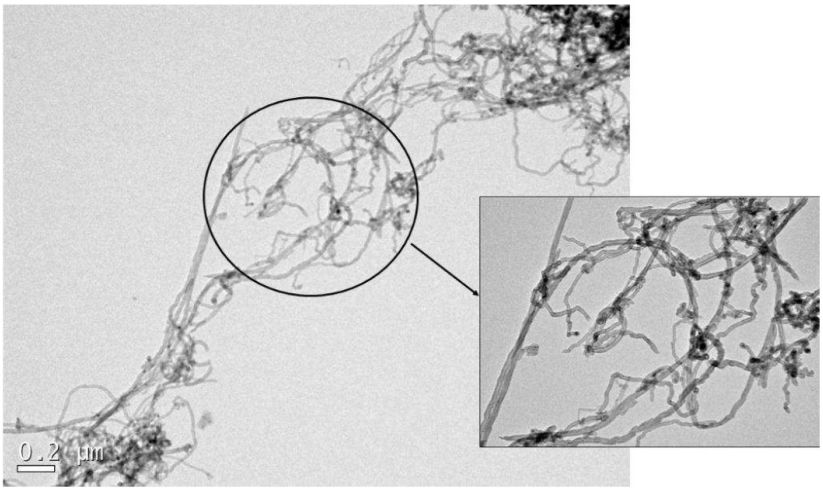

Figure 1. Transmission electron microscopy (TEM) on the CNTs

Table 1. Physical and chemical characterization of ordinary Portland cement.

Physical Analysis	
Specific gravity (kg/dm^3)	3,09
Blaine (cm^2/g)	4698
Chemical analysis	
Loss on ignition (%)	4,8
C3S (%)	55,8
C2S (%)	14,36
C3A (%)	7,1
C4AF (%)	9,59

The solid contents of the surfactants (SA and SB) were characterized according to literature [23]. Surfactants SA and SB were composed of 30.17% and 42.04% solids, respectively. Moreover, Fourier transform infrared spectroscopy (FTIR) was performed to qualitatively identify its components according to absorbance peaks (Figure 2).

FTIR confirmed the presence of polycarboxylates, which is associated with the peaks observed between 3400 and 3200 cm^{-1}, corresponding to -OH stretching vibrations, and the presence of ether groups observed at 1250–950 cm^{-1} [24]–[26]. Surfactants SA and SB exhibited characteristic peaks at 2865 and 2950 cm^{-1}, associated with the symmetrical and asymmetrical stretching vibrations of aliphatic CH, respectively. The peak observed between 1680 and 1620 cm^{-1} corresponds to the absorption of the =C=C group and the stretching vibration band observed at 1105 cm^{-1} corresponds to C-O-C. Additionally, carboxylic acids (1696 cm^{-1}) and CO stretching vibrations (1130–1070 cm^{-1}) were observed. The higher hydroxyl peak for SA may indicate that the surfactant was less concentrated than SB, confirming the solid content test results. Moreover, the peak identifying the carbonyl group was higher in SB than that in SA.

Initially, the solutions were prepared as follows (Figure 3): (1) water only (with and without ultrasonication), a mixture of water with surfactant SA or SB (with and without ultrasonication), a mixture of water with MWCNTs (with and without ultrasonication), and mixtures of water with SA or SB and MWCNTs (with and without ultrasonication). Thus, the type of surfactant, presence/absence of MWCNT, and presence/absence of the ultrasonication process were used as variables. For the sonicated solutions, a Vibra-Cell 750 Watts sonicator coupled to an ultrasonic processor (Series VCX) was used. Ultrasonication was performed for 5 min at 20 s intervals of shaking and rest, at a frequency of 20 kHz and 50% amplitude.

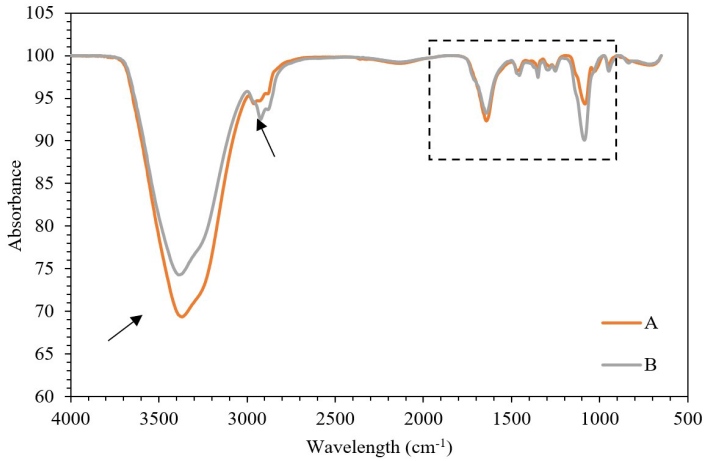

Figure 2. FTIR spectra of surfactants SA and SB.

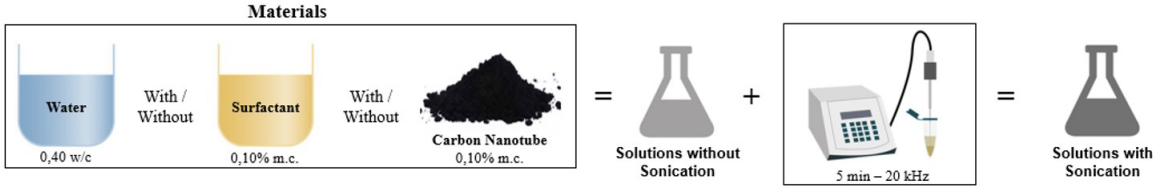

Figure 3. Preparation of solutions containing water, surfactants, and carbon nanotubes with and without the application of ultrasonication.

After obtaining the solutions for the production of the cement pastes, a high-power mixer was used at a speed of 10,000 rpm. A water/cement ratio of 0.40 was selected to obtain pastes without exudation, even in the presence of a surfactant, and ensure an adequate consistency for molding.

The mixing procedure started with the addition of Portland cement to the solution (Figure 4), which was manually mixed for 1 min, followed by 1 min of mixing using a high-power mixer. Subsequently, the mixture was allowed to rest for 1 min. Finally, the process was completed after 1 min of mixing using the high-power mixer. The amount of material used in each Portland cement paste, and the presence or absence of ultrasonication, are listed in Table 2.

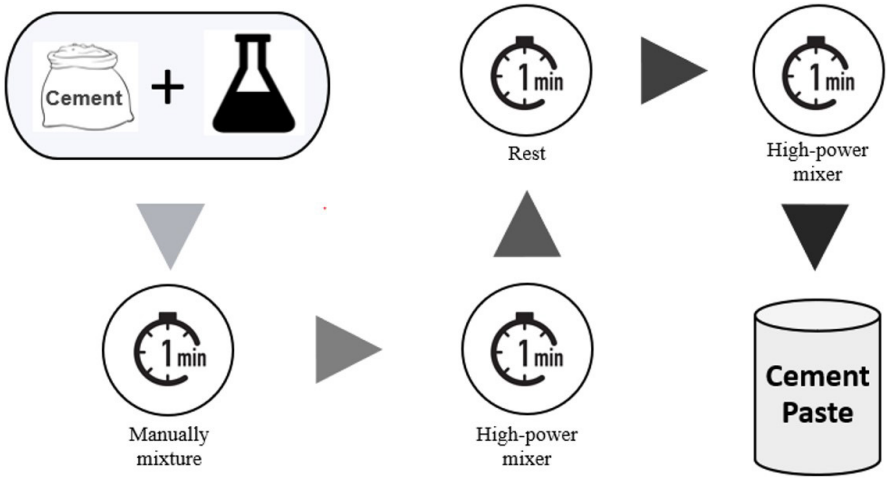

Figure 4. Cement pastes mixing procedure.

Table 2. Mixture compositions of Portland cement pastes.

Mix	Cement (g)	Water(g)	Surfactant (g)		MWCNT (g)	Ultrasonication			
			SA	SB		Water	SA	SB	CNT
Ref	100	40	-	-	-	-	-	-	-
A	100	40	0.10	-	-	-	-	-	-
B	100	40	-	0.10	-	-	-	-	-
Son	100	40	-	-	-	x	-	-	-
SonA	100	40	0.10	-	-	x	x	-	-
SonB	100	40	-	0.10	-	x	-	x	-
CNT	100	40	-	-	0.10	-	-	-	-
Son_CNT	100	40	-	-	0.10	x	-	-	x
SonA_CNT	100	40	0.10	-	0.10	x	x	-	x
SonB_CNT	100	40	-	0.10	0.10	x	-	x	x
A_CNT	100	40	0.10	-	0.10	-	-	-	-
B_CNT	100	40	-	0.10	0.10	-	-	-	-

For the analysis of fresh Portland cement pastes, scattering tests (mini-spreading) and rotational rheometry using parallel plate geometry were performed to evaluate the following rheological parameters: apparent viscosity, dynamic yield strength, and static yield stress. The mini-scatter test was developed by Kantro in 1980 using a conical trunk with smaller and larger diameters of 19 and 38 mm, respectively, and a height of 57 mm supported on a glass plate. After filling and densifying the paste in the mold, it was removed, and the spread was measured in a perpendicular direction. For the rheometry test, approximately 1 mL of sample was added to the rheometer container, and the tests were performed at 23 ± 1 °C according to the following procedure: (i) 60 s pre-shear at 100 s^{-1}; (ii) 60 s rest; (iii) shear from 0.1 to 10 s^{-1} in four steps of 20 s each distributed logarithmically; (iv) shear from 25 to 100 s^{-1} in six steps of 20 s each distributed linearly; (v) reduction of the shear rate to 0.1 s^{-1} in the same steps as (iv) and (iii), to evaluate the yield and dynamic yield stress. The following procedure was used to determine the static yield stress: (i) 60 s pre-shear at 100 s^{-1}; (ii) rest for 30 s; (iii) shear from 0.05 to 10 s^{-1} for 60 s. The rheometry and scattering results were measured 10 min after the production of the mixtures to standardize the time of the analyses. The Herschel–Bulkley model was used to determine the dynamic flow stress of the mixtures because it fits the non-Newtonian fluid behavior of Portland cement pastes better. The linear fit of the Herschel–Bulkley model proposed by de Larrard et al. [23] in Equation 1 was used to determine the equivalent viscosity [27].

$$\tau = \tau_0 + K\gamma n \quad (1)$$

where τ is the shear stress (Pa), τ_0 is the yield stress (Pa), K is the consistency factor, γ̇ is the shear rate (s^{-1}), and n is the pseudoplastic index. In this analysis, the apparent viscosity was calculated at the maximum shear rate (100 s^{-1}).

To determine the compressive strength at 28 d, five cylindrical specimens (20x40 mm) were molded for each mixture. Subsequently, the specimens were demolded after 24 h and submerged in water containing lime prior to testing. A universal testing machine (model Instron 5569) was used at a load speed of 0.50 MPa.s^{-1} with a 30 mm hinge positioned on top of the specimen.

For the dynamic modulus of elasticity and bending at three points, three prismatic specimens (20x20x100 mm) were molded. The three-point bending test was performed using the same equipment as for the compressive strength test, at the same velocity load. The dynamic modulus of elasticity test was performed on equipment from Sonelastic® Systems at ATCP Engenharia using the impulse excitation technique based on the ASTM-E 1876 standard [28].

The test results for the hardened state of the cement pastes were analyzed using the two-way analysis of variance (ANOVA) statistical analysis, and the conclusions were based on the F parameter with a reliability of 95%. OriginPro 2019 software was used for analysis.

3 RESULTS AND DISCUSSIONS

3.1 Fresh state of portland cement pastes

Figure 5 shows the spreading of the produced cement pastes. A decrease in pulp flow was observed with the incorporation of MWCNTs and ultrasonication, which may be attributed to the high specific surface area of the nanomaterials and the quality of their dispersion.

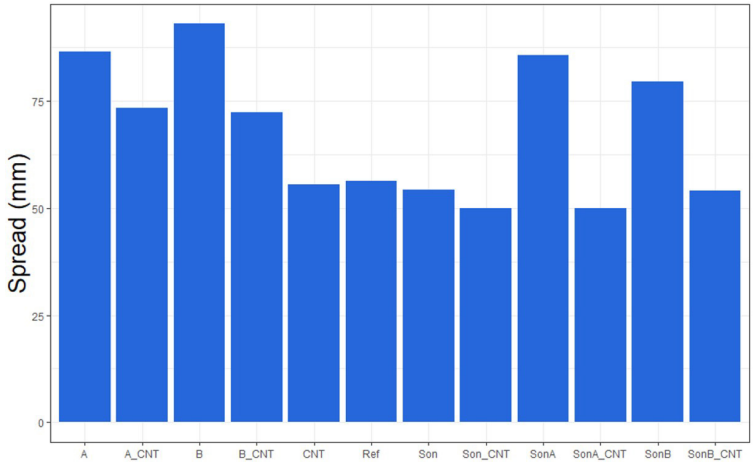

Figure 5. Spread of cement Portland pastes.

As shown in Figure 6, for the present study, both the modified Bingham model and the Herschel-Bulkley model can be used to calculate the rheological parameters of the paste curves. However, the model that best suited the behavior of the pastes was the Herschel-Bulkley model. This better fit can be visualized through the r^2 factor presented in Figure 6.

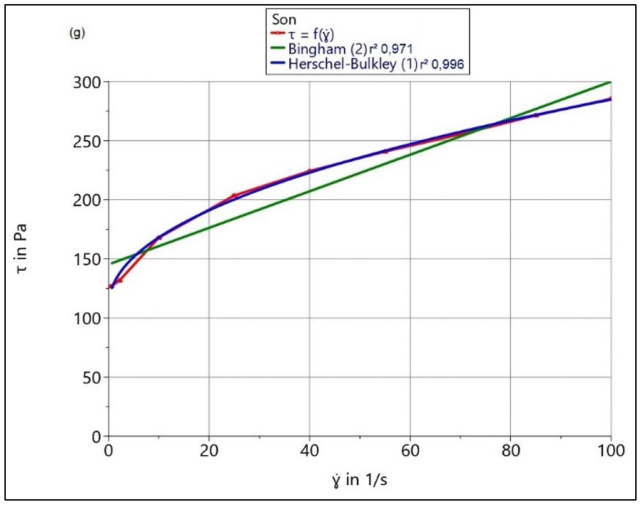

Figure 6. Rheological behavior curves of fresh Portland cement pastes fit with the Herschel-Bulkley and Bingham model.

Figures 7, 8, and 9 show the results of the static and dynamic yield stress and apparent viscosity of the cement pastes, respectively, with and without ultrasonication. It was observed that the combination of ultrasound/MWCNT generated higher static yield stresses compared to the other mixtures. This phenomenon can be due to the ultrasound process, which is responsible for the deagglomeration of MWCNTs. The deagglomeration increases specific surface area and, by doing so, improves the flow [29].

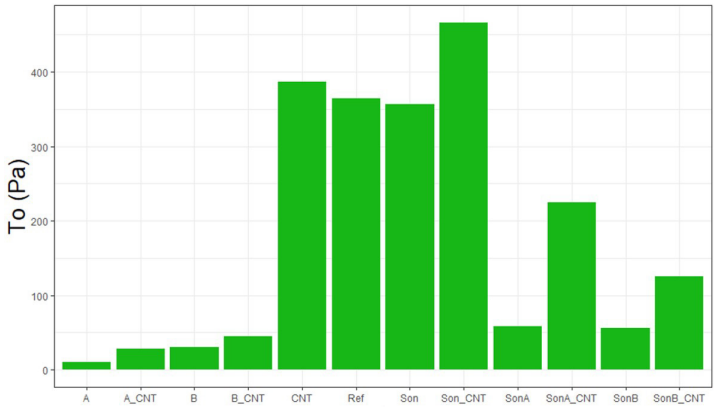

Figure 7. Static yield stress of the fresh Portland cement pastes.

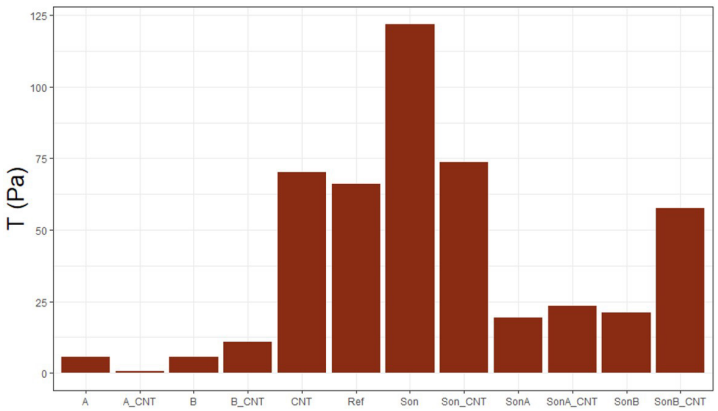

Figure 8. Yield stress of the fresh Portland cement pastes.

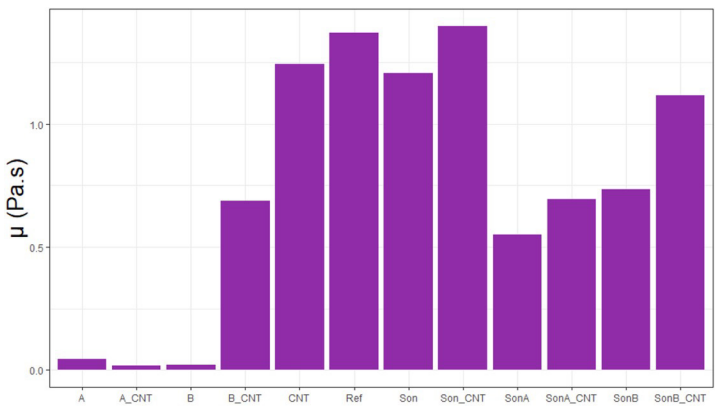

Figure 9. Apparent viscosity of the fresh Portland cement pastes.

Surfactants are used to disperse Portland cement particles, releasing water molecules that can be trapped between the cementitious material by doing so, reducing the yield stress of the system. However, when MWCNTs were added to the mixtures, an overlap of dispersion effects was observed. Therefore, the surfactant acted both in the dispersion of Portland cement particles and in the deagglomeration of the nanotubes [13].

A decrease in the static and dynamic yield strength of the A_CNT and B_CNT pastes was observed compared to the CNT mixture. This behavior may be attributed to the improved dispersion of the nanomaterial, which increases the specific surface area. Thus, the adsorption of the surfactant onto the surface of MWNCTs is enhanced, which reduces

their interactions with the cement [30]. Moreover, [30], [31] the hydrophobic part of the surfactant molecules adhered to the nanotubes, leaving the hydrophilic part available to bind to water molecules. Therefore, the combined utilization of the surfactant and nanomaterial contributed to reducing the amount of water required to lubricate the system.

Regarding the apparent viscosity, Figure 9, the cement pastes prepared with surfactants exhibited lower results than the other pastes. This behavior occurred because the surfactant causes the water trapped in the Portland cement particles to be released, which contributes to the lubrication of the cement mixture owing to improved dispersion [32]. Moreover, ionic and nonionic surfactants can produce air bubbles in the cement mixture, which reduces its viscosity and thereby improves its flowability [33].

These results confirmed that cement pastes prepared with MWCNTs resulted in higher equivalent viscosities. The nanotubes interact with the nonpolar surfactant particles, reducing its availability to interact with Portland cement particles, causing the viscosity of the cement system to increase [34]. Moreover, incorporating the nanomaterial into the cement matrix promoted an increase in the solid/liquid ratio of the system and improved the specific surface area of these solids. As reported in literature [35], when removing lubricating water from the cement system, the distance between fine particles decreases, causing a greater number of collisions between them, which increases the viscosity of the mixture [36].

Therefore, the morphology of the particles directly influences the viscosity of the cement mixture [37]; the greater the sphericity of the particle, the lower the viscosity of the system. It can be concluded that the increase in the system´s rheological properties occurs due to the inclusion of the nanomaterial with tubular morphology.

Furthermore, it is noteworthy that the yield strengths (Figures 7 and 8) were reduced for all cement mixtures containing surfactants, and cement pastes prepared with MWCNTs exhibited increased static yield strength. This is owing to its high specific surface area; the smaller the agglomeration, the greater the specific surface area available for interaction with the surfactant molecules.

The interaction of the two types of surfactants with the matrix and nanomaterial is different, although they have the same chemical basis. This effect is caused by the differences in the physical and chemical properties of the raw materials used in the production of each additive. Notably, additives that adsorb more effectively on Portland cement particles tend to improve the dispersion of the cement system. According to literature [34], [38], [39], surfactants can be adsorbed by MWCNTs, which causes a loss of their dispersion effect on Portland cement particles and induces higher yield stress in the cement mixture. Moreover, these studies noted that depending on the nature of the surfactant, the hydrophobic part will be adsorbed onto the surface of MWCNTs, and the hydrophilic part will interact with water molecules or Portland cement particles.

Finally, the rheological behavior of pastes containing nanotubes, additives and sonication together, obtained worse performances. This fact may be associated with an increase in nanomaterial dispersion due to sonication or even an increase in CNT agglomerates in the composite. Therefore, to validate a possible dispersion or agglomeration, it is necessary to verify other aspects, such as their mechanical properties.

3.2 Hardened state of Portland cement pastes

The mechanical properties at 28 d are shown in Figures 10, 11, 12, and 13. In general, the majority of the cement pastes presented higher mechanical behavior of the reference.

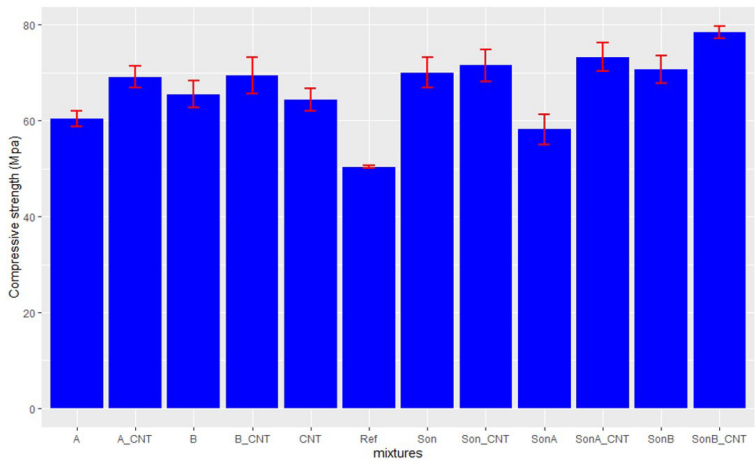

Figure 10. Compressive strength of the hardened Portland cement pastes.

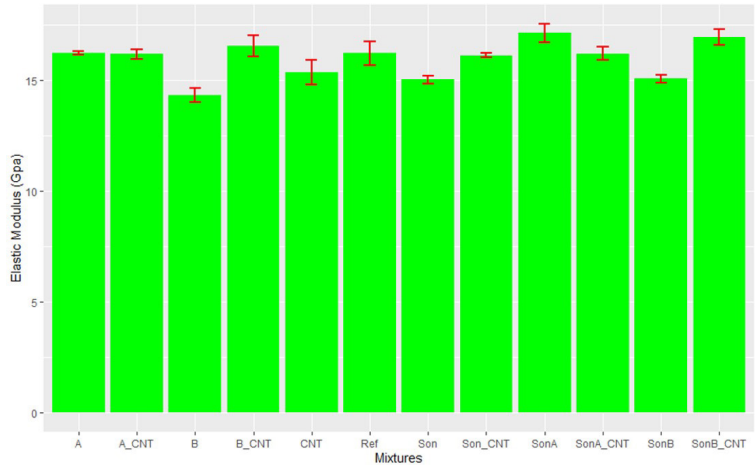

Figure 11. Elastic modulus of the hardened Portland cement pastes.

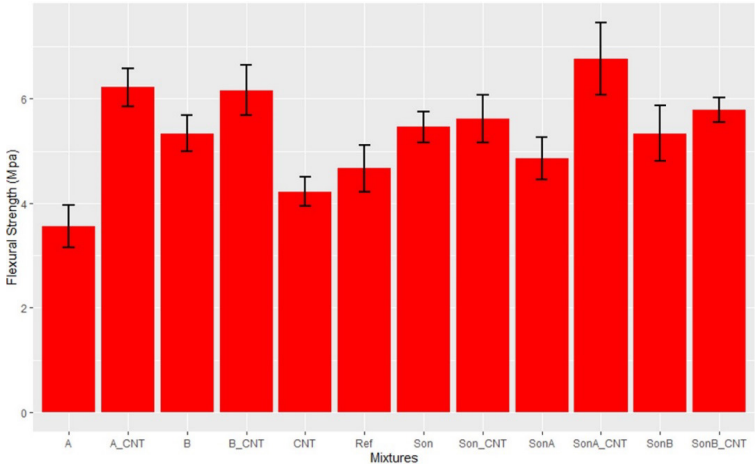

Figure 12. Flexural strength of the hardened Portland cement pastes.

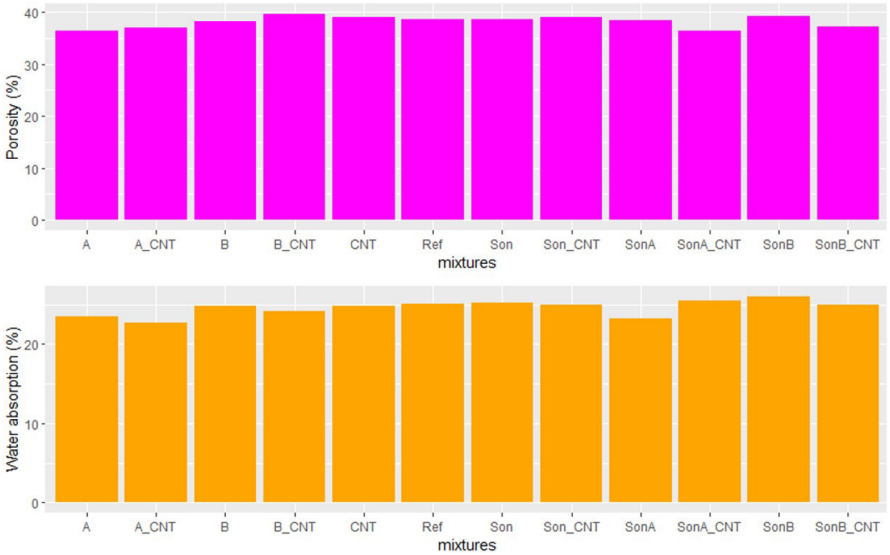

Figure 13. Porosity and water absorption of the hardened Portland cement pastes.

The reference mixture (Ref) presents a lower compressive strength compared with those containing the nanomaterial and surfactant, with or without ultrasonication. According to a report on the mechanical behavior of cementitious composites [28], [40], [41], the use of MWCNTs in pastes improved the compressive strength by up to 19%. These reports indicated that the main reason for this improvement was the performance of MWCNTs as bridging molecules connecting the matrix, which enhanced stress distribution. Furthermore, the nanomaterial acts as a nucleation site for the formation of a C-S-H gel coat on its surface [29]. Furthermore, the addition of nanotubes to cement-based materials promotes a decrease in mesopores, thereby densifying the matrix and improving its mechanical properties and durability [41].

Two-way ANOVA statistical analysis (Table 3) was used to evaluate the influence of the (i) mixture composition and (ii) ultrasonication process on the mechanical behavior of cement pastes. It was concluded that mixture composition significantly affects the compressive strength of Portland cement pastes at 28 d. However, ultrasonication did not significantly influence the compressive strength of the mixtures.

Table 3. Analysis of variance of the compressive strength results of hardened Portland cement pastes.

ANOVA					
Source	**SQ**	**GDL**	**MQ**	**F**	**F 0,05**
Dispersion method	152,59	5	30,51	0,94	5.05
Mixture	316,94	1	316,94	9,83	6,61
Residual	161,19	5	32,23	-	-
Total	630.72	11	-	-	

SQ: sum the squares of each parameter. **GDL**: Degree of spare. **MQ**: Mean Square. **F:** Factor of each calculated parameter. **F 0,05:** Factor of each tabulated parameter with 95% of reliability

To investigate the influence of the ultrasonication process on the compressive strength of the hardened cement pastes, the mixtures with different compositions were compared, considering the presence or absence of the ultrasonication process (Table 4).

Table 4. Statistical analysis of the compressive strength results of hardened Portland cement pastes, comparing the influence of ultrasonication.

Ratio Mixtures	Results
Ref: Son	Significantly different
A: SonA	No significantly different
B: SonB	Significantly different
CNT: Son_CNT	Significantly different
A_CNT: SonA_CNT	No significantly different
B_CNT: SonB_CNT	No significantly different

The analysis revealed a significant difference between the average compressive strengths of the mixtures using MWCNTs without the dispersing surfactant. Based on this result, it was concluded that MWCNTs require one of the dispersion methods, chemical (surfactant) or physical (ultrasonication), in addition to functionalization with carboxyl groups.

Based on the analysis results, it was demonstrated that there is a significant difference in the compressive strength between the Ref and sonicated (Son) mixtures. This behavior is thought to be owing to the release of hydrogen ions during ultrasonication. When these ions are released, the hydration reactions are accelerated, forming a greater amount of C-S-H, and consequently, enhancing the mechanical properties of the cement paste [39].

Figure 12 shows the flexural strength of the hardened cement pastes. The highest average values were observed for those prepared using mixtures containing the surfactant and MWCNTs, with or without ultrasonication. These results are in agreement with the results obtained from compressive strength tests. The improvement in the flexural strength of cementitious matrices with the incorporation of MWCNTs may be owing to the nanomaterial functioning as a reinforcing fiber, forming connections between cracks, and providing greater flexibility [40], [41].

SonA_CNT and SonB_CNT pastes had improved average flexural strengths of 45% and 24% higher compared with Ref, respectively. Moreover, the average flexural strength of A_CNT and B_CNT pastes increased by 33% and 32% compared with Ref, respectively. After statistical analysis was performed with 95% reliability (using the same

software), the hardened cement pastes prepared with the nanomaterial and surfactant, with or without ultrasonication, exhibited greater flexural strength compared with Ref. Furthermore, the flexural strength of the hardened cement pastes prepared with MWCNTs and SA or SB did not differ significantly, with or without ultrasonication.

This result correlates with the results observed by the water absorption and pore volume tests (Figure 13), which were reduced for the pastes mentioned above (SonA_CNT, SonB_CNT, A_CNT, and B_CNT). The reduction in these properties explains the improvement in the mechanical properties of pastes prepared with MWCNTs and SA or SB because the smaller the pore volume in a cementitious matrix, the better its microstructure and, consequently, its mechanical behavior. Furthermore, CNTs are thought to occupy the existing internal pores, causing a filling effect by refining the pores. Thus, a denser C-S-H gel is formed with reduced porosity [38].

The process of ultrasonication of the water in the Son paste resulted in an improvement in the average flexural and compressive strength at 28 d. For this paste, lower pore volume and water absorption were observed compared with those of Ref. However, when performing statistical analysis with 95% confidence, no significant difference was observed between these cement pastes. Thus, it is proposed that there is no significant difference in the porosity and water absorption between the Son and Ref cement pastes. In other words, the improvement in the compressive strength of the Son paste relative to Ref is not attributable to the reduced pore volume.

The elastic modulus of the cement pastes prepared with the MWCNTs and surfactants increased compared with Ref (Figure 11). However, when the statistical test was performed, the elastic modulus results of the cement pastes containing the MWCNTs and SA or SB, with or without ultrasonication, did not significantly differ from each other or Ref.

Based on the experimental data and statistical analysis, it is proposed that the ultrasonication process does not significantly affect the cement mixtures that contain a surfactant (SA or SB) and MWCNTs in the solution. This conclusion indicates that for cement mixtures containing CNTs functionalized with -COOH groups and surfactants, it is not essential to perform ultrasonication to promote greater dispersion, thus enhancing NTC´s applicability in the construction sector.

4 CONCLUSIONS

Based on the experimental studies conducted, the following conclusions were reached:

- The use of surfactants decreased the yield strength and apparent viscosity of the cement mixtures. However, an increase in these properties was observed when MWCNTs were added to the cement mixtures.
- Rheological tests showed that the use of at least one of the dispersion methods (ultrasonication or surfactant addition) improved the dispersion of the nanomaterial in the matrix. This phenomenon has been reported by several researchers; a greater deagglomeration of the nanomaterial increased the specific surface area of the system and caused an increase in the rheological properties.
- The interaction of the two types of surfactants with the nanotubes and cement was different, indicating that surfactants with the same chemical nature may have different effects on the rheological properties of cementitious matrices.
- The cement pastes prepared with MWCNTs and surfactant A or B showed higher compressive and flexural strengths and a reduced permeable pore volume at 28 d.
- Compared with the Ref cement paste, the average compressive strength of the prepared cement pastes improved by up to 50% (SonB_CNT), the average flexural strength increased by up to 44% (SonA_CNT), and the average of elasticity modulus increased by up to 5% (SonB_CNT).
- Generally, cement pastes prepared with MWCNTs using at least one of the dispersion methods or both exhibited an increase in the mechanical properties compared with the Ref cement paste.
- These results correlated with the rheological behavior, confirming that cement pastes prepared using solutions with the application of least one of the dispersion methods had improved nanotube dispersion in the matrix, which improved their mechanical properties.
- Statistically, there was no significant difference between the means of the compressive strength, flexural strength, and modulus of elasticity between the cement mixtures prepared with and without the ultrasonication process in the presence of MWCNTs with SA or SB. Based on the mechanical tests, ultrasonication does not promote greater nanomaterial dispersion, which typically contributes to the expansion of its practical application in cementitious composites, facilitating its use in the civil construction industry.
- Notably, further investigations are required to confirm these hypotheses, which are mainly associated with the quality of nanomaterial dispersion within the cement mixture.

ACKNOWLEDGEMENTS

The authors gratefully acknowledge the Brazilian government research agencies – National Council for Scientific and Technological Development (CNPq) and Santa Catarina Research Foundation (FAPESC) – for providing financial support for this research. Additionally, we acknowledge the Coordination for the Improvement of Higher Education Personnel (CAPES) for having granted a scholarship to the first author.

CITATIONS

[1] F. Collins, J. Lambert, and W. H. Duan, "The influences of admixtures on the dispersion, workability, and strength of carbon nanotube-OPC paste mixtures," *Cement Concr. Compos.*, vol. 34, no. 2, pp. 201–207, 2012, http://dx.doi.org/10.1016/j.cemconcomp.2011.09.013.

[2] I. Rhee and Y. Roh, "Properties of normal-strength concrete and mortar with multi-walled carbon nanotubes," *Mag. Concr. Res.*, vol. 65, no. 16, pp. 951–961, 2013, http://dx.doi.org/10.1680/macr.12.00212.

[3] D. J. Souza, L. Y. Yamashita, F. Dranka, M. H. F. Medeiros, and R. A. Medeiros-Junior, "Repair mortars incorporating multiwalled carbon nanotubes: shrinkage and sodium sulfate attack," *J. Mater. Civ. Eng.*, vol. 29, no. 12, pp. 04017246, 2017, http://dx.doi.org/10.1061/(ASCE)MT.1943-5533.0002105.

[4] A. Hawreen and J. A. Bogas, "Creep, shrinkage and mechanical properties of concrete reinforced with different types of carbon nanotubes," *Constr. Build. Mater.*, vol. 198, pp. 70–81, 2019, http://dx.doi.org/10.1016/j.conbuildmat.2018.11.253.

[5] R. Hamzaoui, S. Guessasma, B. Mecheri, A. M. Eshtiaghi, and A. Bennabi, "Microstructure and mechanical performance of modified mortar using hemp fibres and carbon nanotubes," *Mater. Des.*, vol. 56, pp. 60–68, 2014, http://dx.doi.org/10.1016/j.matdes.2013.10.084.

[6] M. Elkashef, K. Wang, and M. N. Abou-Zeid, "Acid-treated carbon nanotubes and their effects on mortar strength," *Front. Struct. Civ. Eng.*, vol. 10, no. 2, pp. 180–188, 2016, http://dx.doi.org/10.1007/s11709-015-0325-7.

[7] Y. Wang, H. Hu, and C. Rong, "The effect of the diameter of carbon nanotube on the mechanical and electrical properties of cement mortar," *Key Eng. Mater.*, vol. 730, pp. 479–485, 2017, http://dx.doi.org/10.4028/www.scientific.net/KEM.730.479.

[8] M. S. Konsta-Gdoutos, P. A. Danoglidis, M. G. Falara, and S. F. Nitodas, "Fresh and mechanical properties, and strain sensing of nanomodified cement mortars: The effects of MWCNT aspect ratio, density and functionalization," *Cement Concr. Compos.*, vol. 82, pp. 137–151, 2017, http://dx.doi.org/10.1016/j.cemconcomp.2017.05.004.

[9] S. Iijima, "Helical microtubules of graphitic carbon," *Nature*, vol. 354, no. 6348, pp. 56–58, 1991, http://dx.doi.org/10.1038/354056a0.

[10] S. C. Chowdhury, B. Z. G. Haque, T. Okabe, and J. W. Gillespie Jr, "Modeling the effect of statistical variations in length and diameter of randomly oriented CNTs on the properties of CNT reinforced nanocomposites," *Compos., Part B Eng.*, vol. 43, no. 4, pp. 1756–1762, 2012, http://dx.doi.org/10.1016/j.compositesb.2012.01.066.

[11] B. Zou, S. J. Chen, A. H. Korayem, F. Collins, C. M. Wang, and W. H. Duan, "Effect of ultrasonication energy on engineering properties of carbon nanotube reinforced cement pastes," *Carbon*, vol. 85, pp. 212–220, 2015, http://dx.doi.org/10.1016/j.carbon.2014.12.094.

[12] A. Hawreen, J. A. Bogas, and A. P. S. Dias, "On the mechanical and shrinkage behavior of cement mortars reinforced with carbon nanotubes," *Constr. Build. Mater.*, vol. 168, pp. 459–470, 2018, http://dx.doi.org/10.1016/j.conbuildmat.2018.02.146.

[13] O. A. Mendoza Reales, P. Duda, and R. Dias Toledo Fo, "Effect of a carbon nanotube/surfactant aqueous dispersion on the rheological and mechanical properties of Portland cement pastes," *J. Mater. Civ. Eng.*, vol. 30, no. 10, pp. 04018259, 2018., http://dx.doi.org/10.1061/(ASCE)MT.1943-5533.0002452.

[14] C. Zhou, F. Li, J. Hu, M. Ren, J. Wei, and Q. Yu, "Enhanced mechanical properties of cement paste by hybrid graphene oxide/carbon nanotubes," *Constr. Build. Mater.*, vol. 134, pp. 336–345, 2017, http://dx.doi.org/10.1016/j.conbuildmat.2016.12.147.

[15] A. Tamimi, N. M. Hassan, K. Fattah, and A. Talachi, "Performance of cementitious materials produced by incorporating surface treated multiwall carbon nanotubes and silica fume," *Constr. Build. Mater.*, vol. 114, pp. 934–945, 2016, http://dx.doi.org/10.1016/j.conbuildmat.2016.03.216.

[16] S. Alrekabi, A. Cundy, A. Lampropoulos, and I. Savina, "Experimental Investigation on the effect of ultrasonication on dispersion and mechanical performance of multi-wall carbon nanotube-cement mortar composites," *Int. J. Civil Environ. Struct. Constr. Archit. Eng.*, vol. 10, pp. 11, 2016.

[17] O. Mendoza, G. Sierra, and J. I. Tobón, "Influence of super plasticizer and Ca(OH)2 on the stability of functionalized multi-walled carbon nanotubes dispersions for cement composites applications," *Constr. Build. Mater.*, vol. 47, pp. 771–778, 2013, http://dx.doi.org/10.1016/j.conbuildmat.2013.05.100.

[18] L. Silvestro and P. Jean Paul Gleize, "Effect of carbon nanotubes on compressive, flexural and tensile strengths of Portland cement-based materials: a systematic literature review," *Constr. Build. Mater.*, vol. 264, pp. 120237, 2020, http://dx.doi.org/10.1016/j.conbuildmat.2020.120237.

[19] Associação Brasileira de Normas Técnicas, *Aditivos Químicos para Concreto de Cimento Portland. Parte 3: Ensaios de Caracterização*, ABNT NBR 11768-3, 2019.

[20] S. Ma, P. Zhao, Y. Guo, L. Zhong, and Y. Wang, "Synthesis, characterization and application of polycarboxylate additive for coal water slurry," *Fuel*, vol. 111, pp. 648–652, 2013, http://dx.doi.org/10.1016/j.fuel.2013.04.023.

[21] E. Janowska-Renkas, "The influence of the chemical structure of polycarboxylic superplasticizers on their effectiveness in cement pastes," *Procedia Eng.*, vol. 108, pp. 575–583, 2015, http://dx.doi.org/10.1016/j.proeng.2015.06.180.

[22] Z. Li, B. Li, Z. Zhao, W. Ma, W. Li, and J. Wang, "Rapid identification and quantitative analysis of polycarboxylate superplasticizers using ATR-FTIR spectroscopy combined with chemometric methods," *Math. Probl. Eng.*, vol. 2021, pp. 1–13, 2021, http://dx.doi.org/10.1155/2021/6613382.

[23] F. De Larrard, C. F. Ferraris, and T. Sedran, "Fresh concrete: a Herschel-Bulkley material," *Mater. Struct.*, vol. 31, no. 7, pp. 494–498, 1998, http://dx.doi.org/10.1007/BF02480474.

[24] M. S. Strano et al., "The role of surfactant adsorption during ultrasonication in the dispersion of single-walled carbon nanotubes," *J. Nanosci. Nanotechnol.*, vol. 3, no. 1, pp. 81–86, 2003, http://dx.doi.org/10.1166/jnn.2003.194.

[25] O. Matarredona, H. Rhoads, Z. Li, J. H. Harwell, L. Balzano, and D. E. Resasco, "Dispersion of single-walled carbon nanotubes in aqueous solutions of the anionic surfactant NaDDBS," *J. Phys. Chem. B*, vol. 107, no. 48, pp. 13357–13367, 2003, http://dx.doi.org/10.1021/jp0365099.

[26] K. Yurekli, C. A. Mitchell, and R. Krishnamoorti, "Small-angle neutron scattering from surfactant-assisted aqueous dispersions of carbon nanotubes," *J. Am. Chem. Soc.*, vol. 126, no. 32, pp. 9902–9903, 2004, http://dx.doi.org/10.1021/ja047451u.

[27] C. M. Neubauer, M. Yang, and H. M. Jennings, "Interparticle potential and sedimentation behavior of cement suspensions: effects of admixtures," *Adv. Cement Base. Mater.*, vol. 8, no. 1, pp. 17–27, 1998, http://dx.doi.org/10.1016/S1065-7355(98)00005-4.

[28] American Society for Testing and Materials, *Standard Test Method for Dynamic Young's Modulus, Shear Modulus, and Poisson's Ratio by Impulse Excitation of Vibration*, ASTM-E 1876, 1999.

[29] O. A. Mendoza Reales, Y. P. Arias Jaramillo, J. C. Ochoa Botero, C. A. Delgado, J. H. Quintero, and R. D. Toledo Fo, "Influence of MWCNT/surfactant dispersions on the rheology of Portland cement pastes," *Cement Concr. Res.*, vol. 107, pp. 101–109, 2018, http://dx.doi.org/10.1016/j.cemconres.2018.02.020.

[30] F. De Larrard, T. Sedran, C. Hu, J. C. Szitkar, M. Joly, and F. Derkx, "Evolution of the workability of superplasticized concretes: assessment with the BTRHEOM rheometer," in *Production Methods and Workability of Concrete*, P. J. M. Bartos, D. J. Cleland, D. L. Marrs, Eds., 1st ed. London: CRC Press, 1996, pp. 377–388, http://dx.doi.org/10.1201/9781482271782-46.

[31] I. R. Oliveira, A. R. Studart, R. G. Pileggi, and V. C. Pandolfelli, *Dispersão e Empacotamento de Partículas: Princípios e Aplicações em Processamento Cerâmico*. São Paulo: Fazendo Arte, 2000.

[32] M. Nehdi, S. Mindess, and P. C. Aïtcin, "Rheology of high-performance concrete: effect of ultrafine particles," *Cement Concr. Res.*, vol. 28, no. 5, pp. 687–697, 1998, http://dx.doi.org/10.1016/S0008-8846(98)00022-2.

[33] H. Wang, "Dispersing carbon nanotubes using surfactants," *Curr. Opin. Colloid Interface Sci.*, vol. 14, no. 5, pp. 364–371, 2009, http://dx.doi.org/10.1016/j.cocis.2009.06.004.

[34] A. Sobolkina et al., "Surface properties of CNTs and their interaction with silica," *J. Colloid Interface Sci.*, vol. 413, pp. 43–53, 2014, http://dx.doi.org/10.1016/j.jcis.2013.09.033.

[35] S. Parveen, S. Rana, R. Fangueiro, and M. C. Paiva, "Microstructure and mechanical properties of carbon nanotube reinforced cementitious composites developed using a novel dispersion technique," *Cement Concr. Res.*, vol. 73, pp. 215–227, 2015, http://dx.doi.org/10.1016/j.cemconres.2015.03.006.

[36] J. A. Bogas, H. H. Ahmed, and T. Diniz, "Influence of cracking on the durability of reinforced concrete with carbon nanotubes," *Appl. Sci.*, vol. 11, no. 4, pp. 1672, 2021, http://dx.doi.org/10.3390/app11041672.

[37] B. Wang, Y. Xing, and J. Li, "Mechanical properties and microstructure of sulfur aluminate cement composites reinforced by multi-walled carbon nanotubes," *J. Wuhan Univ. Technol. Mater. Sci. Ed.*, vol. 33, no. 1, pp. 102–107, 2018, http://dx.doi.org/10.1007/s11595-018-1793-0.

[38] T. Nochaiya and A. Chaipanich, "Behavior of multi-walled carbon nanotubes on the porosity and microstructure of cement-based materials," *Appl. Surf. Sci.*, vol. 257, no. 6, pp. 1941–1945, 2011, http://dx.doi.org/10.1016/j.apsusc.2010.09.030.

[39] L. N. Assi, Y. A. J. Al-Hamadani, E. E. Deaver, V. Soltangharaei, P. Ziehl, and Y. Yoon, "Effect of sonicated deionized water on the early age behavior of portland cement-based concrete and paste," *Constr. Build. Mater.*, vol. 247, pp. 118571, 2020, http://dx.doi.org/10.1016/j.conbuildmat.2020.118571.

[40] M. M. Sarvandani, M. Mahdikhani, H. Aghabarati, and M. H. Fatmehsari, "Effect of functionalized multi-walled carbon nanotubes on mechanical properties and durability of cement mortars," *J. Build. Eng.*, vol. 41, pp. 102407, 2021, http://dx.doi.org/10.1016/j.jobe.2021.102407.

[41] A. Chaipanich, R. Rianyoi, and T. Nochaiya, "The effect of carbon nanotubes and silica fume on compressive strength and flexural strength of cement mortars," *Mater. Today Proc.*, vol. 4, no. 5, pp. 6065–6071, 2017, http://dx.doi.org/10.1016/j.matpr.2017.06.095.

Author contributions: AVS, JMS, FP: Formal analysis, methodology, conceptualization, and data curation. AVSR, JMS and KF: Writing. PJPG: Supervision and funding acquisition.

Editors: Maria Josefina Positieri, Guilherme Aris Parsekian.

IBRACON Structures and Materials Journal
Revista IBRACON de Estruturas e Materiais
ISSN 1983-4195 ismj.org

ORIGINAL ARTICLE

Effect of duration and pressure of carbonation curing on the chloride profile in concrete

Efeito da duração e pressão da cura por carbonatação do concreto em perfis de cloreto

Roberto Luiz Dias[a]
Neusa Aparecida Munhak Beltrame[a]
Jordi Rius Gonzalez[b]
Ronaldo Alves Medeiros-Junior[c]

[a]Universidade Federal do Paraná – UFPR, Programa de Pós-Graduação em Engenharia Civil – PPEGC, Curitiba, PR, Brasil
[b]Universidade Federal do Paraná – UFPR, Departamento de Construção Civil, Curitiba, PR, Brasil
[c]Universidade Federal do Paraná – UFPR, Centro de Estudos de Engenharia Civil – CESEC, Programa de Pós-Graduação em Engenharia Civil – PPGEC, Curitiba, PR, Brasil

Received 22 October 2022
Accepted 20 January 2023

Abstract: Carbonation curing alters the characteristics of the concrete's microstructure and can interfere with the penetration of aggressive ions. The objective of this article was to evaluate the influence of CO_2 pressure and carbonation cure time on chloride profiles. Concrete specimens were cured by carbonation with CO_2 pressures ranging from 5 to 25 Psi, for a time within the carbonation chamber of 8, 24, and 36 hours. These concretes were subjected to 30 wetting and drying cycles in NaCl solution to stimulate the chloride ingress. The carbonation depth and the microstructure of the concrete were monitored over time. Chloride profiles were obtained and modeled by 4 mathematical equations. The results showed that the combination of less time and CO_2 pressure during carbonation curing potentiated the reduction of chloride penetration in concrete. Also, the carbonation curing conditions of 5 and 10 Psi for 8 hours reduced the chloride diffusion coefficient.

Keywords: carbonation curing, CO_2 pressure, curing time, chloride profiles, modeling.

Resumo: A cura por carbonatação altera as características da microestrutura do concreto e pode interferir na penetração de íons agressivos. O objetivo deste artigo foi avaliar a influência da pressão de CO_2 e do tempo de cura da carbonatação nos perfis de cloreto. As amostras de concreto foram curadas por carbonatação com pressões de CO_2 variando de 5 a 25 Psi, por um tempo dentro da câmara de carbonatação de 8, 24 e 36 horas. Esses concretos foram submetidos a 30 ciclos de umedecimento e secagem em solução de NaCl para estimular o ingresso de cloretos. A profundidade de carbonatação e a microestrutura do concreto foram monitoradas ao longo do tempo. Perfis de cloreto foram obtidos e modelados por 4 equações matemáticas. Os resultados mostraram que a combinação de menor tempo e pressão de CO_2 durante a cura por carbonatação potencializou a redução da penetração de cloretos no concreto. Além disso, as condições de cura por carbonatação de 5 e 10 Psi por 8 horas reduziram o coeficiente de difusão do cloreto.

Palavras-chave: cura por carbonatação, pressão de CO_2, tempo de cura, perfis de cloreto, modelagem.

How to cite: R. L. Dias, N. A. M. Beltrame, J. R. Gonzales, and R. A. Medeiros-Junior, "Effect of duration and pressure of carbonation curing on the chloride profile in concrete", *Rev. IBRACON Estrut. Mater.*, vol. 16, no. 6, e16603, 2023, https://doi.org/10.1590/S1983-41952023000600003

1 INTRODUCTION

Chloride-induced reinforcement corrosion is the main cause of deterioration in reinforced concrete structures located in a marine environment. The formation of expansive ferrous phases from the corrosion of the steel generates

Corresponding author: Neusa Aparecida Munhak Beltrame. E-mail: neusamunhakbeltrame@gmail.com
Financial support: None.
Conflict of interest: Nothing to declare.
Data Availability: Data supporting the findings of this study cannot be shared at this time due to technical or time limitations. The sharing of data necessary to reproduce these findings will be shared later.

internal stresses and the cracking of the concrete. This process significantly reduces the service life of reinforced concrete structures [1]–[4]. Some techniques have been applied to reduce the penetration of chlorides in the concrete. Among these techniques, Zhang and Shao [5] evaluated the possibility of applying early carbonation curing and observed that this technique can be effective in reducing chloride ingress.

The weathering carbonation process is related to the CO_2 reaction mainly with portlandite in hardened concrete at advanced ages. This reaction reduces the pH of the concrete to approximately 9.0 and can destroy the passivation film of the steel reinforcement [3]. C-S-H is also susceptible to decalcification in the presence of CO_2, producing $CaCO_3$ and silica gel [6].

The early-age carbonation curing differs from weathering carbonation since it is performed in a few hours of hydration, followed by an intentional exposure to high CO_2 concentrations (around 99%) [7], [8]. Carbonation curing has been widespread in the literature to accelerate the increase in compressive strength and reduce the permeability of concrete [5], [8]–[13].

Carbonation curing can produce a controlled depth of carbonation and the drop in pH can be recovered by additional curing in water [14]. According to Zhan et al. [11], resistances in concrete blocks tested after 2 hours of carbonation curing are comparable to 6 hours of steam curing. Zhang and Shao [8] found that the absorption of 16% CO_2 by cement content can reduce the pH of the concrete to about 9.2 on the surface. However, the subsequent hydration can raise the surface pH to approximately 12.5 [10], decreasing the risk of steel corrosion due to carbonation in this case.

CO_2 introduced early in the concrete reacts with non-hydrated clinker (especially C_2S and C_3S), $Ca(OH)_2$, and C-S-H. The main phases formed are amorphous $CaCO_3$, C-S-H with less Ca/Si ratio, and silica gel [15], [16]. However, the C-S-H content, the Ca/Si ratio, and the degree of crystallization of $CaCO_3$ increase with the subsequent hydration in water [16]. The $CaCO_3$ generated in the capillary pore walls by carbonation cure leads to a reduction in the larger capillary pores and a denser microstructure, acting as an external shield against external ions [5], [8], [17], [18]. The reduction in the permeability of concrete is due to the formation of a greater amounts of solid phases [7], [8], [16].

Chen and Gao [19] identified that the carbonation cure can considerably influence the pore structure of the cement paste. The superficial (carbonated) region of the specimens had much lower porosities in relation to the internal layers. The proportion of small capillary pores (25 to 1000 nm) decreased, while the large capillary pores (from 1000 nm) increased with the advancing depth of the samples. Besides, total porosity was reduced by 40% in the study by Zhang and Shao [20]. The size of the dominant capillary pores before carbonation curing was 10 to 50 nm and decreased to less than 10 nm after this type of cure. This indicated that carbonation curing can effectively refine the pore structure.

There are two essential influences of carbonation curing on the properties of concrete: (i) the increase in compressive strength and the reduction of water absorption at an early age; and (ii) the changes caused in the microstructure of the concrete due to calcium carbonate precipitation, thus improving performance and durability [21]. This research will focus on the second (resistance to chloride penetration). The variation in compressive strength and water absorption has not been evaluated since this influence has already been excessively addressed in the literature [7], [9], [10]-[13], [22].

Several studies have demonstrated changes in the durability of cement composites in terms of different degradation mechanisms due to carbonation curing. The carbonation cure contributed to the reduction of porosity, permeability, and ettringite formation [10], [16], [23]-[25]. Also, the carbonation cure increased the resistance to attack by external sodium and magnesium sulfates [15], [22], [26], acids [17], carbonation by weathering [5], damage from freeze-thaw [22], drying shrinkage [11], [27], [28], and penetration of chloride ions [5], [16], [20]. The main applications for carbonation curing are related to the production of precast concrete and concrete blocks [23], [27], [28].

The main conclusions of the studies about improving the durability of carbonation-cured concrete are related to the reduction in $Ca(OH)_2$ content on the concrete surface and the decrease in the C_3A content after carbonation curing, making them less vulnerable to the chemical attack of aggressive agents [9], [12], [22]. Zhang and Shao [5], [20] demonstrated that CO_2 curing reduced by 50% and 60% the total and free chloride content of concretes, respectively. Increased resistance to chloride migration has also been reported by Pan et al. [16]. This effect was attributed to the superficial protective layer rich in carbonates, less permeable, less absorptive, and with a comparable pH value. However, these studies applied only one level of CO_2 pressure and carbonation cure time. The main research question of this study is whether the protection remains efficient with the alteration of these parameters.

Although the early carbonation cure technique is widely discussed in the literature, the lack of standardization has led to the adoption of different parameters of time and CO_2 pressure among researchers. The reaction rate of the carbonation cure is mainly controlled by CO_2 diffusion, which can be influenced by the time, concentration, and pressure of the CO_2 gas. Table 1 summarizes some research on carbonation curing with different pre-cure procedures, CO_2 concentration, duration, pressure and subsequent cure.

Table 1: Some recent durability studies concerning carbonation curing.

Ref.	Test samples	Pre-cure	Carbonation			Post-cure
			CO_2 (%)	Pressure (Psi)	Time (h)	
[29]	PC paste	18 h sealed and 3 h (2 ± 1) ºC, 50% RH	99.5	14.50	1, 2, 3, 4, 24, and 72	28 days in water
[15]	PC paste	24 h in mold, (20 ± 3) °C	20.0	--	4	28 d, (20 ± 3) °C, RH 90%
[25]	PC Concrete block	4 h, (23 ± 2) ºC, 60% RH	10	--	20	27 days, (23 ± 2) ºC, 95% RH
[16]	PC mortar	24 h in sealed mold, (20 ± 1) °C, RH ≥ 98%	99.0	29.00	3 and 6	28, 90 and 180 days immersed in water
[20]	PC concrete and cement paste	5 h in mold, 5-6 h 25 °C, RH 50%	99.8	72.52	12	27 days, 25 °C, 95% RH
[24]	PC paste	24 h in mold, 20 ºC	10	14.69	672	--
[23]	PC mortar	6 h, 26 ºC, (50 ± 5) % RH	99.0	10.00	12	28 days, sealed and sprinkling water
[9]	PC mortar and concrete	0-6 h, 22 °C, RH 60%	99.5	29.00	3	27 days immersed in water, 22 ºC
[30]	PC mortar and paste	24 h, 20 ºC	5	14.69	168, 336, 672	--
[10]	PC paste and steel slag	7 days, (23 ± 2) ºC, 98% RH and 2 days 30-40% RH	99.9	14.69	24, 72, and 336	--
[28]	PC block concrete	6h, 50% RH, 25 ºC	99.5	1.45 to 72.52	1, 2, 3, 6, 18, and 24	28 days air
[12]	PC concrete	5 h in the mold and 5.5 h in 25 ºC and (50 ± 5) % RH	99.8	72.52	2, 12, and 24	1, 4, 28, 90, 180, and 360 days, 25 °C, 95% RH
[5]	PC Concrete	5-6 h in mold, 5.5 h 25°C, RH (50 ± 5) %	99.8	72.52	12	27 days, 25 °C, 95% RH
[31]	PC paste and reactive MgO	(24 ± 2) h, (23 ± 2) ºC, 90% RH in mold and 24 h, vacuum	99.9	14.69	168, 672, and 1344	--
[22]	PC concrete	18 h, 25 °C, RH 60%	99.5	21.75	2	27 days sealed and sprinkling water
[27]	Cement block concrete	3-6 h in the mold and 4 h out of the mold	Not indicated	10.00	2	--
[17]	Cement block concrete	2 h and 4 h steam (40-63 °C)	99.5	21.75	2	27 days sealed
[26]	PC paste	4 h, 65 ºC, and 100% RH; 8 h autoclave (180 ºC)	5	--	672	--

The objective of this article was to investigate the effect of duration and pressure of carbonation curing on chloride profiles. Concrete specimens exposed to 30 wetting and drying cycles of NaCl (3.5%) solution were investigated after carbonation curing with pressures ranging from 5, 10, 15, 20, and 25 Psi, and durations of 8, 24, and 32 hours. A reference concrete (conventional curing) was used to compare the results.

The main innovation of this article is in the determination of chloride profiles for concrete cured by carbonation at different levels of CO_2 pressure and curing time. In addition, the profiles were modeled to calculate the diffusion coefficient and the chloride surface concentration for a quantitative evaluation of the results. No article has been found in the literature by these authors that use this approach. Therefore, the results of this article can certainly contribute to the advancement of knowledge on this topic.

2 MATERIALS AND EXPERIMENTAL PROGRAM

Concrete specimens were molded for carbonation curing at different CO_2 pressures and for different times, in addition to the reference concrete (submerged curing in water). These specimens were subjected to wetting and drying cycles in chloride solution for 30 weeks (210 days). After this period, the chloride profiles were determined and modeled from 04 different chloride models available in the literature.

2.1 Materials and concrete production

Brazilian Portland cement CP-II F 32 (equivalent to Portland-limestone cement CEM II / A-L 32.5N) was used. Table 2 shows the characterization of this cement. The fine aggregate was natural river sand with specific gravity of 2.67g/cm^3, bulk density of 1.52g/cm^3, water absorption of 0.95%, fineness modulus of 2.41, and maximum aggregate size of 4.8 mm. The coarse aggregate was basaltic gravel with maximum aggregate size of 9.5 mm, specific gravity of 2.76g/cm^3, bulk density of 1.55g/cm^3, and water absorption of 0.81%.

Cubic concrete specimens were produced (100 mm edge). The proportion of materials (by mass) of the concrete was 1: 1.6: 2.5 (cement: sand: gravel) with a water-to-cement ratio of 0.50. The concrete had a cement content of 416 kg/m^3, consistency (slump test) of (100 ± 20) mm, and a specific gravity of 2,420 kg/m^3. Therefore, a conventional concrete mix was chosen. No chemical additive (superplasticizer) was used in this research. Only a concrete mixture was evaluated since this article focuses on assessing the effect of pressure and duration of carbonation cure in chloride penetration. The effect of the water-to-cement ratio and other types of binders (including pozzolans) on carbonation cure and chloride ingress is well defined in the literature.

Table 2. Characterization of the Portland cement.

Property	Unit	CP-II F	Property	Unit	CP-II F
CaO	%	59.51	Specific gravity	g/cm^3	3.03
SiO_2	%	16.80	Initial setting time	h:min	03:40
Al_2O_3	%	3.86	Final setting time	h:min	04:30
MgO	%	3.13	Fineness Blaine	cm^2/g	3,730
SO_3	%	2.56	# 200	%	0.80
Fe_2O_3	%	2.56	# 325	%	6.70
Loss on ignition	%	10.44	Compressive strength (3 d)	MPa	29.8
Free CaO	%	0.70	Compressive strength (7 d)	MPa	35.2
Insoluble residue	%	0.75	Compressive strength (28 d)	MPa	40.8
Alkaline content (Na_2O and K_2O)	%	0.61			

Five CO_2 pressures inside the carbonation chamber (5, 10, 15, 20, and 25 Psi), and three different carbonation curing times (8, 24, and 32 hours) were used. These parameters were chosen after an extensive literature review on the range of pressures and carbonation cure times applied in other studies. In addition to these carbonation curing parameters, a conventional water curing was also performed on reference concretes (three specimens). These reference specimens were casted and were not subjected to carbonation curing, only chloride penetration. Table 3 shows the codes used to represent the concrete samples.

The concrete specimens were casted according to the NBR 5738 [32] standard. The compressive strength of concrete was (27.8 ± 1.24) MPa at 28 days. The compressive strength was performed only at 28 days to characterize the concrete. The variation in compressive strength during carbonation curing was not evaluated, since several studies in the literature have already done this investigation [7], [11], [13], [14].

Table 3. Carbonation cure parameters used in this research.

Code	Pressure (Psi)	Time (h)	Code	Pressure (Psi)	Time (h)
5p8h	5	8	20p8h	20	8
5p24h	5	24	20p24h	20	24
5p32h	5	32	20p32h	20	32
10p8h	10	8	25p8h	25	8
10p24h	10	24	25p24h	25	24
10p32h	10	32	25p32h	25	32
15p8h	15	8	REF	-	-
15p24h	15	24			
15p32h	15	32			

2.2 Concrete curing

The conventional water curing of the reference concrete was executed for 28 days. The carbonation curing process was developed in four stages: step 1 - mold curing (6 hours); step 2 - pre-cure (18 hours); step 3 - cure within the

carbonation chamber (8, 24, and 32 hours); and step 4 - subsequent hydration (27 days). Figure 1a shows the representation of each of these steps.

2.2.1 Step 1 - mold curing

Soon after mixing and placing the concrete in the forms, the surface of the specimens was protected with plastic film and the concretes remained in a laboratory environment for 6 hours. This period was defined based on the final setting time of the cement (04 hours and 30 minutes, according to Table 2). Therefore, a time slightly longer than the final setting time was determined to ensure that the concretes do not break during their removal from the forms.

2.2.2 Step 2 - pre-cure

After step 1, the concretes were removed from the forms and remained in a climatic room (temperature = 25 ± 1 ºC; and relative humidity = 50 ± 5%) for 18 hours. This step allows part of the free water inside the concrete to evaporate, leaving more space for the carbon dioxide to penetrate since excess water can block the diffusion of CO_2 generating a limitation in the carbonation reaction [8]. The concrete mass was determined before and after step 2 on an electronic scale with an accuracy of 0.01 g. The water loss of the concretes during the 18 hours of pre-curing was 50.43%. El-Hassan et al. [33] and El-Hassan and Shao [34] found a value of water loss of 51% for the same period.

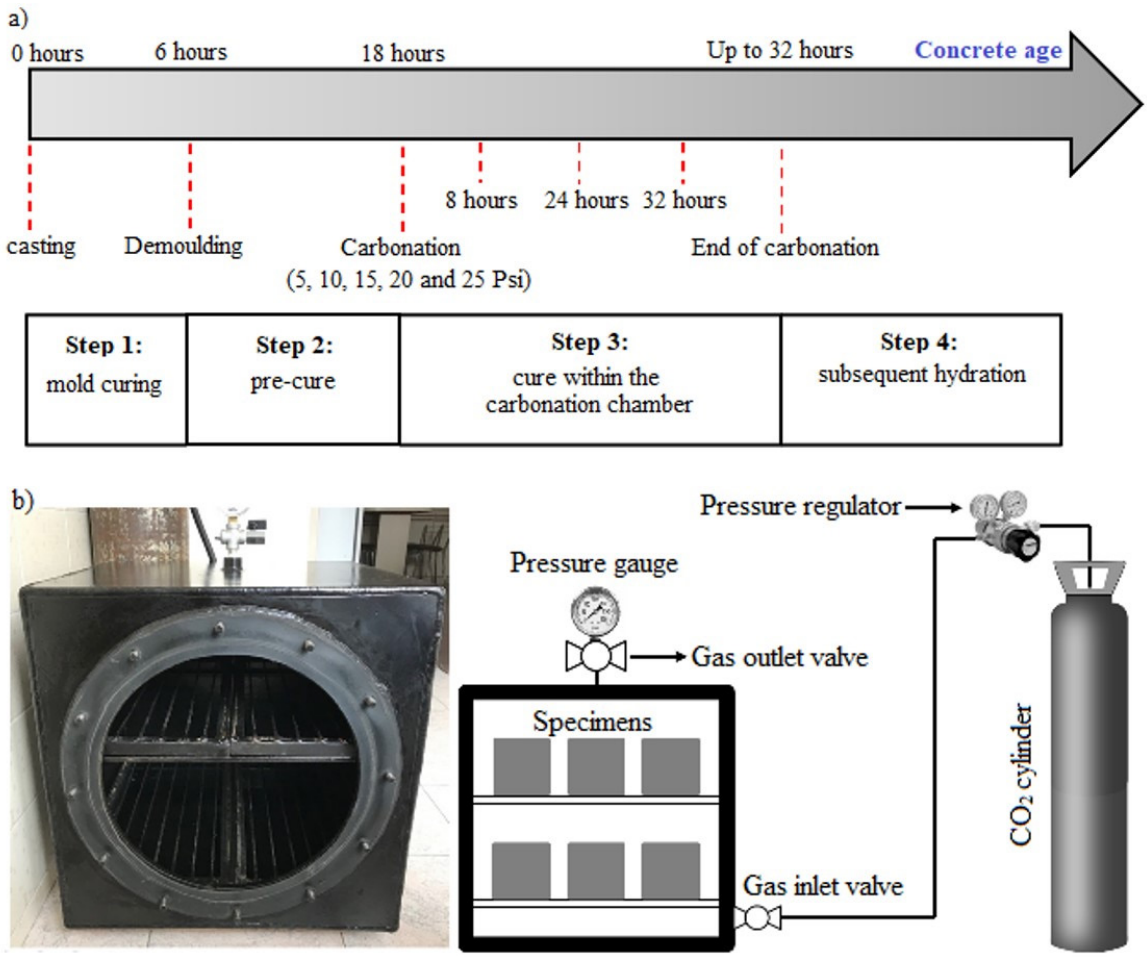

Figure 1: Illustrative schemes showing: (a) carbonation curing steps; (b) carbonation chamber operating system.

2.2.3 Step 3 - cure within the carbonation chamber

The concrete specimens were inserted into the carbonation chamber at this step (Figure 1b). CO_2 with a purity of 99.5% was used, based on the studies by Rostami et al. [17], Abdullahi et al. [35], and Zhan et al. [11]. Two pressure gauges were installed in the chamber. The first served to monitor the pressure of the tank, and the second to indicate the outflow of the gas. Therefore, the internal pressure of the gas was controlled within the pre-defined values (5, 10, 15, 20, and 25 Psi).

Before injecting CO_2, the carbonation chamber was aspirated using a vacuum pump. This process was executed to ensure that the chamber would be fully occupied by CO_2 gas. After this process, the injected CO_2 and the pressure inside the chamber were regulated to remain constant, ensuring a continuous supply of the gas to the equipment throughout the carbonation period.

The concrete specimens remained for 8, 24, or 32 hours inside the carbonation chamber, depending on the desired curing time. Seven specimens were used for each curing time. From these seven specimens, two were used to determine the carbonation depth immediately after step 3, two were used to determine the carbonation depth immediately after step 4, and the remaining three specimens were used in the chloride penetration test. Figure 2 shows a schematic illustrating these procedures.

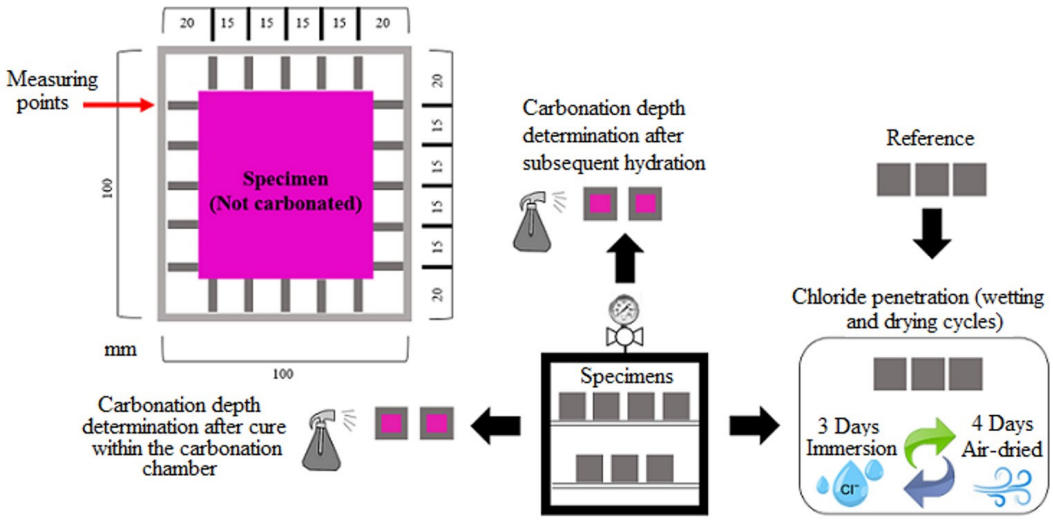

Figure 2. Distribution of specimens subjected to carbonation curing.

The specimens were weighed again immediately after step 3. Then, the increase in concrete mass was calculated from Equation (1) [8], [33] during the period inside the carbonation chamber. This measure compares the mass of the samples before and after the period inside the carbonation chamber, and indirectly estimates the capture of carbon dioxide (Ab_{CO2}) in the concrete, according to [33].

$$Ab_{CO_2}(\%) = \frac{M-m}{M_{cem}} \quad (1)$$

Where M is the mass after the period inside the carbonation chamber; m is the mass of the concrete after the pre-curing step; and M_{cem} is the mass of the cement.

2.2.4 Step 4 - subsequent hydration

The subsequent hydration step is recommended by several studies regarding carbonation cure [5], [12], [36] to ensure an additional hydraulic reaction to cement grains that did not react during the first hours of casting. Therefore, the specimens were immersed in a lime-saturated water solution for 27 days after step 3 [9]. Thus, the total curing period was 28 days, which comprises 1 approximate day of carbonation curing (8, 24, or 32 hours), and 27 days of subsequent hydration.

2.3 Carbonation depth determination

The carbonation depth was determined using a phenolphthalein colorimetric indicator solution, according to RILEM CPC 18 [37]. A solution of 1% phenolphthalein, 29% distilled water and 70% alcohol was sprayed on the newly broken concrete surfaces. The specimens were broken longitudinally using a press. Twenty measurements (Figure 2) on each side of the specimens were made with a digital caliper with a precision of 0.01 mm.

2.4 Chloride penetration

After the curing steps (approximately 28 days), the concrete specimens were subjected to wetting and drying cycles in an aqueous solution with 3.5 wt.% sodium chloride (NaCl). For this purpose, the samples were initially sealed on four sides with waterproof epoxy resin to enable the unidirectional penetration of the chlorides. Each cycle lasted 7 days (three days of total immersion in chloride solution and four days air-dried). During the initial three weeks of testing, the masses of the specimens were measured and the absorption of the solution recorded for permeability characterization. The chloride profiles were determined after 30 complete wetting and drying cycles (210 days). The choice of the number of cycles was made in order to extend the experimental program as long as possible to performed this research, considering issues of logistics, production, cost, storage, and time available for the tests.

The determination of chloride concentrations in concrete was executed using the titration method, according to RILEM TC 178-TCM [38]. This method involves titrating the silver ion in an acid medium with a standard solution of ammonium thiocyanate (NH_4SCN) and the Fe^{3+} ion as an indicator. The precipitate is formed with an excess of standard silver nitrate solution $AgNO_3$.

The concrete samples were taken from the cubic specimens using a circular saw. The dry cut was performed in 4 slices, every 10 mm from the surface of the samples. The concrete slices were crushed using a pan mill to obtain the powdered concrete sample (> 0.16 mm). The powder samples were homogenized to guarantee a representative profile and allow an accurate determination of the chloride content by the chemical procedure, analyzed by titration using an ammonium thiocyanate solution [38]. Three specimens were used for each curing condition (Table 3) applied in this research.

After determining the chloride profiles, the chloride penetration was modeled to estimate the chloride diffusion coefficient and the chloride surface concentration. To increase the reliability of the conclusions, four different models available in the literature were used. The models used were the resolution of the error function of Fick's second law (Equation 2) [39], the modified Holliday equation (Equation 3) [40], [41], the FIB 34 model (Equation 4) [42], and the EHE-08 equation (Equation 5) [43]. The modified Holliday equation can model the peak region of chloride penetration in concrete, while the other three equations model only the chloride diffusion. These models are widely applied in the literature to estimate the penetration of chlorides in concrete [36], [40], [44]–[48]. The adjustment by the least-squares method was applied, considering only the period of diffusion of the chloride profiles for Equations 2, 4, and 5 and the entire profile for Equation 3.

$$C(x,t) = Cs \cdot \left[1 - erf\left(\frac{x}{\sqrt{4.D.t}}\right)\right] \tag{2}$$

$$C(x,t) = \frac{1}{\frac{1}{R1}\cdot\left[1+\frac{(x-R3)^2}{(D.t)}\right]} \tag{3}$$

$$C(x,t) = (Cs, \Delta x) \cdot \left\{1 - erf\left(\frac{x-\Delta x}{2.\sqrt{D.t}}\right)\right\} \tag{4}$$

$$C(x,t) = Cs \cdot \left\{1 - \frac{x}{\sqrt{12.D.t}}\right\}^2 \tag{5}$$

Where C(x,t) = chloride concentration (%) at depth x and time t; Cs = surface chloride concentration (%); *erf* = Gauss error function; x = chloride penetration depth (cm); D = chloride diffusion coefficient (cm^2/s); t = time (s); R_3 = Δx = depth of the convection zone (cm); R_1 = Cs,Δx = chloride concentration (%) at the depth Δx.

2.5 Microstructure and statistical analysis

Samples of the concrete specimens were extracted at two depths (external and internal) to determine the microstructure analysis. The depth designated as external consisted of the samples in a range of 0-10 mm from the surface. This region was expected to be carbonated after carbonation curing. The depth designated as internal consisted of the samples 50 mm away from the surface (core of the specimen and therefore not carbonated).

Cubic samples with an edge of approximately 1 cm were extracted from the specimens for Scanning Electron Microscopy (SEM) analyses associated with X-ray Dispersive Energy Spectroscopy (EDS). The equipment used was the Tescan Mira 3 Microscope with SE/BSE backscattered detectors and the Oxford X-MaxN 50 X-ray Analytical Probe. The samples were sputtered with gold.

The statistical analysis of the results was made from the analysis of variance (ANOVA). ANOVA consists of comparing two factors (Fcalculated and Ftabulated). If the Fcalculated value is higher than the Ftabulated, the influence is considered significant. A 95% confidence level was used. Then, the significant means were compared using the Tukey test.

3 RESULTS AND DISCUSSIONS

3.1 Chloride profiles and modeling of chloride penetration

Table 4 summarizes the carbonation depth and mass increment obtained after carbonation curing, varying the carbonation time and pressure. In addition, the solution absorption rates during the sodium chloride immersion test are also displayed. In general, the longest carbonation time produced the greatest depths of carbonation and mass addition, ranging from 9.42 to 22.54 mm and from 6.46 to 15.19%, respectively. The rates of absorption of the NaCl solution found were 4.1% to 6.6%, depending on the duration and CO_2 pressure.

The results of the chloride profiles were evaluated in two ways. Firstly, the effect of CO_2 pressure on the chloride profile will be discussed. Later the profiles will be evaluated focusing on the effect of carbonate curing time. Finally, the chloride diffusion coefficients will be discussed based on the modeling of the chloride profiles.

Table 4. Sample properties after initial carbonation cure.

Pressure	Depth of carbonation (mm)			Mass increment CO_2 (%)			Absorption (%)		
	8 h	24 h	32 h	8 h	24 h	32 h	8 h	24 h	32 h
5 Psi	11.63	17.51	22.54	6.46	11.48	15.19	4.1	5.2	4.9
10 Psi	9.42	14.65	20.52	7.55	10.42	11.56	5.3	6.6	6.0
15 Psi	12.92	21.58	20.57	6.98	13.01	13.63	4.5	4.8	6.2
20 Psi	13.92	17.87	22.43	7.76	10.37	10.97	4.3	6.0	6.4
25 Psi	14.87	20.44	21.87	8.43	10.97	12.44	5.1	5.4	6.1

Carbonation-cured concrete generally had a lower total chloride content compared to reference concrete (Figure 3). This reduction occurred in all specimens at the first depth (until 10 mm). In the innermost depths (mainly after 20 mm), some concentrations of chlorides in the carbonated concrete were higher than the reference concrete. Zhang and Shao [5] observed that the reduction in chloride concentrations due to carbonation cure is more intense in the first 25 mm. According to these authors, carbonation-cured concrete had chloride contents more than 50% lower than reference concrete. It should be noted that Zhang and Shao [5] did not vary the time and CO_2 pressure, unlike the present article.

The lower concentration of chlorides in the most superficial depths of carbonated concrete is related to the extensive formation of calcium carbonate which physically hinders the initial penetration of chlorides into the concrete during the wetting and drying cycles. This phenomenon occurs due to the structure of the pore network modified by carbonation. In this case, the carbon dioxide precipitate as $CaCO_3$ and mixed with C-S-H gel, resulting in a structure with less permeability in the first layers. The effect of reducing permeability and increasing the compressive strength of concrete cured by carbonation has been confirmed in several studies [7], [22], [10]–[13], [49], [50]. In the innermost depths, the effect of carbonation cure on concrete is less intense, or nonexistent for depths greater than 25 mm.

The greatest reduction in the chloride profiles of carbonated concretes in comparison with the reference concrete occurred for the curing time of 8 hours (Figure 3a). Therefore, using a shorter curing time was more efficient to increase the resistance of the concrete to chloride penetration. According to Table 4, keeping the pressure constant, the lowest absorption (%) occurred for the shortest curing time (8 hours). Also, from 15 Psi onwards, curing for 32 hours also caused greater absorption than curing for 24 hours.

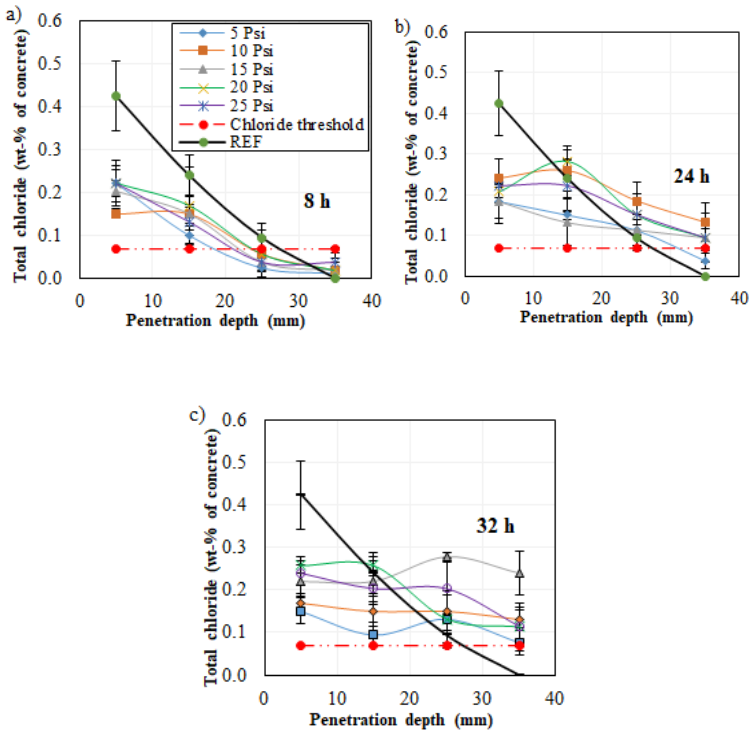

Figure 3. Effect of pressure on the chloride profile: (a) 8 h; (b) 24 h; (c) 32 h

According to Figure 3, the effect of CO_2 pressure on chloride profiles increases with the curing times, and this effect was negative as the CO_2 pressure increases. The chloride profiles with the different pressure levels drifted away with increasing curing time. Furthermore, increasing the pressure can reduce the concrete's resistance to chloride ingress mainly for the curing time of 32 hours. Only the application of the curing time of 8 hours made it possible to reduce the chloride profiles (regardless of pressure) to practically all depths. Therefore, the combination of less time and pressure during carbonation curing potentiated the reduction of chloride penetration in concrete.

Figure 3 also shows the setting of a 0.07 (wt.% concrete) chloride threshold, which is equivalent to 0.40 (wt.% cement). The conversion of the chloride content units was performed using Equation 6 [43]. This is the most widely used value in the literature to assess the chloride threshold for the onset of chloride-induced corrosion [43], [48], [51]. Considering a concrete cover of around 35 mm, only the carbonation cure applied for 8 hours would be able to protect the reinforcement against corrosion regardless of the CO_2 pressure (Figure 3a).

$$Cl(wt \cdot \%\ cement) = Cl(wt \cdot \%\ concrete) \cdot \left(\frac{M_c}{k}\right) \quad (6)$$

Where Cl is the chloride concentration; Mc is the concrete specific gravity; and k is the cement content in concrete. Equation 6 suggests Mc equal to 2,300 kg/m^3 in its original equation from [43]. However, the concrete specific gravity obtained experimentally (= 2,420 kg/m^3) was applied in this article.

According to Figure 4, there is a tendency for the chloride profiles to become higher than the reference concrete with increasing pressure. This reinforces the hypothesis of increasing the CO_2 pressure does not seem to be an adequate solution for the protection of the carbonation-cured concrete against chloride penetration. Moreover, Figure 4 clearly shows that increasing the curing time does not reduce chloride ingress.

The chloride profiles were modeled to quantitatively assess the chloride penetration in the different concrete mixtures. The chloride profiles were modeled considering the total chloride content in wt.% cement (instead of wt.%

concrete) to facilitate the comparison of the results of diffusion coefficients and surface chloride concentrations with the literature. The conversion of the chloride content units was performed using Equation 6.

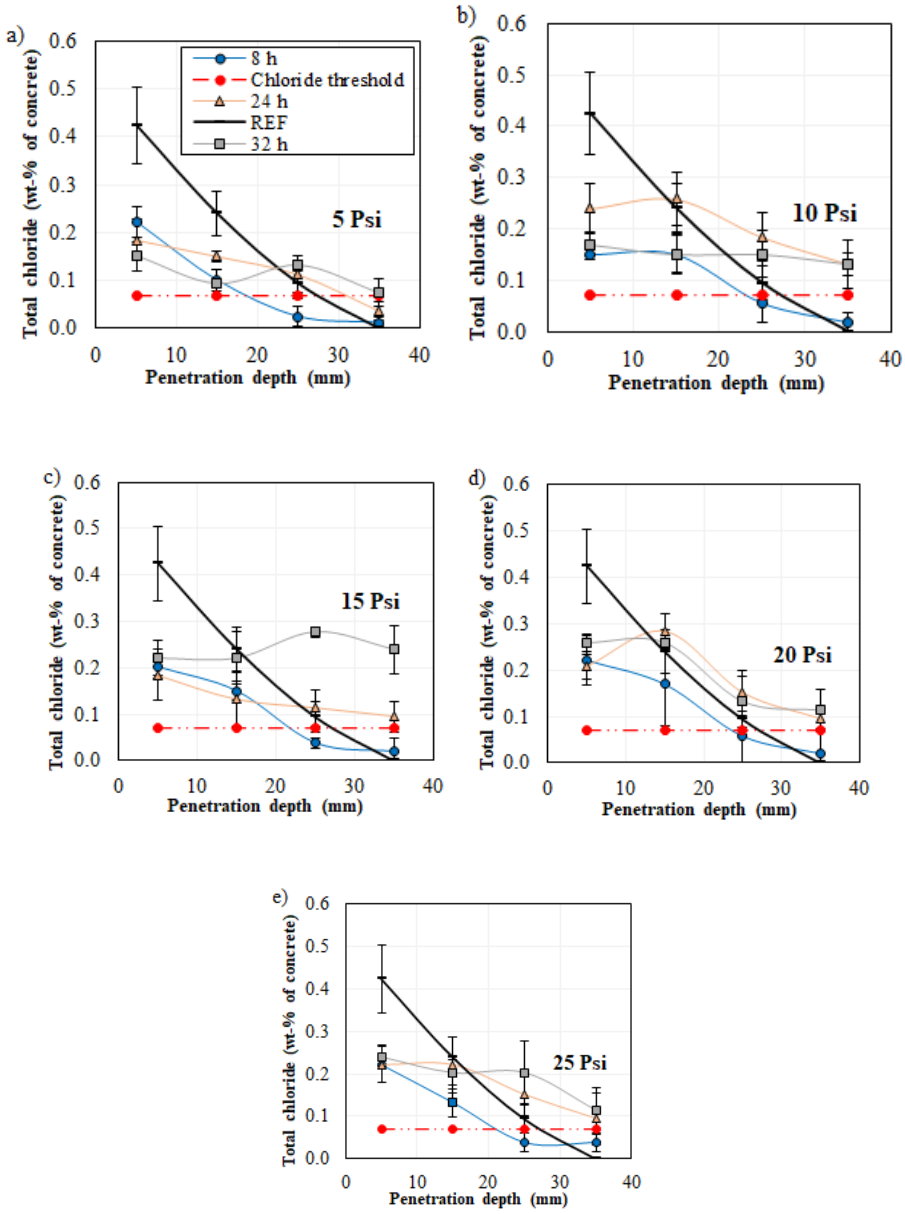

Figure 4. Effect of carbonate curing time on the chloride profile: (a) 5 Psi; (b) 10 Psi; (c) 15 Psi; (d) 20 Psi; (e) 25 Psi.

Figures 5-8 show the estimated chloride diffusion coefficient (*D*), the surface chloride concentration (*Cs*), and the determination coefficients for each profile. There was no significant variation between the modeling curves for the different equations. However, Holliday's equation showed the advantage of being able to model the convection zone, and consequently, estimate the surface concentration of chlorides in the concrete. The four equations applied in this research were able to satisfactorily model almost all chloride profiles. It was not possible to model efficiently the 15p32h concrete (Figure 8c) since this profile did not clearly show the distinction of the convection and diffusion zone. In this case, only the last two points could be used for the diffusion models (Equations 2, 4, and 5). However, the behavior of this profile was simulated using Holliday's modified equation.

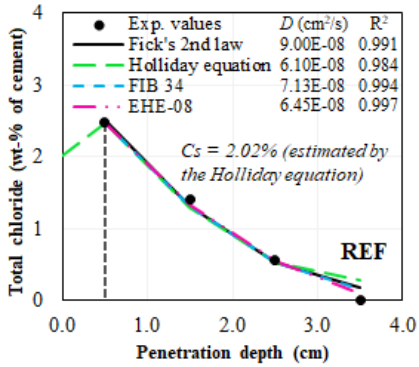

Figure 5. Modeling of chloride penetration – reference concrete.

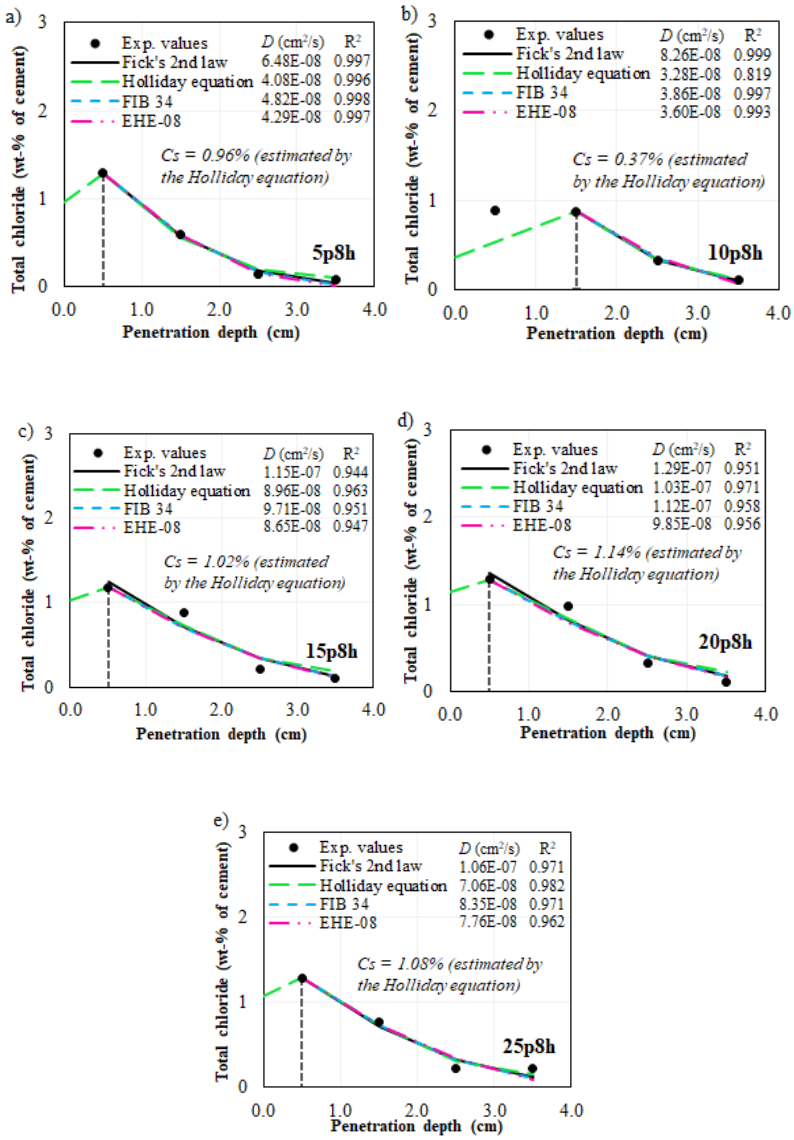

Figure 6. Modeling of chloride penetration curing time of 8 h: (a) 5 Psi; (b) 10 Psi; (c) 15 Psi; (d) 20 Psi; (e) 25 Psi.

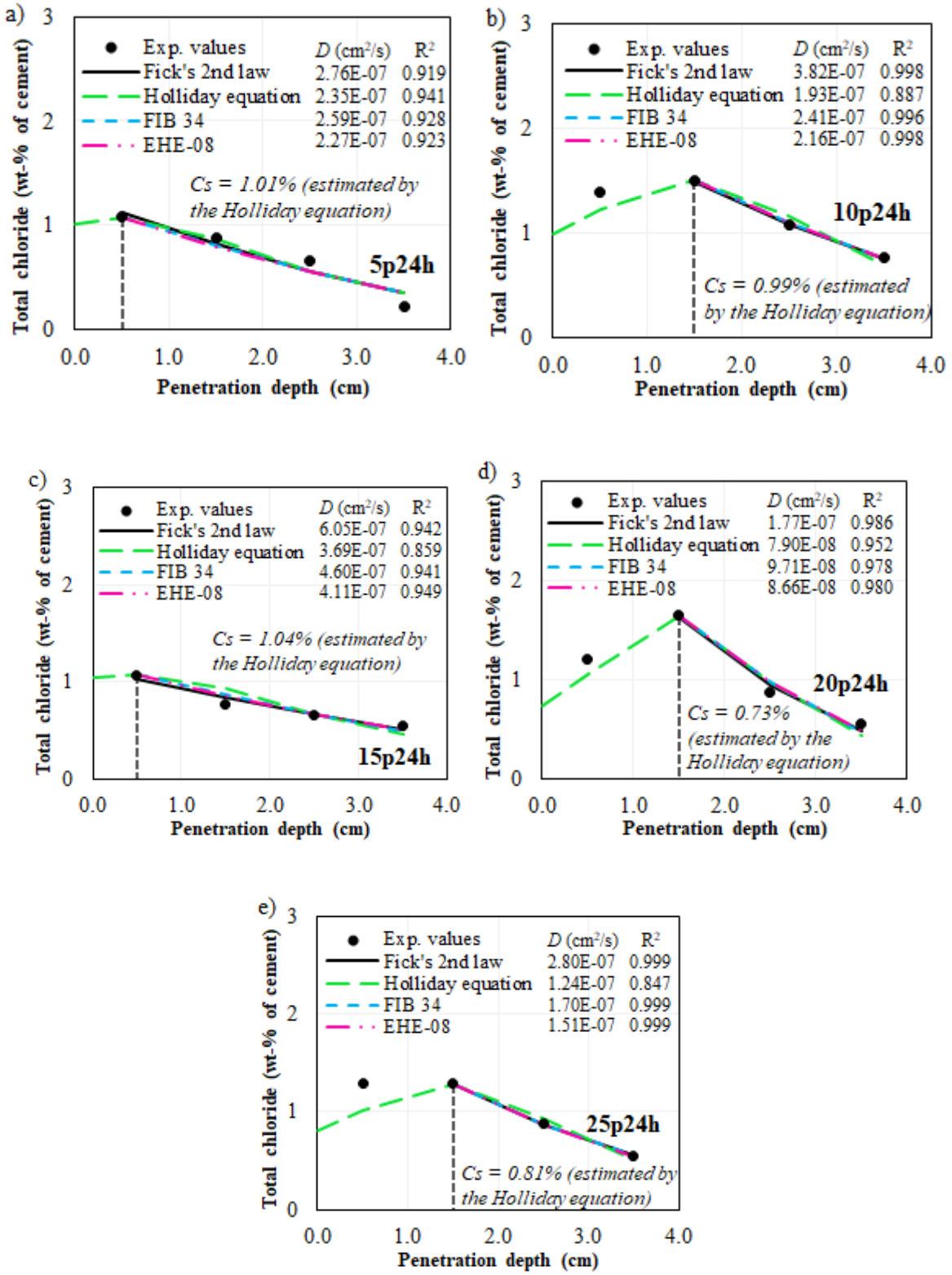

Figure 7. Modeling of chloride penetration – curing time of 24 h: (a) 5 Psi; (b) 10 Psi; (c) 15 Psi; (d) 20 Psi; (e) 25 Psi.

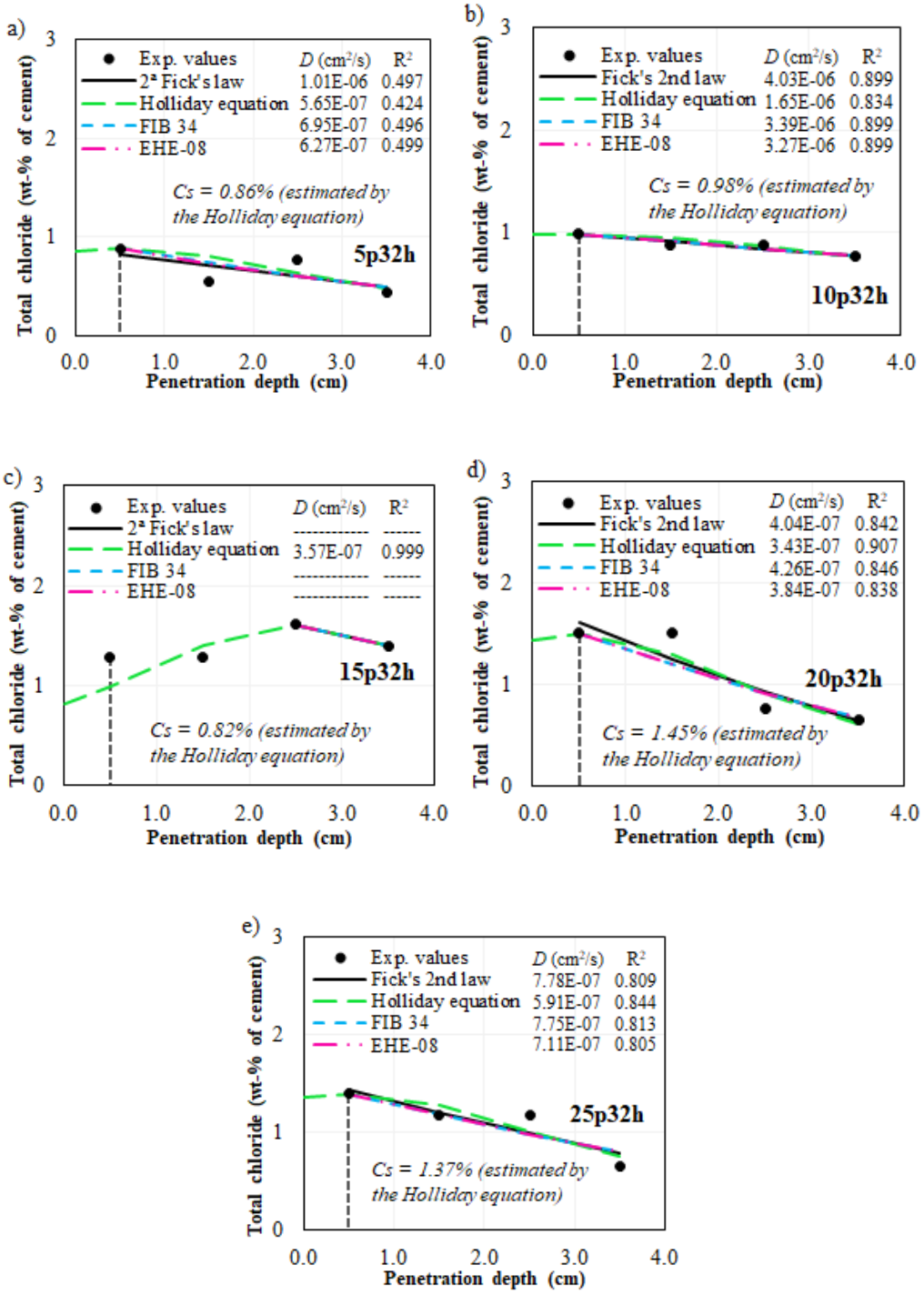

Figure 8. Modeling of chloride penetration – curing time of 32 h: (a) 5 Psi; (b) 10 Psi; (c) 15 Psi; (d) 20 Psi; (e) 25 Psi.

The action of wetting and drying cycles created a convective zone in the chloride profiles. According to Figures 5-8, CO_2 pressure and carbonation curing time did not influence the depth of the convection zone. This zone was around 5 to 15 mm. Ye et al. [52] also found convection zones at depths ranging between 5 and 15 mm when modeling the chloride penetration into cracked concretes subject to drying and wetting cycles.

At the depth of the convective zone, the drying period of the wetting and drying cycles produces a highly concentrated pore solution of chloride ions, which can be transported quickly into the cementitious matrix, due to capillary suction during the subsequent wetting period. The depth of the convection zone is mainly influenced by the depth of the concrete's moisture variation during the wetting and drying cycles. According to [52], this humidity variation is related to the concrete exposure surface. Therefore, this parameter was less affected by carbonation curing, since the concrete exposure surface is the same regardless of the curing condition.

The diffusion coefficient of the reference concrete was between 6.10E-08 and 9.00E-08 cm^2/s. These values are coherent and similar to the coefficients found in different studies for conventionally cured concretes [4], [48], [51]. The carbonation curing conditions of 5 and 10 Psi for 8 hours were the only ones that reduced the chloride diffusion coefficient compared to the reference concrete. According to Figures 5 and 6, the concretes cured in the other three pressure levels (15, 20, and 25 Psi) for 8 hours had diffusion coefficients similar to the reference concrete, with values between 7.76E-08 to 12.9E-08 cm^2/s. However, the estimated chloride surface concentration for all concretes cured for 8 hours in the carbonation chamber was lower than the reference concrete. Thus, the carbonation cure applied over 8 hours was efficient to increase the concrete's resistance to chloride penetration. The use of four different models generated ranges of diffusion coefficient (and not a single value), increasing the reliability of the discussions of these results.

The chloride profiles became more horizontal with increasing CO_2 pressure and time. This means that the values of the diffusion coefficients have increased. However, the surface chloride concentration of all concrete mixtures cured by carbonation was lower than the reference concrete. Therefore, chlorides had greater difficulty in initially entering concrete cured by carbonation, due to the higher density of the surface layers of the cementitious matrix related to the formation of calcium carbonate. The capillary pores of the concrete are partially filled and blocked due to the deposit of calcium carbonate ($CaCO_3$). Thus, the intensity of capillary suction is decreased due to a reduction in capillary porosity on the surface and the loss of connectivity between pores within the concrete, as showed by [5], [19], [53]. Therefore, the chloride content in carbonated concrete samples is lower in the surface region.

However, once inside the concrete, chlorides had greater mobility in concrete cured by carbonation at high pressures during the longest times. This behavior is related to the greater difficulty of carbonated concrete to chemically fix chloride ions for the formation of Friedel's salt. In this study, Friedel's salt was easily found in the reference concretes in the first depth of analysis (0-10 mm) after exposure to thirty weeks of wetting and drying cycles in chloride solution. However, the identification of this salt was more difficult (it required more samples and more time for analysis) and in a smaller amount for carbonation-cured concretes (Figure 9), in addition to occurring in more internal depths (between 25-35 mm). The confirmation of Friedel's salt was performed through EDS and stoichiometric calculations.

The chemical bonding capacity of chlorides with the hydrated cement phases for the formation of Friedel's salt is related to the content of aluminates in the cement composition [54]. The results of this article indicate that Friedel's salt is more unstable in carbonated concrete, mainly due to the pH reduction caused by carbonation, similarly to other studies that evaluated the interaction between carbonation and chloride ingress [3], [44], [53]. Therefore, depending on the CO_2 pressure and curing time during carbonation curing, concrete may be less resistant to chloride-induced corrosion. For these cases, although the surface concentration of chlorides is less than a conventionally cured concrete (reference), the chlorides can reach the concrete cover more quickly due to the greater diffusion coefficient.

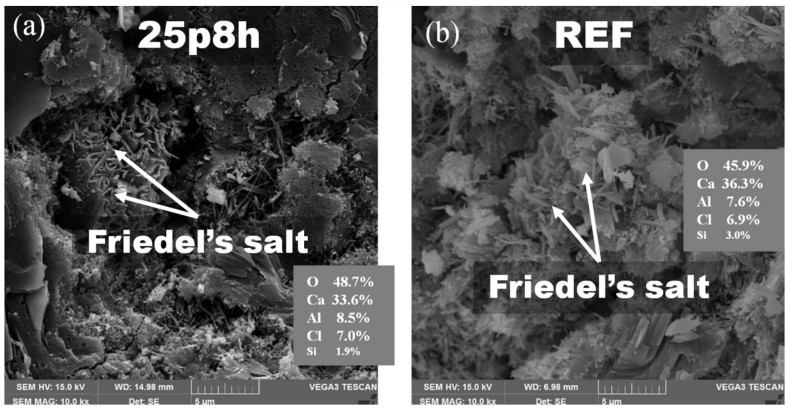

Figure 9. Friedel's salt formation: (a) concrete 25p8h (depth of 25-35 mm); (b) reference concrete (depth of 0-10 mm).

4 CONCLUSIONS

The following conclusions were obtained from the execution of this research:

- The effect of CO_2 pressure on chloride profiles was negative and increased with the curing times. The application of 8 hours of curing time was the only one that reduced the chloride profiles to practically all depths, regardless of pressure. Therefore, the combination of less time and pressure during carbonation curing potentiated the reduction of chloride penetration in concrete. There was a tendency for the chloride profiles to become higher than the reference concrete with increasing pressure. Therefore, increasing the CO_2 pressure does not seem to be an adequate solution for the protection of the concrete against the chloride ingress.
- The carbonation curing conditions of 5 and 10 Psi for 8 hours reduced the chloride diffusion coefficient compared to the reference concrete. The concretes cured in the other three pressure levels (15, 20, and 25 Psi) for 8 hours showed diffusion coefficients similar to the reference concrete. However, the estimated chloride surface concentration for all concretes cured for 8 hours in the carbonation chamber was lower than the reference concrete. Thus, the carbonation cure applied over 8 hours was efficient to increase the concrete's resistance to chloride penetration.
- The chloride diffusion coefficients were generally greater (chloride profiles became more horizontal) with increased CO_2 pressure and time. However, the surface chloride concentration of concrete cured by carbonation was lower than the reference concrete. Thus, chlorides had greater difficulty in initially entering concrete cured by carbonation, due to the higher density of the surface layers of the cement matrix. However, chlorides had greater mobility in carbonation-cured concrete at high pressures during the longest times. This behavior was related to the greater difficulty of concrete cured by carbonation to chemically fix chloride ions for the formation of Friedel's salt.

ACKNOWLEDGEMENTS

The authors thank the Brazilian Federal Agency for the Support and Evaluation of Graduate Education (Coordenação de Aperfeiçoamento de Pessoal de Nível Superior - CAPES), the National Council for Scientific and Technological Development (Conselho Nacional de Desenvolvimento Científico and Tecnológico - CNPQ), the Araucária Foundation (grant number 044/2020), and the Electron Microscopy Center (Centro de Microscopia Eletrônica - CME UFPR) for their support in conducting this study.

REFERENCES

[1] W. Shi, M. Najimi, and B. Shafei, "Reinforcement corrosion and transport of water and chloride ions in shrinkage-compensating cement concretes," *Cement Concr. Res.*, vol. 135, pp. 106121, Sept. 2020, http://dx.doi.org/10.1016/j.cemconres.2020.106121.

[2] R. A. Medeiros-Junior, "Impact of climate change on the service life of concrete structures," in *Eco-efficient Repair and Rehabilitation of Concrete Infrastructures*, F. Pacheco-Torgal, R. Melchers, N. Belie, X. Shi, K. Van Tittelboom, A.S. Perez, Eds., Duxford, UK: Woodhead Publishing, 2018, pp. 43–68.

[3] X. Xie, Q. Feng, Z. Chen, L. Jiang, and W. Lu, "Diffusion and distribution of chloride ions in carbonated concrete with fly ash," *Constr. Build. Mater.*, vol. 218, pp. 119–125, Sept. 2019, http://dx.doi.org/10.1016/j.conbuildmat.2019.05.041.

[4] R. A. Medeiros-Junior and D. H. Bem, "Study of the environment factor from Fick's and electrical resistivity models by simulation of chloride diffusivity prediction," *Adv. Struct. Eng.*, vol. 23, no. 10, pp. 2097–2109, 2020, http://dx.doi.org/10.1177/1369433220906932.

[5] D. Zhang and Y. Shao, "Effect of early carbonation curing on chloride penetration and weathering carbonation in concrete," *Constr. Build. Mater.*, vol. 123, pp. 516–526, Oct. 2016, http://dx.doi.org/10.1016/j.conbuildmat.2016.07.041.

[6] C. J. Goodbrake, J. F. Young, and R. L. Berger, "Reaction of hydraulic calcium silicates with carbon dioxide and water," *J. Am. Ceram. Soc.*, vol. 62, pp. 488–491, Sept. 1979, http://dx.doi.org/10.1111/j.1151-2916.1979.tb19112.x.

[7] V. Rostami, Y. Shao, A. J. Boyd, and Z. He, "Microstructure of cement paste subject to early carbonation curing," *Cement Concr. Res.*, vol. 42, pp. 186–193, Jan. 2012, http://dx.doi.org/10.1016/j.cemconres.2011.09.010.

[8] D. Zhang and Y. Shao, "Early age carbonation curing for precast reinforced concretes," *Constr. Build. Mater.*, vol. 113, pp. 134–143, June 2016, http://dx.doi.org/10.1016/j.conbuildmat.2016.03.048.

[9] P. He, C. Shi, Z. Tu, C. S. Poon, and J. Zhang, "Effect of further water curing on compressive strength and microstructure of CO_2-cured concrete," *Cement Concr. Compos.*, vol. 72, pp. 80–88, Sept. 2016, http://dx.doi.org/10.1016/j.cemconcomp.2016.05.026.

[10] L. Mo, F. Zhang, and M. Deng, "Mechanical performance and microstructure of the calcium carbonate binders produced by carbonating steel slag paste under CO_2 curing," *Cement Concr. Res.*, vol. 88, pp. 217–226, Oct. 2016., http://dx.doi.org/10.1016/j.cemconres.2016.05.013.

[11] B. J. Zhan, C. S. Poon, and C. J. Shi, "Materials characteristics affecting CO_2 curing of concrete blocks containing recycled aggregates," *Cement Concr. Compos.*, vol. 67, pp. 50–59, Mar. 2016, http://dx.doi.org/10.1016/j.cemconcomp.2015.12.003.

[12] D. Zhang, X. Cai, and Y. Shao, "Carbonation curing of precast fly ash concrete," *J. Mater. Civ. Eng.*, vol. 28, no. 11, pp. 04016127, Nov. 2016, http://dx.doi.org/10.1061/(ASCE)MT.1943-5533.0001649.

[13] S. Ahmad, R. A. Assaggaf, M. Maslehuddin, O. S. B. Al-Amoudi, S. K. Adekunle, and S. I. Ali, "Effects of carbonation pressure and duration on strength evolution of concrete subjected to accelerated carbonation curing," *Constr. Build. Mater.*, vol. 136, pp. 565–573, Apr. 2017, http://dx.doi.org/10.1016/j.conbuildmat.2017.01.069.

[14] Z. Liu and W. Meng, "Fundamental understanding of carbonation curing and durability of carbonation-cured cement-based composites: A review," *J. CO2 Util.*, vol. 44, pp. 101428, Feb. 2021, http://dx.doi.org/10.1016/j.jcou.2020.101428.

[15] L. Qin, X. Gao, A. Su, and Q. Li, "Effect of carbonation curing on sulfate resistance of cement-coal gangue paste," *J. Clean. Prod.*, vol. 278, pp. 123897, Feb. 2021, http://dx.doi.org/10.1016/j.jclepro.2020.123897.

[16] X. Pan, C. Shi, N. Farzadnia, X. Hu, and J. Zheng, "Properties and microstructure of CO_2 surface treated cement mortars with subsequent lime-saturated water curing," *Cement Concr. Compos.*, vol. 99, pp. 89–99, May 2019, http://dx.doi.org/10.1016/j.cemconcomp.2019.03.006.

[17] V. Rostami, Y. Shao, and A. J. Boyd, "Durability of concrete pipes subjected to combined steam and carbonation curing," *Constr. Build. Mater.*, vol. 25, no. 8, pp. 3345–3355, Aug. 2011, http://dx.doi.org/10.1016/j.conbuildmat.2011.03.025.

[18] Q. T. Phung et al., "Effect of limestone fillers on microstructure and permeability due to carbonation of cement pastes under controlled CO_2 pressure conditions," *Constr. Build. Mater.*, vol. 82, pp. 376–390, May 2015, http://dx.doi.org/10.1016/j.conbuildmat.2015.02.093.

[19] T. Chen, X. Gao, "Effect of carbonation curing regime on strength and microstructure of Portland cement paste," *J. CO2 Util.*, vol. 34, pp. 74-86, Dec. 2019, https://doi.org/10.1016/j.jcou.2019.05.034.

[20] D. Zhang and Y. Shao, "Enhancing chloride corrosion resistance of precast reinforced concrete by carbonation curing," *ACI Mater. J.*, vol. 116, pp. 3–12, May 2019., http://dx.doi.org/10.14359/51714461.

[21] L. Qin and X. Gao, "Properties of coal gangue-Portland cement mixture with carbonation," *Fuel*, vol. 245, pp. 1–12, June 2019., http://dx.doi.org/10.1016/j.fuel.2019.02.067.

[22] V. Rostami, Y. Shao, A.J. Boyd, "Carbonation curing versus steam curing for precast concrete production", *J. Mater. Civil Eng.*, vol. 24, n. 9, pp. 1221-1229, Sept., 2012, https://doi.org/10.1061/(ASCE)MT.1943-5533.0000462.

[23] D. Sharma and S. Goyal, "Accelerated carbonation curing of cement mortars containing cement kiln dust: An effective way of CO_2 sequestration and carbon footprint reduction," *J. Clean. Prod.*, vol. 192, pp. 844–854, Aug. 2018, http://dx.doi.org/10.1016/j.jclepro.2018.05.027.

[24] J. H. Seo, S. M. Park, and H. K. Lee, "Evolution of the binder gel in carbonation-cured Portland cement in an acidic medium," *Cement Concr. Res.*, vol. 109, pp. 81–89, July 2018, http://dx.doi.org/10.1016/j.cemconres.2018.03.014.

[25] Y. Liu et al., "Properties and microstructure of concrete blocks incorporating drinking water treatment sludge exposed to early-age carbonation curing," *J. Clean. Prod.*, vol. 261, pp. 121257, July 2020, http://dx.doi.org/10.1016/j.jclepro.2020.121257.

[26] T. Saito, S. Khamhou, T. Yumoto, and N. Otsuki, "Permeability of sulfate ions in cementitious materials containing γ-Ca_2SiO_4 after autoclave curing and accelerated carbonation," *J. Adv. Concr. Technol.*, vol. 9, pp. 223–230, Oct. 2011., http://dx.doi.org/10.3151/jact.9.223.

[27] C. Shi, D. Wang, F. He, and M. Liu, "Weathering properties of CO_2-cured concrete blocks," *Resour. Conserv. Recycling*, vol. 65, pp. 11–17, Aug. 2012, http://dx.doi.org/10.1016/j.resconrec.2012.04.005.

[28] D. Xuan, B. Zhan, and C. S. Poon, "Development of a new generation of eco-friendly "concrete blocks by accelerated mineral carbonation," *J. Clean. Prod.*, vol. 133, pp. 1235–1241, Oct. 2016, http://dx.doi.org/10.1016/j.jclepro.2016.06.062.

[29] M. Liu, S. Hong, Y. Wanga, J. Zhang, D. Hou, and B. Dong, "Compositions and microstructures of hardened cement paste with carbonation curing and further water curing," *Constr. Build. Mater.*, vol. 267, pp. 121724, Jan. 2021, http://dx.doi.org/10.1016/j.conbuildmat.2020.121724.

[30] J. Jang and H. Lee, "Microstructural densification and CO_2 uptake promoted by the carbonation curing of belite-rich Portland cement," *Cement Concr. Res.*, vol. 82, pp. 50–57, Apr. 2016, http://dx.doi.org/10.1016/j.cemconres.2016.01.001.

[31] L. Mo and D. K. Panesar, "Effects of accelerated carbonation on the microstructure of Portland cement pastes containing reactive MgO," *Cement Concr. Res.*, vol. 42, pp. 769–777, June 2012, http://dx.doi.org/10.1016/j.cemconres.2012.02.017.

[32] Associação Brasileira de Normas Técnicas, *Concreto – Procedimento para moldagem e cura de corpos de prova*, ABNT NBR 5738, 2015.

[33] H. El-Hassan, Y. Shao, and Z. Ghouleh, "Effect of initial curing on carbonation of lightweight concrete masonry units," *ACI Mater. J.*, vol. 110, pp. 441–450, July 2013, http://dx.doi.org/10.14359/51685791.

[34] H. El-Hassan and Y. Shao, "Early carbonation curing of concrete masonry units with Portland limestone cement," *Cement Concr. Compos.*, vol. 62, pp. 168–177, Sept. 2015, http://dx.doi.org/10.1016/j.cemconcomp.2015.07.004.

[35] M. Abdullahi, J.O. Odigure, A.S. Koyo, A.S. Abdulkareem, "Characterization and predictive reaction model for cement-sand-kaolin composite for CO2 sequestration," *J. CO2 Util.*, vol. 16, pp. 169-181, Dec., 2016, https://doi.org/10.1016/j.jcou.2016.06.008.

[36] Y. Zhang, M. Zhang, and G. Ye, "Influence of moisture condition on chloride diffusion in partially saturated ordinary Portland cement mortar," *Mater. Struct.*, vol. 51, pp. 36, Feb. 2018, http://dx.doi.org/10.1617/s11527-018-1162-7.

[37] Réunion Internationale des Laboratories D'essais de Recherches Sur Les Matériaux Et Les Constructions, "CPC-18, "Measurement of hardened concrete carbonation depth," *Mater. Struct.*, vol. 21, pp. 453–455, Nov. 1988, http://dx.doi.org/10.1007/BF02472327.

[38] Réunion Internationale des Laboratories D'essais de Recherches Sur Les Matériaux Et Les Constructions, "Analysis of total chloride content in concrete," *Mater. Struct.*, vol. 35, pp. 583–585, Nov. 2002, http://dx.doi.org/10.1007/BF02483128.

[39] J. Crank, *The Mathematics of Diffusion*, 1. ed. Grã Bretanha: Oxford University Press, 1970.

[40] C. E. T. Balestra, T. A. Reichert, W. A. Pancera, and G. Savaris, "Chloride profile modeling contemplating the convection zone based on concrete structures present for more than 40 years in different marine aggressive zones," *Constr. Build. Mater.*, vol. 198, pp. 345–358, Feb. 2019, http://dx.doi.org/10.1016/j.conbuildmat.2018.11.271.

[41] C. E. T. Balestra, T. A. Reichert, G. Savaris, W. A. Pansera, and R. A. Medeiros-Junior, "Nondestructive method for estimation of chloride profiles: correlation between electrical resistivity and Holliday-empirical equation," *J. Constr. Eng. Manage.*, vol. 146, pp. 04020119, Oct. 2020, http://dx.doi.org/10.1061/(ASCE)CO.1943-7862.0001907.

[42] Fédération Internationale du Béton, *Model Code for Service Life Design*, CEB-FIB-34, 2006.

[43] Comisión Permanente Del Hormigón, *Instrucción del Hormigón Estructural,* EHE-08, 2010.

[44] J. Liu, M. Ba, Y. Du, Z. He, and J. Chen, "Effects of chloride ions on carbonation rate of hardened cement paste by X-ray CT techniques," *Constr. Build. Mater.*, vol. 122, pp. 619–627, Sept. 2016, http://dx.doi.org/10.1016/j.conbuildmat.2016.06.101.

[45] Y. Gao, J. Zhang, S. Zhang, and Y. Zhang, "Probability distribution of convection zone depth of chloride in concrete in a marine tidal environment," *Constr. Build. Mater.*, vol. 140, pp. 485–495, June 2017, http://dx.doi.org/10.1016/j.conbuildmat.2017.02.134.

[46] H. Chang, S. Um, D. Xie, and P. Wang, "Influence of pore structure and moisture distribution on chloride "maximum phenomenon" in surface layer of specimens exposed to cyclic drying-wetting condition," *Constr. Build. Mater.*, vol. 131, pp. 16–30, Jan. 2017, http://dx.doi.org/10.1016/j.conbuildmat.2016.11.071.

[47] R. Cai et al., "Skin effect of chloride ingress in marine concrete: A review on the convection zone," *Constr. Build. Mater.*, vol. 262, pp. 120566, Nov. 2020, http://dx.doi.org/10.1016/j.conbuildmat.2020.120566.

[48] S. R. Pinto, C. Angulski da Luz, G. S. Munhoz, and R. A. Medeiros-Junior, "Resistance of phosphogypsum-based supersulfated cement to carbonation and chloride ingress," *Constr. Build. Mater.*, vol. 263, pp. 120640, Dec. 2020, http://dx.doi.org/10.1016/j.conbuildmat.2020.120640.

[49] W. Klemm and R. Berger, "Accelerated curing of cementitious systems by carbon dioxide: part I. Portland cement," *Cement Concr. Res.*, vol. 2, pp. 567–576, Sept. 1972, http://dx.doi.org/10.1016/0008-8846(72)90111-1.

[50] J. F. Young, R. L. Berger, and J. Breese, "Accelerated curing of compacted calcium silicate mortars on exposure to CO_2," *J. Am. Ceram. Soc.*, vol. 57, pp. 394–397, Sept. 1974, http://dx.doi.org/10.1111/j.1151-2916.1974.tb11420.x.

[51] R. A. Medeiros-Junior, M. G. Lima, P. C. Brito, and M. H. F. Medeiros, "Chloride penetration into concrete in an offshore platform-analysis of exposure conditions," *Ocean Eng.*, vol. 103, pp. 78–87, July 2015, http://dx.doi.org/10.1016/j.oceaneng.2015.04.079.

[52] H. Ye, N. Jin, X. Jin, and C. Fu, "Model of chloride penetration into cracked concrete subject to drying–wetting cycles," *Constr. Build. Mater.*, vol. 36, pp. 259–269, Nov. 2012, http://dx.doi.org/10.1016/j.conbuildmat.2012.05.027.

[53] J. Liu et al., "Understanding the interacted mechanism between carbonation and chloride aerosol attack in ordinary Portland cement concrete," *Cement Concr. Res.*, vol. 95, pp. 217–225, May 2017, http://dx.doi.org/10.1016/j.cemconres.2017.02.032.

[54] J. R. Hino Jr, C. E. T. Balestra, and R. A. Medeiros-Junior, "Comparison of test methods to determine resistance to chloride penetration in concrete: Sensitivity to the effect of fly ash," *Constr. Build. Mater.*, vol. 277, pp. 122265, Mar. 2021, http://dx.doi.org/10.1016/j.conbuildmat.2021.122265.

Author contributions: RLD: conceptualization, formal analysis, methodology and writing; NAMB: conceptualization, methodology and writing; RAM and JRG: supervision, methodology, data curation and writing.

Editors: Bruno Briseghella, Guilherme Aris Parsekian.

IBRACON Structures and Materials Journal
Revista IBRACON de Estruturas e Materiais
ISSN 1983-4195 ismj.org

ORIGINAL ARTICLE

Simplified DEWS test for steel fibre-reinforced concrete characterisation

Ensaio DEWS simplificado para caracterização do concreto reforçado com fibras de aço

Renata Monte[a]
Ludmily da Silva Pereira[b]
Antonio Domingues de Figueiredo[a]
Ana Blanco[c]
Luís Antônio Guimarães Bitencourt Júnior[b]

[a]Universidade de São Paulo – USP, Departamento de Engenharia de Construção Civil – PCC, São Paulo, SP, Brasil
[b]Universidade de São Paulo – USP, Departamento de Engenharia de Estruturas e Geotécnica – PEF, São Paulo, SP, Brasil
[c]Loughborough University, School of Architecture, Building and Civil Engineering, Loughborough, Leicestershire, United Kingdom

Received 17 August 2022
Accepted 26 January 2023

Abstract: Fibre Reinforced Concrete (FRC) is internationally recognised as a structural material in the *fib* Model Code 2010 and at a national level in the recently published ABNT standard NBR 16935, which establishes the structural design procedure based on post-cracking parameters. This publication should foster an increase in the number of applications of FRC in Brazil in the next years. In this context, many researchers have investigated the use of the DEWS test for the FRC characterisation as an alternative to the three-point bending test (3PBT) usually recommended by standards. The DEWS test is conducted by applying a compressive load on specimens with triangular grooves that induce a pure mode-I tensile fracture. Despite the advantages of the test, such as a smaller specimen and simpler testing procedure to obtain the anisotropic/orthotropic material properties, it still requires transducers to measure crack opening and generate the triangular grooves in the specimen, which is more complex, and labour demanding. This study addresses these issues by proposing a simplified test method and preparation consisting of removing the transducers (correlating the machine stroke and the crack opening) and generating the triangular groves during the casting instead of sawing afterwards. These modifications made the testing procedure much easier to perform. The experimental program assesses the modifications in the DEWS test setup and their influence on the post-cracking characterisation of FRC. Additionally, the effective fibre content and orientation were assessed by performing the inductive test. The results show that FRC characterisation can be successfully conducted using a simpler configuration of the DEWS test. This alternative test presents some advantages in comparison with the 3PBT test for FRC quality control, especially the lower volume of material and the test control by machine displacement.

Keywords: fibre reinforced concrete, mechanical characterisation, indirect tensile test, DEWS.

Resumo: O Concreto Reforçado com Fibras (CRF) é reconhecido internacionalmente como material estrutural pelo *fib* Model Code 2010 e em nível nacional, na recém publicada norma ABNT NBR 16935, que estabelece o procedimento de projeto estrutural baseado nos parâmetros pós-fissuração do compósito. Esta publicação deve propiciar um aumento do número de aplicações de CRF no Brasil nos próximos anos. Nesse contexto, muitos pesquisadores têm investigado o uso do teste DEWS para a caracterização de CRF como alternativa ao ensaio de flexão em três pontos (3PBT) usualmente recomendado pelas normas. O ensaio DEWS é realizado aplicando-se uma carga compressiva em corpos de prova com duplo corte à 45^0 que induzem uma falha em modo-I de fratura. Apesar das vantagens, como uso de corpo de prova menor e procedimento de ensaio mais simples para obter as propriedades anisotrópicas/ortotrópicas do material, ele ainda requer transdutores para medir a

Corresponding author: Luís Antônio Guimarães Bitencourt Júnior. E-mail: luis.bitencourt@usp.br
Financial support: Renata Monte would like to acknowledge the financial support of the Brazilian National Council for Scientific and Technological Development – CNPq (Proc. N°: 437143/2018-0). Ludmily Pereira acknowledges that this study was financed in part by the Coordenação de Aperfeiçoamento de Pessoal de Nível Superior – Brazil (CAPES) – Finance Code 001. Antonio D. de Figueiredo gratefully acknowledges the CNPq for the support (Proc. N°: 305055/2019-4). Luís A.G. Bitencourt Jr. would also like to extend his acknowledgements to the financial support of the CNPq (Proc. N°: 310401/2019-4 and N°: 406205/2021-3) and São Paulo Research Foundation – FAPESP (Proc. N°: 24487-2/2019).
Conflict of interest: Nothing to declare.
Data Availability: the data that support the findings of this study are available from the corresponding author, upon reasonable request.

abertura da fissura e gerar os cortes triangulares no corpo de prova, o que é mais complexo e trabalhoso. Este estudo aborda essas questões propondo um método de ensaio e preparação simplificado que consiste em remover os transdutores (correlacionando o deslocamento da máquina e a abertura da fissura) e gerar os cortes triangulares à 45^0 durante a moldagem em vez de cortar posteriormente. Essas modificações tornaram o procedimento de ensaio muito mais fácil de ser realizado. O programa experimental avalia as modificações na configuração do ensaio DEWS e sua influência na caracterização pós-fissuração do CRF. Além disso, o conteúdo efetivo de fibra e a orientação foram avaliados através da realização do ensaio indutivo. Os resultados mostram que a caracterização do FRC pode ser realizada com sucesso usando uma configuração mais simples. Esse ensaio alternativo apresenta vantagens em comparação ao ensaio 3PBT para o controle tecnológico do CRF, principalmente em relação as dimensões do corpo de prova e controle do ensaio pelo deslocamento do equipamento.

Palavras-chave: concreto reforçado com fibras, caracterização mecânica, teste de tração indireta, DEWS.

How to cite: R. M. Monte, L. S. Pereira, A. D. Figueiredo, A. Blanco, and L. A. G. Bitencourt Jr, "Simplified DEWS test for steel fibre-reinforced concrete characterisation," *Rev. IBRACON Estrut. Mater.*, vol. 16, no. 6, e16604, 2023, https://doi.org/10.1590/S1983-41952023000600004

1 INTRODUCTION

The publication of the *fib* Model Code 2010 [1] promoted the use of fibre-reinforced concrete (FRC) in structural applications [2]. More recently, the publication of the Brazilian standard ABNT NBR 16935 [3] to design FRC structures has provided normative support for its application in Brazil. Due to the complexity of executing uniaxial tensile tests, standards have traditionally recommended bending tests, such as EN14651 [4] and ASTM C1609 [5], on notched or unnotched beams for material characterisation. The *fib* Model Code 2010 [1] refers to the European standard EN14651 [4] to determine the tensile behaviour of FRC (notched three-point bending test (3PBT)). Similarly, the Brazilian standard ABNT NBR 16940 [6] also proposes a 3PBT. Based on this test, a curve of applied load (F) versus crack mouth opening displacement (CMOD) is obtained.

Despite being the most widely used standard method, the 3PBT involves a complex setup, specialist equipment (closed loop) and relatively big specimens. This becomes particularly evident when a quality program for a major infrastructure project is defined, with the additional challenge of balancing the expectations and/or requirements of the designers and the equipment and resources in most professional laboratories. In addition, the scepticism on the use of FRC as structural material can be directly related to the variability observed in the material characterisation [7]. Pleesudjai et al. [8] reported the number of beams required to comply with the quality control program of a tunnel project, which rose to the staggering figure of 378 beams (ASTM C1609 [5]), representing 4.5 m^3 of FRC.

Quality control programs in major infrastructure projects could significantly benefit from adopting alternative approaches accepted in design recommendations based on indirect tensile tests, which do not require closed-loop equipment and use smaller specimens. Even for obtaining design parameters, the *fib* Model Code 2010 [1] accepts alternative methods if a correlation with the reference test is proved, and the Brazilian standard accepts the double punch test only if indicated by the designer and a correlation with the 3PBT is previously established.

Examples of these indirect tensile tests include the Double Punch test (DPT or BCN) [9], the Montevideo test (MVD) [10] and the Double Edge Wedge Splitting test (DEWS) [11], [12]. Among these, only the DPT have the test procedure established in standards in Brazil (ABNT NBR 16939 [13]) and in Europe (UNE 83515 [14]). Oppositely, the DEWS test exhibits some advantages compared to the DPT test. In the DPT, the failure mechanism commonly presents three radial cracks, although in some cases, four planes can be observed, induced by penetration of two cones formed under the punches. The unpredictable number of fracture planes and the complex failure mechanism are drawbacks of the DPT. This greater behavioural complexity makes obtaining constitutive equations for FRC more challenging once it depends on the inference of the material's internal friction coefficient [15]. The friction problem also occurs with the MVD at an intense level due to the contact between the wedge and the angles positioned on the edge of the notch, making it challenging to obtain constitutive equations [10]. On the other hand, the DEWS test is conducted by applying a compressive load on specimens with triangular grooves, which induces a pure Mode I tensile fracture [11].

The original proposition of the DEWS test presents difficulties associated with specimen preparation, as cutting the triangular grooves demands high accuracy and perfect parallelism of the specimen faces and the installation of transducers to measure the crack opening [11]. These difficulties increase the performing time and costs of the test and, consequently, can be considered a drawback for quality control. MVD and DPT tests have an easier preparation to overcome this last drawback by using stroke displacement [10], [16]. However, both tests present the difficulty of

obtaining constitutive equations due to the friction inherent to the test methods. DPT and DEWS were evaluated as alternative tests to characterise the post-cracking tensile response of fibre reinforced sprayed concrete [17]. These authors recognise significant advantages of the DEWS test in comparison with flexural and DPT tests but pointed out the specimen's preparation as a relevant drawback for quality control. Thus, the use of the simplified DEWS test can mean the combination of two major advantages by facilitating the test procedure and the achievement of constitutive equations for FRC structural ability evaluation.

In this scenario, the aim of this paper is to propose and evaluate alterations to the DEWS test setup that result in a simpler but still reliable test for the systematic quality control of the residual tensile strength of FRC.

2 POST-CRACKING PARAMETERS FOR FRC

As mentioned above, the parameters that characterise the competence of the FRC for structural applications are obtained primarily through the 3PBT. The design parameters are the residual flexural tensile strength $f_{R,j}$ (j = 1,2,3,4) corresponding to $CMOD_j$ ($CMOD_1$ = 0.5 mm, $CMOD_2$ = 1.5 mm, $CMOD_3$ = 2.5 mm and $CMOD_4$ = 3.5 mm), calculated by the Equation 1.

$$f_{R,j} = \frac{3 \cdot F_j \cdot l}{2 \cdot b \cdot h_{SP}^2} \tag{1}$$

where F_j is the load corresponding to j, l is the span length, b is the width, and h_{SP} is the distance between the tip of the notch and the top of the beam in the mid-span section.

In both codes, *fib* Model Code 2010 [1] and ABNT NBR 16935 [3], the parameters adopted to design structures with FRC are based on the characteristic residual flexural tensile strengths f_{R1k} (corresponding to $CMOD_1$ = 0.5 mm) and f_{R3k} (corresponding to $CMOD_3$ = 2.5 mm), for the design at service limit state (SLS) and ultimate limit state (ULS), respectively.

On the other hand, the DEWS test results could be achieved from equilibrium considerations [11]. The transverse "splitting tensile" force F_{SP} induced by the applied vertical load P can be calculated by Equation 2:

$$F_{SP} = \mathrm{P} \frac{\cos\vartheta - \mu \sin\vartheta}{\sin\vartheta + \mu \cos\vartheta} \tag{2}$$

where ϑ is the inclination angle of the wedge grooves (ϑ = 45°); and μ is the friction coefficient of 0.06. Consequently, the splitting tensile force F_{SP} = 0.89 P.

The tensile stress (f_t) was calculated from Equation 3, where t is the specimen thickness and h_{lig} is the ligament depth.

$$f_t = \frac{F_{SP}}{t \cdot h_{lig}} \tag{3}$$

The referential post-cracking tensile strength values obtained with the DEWS test could also be associated with the SLS and the ULS adopting crack opening displacement (COD) values equal to 0.5 mm and 2.5 mm, respectively. These COD values were adopted to maintain the same crack mouth opening recommended in EN 14651 [3] and NBR 16940 [6]. In this way, it is possible to obtain adequate parallelism of results between both test methods.

3 EXPERIMENTAL PROGRAM

3.1 Materials and mix design

The concrete matrix was composed of Portland cement, siliceous aggregates, tap water and hooked-end steel fibres. Two fibre reinforced concretes T20 and T50 were produced, and the mix design is described in Table 1. The geometric and mechanical characteristics of the steel fibre are summarised in Table 2.

Table 1. Mix design of steel fibre reinforced concretes.

Component	Dosage (kg/m³)	
	T20	T50
Cement CP V-ARI	380	
Granite coarse aggregate (4.8-12.5 mm)	711	
Artificial sand (0-4.8 mm)	968	
Water	224	
Fibre	20	50

Table 2. Geometric and mechanical characteristics of the steel fibre.

Characteristic		Value
Length	l (mm)	35
Diameter	d (mm)	0.75
Aspect ratio	(l/d)	45
Elastic modulus	(GPa)	210
Tensile strength	(MPa)	1225

3.2 Casting and specimen production

For each fibre dosage, 5 cylinders of size ϕ100 × 200 mm were cast to assess the compressive strength and elastic modulus. For the DEWS tests, 24 cubic moulds of 100 mm were used, 12 for each fibre content (T20 and T50). For 6 moulds of each fibre content, two triangular prisms with a 45° inclination were glued in opposite faces to induce the triangular grooves (Figure 1a). The concrete casting was in the axis Z, considering the coordinates shown in Figure 1a. After the cast, the specimens were kept in their moulds for 24 h, covered with plastic to prevent air drying, and remained in a humid chamber for 24 days.

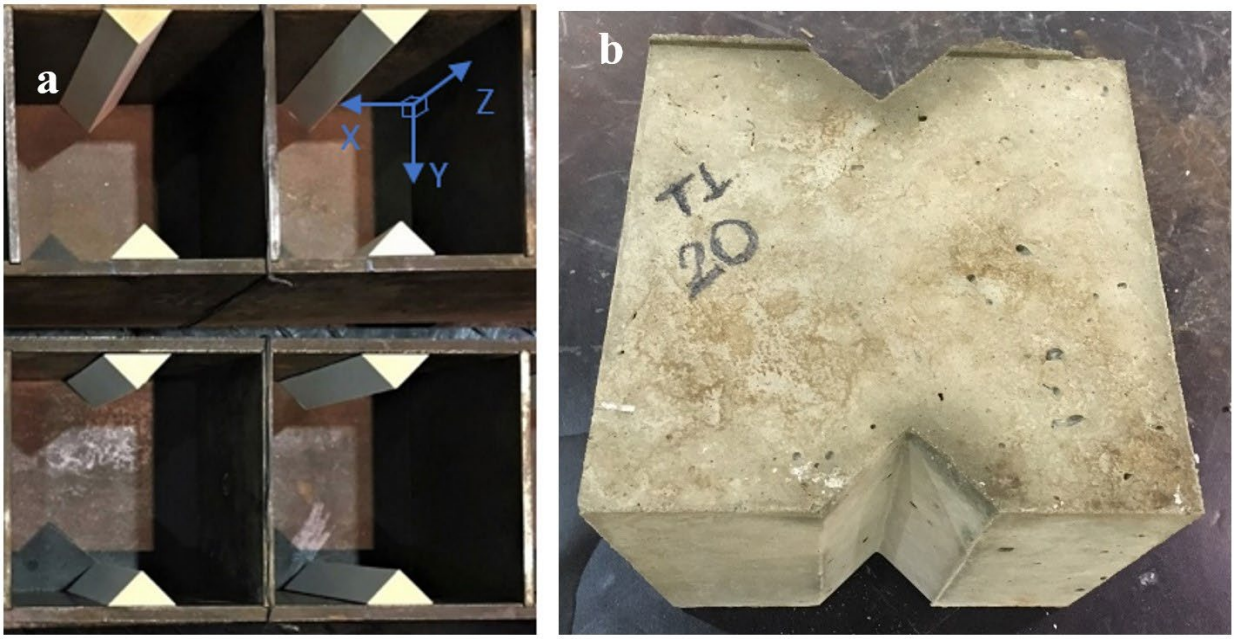

Figure 1. a) Moulds with triangular prims glued in opposite faces; b) Specimen with triangular grooves produced by casting.

For the specimens with triangular grooves not produced by casting, the cut was made one day before testing to generate the grooves (Figure 2). This preparation step is time-consuming and should be done carefully for satisfactory test performance [12].

Figure 2. Cutting the triangular grooves.

For the specimens with moulded triangular grooves, only the two notches starting from the groove vertices were cut. The identification of the specimens is T20-M or T50-M for grooves induced in the mould during cast and T20-C or T50-C for grooves generated by cutting after casting.

3.3 Test methods

3.3.1 DEWS

In the DEWS test, steel rollers are used as a loading device located in the grooves of the specimen (Figure 3). The compressive load applied by the actuator deviates through the grooves, inducing a uniaxial tensile stress state at the "ligament" (vertical fracture surface) [11]. To reduce friction, brass platens were glued to the groove edges, and the contact surfaces were lubricated with graphite, which resulted in a friction coefficient $\mu = 0.06$ [11].

Figure 3. View of the DEWS test setup.

The tests were performed employing a servo-hydraulic machine, and the actuator displacement was used to control the test speed of 0.12 mm/min [12]. To measure the crack opening displacement (COD) in the DEWS test,

Prisco et al. [11] used six linear variable differential transformers (LVDTs) attached to the specimens (three per side). To simplify the procedure of measuring the COD, Borges et al. [12] propose a test configuration using two transducers attached to opposite faces of the specimen, measuring the average COD at the middle height of the specimen. Recently, Pereira et al. [18] performed some experimental DEWS tests to correlate the vertical displacement of the machine and COD, as depicted in Figure 4.

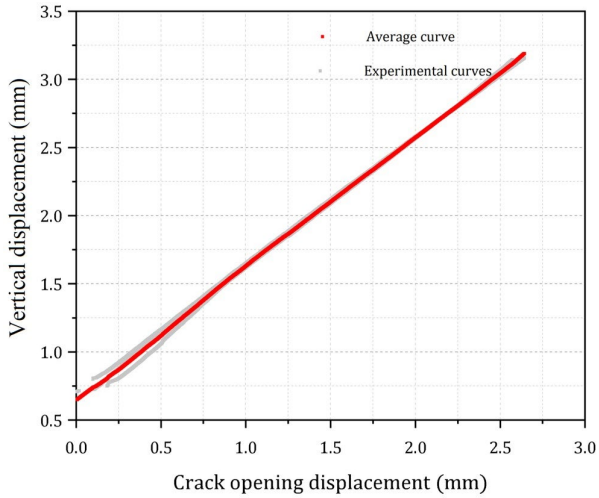

Figure 4. The relationship between vertical displacement (mm) and crack opening displacement – COD (mm) (adapted from Pereira et al. [18]).

Based on these results and using linear regression ($R^2 = 0.9997$), these authors proposed Equation 4, in which the COD can be obtained directly from the measure of the vertical displacement of the machine without the need for transducers.

$$D = 0{,}963 \times COD + 0{,}650 \tag{4}$$

Therefore, the residual strengths $f_{0.5}$, for COD = 0.5 mm, and $f_{2.5}$, for COD = 2.5 mm, can be obtained by means of the DEWS tests.

It is essential to mention that Equation 4, proposed by Pereira et al. [18], was obtained from a steel fibre-reinforced concrete with 40 MPa (compressive strength) and fibre content of 35kg/m^3. However, adopting the hypothesis that vertical displacement versus COD is a geometric relationship derived from a rigid body motion of the specimen, this equation can also be used for other concretes with distinct compressive strengths and fibre contents. In addition, it is also important to note that assuming this hypothesis, the theoretical relationship between vertical displacement and COD can be written as: D = 1.0 x COD + 0.0. The slight discrepancy between Equation 4 from the theoretical relationship is due to imperfections and accommodations in the test, which can be due to the concrete strength and stiffness, any specimen rotation after cracking, or the friction between the steel rollers and brass platens glued to the groove edges. The term 0.65 in Equation 4 represents the elastic strain of the specimen before concrete cracking.

3.3.2 Inductive method

Before the mechanical DEWS tests, the inductive method (non-destructive test) [19] was used to assess the content and the distribution of steel fibres in the specimens. This evaluation was performed to test if any significant difference can be attributed to the method of producing the grooves.

The inductive method [19] is based on the inductance change produced when a steel fibre reinforced specimen is exposed to a magnetic field. The equipment is composed of an impedance analyser and a coil (Figure 5). The magnetic field generated in the coil by the current flow is altered by the ferromagnetic nature of the steel fibres, which increases the permeability of the medium and produces an inductance variation measured by the analyser.

Figure 5. Coil and impedance analyser.

The test is compatible with cubic and cylindrical specimens. When the cubic specimen is used, the specimen is placed inside the coil, and the inductance is measured in the main directions perpendicular to its faces. For a given set of axes, each measurement will represent ΔLx, ΔLy and ΔLz for the axis X, Y and Z, respectively.

Torrents et al. [20] show that the summed inductance (ΔL) for the three axes holds a linear relation with the fibre content. Consequently, a calibration curve for the type of fibre being used is needed to determine the content of fibre (C_f). This calibration can be made by crushing the specimen after measuring the inductance in the axis X, Y and Z, or by using a known content of fibres (the same fibre used in the experiment) in polystyrene pieces (Figure 6).

Figure 6. Piece of polystyrene with a known content of fibre.

The parameter used to assess the contribution of the fibres in a certain direction is the average orientation number (η_i), given by the average of the cosine of the angle formed between the fibres and a line parallel to the direction of consideration. Cavalaro et al. [19] defined Equation 5 to assess the orientation number for FRC:

$$\eta_i = 1.03 \cdot \sqrt{\frac{\Delta L_i \cdot (1+2\cdot\gamma) - \Delta_L \cdot \gamma}{\Delta_L \cdot (1-\gamma)}} - 0.1 \tag{5}$$

where:

• η_i is the orientation number for each i axes.
• ΔLi is the variation in inductance in each axis, in Henry.
• ΔL is the summed inductance for the three axes, in Henry.
• γ is the shape factor equal to 0.05 for the fibre employed.

The orientation number can be used to estimate the relative contribution of the fibres in a direction i (C_i), using Equation 6.

$$C_i = \frac{\eta_i}{\sum_{i=x,y,z} \eta_i} \quad (6)$$

4 RESULTS AND DISCUSSIONS

4.1 Compressive strength and elastic modulus

The average and standard deviation results at 28 days of the compressive strength (f_{cm}) and elastic modulus (E_{cm}) are presented in Table 3.

Table 3. Mechanical properties of the FRCs with their respective standard deviation.

	f_{cm} (MPa)	E_{cm} (GPa)
T20	38.9±2.0	25.402±0.008
T50	35.9±0.4	25.76±0.02

For the relatively low fibre content (less than 1%), the fibre has no expected effect on compressive strength or elastic modulus. The results presented in Table 3 denoted a slight reduction of the average compressive strength when 50 kg/m^3 of fibres were added, which can be related to the impact of the fibre addition in the concrete consistency and, consequently, more difficulty in casting the specimens. However, an ANOVA analysis showed a non-significant difference between T20 and T50 compressive strengths. The null hypothesis for the test that the two means are equal was accepted with a p-value of 0.176 (considering significance level of 0.05).

4.2 Fibre content, orientation number and relative contribution of the fibres

Figure 7 shows the calibration curve, represented by the amount of inductance (ΔL) measured and the mass of fibres introduced in the polystyrene pieces.

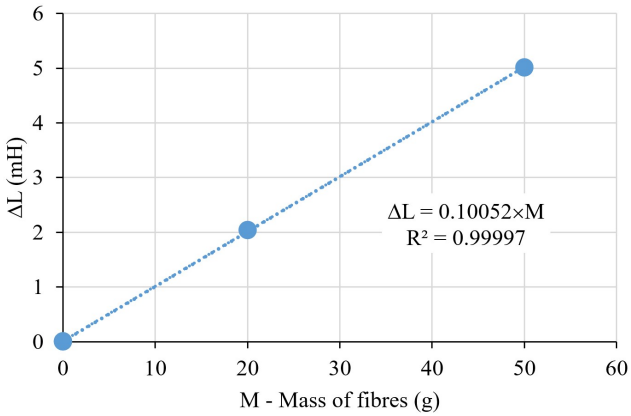

Figure 7. Calibration curve obtained for the fibre used.

The calibration equation (ΔL=0.10052×M) allows the determination of the mass of fibres in each DEWS specimen, measuring the inductance variation in each axis. Table 4 presents the nominal values of fibre content, the average fibre content calculated with the inductive method.

Table 4. Fibre content nominal values and average result measured with the inductive method and their respective standard deviation.

	Fibre content	
	Nominal (kg/m³)	**Measure with inductive (kg/m³)**
T20-M	20	25±2
T20-C		27±1
T50-M	50	57±2
T50-C		56±7

The results in Table 4 showed no significant difference between the fibre content of specimens with triangular grooves produced during the cast or cut after the cast. Thus, the results can be considered comparable because the fibre content is equivalent in both situations. Moreover, the inductive method revealed that the real fibre contents are significantly higher than the nominal values (30% for T20 and 13% for T50). The inductive method also assesses the estimation of the fibre orientation in the specimen, the orientation number (η_i) and the relative contribution of the fibres in a certain direction (C_i) (Table 5).

Table 5. Orientation number and relative contribution of the fibres in each direction with their respective standard deviation.

	Orientation number per axis			Fibre contribution per axis		
	η_X (%)	**η_Y (%)**	**η_Z (%)**	**C_X (%)**	**C_Y (%)**	**C_Z (%)**
T20-M	52±3	52±4	47±4	34±2	34±1	31±1
T20-C	58±8	54±3	51±3	36±3	33±1	31±2
T50-M	89±5	91±3	77±6	35±1	35±1	30±2
T50-C	85±8	90±8	79±10	33±2	36±2	31±2

As can be seen in Table 5, the η_i and C_i results are similar for the specimens with triangular grooves moulded or cut. Consequently, producing the grooves in the casting process does not induce fibre orientation.

4.3 Post-cracking characterisation – DEWS tests

The results of the DEWS tests are load and vertical displacement. The tensile stress and COD results were calculated using Equations 3-4. The stress *vs.* COD curves for the fibre content of 20 kg/m³ with triangular grooves moulded (T20-M) or cut (T20-C) are presented in Figures 8 and 9, respectively.

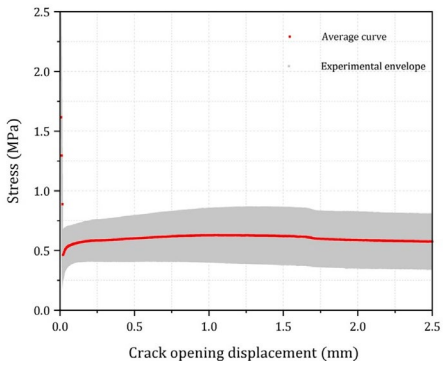

Figure 8. Stress *vs.* COD curves for DEWS tests with 20 kg/m³ of steel fibres and triangular grooves moulded (T20-M).

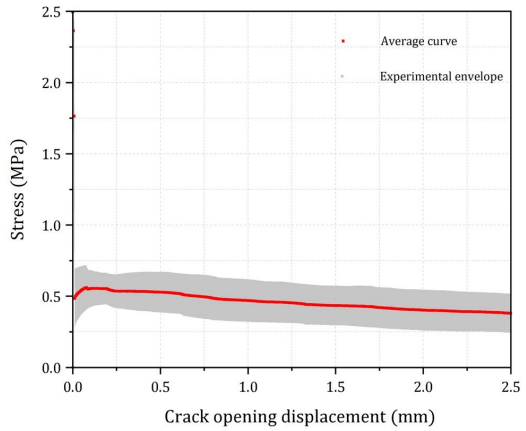

Figure 9. Stress *vs.* COD curves for DEWS tests with 20 kg/m^3 of steel fibres and triangular grooves cut (T20-C).

The experimental envelope of the tests with triangular grooves moulded is wider than those produced by cut. Such an outcome cannot be attributed to the method used for inducing the triangular grooves since this pattern does not occur for the specimens containing 50 kg/m^3 (see Figures 10-11).

The stress *vs.* COD curves for the fibre content of 50 kg/m^3 with triangular grooves moulded or cut are presented in Figures 10 and 11, respectively.

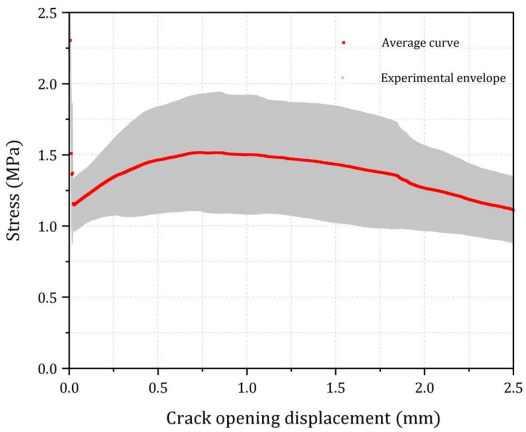

Figure 10. Stress *vs.* COD curves for DEWS tests with 50 kg/m^3 of steel fibres and triangular grooves moulded (T50-M).

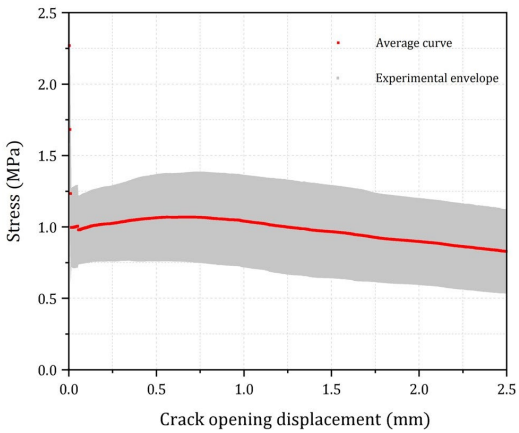

Figure 11. Stress *vs.* COD curves for DEWS tests with 50 kg/m^3 of steel fibres and triangular grooves cut (T50-C).

The curves of the tests with triangular grooves moulded suggest better performance than those produced by cut. Despite the scatter in the results, statistical tests did not reveal significant differences between the average residual tensile strengths obtained in specimens with moulded or cut grooves. A summary of the residual tensile strengths ($f_{0.5}$ for COD = 0.5 mm and $f_{2.5}$ for COD = 2.5 mm), with their respective standard deviation is presented in Table 6. Also, the average values were compared by a t-test with a significance level of 5%. The null hypothesis is that the average values are equal, independent of the method to produce the triangular grooves, and it is rejected for p-values below 0.05.

Table 6. Residual tensile strength: average, standard deviation and p-value in two-sample t-test.

	$f_{0.5}$		$f_{2.5}$	
	MPa	**p-value**	**MPa**	**p-value**
T20-M	0.61±0.20	0.372	0.54±0.23	0.109
T20-C	0.52±0.14		0.33±0.16	
T50-M	1.36±0.24	0.215	0.92±0.12	0.487
T50-C	1.11±0.33		0.83±0.24	

The results in Table 6 indicate that the average residual tensile strengths $f_{0.5}$ and $f_{2.5}$ are higher when the triangular groove is moulded. This may be associated with changes in fibre local orientation at the triangular grooves for moulding the specimens, which is minimised by the fact that there are notch cuts in both situations, which reduces the wall effect. Also, the cuts of triangular grooves can produce material damage in the specimens. However, considering the variability of residual strength obtained in the experimental tests, it can be noted that there is no statistical difference between the average results (p-value is above 0.05). In further studies, it is important to investigate the influence of the cuts in the post-cracking behaviour.

5 CONCLUSIONS

This paper addresses some of the issues identified as hindering the universal use of the DEWS test as a method for FRC characterisation. The results of the experimental program suggest that the modifications proposed in the test setup simplify the execution of the test without compromising its reliability for evaluating the mechanical behaviour of FRC. Based on the analysis conducted in this study, the following conclusions are drawn:

- Moulding the triangular grooves in the DEWS specimen while casting is feasible and significantly reduces the preparation steps.
- The fibre content of specimens with moulded and cut triangular grooves is similar. Also, the production of the grooves during the casting process does not affect the overall fibre orientation in the specimen, although some local influence could occur at the triangular grooves regions.
- The fact that the notches are sawed in the two situations of production of specimens minimises the wall effect of orientation of the fibres in the superior and inferior extremes of the ligament section.
- The deformation in the DEWS test can be measured using axial displacement instead of transducers, thus simplifying the execution and facilitating the adoption of the test in quality control laboratories.
- The residual tensile strength obtained in specimens with moulded and cut triangular grooves is comparable in terms of average and scatter. Hence, cutting the grooves is recommended only if the DEWS test will be used in cores drilled from real structures.

REFERENCES

[1] Fédération Internationale du Béton, *Fib Model Code for Concrete Structures 2010*. Lausanne: FIB, 2013.

[2] Y. T. Trindade, L. A. G. Bitencourt Jr, R. Monte, A. D. Figueiredo, and O. L. Manzoli, “Design of SFRC members aided by a multiscale model: part i - predicting the post-cracking parameters,” *Compos. Struct.*, vol. 241, p. 112078, Jun. 2020, http://dx.doi.org/10.1016/j.compstruct.2020.112078.

[3] Associação Brasileira de Normas Técnicas, *Projeto de Estruturas de Concreto Reforçado com Fibras – Procedimento*, ABNT NBR 16935, 2021.

[4] European Standards, *Test Method for Metallic Fiber-Reinforced Concrete – Measuring the Flexural Tensile Strength (Limit of Proportionality (LOP), Residual*, EN 14651, 2007.

[5] American Society for Testing and Materials, *12 Standard Test Method for Flexural Performance of Fibre-Reinforced Concrete*, ASTM C1609/C1609M, 2012.

[6] Associação Brasileira de Normas Técnicas, *Concreto Reforçado com Fibras – Determinação das Resistências à Tração na Flexão (Limite de Proporcionalidade e Resistências Residuais) – Método de Ensaio*, ABNT NBR 16940, 2021.

[7] Y. T. Trindade, L. A. G. Bitencourt Jr, and O. L. Manzoli, "Design of SFRC members aided by a multiscale model: part II - predicting the behavior of RC-SFRC beams," *Compos. Struct.*, vol. 241, p. 112079, Jun. 2020, http://dx.doi.org/10.1016/j.compstruct.2020.112079.

[8] C. Pleesudjai, D. Patel, M. Bakhshi, V. Nasri, and B. Mobasher, "Applications of statistical process control in the evaluation of QC test data for residual strength of FRC samples of tunnel lining segments," in *Fibre Reinforced Concrete: Improvements and Innovations* (RILEM Bookseries 30), P. Serna, A. Llano-Torre, J. R. Martí-Vargas, and J. Navarro-Gregori, Eds., Cham, Switzerland: Springer, 2021, pp. 815–826.

[9] C. Molins, A. Aguado, and S. Saludes, "Double punch test to control the energy dissipation in tension of FRC (Barcelona test)," *Mater. Struct.*, vol. 42, no. 4, pp. 415–425, May 2008.

[10] L. Segura-Castillo, R. Monte, and A. D. Figueiredo, "Characterisation of the tensile constitutive behaviour of fibre-reinforced concrete: a new configuration for the Wedge Splitting Test," *Constr. Build. Mater.*, vol. 192, pp. 731–741, Dec. 2018, https://doi.org/10.1016/j.conbuildmat.2018.10.101.

[11] M. Prisco, L. Ferrara, and M. G. L. Lamperti, "Double edge wedge splitting (DEWS): an indirect tension test to identify post-cracking behaviour of fibre reinforced cementitious composites," *Mater. Struct.*, vol. 46, pp. 1893–1918, Feb. 2013, http://dx.doi.org/10.1617/s11527-013-0028-2.

[12] L. A. C. Borges, R. Monte, D. A. S. Rambo, and A. D. Figueiredo, "Evaluation of postcracking behavior of fiber reinforced concrete using indirect tension test," *Constr. Build. Mater.*, vol. 204, pp. 510–519, Apr. 2019, https://doi.org/10.1016/j.conbuildmat.2019.01.158.

[13] Associação Brasileira de Normas Técnicas, *Concreto Reforçado com Fibras – Determinação das Resistências à Fissuração e Residuais à Tração por Duplo Puncionamento – Método de Ensaio*, ABNT NBR 16939, 2021.

[14] Asociación Española de Normalización, *Hormigones con Fibras. Determinación de la Resistencia a Fisuración Tenacidad y Resistencia Residual a Tracción. Método Barcelona*, UNE 83515: 2010, 2010.

[15] A. Blanco, P. Pujadas, S. Cavalaro, A. Fuente, and A. Aguado, "Constitutive model for fiber reinforced concrete based on the Barcelona test," *Cement Concr. Compos.*, vol. 54, pp. 327–340, Oct. 2014.

[16] P. Pujadas, A. Blanco, S. Cavalaro, A. Fuente, and A. Aguado, "New analytical model to generalize the Barcelona test using axial displacement," *J. Civ. Eng. Manag.*, vol. 19, pp. 259–271, Apr. 2013, http://dx.doi.org/10.3846/13923730.2012.756425.

[17] A. R. E. Cáceres, S. H. P. Cavalaro, R. Monte, and A. D. Figueiredo, "Alternative small-scale tests to characterize the structural behaviour of steel fibre-reinforced sprayed concrete," *Constr. Build. Mater.*, vol. 296, p. 123168, Aug. 2021, https://doi.org/10.1016/j.conbuildmat.2021.123168.

[18] L. Pereira, R. Monte, L. A. G. Bitencourt Jr, and A. D. Figueiredo, "Caracterização e controle do concreto com fibras para obras de infraestrutura com ensaios de tração indireta," in *61º Congr. Brasileiro Concr.*, Fortaleza, CE, Brazil Oct. 2019, pp. 1–12.

[19] S. H. P. Cavalaro, R. López, and J. M. Torrents, "Improved assessment of fibre content and orientation with inductive method in SFRC," *Mater. Struct.*, vol. 48, pp. 1859–1873, Mar. 2015, http://dx.doi.org/10.1617/s11527-014-0279-6.

[20] J. Torrents, A. Blanco, P. Pujadas, A. Aguado, P. Juan-García, and M. Sánchez-Moragues, "Inductive method for assessing the amount and orientation of steel fibers in concrete," *Mater. Struct.*, vol. 45, pp. 1577–1592, Apr. 2012, http://dx.doi.org/10.1617/s11527-012-9858-6.

Author contributions: RM: conceptualization, methodology, formal analysis, investigation, data curation, writing - original draft; LSP: investigation, data curation, writing - original draft; ADF: conceptualization, formal analysis, writing - review & editing; AB: formal analysis, writing - review & editing; LAGBJ: conceptualization, methodology, formal analysis, investigation, writing - review & editing, project administration, funding acquisition.

Editors: Yury Villagrán Zaccardi, Guilherme Aris Parsekian.

IBRACON Structures and Materials Journal
Revista IBRACON de Estruturas e Materiais
ISSN 1983-4195 ismj.org

ORIGINAL ARTICLE

Numerical evaluation of aggregate size influence on concrete mechanical damage under high temperatures

Análise numérica da influência do tamanho do agregado no dano mecânico do concreto sob altas temperaturas

Matheus Fernandes Dal-Sasso[a]
Lahis Souza de Assis[a]
Michèle Cristina Resende Farage[a]
Flávia de Souza Bastos[a]
Anne-Lise Beaucour[b]

[a]Universidade Federal de Juiz de Fora – UFJF, Juiz de Fora, MG, Brasil
[b]Université de Cergy-Pontoise – UCP, Cergy-Pontoise, France

Received 07 October 2022
Accepted 01 February 2023

Abstract: The influence of aggregate size on the degradation process of material exposed to high temperatures is not a consensus among the scientific community because changes in the microstructure impact the macrostructural performance. To contribute to this investigation this work presents a thermomechanical model to evaluate aggregate size influence on the concrete mechanical damage under high temperatures. The material is considered as two-phase - aggregate and matrix - and three-phase - in which the interfacial transition zone is added. Concerning geometries, models in 2D and 3D are simulated. A finite element software is used with a weak coupling strategy that reduces the computational cost, and a user subroutine is implemented to define the constitutive model. The results show that the aggregate size influences both the average damage and the damage distribution along the synthetic specimen.

Keywords: concrete, high temperature, computational modeling, damage, size aggregates.

Resumo: A influência do tamanho do agregado no processo de danificação do material exposto a altas temperaturas não é um consenso entre a comunidade científica, pois alterações na microestrutura impactam no desempenho macroestrutural. Para contribuir com esta investigação, este trabalho apresenta um modelo termomecânico para avaliar a influência do tamanho do agregado no dano mecânico do concreto sob altas temperaturas. O material é considerado como bifásico - agregado e matriz - e trifásico - no qual é adicionada zona de transição na interface. No que diz respeito às geometrias, são simulados modelos em 2D e 3D. Um software de elementos finitos é utilizado com uma estratégia de acoplamento fraco que reduz o custo computacional, e uma sub-rotina de usuário é implementada para definir o modelo constitutivo. Os resultados mostram que o tamanho do agregado influencia tanto o dano médio quanto a distribuição do dano ao longo do corpo de prova sintético.

Palavras-chave: concreto, altas temperaturas, modelagem computacional, dano, tamanho do agregado.

How to cite: M. F. Dal-Sasso, L. A. Assis, M. C. R. Farage, and A.-L. Beaucour, "Numerical evaluation of aggregate size influence on concrete mechanical damage under high temperatures," *Rev. IBRACON Estrut. Mater.*, vol. 16, no. 6, e16605, 2023, https://doi.org/10.1590/S1983-41952023000600005

1 INTRODUCTION

Concrete, a heterogeneous mixture basically composed of cement, coarse aggregate, fine aggregate and water, is amongst the most widely adopted construction materials in the world [1]–[3], with an annual consumption of about 4,7

Corresponding author: Matheus Fernandes Dal-Sasso. E-mail: matheus.dal-sasso@engenharia.ufjf.br
Financial support: CAPES, FAPEMIG, CNPq, UFJF and UCP.
Conflict of interest: Nothing to declare.
Data Availability: The data that support the findings of this study are available from the corresponding author, MFDS, upon reasonable request.

tons per inhabitant per year [4]. Its intrinsic complexity, especially regarding microstructure changes under extreme situations, such as high temperature, justifies the need for investigation by the scientific community.

Exposure of the structure to high temperatures may occur accidentally, in fire episodes, or as ordinary service conditions, as in nuclear powers, blast furnaces and radioactive waste repositories. In both situations, it is very important to have information on the material's response to high temperatures, so as to allow an adequate executive or corrective design. In this context, several computational and experimental studies about the subject have been carried out.

Amongst the available experimental studies, some are interested in post-fire mechanical properties. Arioz [5] studied the effects of high temperatures on the physical and mechanical properties in various concrete mixtures, determining weight loss and compressive strength after exposure, and concluded that both are directly linked and decrease significantly with temperature increase. Morales et al. [6] studied cylindrical mortar specimens submitted to temperature rise, determined their residual strength after cooling and concluded that in all analyzed temperatures there was a strength decrease. Teixeira [7] evaluated the influence of initial strength, temperature level and unheating rate on concrete Young's modulus after a fire and concluded that the lower the initial strength, the greater the decrease in stiffness and that abrupt unheating has a stronger effect on the mechanical residual properties.

Dealing with structures, Bailey and Toh [8] tested forty-eight horizontally unrestrained two-way spanning reinforced concrete slabs at ambient and elevated temperatures, comparing the observed failure modes to provide data to be used in the development of simple design methods. Ehrenbring et al. [9] performed an inspection of a prefabricated hollow core slab of an industrial building, which was exposed to high temperatures due to a fire, estimating the strength loss of structural element and attesting structure safety after the accident.

Regarding computational studies, there are some Ph.D. and M.S thesis talking about it. Ribeiro [10] developed a computer system for simulating structural elements behavior in a fire situation, and had good agreement with experimental tests. Santiago Filho [11] carried out an analysis of the effects of temperature rise in reinforced concrete slabs, and the results were validated through experimental data available in the literature. Ferreira [12] developed a model for simulation of reinforced concrete columns under a fire situation, based on the Finite Element Method, to predict structural behavior under high temperatures.

There are also scientific articles interested in this issue. Using the Finite Element Method (FEM) framework, Grassl and Pearce [13] adopted a mesoscale approach through a damage-plasticity model by considering concrete as a three-phase material composed of aggregate, matrix and interfacial transition zone (ITZ) so as to evaluate transient thermal creep, concluding that this phenomenon results from a mismatch of thermal expansion of mesoscale constituents. Mazzucco et al. [14] evaluated numerically the complex mechanism of polypropylene contribution on concrete behavior under thermal conditions through a coupled hygro-thermal–mechanical formulation. Srivastava and Prakash [15] developed a novel coupled framework for analysis of reinforced concrete and steel planar frames subjected to fire with three-way coupling between heat transfer, mechanical deformations and pore pressure build-up and used several numerical examples to demonstrate the accuracy and applicability of the framework. Padre et al. [3] implemented an algorithm to check the resistance of reinforced concrete sections to oblique unsymmetrical bending at ambient temperature and in a fire situation. Magisano et al. [16] proposed an automatic procedure for evaluating the axial force-biaxial bending yield surface of reinforced concrete sections in fire and a strategy to determine the limit fire duration, that is, the time of exposure which leads to structural collapse. Schulthess et al. [17] presented a method named hybrid fire testing and validated it with multiple proof-of-concept tests covering the entire temperature range relevant to structural fire engineering. Assis et al. [18] applied a thermomechanical model to assess concrete mechanical damage under high temperatures using Mazars' [19] theory and experimental data for validation.

Using other approaches, Liao and Huang [20] developed a robust finite element procedure for modeling the localized fracture of reinforced concrete beams at elevated temperatures and validated it against previous fire test results on the concrete beams. Nguyen et al. [21] studied the change in thermal conductivity of concrete when exposed to mechanical and thermal loading through a three-phase plane model using lattice discretization, where the damage variable is accounted for via crack width. They used numerical examples to illustrate and validate the proposal. Dias et al. [22] studied concrete under high temperatures and concluded that, in this situation, the material undergoes significant deterioration with spalling and a decrease in Young's modulus, compressive strength and durability.

There are also in the bibliography studies that deal with the influence of aggregate type and size in concrete under high temperatures behavior. Nince and Figueiredo [23], Kong and Sanjayan [24], Pan et al. [25] and Ali et al. [26] studied the relation between the aggregate size and degradation process of concrete under high

temperatures, by observing the spalling of the structure superficial layers, and concluded that spalling increase and aggregate size are inversely proportional. On the other hand, Jansson and Bostrom [27] state that spalling extent is proportional to aggregate size. Souza and Moreno [28] investigated the strength decrease of concrete produced with different aggregates and exposed to 573.15K and 873.15K and found a large decay of compressive strength under the higher temperature value. Fanton [29] reviewed reinforced concrete slab behavior in a fire situation through finite elements software and concluded that concrete produced with limestone is better than one with siliceous aggregate in these situations.

Aiming to contribute to this subject, this work proposes a computational analysis of the aggregate size influence on the mechanical behavior of concrete under high temperatures, applying the Mazars' [19] damage model. Analyses were performed by representing the problem's geometry in 2 and 3 dimensions. For the material modeling, two different approaches were adopted: a two-phase medium, composed of coarse aggregate and mortar, and a three-phase medium, by adding the interfacial transition zone.

2 METHODOLOGY

In this work, a thermomechanical model in finite elements was implemented in Abaqus [30] and applied to assess the influence of aggregate size on concrete behavior when exposed to high temperatures. This model was developed using a weak coupling strategy in which thermal and mechanical analyses are performed separately, for the sake of computational cost, which allowed the use of a mesh with a satisfactory refinement level.

Analysis was performed in three groups of computational samples, concerning the problem and the material representations: two-phase in 2D, three-phase in 2D and two-phase in 3D. In each group, different aggregate grading was adopted so that computational samples were significantly distinct regarding aggregate size.

Synthetic cylindric concrete samples were generated via a Python script in which aggregate particles, with or without an interfacial transition zone, are randomly distributed over a concrete area or volume, concerning a two or a three dimensional representation, respectively, in order to reproduce the grading curve and phase proportion.

Damage in the material was evaluated by means of Mazars' [19] theory, which is not available in the Abaqus' [30] library. Thus, it was necessary to develop a user subroutine in Fortran, to describe the adopted constitutive model.

2.1 Governing equations

Concerning thermal analysis, it was considered only heat transfer by conduction. Thus, Equation 1 gives the temperature field, provided the initial temperature field and boundary conditions:

$$\rho c \frac{\partial T}{\partial t} - \nabla \cdot (\kappa \nabla T) = q, \tag{1}$$

where ρ is the density, c is the specific heat, T is the temperature, t is the time, κ is the thermal conductivity and q is a source or a sink.

Once the temperature field was obtained, it was applied as a thermal loading so as to solve a mechanical problem, being the relationship between temperature and deformation obtained from Equation 2:

$$\epsilon_t = \alpha(T - T_0)I, \tag{2}$$

where α is the thermal expansion coefficient, T_0 is the initial temperature, I is the identity matrix and ϵ_t is the thermal deformation.

For the mechanical problem resolution, the Cauchy equilibrium equation (Equation 3) was solved with adequate boundary conditions:

$$B + \nabla \cdot \sigma = 0, \tag{3}$$

where B are the body forces and σ is the stress tensor.

The linear elastic constitutive model was modified by a damage variable for mortar and interfacial transition zone. Classical Hooke's law, given by Equation 4, was considered for the aggregate:

$$\sigma = 2\mu\epsilon + \lambda(\nabla \cdot u)I - (3\lambda + 2\mu)\epsilon_t, \tag{4}$$

where u is the displacement, ϵ is the strain and μ and λ are the Lamé constants with:

$$\mu = \frac{E}{2(1+\upsilon)}, \tag{5}$$

and

$$\lambda = \frac{E\upsilon}{(1+\upsilon)(1-2\upsilon)}, \tag{6}$$

where E is the Young's modulus and υ is the Poisson's ratio.

The damage variable d affects directly Young's modulus through the relation given by Equation 7:

$$E_d = (1-d)E, \tag{7}$$

with E_d being the damaged Young's modulus. In turn, damage variable d is obtained from linear combination of tension and compression components (d_t and d_c), with weights α_t and α_c according to Equation 8:

$$d = \alpha_t d_t + \alpha_c d_c, \tag{8}$$

Tension and compression damage variables are both described by Equation 9:

$$d_{t,c} = 1 - \frac{\epsilon_{d0}(1-A_{t,c})}{\tilde{\epsilon}} - \frac{A_{t,c}}{e^{B_{t,c}(\tilde{\epsilon}-\epsilon_{d0})}}, \tag{9}$$

where the subscripts t and c refer to tension and compression, respectively, ϵ_{d0}, $A_{t,c}$ and $B_{t,c}$ are the Mazars' [19] model parameters - extracted from uniaxial stress x strain curves via geometrical fitting procedures - and $\tilde{\epsilon}$ is the equivalent deformation given by Equation 10:

$$\tilde{\epsilon} = \sqrt{\sum_{i=1}^{n}\left(\epsilon_{(i)+}\right)^2} \tag{10}$$

in which $\epsilon_{(i)+}$ is the positive principal deformation.

2.2 Material properties

The thermal and mechanical properties of each concrete constituent phase were obtained from specific codes or literature references. Concerning thermal properties, aggregate and mortar thermal expansion coefficients were considered as temperature linear function, derived from experimental data approximation available in Razafinjato [31]. The specific heat of granite and the initial value of specific heat of mortar were obtained from NBR 15220-2 [32]. However, the value for granite was considered constant and the value for mortar was adopted as a temperature linear function. Aggregate and mortar thermal conductivity were considered constants and obtained from NBR 15220-2 [32]. Aggregate and mortar density were also considered constant but obtained from Razafinjato [31]. In the absence of

available data for the interfacial transition zone, the same thermal properties used for mortar were considered for this phase. Thermal properties for the three phases are shown in Table 1.

Table 1. Thermal properties, *T* being the temperature considered.

Phase	Thermal conductivity *(J/mmKmin)*	Thermal expansion coefficient *(1/K)*	Specific heat *(J/KgK)*	Density *(Kg/mm³)*
Aggregate	0.042	(0.065T - 15.02) 10^{-6}	800	$2.500 \cdot 10^{-6}$
Mortar	0.069	(0.021T - 6.00) 10^{-6}	1.39T + 591.89	$2.252 \cdot 10^{-6}$
ITZ	0.069	(0.021T - 6.00) 10^{-6}	1.39T + 591.89	$2.252 \cdot 10^{-6}$

Concrete and mortar Young's modulus were known experimentally from Razafinjato [31]. Aggregate Young's modulus and aggregate and mortar Poisson's ratio were obtained from an inverse method. For this, a python script solved a mechanical model in which unknown properties were estimated, by trial and error, until the computational sample Young's modulus was adjusted to experimental values. For the interfacial transition zone, it was considered 50% of mortar Young's modulus and the same Poisson's ratio of mortar according to Ramesh et al. [33]. Mechanical properties for the three phases are shown in Table 2.

Table 2. Mechanical properties.

Phase	Young's modulus (*MPa*)	Poisson's ratio
Aggregate (Two-phase)	39437	0.201
Aggregate (Three-phase)	40174	0.226
Mortar (Two-phase)	31000	0.129
Mortar (Three-phase)	31000	0.133
ITZ (Three-phase)	15500	0.129

From experimental data of concrete Young's modulus for some temperatures [31], the parameters of Mazars' [19] damage model were obtained applying a method described in previous works [18] [34] and then applied to the computational sample to obtain Young's modulus for each evaluated temperature.

In the studied problem the temperature was monotonically increasing, that is, cooling was not considered. Thus, the observed compression level was low and, consequently, the estimated value for α_c was insignificant when compared to α_t. So α_c was neglected and parameters were reduced to ϵ_{d0}, A_t and B_t. Obtained parameters for the three computational sample groups are shown in Table 3.

Table 3. Mazars' parameters.

Parameter	Two-phase in 2D	Three-phase in 2D	Two-phase in 3D
A_t	0.667	0.669	0.703
B_t	258.120	251.500	220.430
ϵ_{d0}	$3.470 \cdot 10^{-4}$	$3.460 \cdot 10^{-4}$	$3.390 \cdot 10^{-4}$

2.3 Geometric modeling

The analysis comprised three different geometric approaches to represent a cylindrical (150mm x 300mm) concrete sample: two-phase in 2D, three-phase in 2D and two-phase in 3D. Aggregate particles were considered as spherical, for simplification purposes. The synthetic samples were generated with the help of an algorithm developed by Bonifacio [35] in Python. The grading curves shown in Figure 1 and an aggregate's proportion of 40% were adopted as input data so as to randomly determine the particles' distribution in the mortar medium. Figure 2 and Figure 3 show, respectively, the 2D and 3D geometries adopted for the samples - in the 2D model, it was considered a quarter of the plane section while the 3D model consisted of one-eighth of the cylinder.

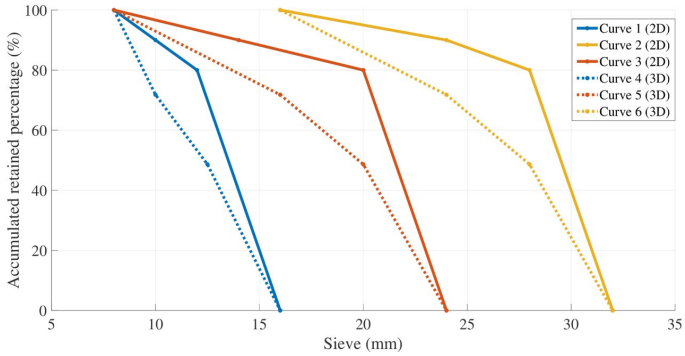

Figure 1. Grading curves adopted for the 2D and 3D synthetic concrete samples.

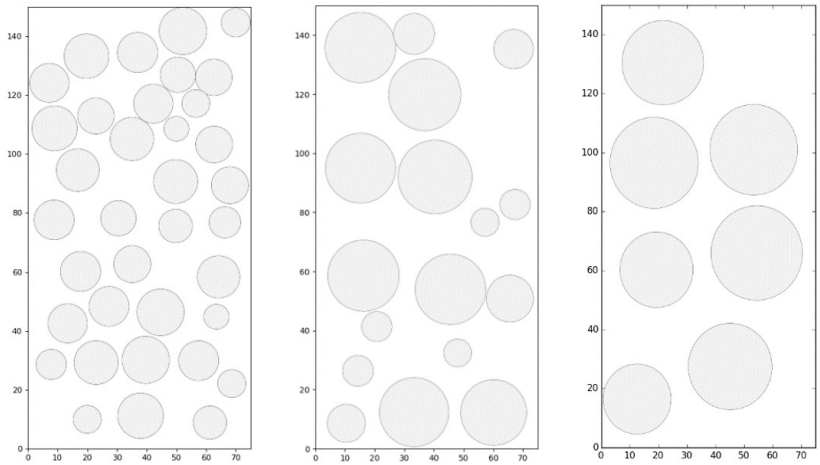

Figure 2. Two-phase in 2D computational samples for curves 1 to 3, from left to right.

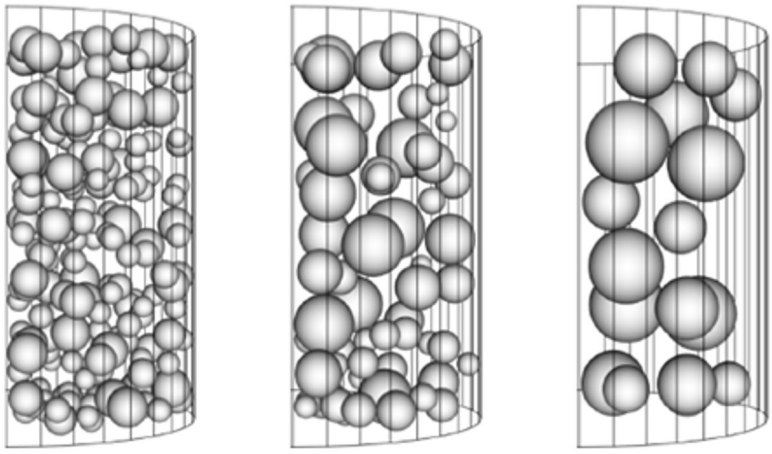

Figure 3. Two-phase in 3D computational samples for curves 4 to 6, from left to right.

Six grading curves, shown in Figure 1, were strategically chosen so as to generate significantly different synthetic concrete samples: curves 1, 2, and 3 were adopted for 2D samples and curves 4, 5 and 6 were considered as input data for 3D samples. The 2D geometries shown in Figure 2 adopted grading curves 1, 2 and 3, while Figure 3 shows 3D synthetic samples resulting from grading curves 4, 5 and 6.

The 2D geometries shown in Figure 2 were applied to simulate concrete as two-phase (mortar and aggregate) and three-phase (mortar, aggregate and interfacial transition zone). The interfacial transition zone (ITZ) was included around every aggregate particle of diameter $2r$ by means of a concentric circle of diameter $2r + 2e$ where e is the thickness of the interfacial transition zone and r is the radius. According to Mehta and Monteiro [36], the ITZ thickness varies from 0.01mm to 0.05mm. In the present work, it was adopted e = 0.05mm, for the 2D three-phase model. The 3D counterpart, however, was not performed due to the occurrence of mesh distortions related to the small thickness of the ITZ.

For the finite elements modeling, 2D samples were discretized with DC2D4 (4-node linear heat transfer quadrilateral) and DC2D3 (3-node linear heat transfer triangle) elements for thermal analysis and CPS4 (4-node bilinear plane stress quadrilateral) and CPS3 (3-node linear plane stress triangle) elements were used for mechanical analysis. DC3D4 (4-node linear heat transfer tetrahedron) elements were applied for 3D thermal analysis and C3D4 (4-node linear tetrahedron) elements were adopted for 3D mechanical analysis.

2.4 Thermomechanical model

This work adopts a weak coupling strategy to perform a thermomechanical analysis which consists of two models: a transient thermal one, in which the temperature field is obtained for a thermal boundary condition, followed by a mechanical one, with suitable boundary conditions, where the mechanical damage generated by thermal loading is evaluated. Figure 4 shows the boundary conditions in each face for the 2D and 3D cases. In the first model, T = 573.15K, 723.15K, 803.15K was applied on exterior faces and q = 0 on internal faces, with the initial condition T_0 = 293.15K. In the second model, a displacement restriction was applied on internal faces.

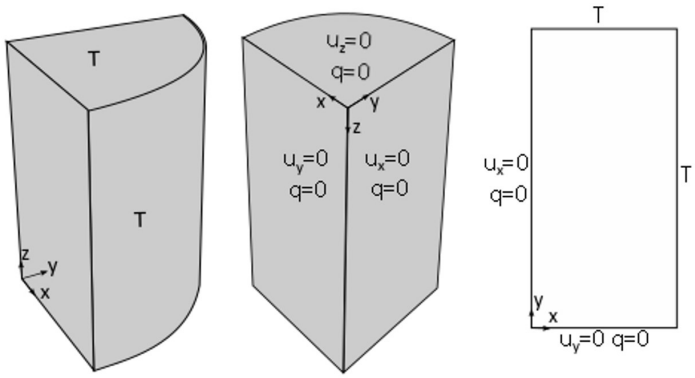

Figure 4. Faces of the 2D and 3D models.

Material damage was incorporated via the Mazars' [19] constitutive model, implemented in a Fortran subroutine named UMAT. In this case, software accomplishes the pre-processing and post-processing normally while the algorithm developed externally for the user is used for the processing. This subroutine is schematically shown in Figure 5.

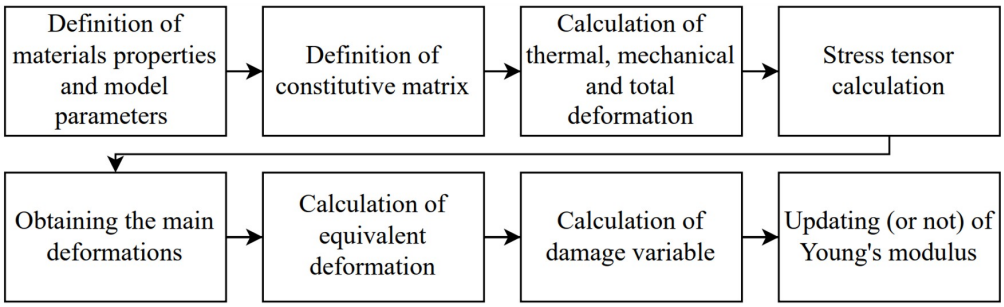

Figure 5. UMAT subroutine for Mazars' model.

3 RESULTS

Figure 6 shows the temperature field results referring to the maximal imposed temperature (803.15K) for the two-phase in 2D model, which were quite similar to those related to the three-phase in 2D model. The results for the two-phase in 3D geometry are shown in Figure 7, for a vertical section of the computational sample. It is noted in all cases that the highest temperatures are located on the faces in contact with the heat flow, as expected. Furthermore, Figure 7 indicates that aggregate diameters do not seem to have significantly affected temperature distribution. However, there is a higher average temperature in 3D geometries (approximately 788K), which is evidenced by the significantly higher minimum temperature compared to those verified for 2D geometries.

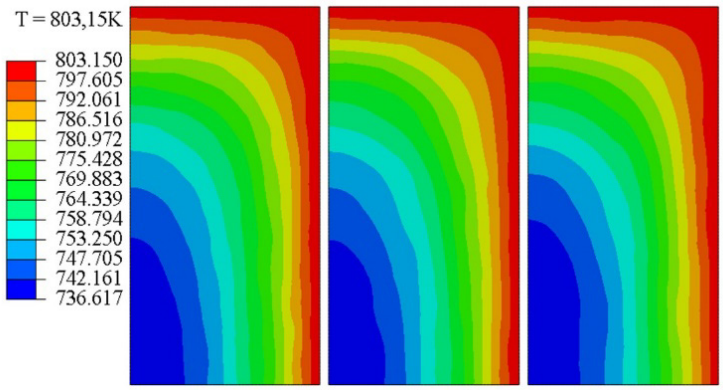

Figure 6. Temperature field in Kelvin for curves 1, 2 and 3 (two-phase in 2D), from left to right, at 803.15K.

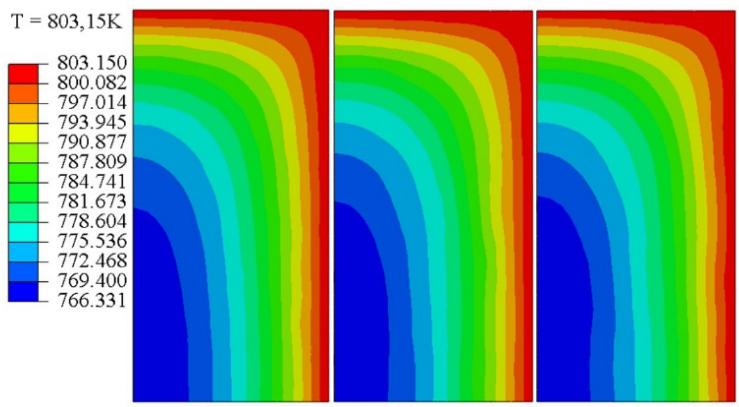

Figure 7. Temperature field in Kelvin for curves 4, 5 and 6 (two-phase in 3D), from left to right, at 803.15K.

Subsequently, this thermal loading was applied to the mechanical model with damage from which it was possible to obtain the damage map for the 2D cases, as shown in Figures 8 and 9. For the two-phase in 3D case, the results for a vertical section are shown in Figure 10. In all geometries, greatest damage is located close to the aggregates. In addition, for all cases, there is a high degree of damage in practically the entire section. It is also observed that for larger aggregates there are more regions with high damage values (red color) between the particles, although least damaged regions (yellow color) are observed in the computational sample as a whole.

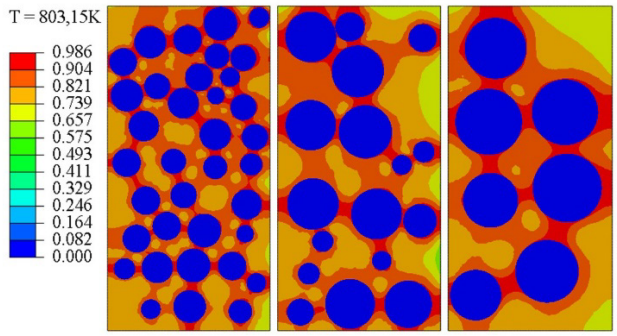

Figure 8. Damage map for curves 1, 2 and 3 (two-phase in 2D), from left to right, at 803.15K.

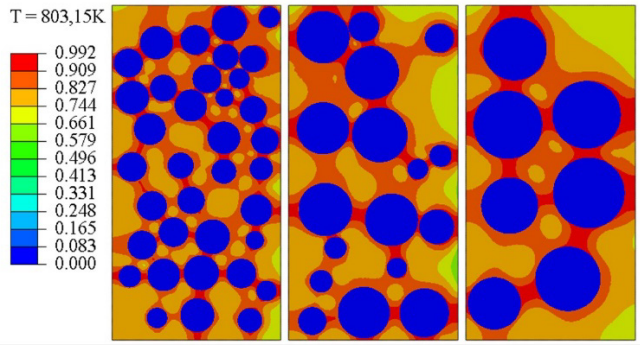

Figure 9. Damage map for curves 1, 2 and 3 (three-phase in 2D), from left to right, at 803.15K.

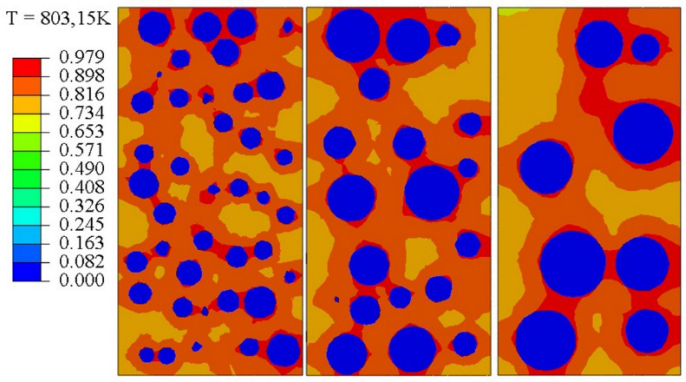

Figure 10. Damage map for curves 4, 5 and 6 (two-phase in 3D), from left to right, at 803.15K.

Graphs in Figure 11 present the average damage values obtained for each computational sample considered. Through them it is possible to quantitatively assess that the average damage is inversely proportional to the diameter of the aggregate. By considering that spalling is an important damage process, the results are in agreement with studies developed by Nince and Figueiredo [23], Kong and Sanjayan [24], Pan et al. [25] and Ali et al. [26]. Still in Figure 11, more significant differences may be identified in the 2D cases and it is possible to notice that the temperature at which the damage starts is not highly influenced by the particle's size.

According to Figure 11, for the two-phase in 2D geometries, the highest average damage was 0.729 for curve 1 and the lowest was 0.711 for curve 3. For the three-phase in 2D geometries the highest average damage was 0.728 for curve 1 and the lowest was 0.711 for curve 3. For the two-phase in 3D geometries, the highest average damage was 0.740 for curve 4 and the lowest was 0.734 for curve 6.

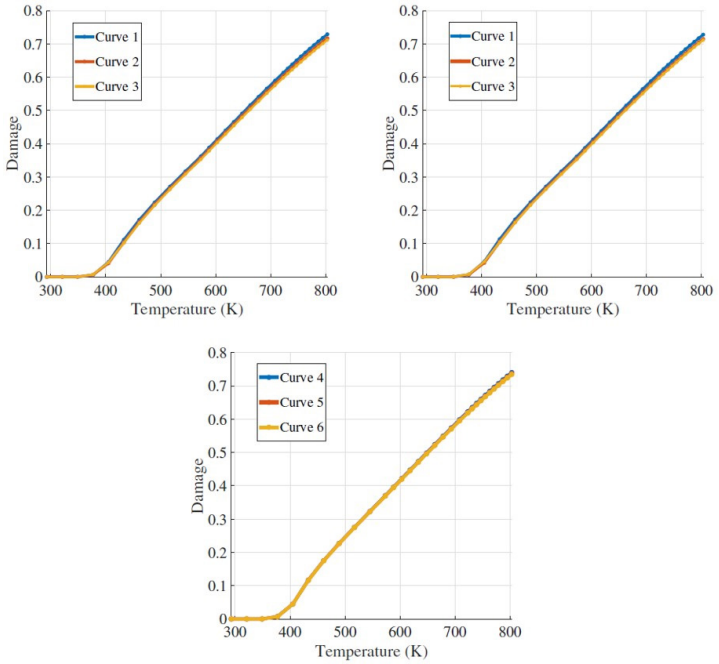

Figure 11. Average damage obtained in each computational sample evaluated for the two-phase in 2D case, three-phase in 2D case and two-phase in 3D case.

Figures 12 and 13 show the Young's modulus map obtained from the mechanical model with damage for 2D computational samples. Figure 14 shows these results for the two-phase in 3D geometries for a vertical section. Damage is quantified by means of E decay. There is also a more uniform distribution of Young's modulus values in the sections with smaller aggregates, while in the sections with larger aggregates regions with more discrepant values are found.

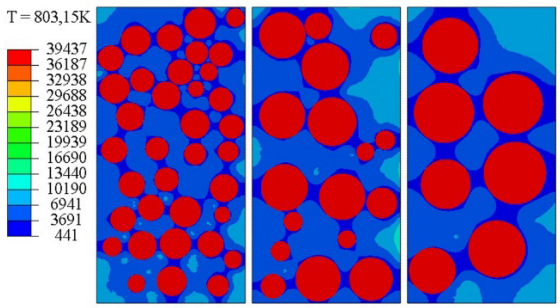

Figure 12. Young's modulus (MPa) map for curves 1, 2 and 3 (two-phase in 2D), from left to right, at 803.15K.

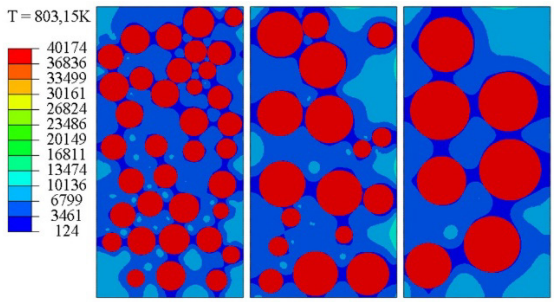

Figure 13. Young's modulus (MPa) map for curves 1, 2 and 3 (three-phase in 2D), from left to right, at 803.15K.

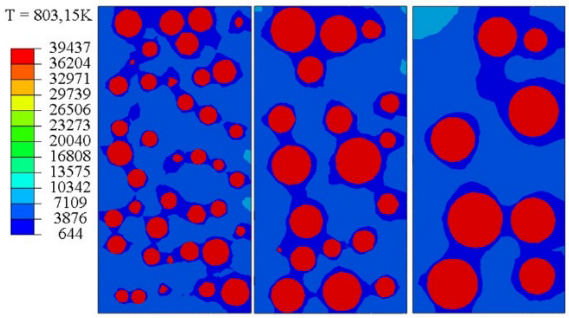

Figure 14. Young's modulus (MPa) map for curves 4, 5 and 6 (two-phase in 3D), from left to right, at 803.15K.

Finally, graphs in Figure 15 present the average Young's modulus values obtained for each computational sample considered. It is possible to quantitatively assess that this property is higher for larger aggregates, while it becomes relatively lower for smaller aggregates, which is explained by the inverse relationship between this property and damage. The graphs also show the experimental reference [31] applied for calibration purposes. It is possible to notice that results related to 2D computational samples (curve 1) are in better agreement with the experimental counterpart. Results obtained for the 3D analyses were practically coincident.

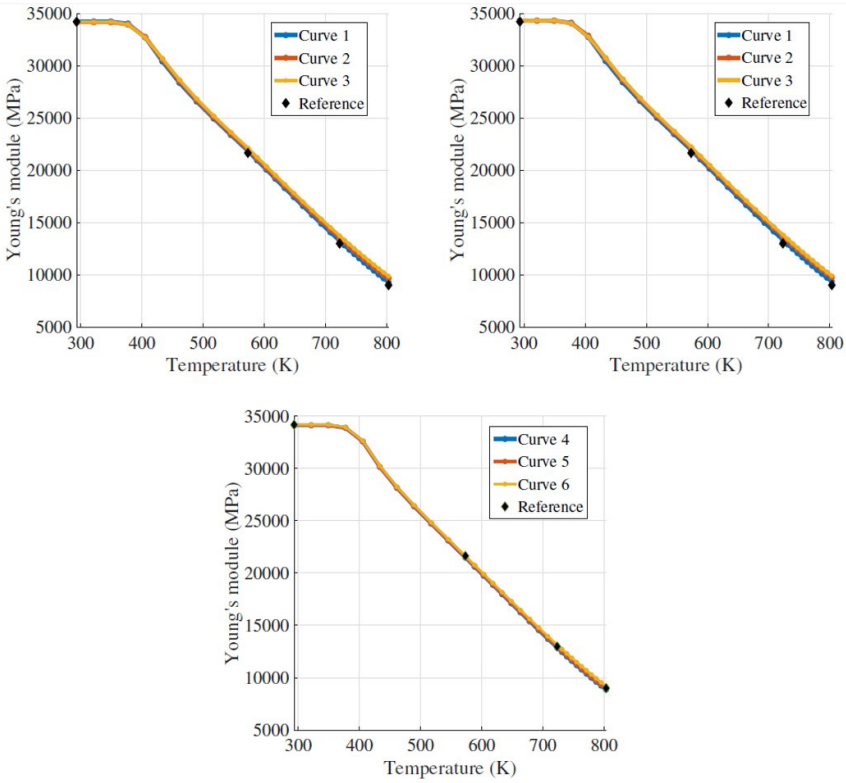

Figure 15. Average Young's modulus obtained in each computational sample evaluated for the two-phase in 2D case, three-phase in 2D case and two-phase in 3D case.

Considering the maximal imposed temperature (T=803.15K), results denote that for the two-phase in 2D computational samples the highest average Young's modulus was 9868MPa for curve 3 and the lowest was 9286MPa for curve 1. For the three-phase in 2D computational samples, the highest average Young's modulus was 9906MPa for curve 3 and the lowest was 9350MPa for curve 1. Finally, for the two-phase in 3D computational samples, the highest

average Young's modulus was 9073MPa for curve 6 and the lowest was 8867MPa for curve 4. It should be noted that the experimental reference value is 9000MPa.

As observed computationally, the thermal model was not influenced by the aggregate grading. The mechanical model with damage denotes that smaller aggregates lead to a higher average damage. Nevertheless, more elements with higher damage are observed in samples with large aggregates. In contrast, for small aggregates the damage is better distributed throughout the section. In relation to Young's modulus, due to its inverse relationship with damage, it is noticed that higher mean values are observed for large aggregates.

Regarding the sensitivity of the computational model, the 2D cases are apparently more sensitive to aggregate grading, while 3D geometry results did not indicate a significant influence of this parameter.

Concerning the 2D representation of concrete composition, results for the two-phase and three-phase geometries were quite similar. It is worth mentioning that the only aspect considered distinct between the samples of the same group was the size of the aggregates. Thus, the observed sensitivity was considered satisfactory and future adjustments in the thermal and mechanical properties, which undergo changes according to the particle size, will contribute to more distinct results.

The influence of aggregate grading on concrete damage is a controversial issue in the technical literature. A number of experimental researches lead to divergent results, while there is a lack of numerical studies on this topic. In such a context, the present work aims to contribute for a better knowledge on the subject, by means of a numerical tool capable of relating aggregate diameters to damage evolution in a concrete medium.

3 CONCLUSION

This work presents a thermomechanical model applied to the simulation of concrete behavior under imposed temperature raise. The material was represented as an heterogeneous medium, composed of aggregate-mortar and or aggregate-mortar-ITZ, mostly aiming to verify the analysis sensitivity to aggregate grading concerning damage evolution, which was evaluated according to Mazar's Model.

Results denote that aggregates' particle size influences the damage distribution in the medium. Synthetic concrete samples with smaller inclusions show a more homogeneous damage distribution in spite of a higher average damage than that verified in computational samples with aggregates of larger dimensions.

An important aspect of the proposed weak coupling strategy is the fact that it demands low computational cost and a small set of experimental data so as to provide information on the material's degradation under temperature exposition.

In this context, the average processing time of thermal models was 7.0 minutes for the two-phase in 2D, 26.8 minutes for the three-phase in 2D and 68.3 minutes for the two-phase in 3D. For the mechanical model, the average processing time was 0.5 minutes for the two-phase in 2D, 2.5 minutes for the three-phase in 2D and 10.3 minutes for the two-phase in 3D. In both cases a machine with a Intel(R) Core(TM) i7-7500U CPU @ 2.70GHz 2.90 GHz processor was used.

The sensitivity presented by the computational model encourages further improvements so as to contribute to the understanding of concrete's behavior under high temperatures.

ACKNOWLEDGEMENTS

To the funding agencies - CAPES, FAPEMIG, and CNPq - and to the Federal University of Juiz de Fora

REFERENCES

[1] P. J. M. Monteiro, S. A. Miller, and A. Horvath, "Towards sustainable concrete," *Nat. Mater.*, vol. 16, pp. 698–699, 2017, http://dx.doi.org/10.1038/nmat4930.

[2] F. L. Pedroso, "Concreto: as origens e a evolução do material construtivo mais usado pelo homem," *Concr. Constr.*, no. 53, pp. 14–19, 2009.

[3] E. P. G. Padre, J. C. L. Ribeiro, R. C. S. S. Alvarenga, and R. C. Silva, "Algoritmo computacional para verificação de seções de concreto armado em situação de incêndio," *Rev. IBRACON Estrut. Mater.*, vol. 12, no. 4, pp. 932-955, 2019, https://dx.doi.org/10.1590/S1983-41952019000400012.

[4] International Organization for Standardization, *Concrete, Reinforced Concrete and Pre-stressed Concrete*, ISO/TC 71, 1949, https://www.iso.org/committee/49898.html (accessed Feb. 23, 2022).

[5] O. Arioz, "Effects of elevated temperatures on properties of concrete," *Fire Saf. J.*, vol. 42, no. 8, pp. 516–522, 2007., http://dx.doi.org/10.1016/j.firesaf.2007.01.003.

[6] G. Morales, A. Campos, and A. M. P. Faganello, "A ação do fogo sobre os componentes do concreto," *Semin. Ciênc. Exatas Tecnol.*, vol. 32, no. 1, pp. 47–55, 2011, http://dx.doi.org/10.5433/1679-0375.2011v32n1p47.

[7] G. P. Teixeira, "Análise experimental da resistência e do módulo de elasticidade pós incêndio de concretos com agregados da região de Viçosa-MG," M.S. thesis, Univ. Fed. Viçosa, Viçosa, Brasil, 2018.

[8] C. G. Bailey and W. S. Toh, "Small-scale concrete slab tests at ambient and elevated temperatures," *Eng. Struct.*, vol. 20, no. 10, pp. 2775–2791, 2007, http://dx.doi.org/10.1016/j.engstruct.2007.01.023.

[9] H. Z. Ehrenbring, V. Ortolan, F. Bolina, F. Pacheco, A. M. Gil, and B. F. Tutikian, "Avaliação da resistência residual de lajes alveolares em concreto armado em uma edificação industrial após incêndio," *Materia (Rio J.)*, vol. 22, no. 3, pp. 1–10, 2017, http://dx.doi.org/10.1590/S1517-707620170003.0208.

[10] J. C. L. Ribeiro, "Desenvolvimento e aplicação de um sistema computacional para simulação via método dos elementos finitos do comportamento de estruturas de aço e mistas em situação de incêndio," Ph.D. thesis, Univ. Fed. Minas Gerais, Belo Horizonte, Brasil, 2009.

[11] H. A. Santiago Fo., "Estudo do comportamento de lajes de concreto armado em situação de incêndio," M.S. thesis, Univ. Fed. Pernambuco, Recife, Brasil, 2018.

[12] M. W. Ferreira, "Estudo numérico dos efeitos estruturais da exposição de pilares em concreto armado a altas temperaturas," M.S. thesis, Univ. Fed. Rio Gde. do Sul, Porto Alegre, Brasil, 2018.

[13] P. Grassl and C. Pearce, "Mesoscale approach to modeling concrete subjected to thermomechanical loading," *J. Eng. Mech.*, vol. 136, pp. 1–7, 2010, http://dx.doi.org/10.1061/(ASCE)0733-9399(2010)136:3(322).

[14] G. Mazzucco, C. E. Majorana, and V. A. Salomoni, "Numerical simulation of polypropylene fibers in concrete materials under fire conditions," *Comput. Struc.*, vol. 154, pp. 17–28, 2015, http://dx.doi.org/10.1016/j.compstruc.2015.03.012.

[15] G. Srivastava and P. R. Prakash, "An integrated framework for nonlinear analysis of plane frames exposed to fira using the direct stiffness method," *Comput. Struc.*, vol. 190, pp. 173–185, 2017, http://dx.doi.org/10.1016/j.compstruc.2017.05.013.

[16] D. Magisano, F. Liguori, L. Leonetti, D. Gregorio, G. Zuccaro, and G. Garcea "A quasi-static nonlinear analysis for assessing the fire resistance of reinforced concrete 3D frames exploiting time-dependent yield surfaces," in: *XV Int. Conf. Comput Plast.*, 2019, pp. 100-111.

[17] P. Schulthess, M. Neuenschwander, K. M. Mosalam, and M. Knobloch, "A computationally rigorous approach to hybrid fire testing," *Comput. Struc.*, vol. 238, pp. 1–20, 2020, http://dx.doi.org/10.1016/j.compstruc.2020.106301.

[18] L. S. Assis, M. F. Dal Sasso, M. C. R. Farage, F. S. Bastos, and A. L. Beaucour, "Numerical analysis of mechanical damage on concrete under high temperatures," *Rev. IBRACON Estrut. Mater.*, vol. 15, no. 1, pp. 1-14, 2022, http://dx.doi.org/10.1590/S1983-41952022000100011.

[19] J. Mazars, "Application de la mécanique de l'endommagement au comportement non linéaire et à la rupture du béton de structure," Ph.D. thesis, Univ. Pierre et Marie Curie, Paris, France, 1984.

[20] F. Liao and Z. Huang, "An extended finite element model for modeling localized fracture of reinforced concrete beams in fire," *Comput. Struc.*, vol. 152, pp. 11–26, 2015, http://dx.doi.org/10.1016/j.compstruc.2015.02.006.

[21] T. D. Nguyen, D. T. Pham, and M. N. Vu, "Thermo-mechanically-induced thermal conductivity change and its effect on the behavior of concrete," *Constr. Build. Mater.*, vol. 198, pp. 98–105, 2019, http://dx.doi.org/10.1016/j.conbuildmat.2018.11.146.

[22] A. R. O. Dias, F. A. Amâncio, M. F. C. Rafael, and A. E. B. Cabral, "Comportamento do concreto submetido a altas temperaturas," *Materia (Rio J.)*, vol. 25, no. 2, pp. 1–14, 2020, http://dx.doi.org/10.1590/S1517-707620200002.1029.

[23] A. A. Nince and A. D. Figueiredo, "The influence of aggregate size in the risk of spalling in normal and high-strength concrete subjected to hydrocarbon fire," in: *Int. Conf. Concr. Struct.*, 2005, pp. 9-20.

[24] D. L. Y. Kong and J. G. Sanjayan, "Damage behavior of geopolymer composites exposed to elevated temperatures," *Cement Concr. Compos.*, vol. 30, no. 10, pp. 986–991, 2008, http://dx.doi.org/10.1016/j.cemconcomp.2008.08.001.

[25] Z. Pan, J. G. Sanjayan, and D. L. Y. Kong, "Effect of aggregate size on spalling of geopolymer and portland cement concretes subjected to elevated temperatures," *Constr. Build. Mater.*, vol. 36, pp. 365–372, 2012, http://dx.doi.org/10.1016/j.conbuildmat.2012.04.120.

[26] A. Z. M. Ali, J. G. Sanjayan, and M. Guerrieri, "Specimen size, aggregate size and aggregate type effect on spalling of concrete in fire," *Fire Mater.*, vol. 42, no. 1, pp. 59–68, 2018, http://dx.doi.org/10.1002/fam.2457.

[27] R. Jansson, L. Boström, "Experimental study of the influence of polypropylene fibres on material propertiesand fire spalling of concrete," in: *Proc. fib Task Group 4.3 Workshop Fire Design of Concr. Struct. – From Mater. Modelling to Struct. Performance*, 2007, pp. 177–188.

[28] A. A. A. Souza and A. L. Moreno, "Avaliação do tipo de agregado e da reidratação do concreto submetido a elevadas temperaturas," *Rev. IBRACON Estrut. Mater.*, vol. 3, no. 4, pp. 477-493, 2010, https://doi.org/10.1590/S1983-41952010000400007.

[29] A. R. Fanton, "Análise numérica do comportamento termomecânico de lajes de concreto armado expostas ao fogo," M.S. thesis, Univ. Estad. Campinas, Campinas, Brasil, 2019.

[30] Abaqus, "Abaqus User's Manual." Abaqus. http://130.149.89.49:2080/v6.11/index.html (accessed Feb. 23, 2022).

[31] R. N. Razafinjato, "Comportement des bétons à haute température: influence de la nature du granulat," Ph.D. thesis, Univ. Cergy-Pontoise, Paris, France, 2015.

[32] Associação Brasileira de Normas Técnicas, *Desempenho de Edificações – Parte 2 – Método de Cálculo da Transmitância Térmica, da Capacidade Térmica, do Atraso Térmico e do Fator Solar de Elementos e Componentes de Edificações*, NBR 15220-2, 2005.

[33] G. Ramesh, E. D. Sotelino, and W. F. Chen, "Damage behavior of geopolymer composites exposed to elevated temperatures," *Cement Concr. Res.*, vol. 26, no. 4, pp. 611–622, 1996, http://dx.doi.org/10.1016/0008-8846(96)00016-6.

[34] M. F. Dal-Sasso, "Análise computacional do dano em estruturas de concreto submetidas a altas temperaturas," M.S. thesis, Univ. Fed. Juiz de Fora, Juiz de Fora, Brasil, 2019.

[35] A. L. Bonifácio, "Estratégia computacional para avaliação de propriedades mecânicas de concreto de agregado leve," Ph.D. thesis, Univ. Fed. Juiz de Fora, Juiz de Fora, Brasil, 2015.

[36] P. K. Mehta and P. J. M. Monteiro, *Concrete – Microstructure, Properties, and Materials*, 3rd ed. Berkeley, United States: McGraw-Hill Education, 2006.

Author contributions: MFDS and LSA: formal analysis, methodology, validation, visualization, writing-original draft; MCRF and FSB: conceptualization, supervision, writing-review & editing; ALB: data curation.

Editors: Osvaldo Manzoli, Guilherme Aris Parsekian.

IBRACON Structures and Materials Journal
Revista IBRACON de Estruturas e Materiais
ISSN 1983-4195 ismj.org

ORIGINAL ARTICLE

Topological optimization of composite trusses considering CO_2 emission via metaheuristics algorithms

Otimização topológica de treliças mistas considerando a emissão de CO_2 por meio de algoritmos meta-heurísticos

Gabriel Erlacher[a]
Adenilcia Fernanda Grobério Calenzani[a]
Élcio Cassimiro Alves[a]

[a]Universidade Federal do Espírito Santo – UFES, Departamento de Engenharia Civil, Vitória, ES, Brasil

Received 28 November 2022
Accepted 05 February 2023

Abstract: In order to provide more sustainable solutions to the design of composite truss beams, the present work proposes a formulation to optimize dimensional, geometric and topologic parameters aiming to minimize CO_2 emissions. Genetic Algorithm (GA) and Particle Swarm Optimization (PSO) are used to solve the optimization problem considering the choice of steel profiles, characteristic strength of concrete, formwork, number of panels and truss total height. The methodology is applied to three problems where three different types of profile geometry and three models of truss are considered in order to compare and analyze its results. The program considers double angles, circular hollow tubes and circular concrete-filled tubes, as well as Pratt, Howe and Warren models. The three problems are identical, with the exception of the span size, varying between 8, 24 and 40 meters. In conclusion, results show the algorithms provide equal or similar solutions, with the Warren model and circular concrete-filled tube being the best solutions in all cases, especially for larger spans, reaching an emission reduction of up to 40% in relation to the Howe model using double angles. The critical criterion in the sizing of all cases attained a design-resistant effort relation greater than 90% in all cases, confirming the effectiveness of the optimization, being the combined criterion the critical in most of them.

Keywords: optimization, composite truss, meta-heuristic algorithm, environmental impact, topological optimization.

Resumo: A fim de fornecer soluções mais sustentáveis para o projeto de vigas mistas treliçadas, o presente trabalho propõe uma formulação para otimizar parâmetros dimensionais, geométricos e topológicos visando minimizar as emissões de CO2. Algoritmo Genético (GA) e Otimização por Enxame de Partículas (PSO) são utilizados para resolver o problema de otimização considerando a escolha dos perfis de aço, resistência característica do concreto, formas, número de painéis e altura total da treliça. A metodologia é aplicada a três problemas onde são considerados três tipos diferentes de geometria de perfil e três modelos de treliça para comparar e analisar seus resultados. O programa considera cantoneiras duplas, tubos circulares vazados e tubos circulares preenchidos com concreto, bem como os modelos de treliça Pratt, Howe e Warren. Os três problemas são idênticos, com exceção do tamanho do vão, que varia entre 8, 24 e 40 metros. Em conclusão, os resultados mostram que os algoritmos fornecem soluções iguais ou semelhantes, sendo o modelo de Warren e o tubo circular preenchido com concreto o mais eficiente em todos os casos, especialmente para vãos maiores, atingindo uma redução de emissão de até 40% em relação ao modelo Howe utilizando cantoneiras duplas. O critério crítico no dimensionamento de todos os casos atingiu uma relação entre esforço solicitante e resistente maior que 90% em todos os casos, confirmando a eficácia da otimização, sendo o critério de flexão combinada o crítico na maioria deles.

Palavras-chave: otimização, viga mista, algoritmo meta-heurístico, impacto ambiental, otimização topológica.

How to cite: G. Erlacher, A. F. G. Calenzani, and E. C. Alves, "Topological optimization of composite trusses considering CO_2 emission via metaheuristics algorithms," *Rev. IBRACON Estrut. Mater.*, vol. 16, no. 6, e16606, 2023, https://doi.org/10.1590/S1983-41952023000600006

Corresponding author: Élcio Cassimiro Alves. E-mail: elcio.calves1@email.com
Financial support: The authors acknowledge the Brazilian Federal Government Agency CAPES for the financial support provided during the development of this research. The second author thanks the Brazilian Federal Government Agency CNPq for the productivity research grant number 309741/2020-3.
Conflict of interest: Nothing to declare.
Data Availability: Data-sharing is not applicable to this article as no new data were created or analyzed in this study.

1 INTRODUCTION

Reducing greenhouse gas emissions is one of the greatest challenges on this century [1]. The IPCC's Sixth Assessment Report estimates that the emission of greenhouse gases from human activities is responsible for approximately 1.1°C of warming compared to pre-industrial levels and it is expected to reach or exceed 1.5°C of warming [2]. In 2020, even though the economic activity was severely reduced due to the pandemic, building construction demand for steel and cement was still responsible for 3.2 gigatons of CO_2 in energy-related emissions and, thereby, contributing with 10% of global carbon emissions [3]. Therefore, it is essential that actions are taken in favor of decreasing greenhouse gas emissions and avoiding even more consequences that arise from global warming.

Many studies have pointed to structural optimization as an option to reduce environmental impact, as it allows a more efficient and rational use of construction materials [4]–[11]. This is mainly because the current dimensioning method is usually done by trial-and-error, making the solution's efficiency depend on the designer's experience or at the expense of laborious manual adjustment work [12]. In this way, with the structural optimization, it is possible to obtain the combination of parameters that minimizes the impact caused by the construction, which makes the process more practical and the structure more efficient while still meeting security conditions [13].

Different methodologies have been employed to measure the environmental impact of buildings, among them the Life Cycle Assessment (LCA), which is a method that studies the environmental inputs and outputs related to a product or service life-cycle from its production until the end of its service life [14]. A parameter that is often used to account for this impact on structural optimization of various structures is the CO_2 emission, as done by Payá-Zaforteza et al. [4], García-Segura and Yepes [15] and Santoro and Kripka [16].

Recent studies have been using several different algorithms in the structural optimization, such as Genetic Algorithms (GA) and Particle Swarm Optimization (PSO). GA was first proposed by John Holland and is based on Darwin's theory of evolution: it starts with an initial population of solutions to the problem and, in each generation, crossings are made from the most fit individuals and mutations are added, simulating natural selection and resulting, in the end, in the best solution to the problem [10]. PSO, on the other hand, was first proposed by Kennedy, Eberhart and Shi and it is based on a population of solutions, called particles, which are classified according to their fitness. Then, each particle is accelerated towards the best particle and also towards their own best previously found solution. In each iteration, particles approach the best solution from a different direction and will very likely find a position, that is, a solution that is better than the initial one, creating a new best solution to be followed in the next iteration. The optimization is finished when the maximum number of iterations is reached [17].

Several studies have used GA and PSO to optimize a large range of structures, such as reinforced concrete [18]–[20], composite beams [21]–[23], composite cellular beams [24]–[25], steel trusses [26]–[28], steel endplate semi-rigid joints [29], etc. However, the topological optimization of composite truss beams considering environmental impact is yet to be undertaken.

Composite trusses are structures composed of a steel truss united by shear connectors to a concrete slab. The consideration of the concrete slab as a compressive resistant element provides a significant increase to the flexural strength of the beam, since, in general, about 50% of the weight of a truss arises from the compressed flange [30]. In this way, composite truss beam presents itself as an economical option, especially in situations where it is necessary to overcome spans greater than 20 meters [31]. Another advantage of composite trusses is the fact that they are relatively light and allow the passage of complex electrical, ventilating and communication systems, while still overcoming building height limitations or allowing the construction of higher beams, which minimizes deflection and vibrations [32], [33].

The composite slab is composed of a metallic formwork covered with a layer of concrete and a reinforcing mesh to absorb concrete's retraction stresses on its upper part. The shape of the truss can consist of different types of profiles, such as tubular, double angles brackets, etc. and follow different assembly models, like Pratt, Howe and Warren.

Multiple factors can influence the distribution of forces in each bar of a truss, such as dimensions, geometry and topology. Consequently, performing an optimization of these parameters can significantly decrease the weight of the structure, as it allows for a better exploitation of the material. Dimensional optimization refers to the consideration of the structure's dimensions as variables, such as profile shapes; geometric optimization considers the position of each element as a variable, such as the position of the nodes; and the topological optimization considers the parameters that change the quantity and distribution of elements as a variable. Studies, such as Kaveh and Ahmadi's [34] and Tarabay and Lima [35], indicated that the best solutions are found in the simultaneous optimization of these three parameters and Müller and van der Klashorst [36] corroborate them, showing an average economy of 22% in comparison to the dimensional-only optimization.

Therefore, the present work proposes the formulation of the dimensional and topological optimization problem of a composite steel-concrete truss beam, considering the current safety verifications and aiming to find the solution that causes minimum environmental impact, through different metaheuristic algorithms - GA and PSO. The algorithm is applied to different combinations of truss models and profile shapes, allowing the comparison between solutions and a

conclusion on what is the most efficient combination of steel profiles, concrete resistance, formwork and truss topology. The dimensional optimization is done by varying the profile used in each element of the truss and the topological optimization is achieved by varying the number of elements, as well as their positions.

2 OPTIMIZATION PROBLEM FORMULATION

2.1 Design Variables

Figure 1 presents the design variables considered by the program in the optimization.

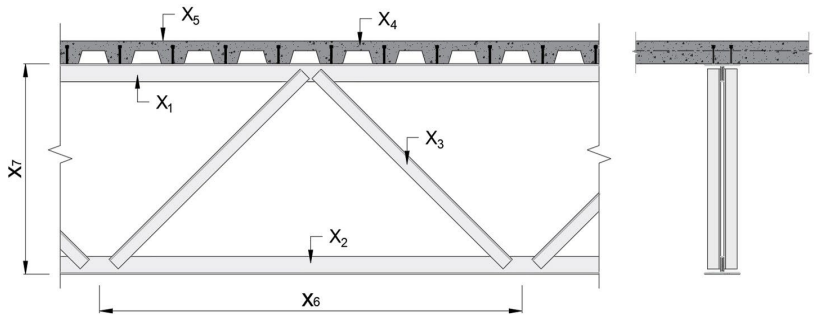

Figure 1. Design variables.

Where $x(1)$ is the upper chord profile; $x(2)$ is the lower chord profile; $x(3)$ is the web Members profile; $x(4)$ is the characteristic strength of the concrete slab (f_{ck}); $x(5)$ is the decking profile; $x(6)$ is the number of panels in the truss; and $x(7)$ is the Truss height.

When using double angles (DA) and circular hollow tubes (CHT), the program considers seven variables, but when using circular concrete-filled tubes (CCFT) an eighth variable is considered. This variable is identified as $x(8)$ and represents the characteristic strength of the concrete infill.

2.2 Search Range

The lower and upper bounds to each variable are presented by Equation 1 and Equation 2, respectively.

$$LB = \{1, 1, 1, 1, 1, 1, L/15\,, 1\} \tag{1}$$

$$UP = \{N, N, N, 7, 48, 2L, L/8\,, 7\} \tag{2}$$

Where the first three elements of each vector represent the number of available profile choices according to the catalogs used, N being 50, for double angles [37], and 142, for tubular profiles [38]; The fourth element represents the variation of the slab f_{ck}, varying between 20, 25, 30, 35, 40, 45 and 50MPa; The fifth element refers to the number of choices of formwork available in the catalog used [39], which in this case were 48; The sixth element represents the maximum number of truss panels, which for Pratt and Howe trusses must be an even number to ensure symmetry. The minimum size for a panel was 500 mm, thus making the maximum number of panels two times the total span (L). The seventh element represents the number of options for the height of the truss, taken arbitrarily as values between one fifteenth and one eighth of the span, varying from 50 to 50 mm. The eighth element is only relevant when using CCFT profile and represents the compressive strength of the filling concrete, as considered for the fourth element.

2.3 Objective Function

The objective function proposed in this work refers to the minimization of the CO_2 emission of composite trusses and it is presented in Equation 3.

$$E_{total} = E_s + E_c + E_f + E_m + E_{sc} + E_{cf} \quad (3)$$

Where E_{total} corresponds to the total emission of CO_2 caused by the composite truss. E_s, E_c, E_f, E_m, E_{sc} and E_{cf} correspond to the emission caused by the production of steel profiles, concrete used in the slab, steel formwork, reinforcing mesh, shear connectors and concrete fill, respectively. When using DA or CHT, E_{cf} is null.

The way in which each of these variables is calculated is expressed by Equation 4 to 9.

$$E_s = (m_p + m_{cn}) \times U_s \quad (4)$$

$$E_c = V_{c,u} \times e \times L \times U_c \quad (5)$$

$$E_f = m_{f,u} \times e \times L \times U_f \quad (6)$$

$$E_m = m_{m,u} \times e \times L \times U_m \quad (7)$$

$$E_{sc} = n_{sc} \times m_{sc,u} \times U_s \quad (8)$$

$$E_{cf} = A_{cf} \times L \times U_{cf} \quad (9)$$

Where m_p is the total mass of steel profiles; m_{cn} is the mass of connections, estimated as 10% of the mass of profiles; U_s is the unitary emission of CO_2 per unit of steel mass; $V_{c,u}$ is the volume of concrete per unit of slab area, given in function of the formwork's geometry; e is the distance between beams; L is the span; U_c is the unitary emission of CO_2 per unit of concrete volume, given in function of its resistance; $m_{f,u}$ is the mass of steel formwork per unit of slab area, given in function of the formwork width; U_f is the unitary emission of CO_2 per unit of steel formwork mass; $m_{m,u}$ is the mass of reinforcing mesh per unit of slab area, given in function of the slab's width [39]; U_m is the unitary emission of CO_2 per unit of reinforcing mesh mass; n_{sc} is the number of shear connectors used in the whole beam; $m_{sc,u}$ is the mass of one shear connector; A_{cf} is the internal area of the upper chord profile (CCFT); and, similarly to U_c, U_{cf} is the is the unitary emission of CO_2 per unit of volume of filling concrete.

The unitary emissions used in the program and their sources are exhibited in Table 1.

Table 1 – Unitary emissions.

Material	CO_2 Emission	Source
Concrete (f_{ck} = 20 MPa)	140.05 $kgCO_2/m^3$	Santoro and Kripka [16]
Concrete (f_{ck} = 25 MPa)	149.26 $kgCO_2/m^3$	
Concrete (f_{ck} = 30 MPa)	157.65 $kgCO_2/m^3$	
Concrete (f_{ck} = 35 MPa)	171.64 $kgCO_2/m^3$	
Concrete (f_{ck} = 40 MPa)	182.14 $kgCO_2/m^3$	
Concrete (f_{ck} = 45 MPa)	194.70 $kgCO_2/m^3$	
Concrete (f_{ck} = 50 MPa)	225.78 $kgCO_2/m^3$	
Steel Profile (VMB350)	1.12 $kgCO_2/kg$	Worldsteel Association [40]
Steel Formwork [39]	2.64 $kgCO_2/kg$	
Reinforcing Mesh (CA60)	1.92 $kgCO_2/kg$	
Stud Bolt (ø19mm, 105mm)	0.23 $kgCO_2$/unit	

The CO_2 emissions of each material were defined based on the Life Cycle Assessment (LCA) methodology. The method consists of analyzing all the constructive stages of the material: extraction, production, transport, use, maintenance and also the end of the life cycle, represented by the stages of demolition, landfill or reuse.

2.4 Security Constraints

In order to be valid, a solution must follow the criteria of ultimate limit states (ULS) and serviceability limit states (SLS) prescribed by the current Brazilian standards [41], [42], which is done by the constraints presented in Equations 10 to 22.

$$C(1): \frac{N_{Sd,bs,ac}}{N_{c,Rd}} - 1 \leq 0 \tag{10}$$

$$C(2): \frac{N_{Sd,bs,dc}}{N_{c,Rd}} - 1 \leq 0 \tag{11}$$

$$C(3): \frac{N_{Sd,bi,ac}}{N_{t,Rd}} - 1 \leq 0 \tag{12}$$

$$C(4): \frac{N_{Sd,bi,dc}}{N_{t,Rd}} - 1 \leq 0 \tag{13}$$

$$C(5): \frac{N_{Sd,dm,ac}}{N_{c,Rd}} - 1 \leq 0 \tag{14}$$

$$C(6): \frac{N_{Sd,dm,dc}}{N_{c,Rd}} - 1 \leq 0 \tag{15}$$

$$C(7): \frac{M_{Sd,mista}}{M_{Rd}} - 1 \leq 0 \tag{16}$$

$$\begin{cases} if\ \frac{N_{Sd,ac}}{N_{Rd}} \geq 0.2 \Rightarrow\ C(8): \frac{N_{Sd,ac}}{N_{Rd}} + \frac{8}{9}\frac{M_{Sd,ac}}{M_{Rd}} - 1 \leq 0 \\ if\ \frac{N_{Sd,ac}}{N_{Rd}} < 0.2 \Rightarrow\ C(8): \frac{N_{Sd,ac}}{2\,N_{Rd}} + \frac{M_{Sd,ac}}{M_{Rd}} - 1 \leq 0 \end{cases} \tag{17}$$

$$\begin{cases} if\ \frac{N_{Sd,dc}}{N_{Rd}} \geq 0.2 \Rightarrow\ C(9): \frac{N_{Sd,dc}}{N_{Rd}} + \frac{8}{9}\frac{M_{Sd,dc}}{M_{Rd}} - 1 \leq 0 \\ if\ \frac{N_{Sd,dc}}{N_{Rd}} < 0.2 \Rightarrow\ C(9): \frac{N_{Sd,dc}}{2\,N_{Rd}} + \frac{M_{Sd,dc}}{M_{Rd}} - 1 \leq 0 \end{cases} \tag{18}$$

$$C(10): \frac{\delta_0}{\delta_{Adm}} - 1 \leq 0 \tag{19}$$

$$C(11): \frac{\delta_{Total}}{\delta_{Adm}} - 1 \leq 0 \tag{20}$$

$$C(12): \frac{n_{total,cs}}{n_{máx,cs}} - 1 \leq 0 \tag{21}$$

Where $C(1)$ and $C(2)$ refers to the limitation on the upper chord's axial loading before and after curing, respectively; $C(3)$ and $C(4)$ refers to the limitation on the lower chord's axial loading before and after curing, respectively; $C(5)$ and $C(6)$ refers to the limitation on the web members' axial loading before and after curing, respectively; $C(7)$ refers to the limitation on the composite section's bending moment; $C(8)$ and $C(9)$ refers to the limitation on the combined bending on the upper chord before and after curing, respectively; $C(10)$ and $C(11)$ refers to the limitation of deflection before and after curing; and $C(12)$ refers to a verification on the number of shear connectors, in order to make sure the spacing between them is higher than the criteria established by current standards [41].

Aiming to solve the optimization problem proposed, the program uses Matlab's native Genetic Algorithm. As for the PSO, it was implemented in Matlab with the Adaptive Penalty Method (APM) proposed by Lemonge and Barbosa [27]. For the PSO, a population of one hundred individuals was considered, 75 iteration steps and a tolerance of 10^{-6} as a stopping

criterion and solution convergence. For GA, the initial population contains 120 individuals, the rate of elite individuals and crossing of the intermediate type are 0.05 and 0.8, respectively, whereas the mutation rate is random.

3. RESULTS AND DISCUSSIONS

In order to compare the algorithms, truss models and profile shapes, the developed program was applied to three composite beams, with identical materials and loading conditions, and span lengths of 8, 24 and 40 meters. In each case, Genetic Algorithm (GA) and Particle Swarm Optimization (PSO) were used to optimize each combination between truss model – Pratt, Howe and Warren – and profile geometry – Double Angle (DA), Circular Hollow Tube (CHT) and Circular Concrete-Filled Tube (CCFT) – obtaining 18 solutions for each problem. In all of them, the following loading conditions were considered: live load of 2 kN/m^2, live or fixed partitions of 1 kN/m^2 and floor coverings of 0.15 kN/m^2. The other loads, due to self-weight, are calculated according to the elements chosen by the solution and the combinations of actions considered according to Brazilian standards [43]. The concrete used is produced with gneiss aggregate and the composite slab has ribs parallel to the beams, which are spaced 2 meters apart and shored before curing. It was also considered that the steel has a modulus of elasticity of 200 GPa and the modulus of rupture of the connectors' steel is 450 MPa. The yield strength of the steel is 355 MPa to the profiles, 600 MPa to the reinforcing mesh and 280 MPa to the formwork.

3.1 Truss with 8 meters

The first situation analyzed is a composite truss with a span of 8 meters. All solutions pointed to the same slab characteristics: 20 MPa concrete, 110 mm of width, thickness of 0.8 mm, rib of 50 mm and reinforcement mesh composed of bars of 3.8mm diameter, spaced from 150 to 150 mm. Consequently, the emission due to the slab was the same, equal to 190.47 kg for concrete, 354.13 kg for the formwork and 186.24 for the reinforcement mesh. It is important to note that 20MPa was the minimum permissible resistance to the concrete and the choice of shape was also the minimum emission. The convergence between solutions can be explained by the constancy of loading conditions and spacing between beams. In addition, the results corroborate the work of Santoro and Kripka [16], who concluded that, in reinforced concrete elements submitted to bending moment, it is more advantageous to use concrete with lower compressive strengths when considering only CO_2 emissions. However, it is important to mention that the evaluation the durability of the structural element could lead to different results, as the increase of concrete's compressive resistance also provides a gain of durability.

The number of connectors also remained the same, most likely due to the constancy of the slab configurations. The strength of a connector depends on the slab and shear connectors parameters. As both remained constant, the resistance of a connector also continued the same. The number of shear connectors, on the other hand, depends on two criteria: bearing stress on the slab concrete and the yield of the connector steel. Because the slab conditions also remained constant and the concrete bearing stress criterion was critical in all cases, the number of connectors remained constant in all solutions. The solution indicated 17 connectors, generating an emission of 4.43 kgCO_2 and totaling 586.28 kgCO_2. The emission due to steel profiles and concrete filling, however, varied from case to case and is presented in Table 2.

Table 2. CO_2 emission of each solution to the 8-m truss.

Truss Model	Profile Shape	Truss Model	Profile Shape		
			PROFILE	FILLING	TOTAL*
Pratt	DA	GA	178.48	-	764.75
		PSO	178.48	-	764.75
	CHT	GA	133.43	-	719.70
		PSO	133.43	-	719.70
	CCFT	GA	90.90	1.14	677.18
		PSO	90.90	1.14	677.18
Howe	DA	GA	185.48	-	771.76
		PSO	185.48	-	771.76
	CHT	GA	137.29	-	723.57
		PSO	137.29	-	723.57
	CCFT	GA	108.33	0.69	695.30
		PSO	108.33	0.69	695.30
Warren	DA	GA	171.48	-	757.75
		PSO	171.48	-	757.75
	CHT	GA	130.36	-	716.63
		PSO	130.36	-	716.63
	CCFT	GA	87.66	0.79	674.73
		PSO	87.66	0.79	674.73

*The total emission is the sum of the emission from the profiles, filling, and slab.

As can be seen in Table 2, both algorithms converged to the same solution in all cases, confirming its accuracy. The solution that presented the best result was the Warren truss using CCFT and the worst solution was obtained in the Howe truss using DA, causing 14.4% more emission, as shown in Figure 2, where the total emission of each solution is compared to the best solution. In general, the solutions given by DA were the least efficient, generating, on average, 11.8% more CO_2 than CCFT solutions. It is also noted that solutions using CHT are, on average, 5.4% less efficient than the solution of the same model using CCFT, reinforcing the relevance of this structural element. Table 3 presents the geometric properties of each solution, and Figure 3 presents the best solutions to each truss model, as well as the best solution using DA.

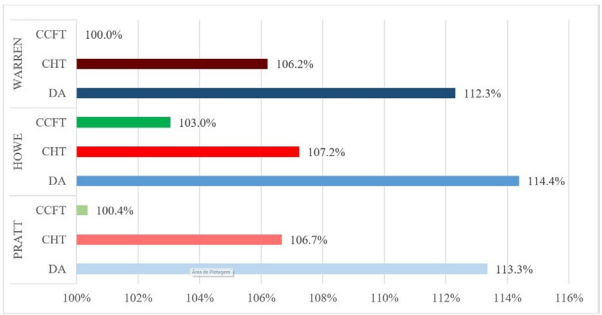

Figure 2. Comparison between solutions provided to the 8-m truss.

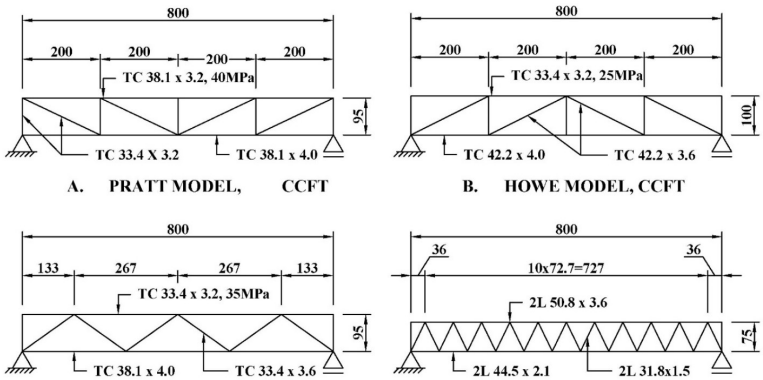

Figure 3. Final geometry of the best solutions to the eight meters truss.

Table 3. Geometric parameters of solutions provided to the 8-m truss.

Truss Model	Profile Shape	Alg.	Lower Chord	Upper Chord	Web Members	N° Panels	Height [mm]	Filling f_{ck} [MPa]
Pratt	DA	GA	2L 38.1 x 1.8	2L 50.8 x 3.6	2L 38.1 x 1.8	12	800	-
		PSO	2L 38.1 x 1.8	2L 50.8 x 3.6	2L 38.1 x 1.8	12	800	-
	CHT	GA	TC 42.2 x 4.0	TC 60.3 x 4.0	TC 33.4 x 3.2	8	900	-
		PSO	TC 42.2 x 4.0	TC 60.3 x 4.0	TC 33.4 x 3.2	8	900	-
	CCFT	GA	TC 38.1 x 4.0	TC 38.1 x 3.2	TC 33.4 x 3.2	4	950	40
		PSO	TC 38.1 x 4.0	TC 38.1 x 3.2	TC 33.4 x 3.2	4	950	40
Howe	DA	GA	2L 44.5 x 2.1	2L 50.8 x 3.6	2L 38.1 x 1.8	11	750	-
		PSO	2L 44.5 x 2.1	2L 50.8 x 3.6	2L 38.1 x 1.8	11	750	-
	CHT	GA	TC 42.2 x 4.0	TC 60.3 x 4.0	TC 33.4 x 3.2	8	1000	-
		PSO	TC 42.2 x 4.0	TC 60.3 x 4.0	TC 33.4 x 3.2	8	1000	-
	CCFT	GA	TC 42.2 x 4.0	TC 33.4 x 3.2	TC 42.2 x 3.6	4	1000	25
		PSO	TC 42.2 x 4.0	TC 33.4 x 3.2	TC 42.2 x 3.6	4	1000	25
Warren	DA	GA	2L 44.5 x 2.1	2L 50.8 x 3.6	2L 31.8 x 1.5	11	750	-
		PSO	2L 44.5 x 2.1	2L 50.8 x 3.6	2L 31.8 x 1.5	11	750	-
	CHT	GA	TC 38.1 x 4.0	TC 73.0 x 3.6	TC 33.4 x 3.2	6	1000	-
		PSO	TC 38.1 x 4.0	TC 73.0 x 3.6	TC 33.4 x 3.2	6	1000	-
	CCFT	GA	TC 38.1 x 4.0	TC 33.4 x 3.2	TC 33.4 x 3.6	3	950	35
		PSO	TC 38.1 x 4.0	TC 33.4 x 3.2	TC 33.4 x 3.6	3	950	35

It can be noted by the analysis of the Table that the trusses constituted by DA have lower heights and a higher number of panels than the others. This is because, compared to CHT profiles and especially to CCFT, DA profiles are slender, which restricts the size of the elements. The filling of tubular profiles significantly increases the stiffness of the elements, making the upper chord more resistant to compression. This resistance gain allows reducing considerably the steel area of the upper chord profiles and also increasing its length, allowing larger panels. The increase in emission caused by the concrete used in the filling of the profiles is insignificant when compared to the emission avoided by the reduction of the steel area, as shown in Table 2 and in accordance with the work by Guimarães et al. [44] and Lourenção et al. [45]. Figure 4 shows the emission composition of each solution.

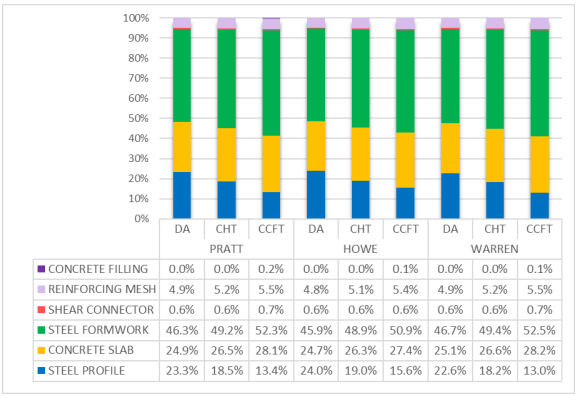

	PRATT			HOWE			WARREN		
	DA	CHT	CCFT	DA	CHT	CCFT	DA	CHT	CCFT
CONCRETE FILLING	0.0%	0.0%	0.2%	0.0%	0.0%	0.1%	0.0%	0.0%	0.1%
REINFORCING MESH	4.9%	5.2%	5.5%	4.8%	5.1%	5.4%	4.9%	5.2%	5.5%
SHEAR CONNECTOR	0.6%	0.6%	0.7%	0.6%	0.6%	0.6%	0.6%	0.6%	0.7%
STEEL FORMWORK	46.3%	49.2%	52.3%	45.9%	48.9%	50.9%	46.7%	49.4%	52.5%
CONCRETE SLAB	24.9%	26.5%	28.1%	24.7%	26.3%	27.4%	25.1%	26.6%	28.2%
STEEL PROFILE	23.3%	18.5%	13.4%	24.0%	19.0%	15.6%	22.6%	18.2%	13.0%

Figure 4. CO_2 Emission Composition of solutions provided to the 8-m truss.

Figure 4 confirms that the emission due to the concrete used in filling the upper chords represents 0.1% to 0.2% of the total emission, while the emission of steel reduces from 3.4% to 5.2% only by filling the profiles. In the cases analyzed, the steel formwork was the largest responsible for the emission, generating more than 45% of the emissions, followed by the concrete slab, with more than 24%. Figure 5 shows which constraints predominated in the optimization problem and Table 4 shows the relation between design and resistant efforts.

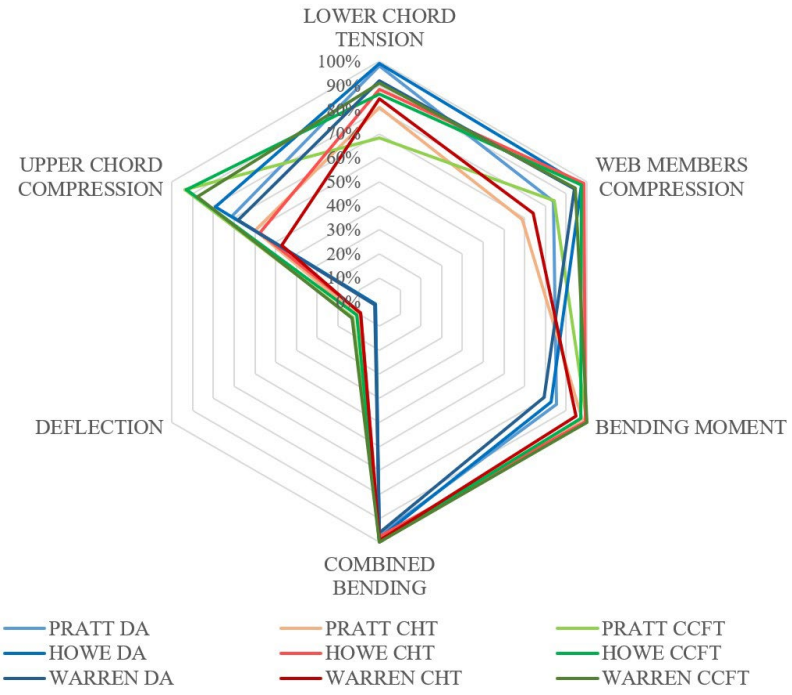

Figure 5. Constraints analysis provided to the 8-m truss.

Table 4. Relation between design and resistant efforts of the solutions.

Truss Model	Profile Shape	Upper Chord Compression	Lower Chord Tension	Web Members Compression	Bending Moment	Combined Bending	Deflection
Pratt	DA	71.05%	**98.06%**	83.74%	85.17%	96.80%	1.78%
	CHT	59.70%	80.90%	68.98%	97.61%	**99.92%**	10.53%
	CCFT	93.60%	68.30%	84.04%	**99.85%**	98.59%	12.83%
Howe	DA	79.22%	**99.24%**	97.40%	82.87%	98.14%	1.95%
	CHT	57.44%	88.56%	98.60%	**99.24%**	97.66%	9.09%
	CCFT	93.11%	86.41%	97.26%	96.83%	**99.90%**	11.03%
Warren	DA	68.13%	92.01%	94.04%	79.28%	**96.07%**	2.35%
	CHT	47.17%	84.41%	74.16%	95.77%	**99.36%**	9.22%
	CCFT	87.79%	90.96%	94.44%	**99.80%**	99.75%	13.31%

As shown in Table 4, the lower chord tension criterion was critical only for solutions using DA, while the bending moment was more restrictive for the others, reaching more than 95% and being the critical in three of them. For all solutions, the combined bending was a very expressive criterion, reaching more than 95% and proving to be a significant criterion on the sizing of composite trusses. This criterion evaluates the upper chord's ability to resist the combination of compression and bending moment. The resistance gain and consequent CO_2 emission reduction could be explained by the fact that the concrete filling considerably reduces the dimension of the profile used in the upper chord without losing its resistant capacity.

3.2 Truss with 24 meters

In the second example, a 24-meter-long truss with the same slab configurations as the previous example is analyzed. The emission of concrete slab, formwork and reinforcing mesh increased to 571.40, 1062.38 and 111.75 $kgCO_2$, respectively, proportionally to the span growth. The number of connectors also increased to 50 connectors, representing an emission of 13.04 $kgCO_2$ and totaling 1745.53 $kgCO_2$.

The emission due to the steel profiles and the concrete filling of the upper chords is shown in Table 5, where it can be noted that the algorithms diverged in most cases, but provided solutions with total emissions that differ by less than 2% from one another. Only in one case the GA led to a more efficient solution than the PSO; in two cases there was convergence and; in six, the PSO obtained the best solutions, indicating a greater efficiency of the algorithm for this type of problem. Table 6 shows the geometric characteristics for the final solutions of the optimization problem and Figure 6 presents the geometry of the best solutions to each truss model, as well as the best solution using DA.

Table 5. CO_2 emission of each solution to the 24-m truss.

Truss Model	Profile Shape	Algorithm	CO_2 Emission ($kgCO_2$)		
			Profile	Concrete	Total*
Pratt	DA	GA	1934.18	-	3692.75
		PSO	1934.18	-	3692.75
	CHT	GA	1211.26	-	2969.83
		PSO	1194.85	-	2953.42
	CCFT	GA	824.49	18.95	2583.06
		PSO	810.56	15.50	2569.13
Howe	DA	GA	1987.66	-	3746.23
		PSO	1987.66	-	3746.23
	CHT	GA	1343.05	-	3101.62
		PSO	1314.43	-	3073.00
	CCFT	GA	979.41	14.75	2752.73
		PSO	1000.35	14.05	2772.97
Warren	DA	GA	1863.13	-	3601.70
		PSO	1808.14	-	3566.71
	CHT	GA	1154.83	-	2913.40
		PSO	1150.50	-	2909.07
	CCFT	GA	758.04	16.51	2533.12
		PSO	755.94	16.51	2531.02

*The total emission is the sum of the emission from the profiles, filling, and slab.

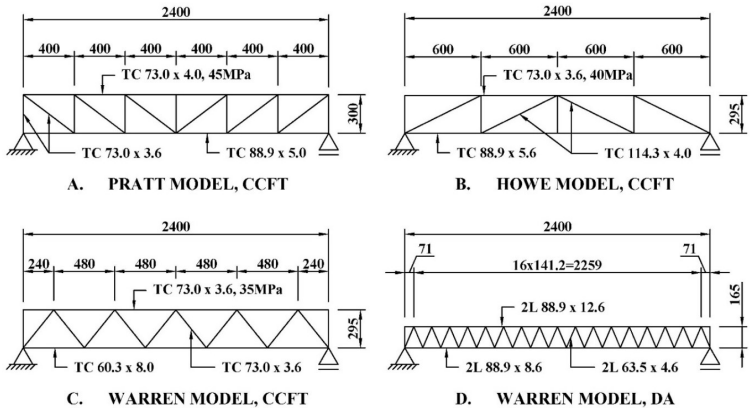

Figure 6. Final geometry to the best solutions to the 24-m truss.

Table 6. Geometric parameters of solutions provided to the 24-m truss.

Truss Model	Profile Shape	Alg.	Lower Chord	Upper Chord	Web Members	N° Panels	Height [mm]	f_{ck} [MPa]
Pratt	DA	GA	2L 88.90 x 8.6	2L 101.6 x 14.6	2L 76.20 x 5.5	14	1600	-
		PSO	2L 88.90 x 8.6	2L 101.6 x 14.6	2L 76.20 x 5.5	14	1600	-
	CHT	GA	TC 101.6 x 5.0	TC 141.3 x 5.6	TC 73.0 x 3.6	8	2700	-
		PSO	TC 60.3 x 8.8	TC 141.3 x 5.0	TC 73.0 x 3.6	10	2650	-
	CCFT	GA	TC 73.0 x 6.4	TC 88.9 x 3.6	TC 73.0 x 3.6	6	2850	25
		PSO	TC 88.9 x 5.0	TC 73.0 x 4.0	TC 73.0 x 3.6	6	3000	45
Howe	DA	GA	2L 88.90 x 8.6	2L 88.90 x 12.6	2L 76.20 x 5.5	18	1650	-
		PSO	2L 88.90 x 8.6	2L 88.90 x 12.6	2L 76.20 x 5.5	18	1650	-
	CHT	GA	TC 73.0 x 8.0	TC 141.3 x 5.0	TC 73.0 x 4.5	10	2650	-
		PSO	TC 73.0 x 7.1	TC 141.3 x 5.6	TC 88.9 x 3.6	8	2900	-
	CCFT	GA	TC 88.9 x 5.6	TC 73.0 x 3.6	TC 114.3 x 4.0	4	2950	40
		PSO	TC 114.3 x 4.5	TC 73.0 x 3.6	TC 114.3 x 4.0	4	3000	35
Warren	DA	GA	2L 76.20 x 7.3	2L 101.6 x 14.6	2L 76.20 x 5.5	11	2000	-
		PSO	2L 88.90 x 8.6	2L 88.9 x 12.6	2L 63.50 x 4.6	17	1650	-
	CHT	GA	TC 88.9 x 5.0	TC 114.3 x 5.6	TC 60.3 x 4.0	11	3000	-
		PSO	TC 60.3 x 8.8	TC 141.3 x 5.0	TC 60.3 x 4.0	10	2650	-
	CCFT	GA	TC 88.9 x 5.0	TC 73.0 x 3.6	TC 73.0 x 3.6	5	2950	35
		PSO	TC 60.3 x 8.0	TC 73.0 x 3.6	TC 73.0 x 3.6	5	2950	35

According to Table 6, it is noticeable that trusses using DA have the lowest truss heights, as well as the highest number of panels, while the others presented similar and significantly higher heights. Once again, it is observed that most solutions using CCFT point to concretes with resistance greater than 35MPa, indicating that, for this purpose, concretes with higher strength are more effective. This is because, comparing the profiles used in the upper chords of CHT and CCFT solutions, there is a significant reduction in the dimensions of the profiles used. Figure 7 presents a comparison between each solution and the minimum emission, only being indicated the best solution found between GA and PSO, to each case.

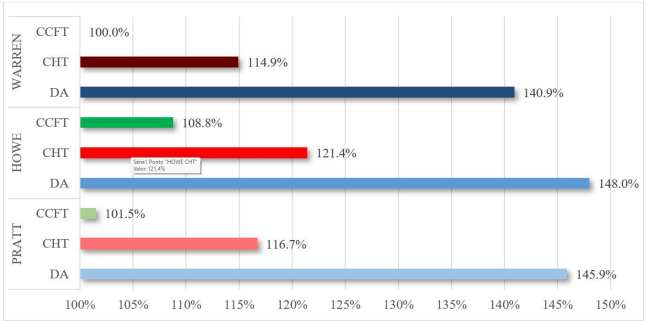

Figure 7. Comparison between solutions provided to the 24-m truss.

As in the previous example, the Warren model solution using CCFT was the most efficient and the Howe model using DA the least efficient, a difference even larger than the previous example, reaching 48.0%. The average difference between the solutions provided by the different profile geometries also increased, with the emission of the CHT being 14.37% higher and the DA 34.11% higher than the emission of the CCFT. This relative increase is justified by the greater expressiveness of the emission caused by steel profiles, as shown in Figure 8.

The largest emission for this example varied, being again the steel formwork in the trusses using CCFT and the steel profiles in the others, something that is justified by the greater difference between the emissions of each solution. The other elements have lost some expressiveness for this length of span. Figure 9 shows the constraints that governed the problem and Table 7 shows the proportions between design and resistant efforts of each case.

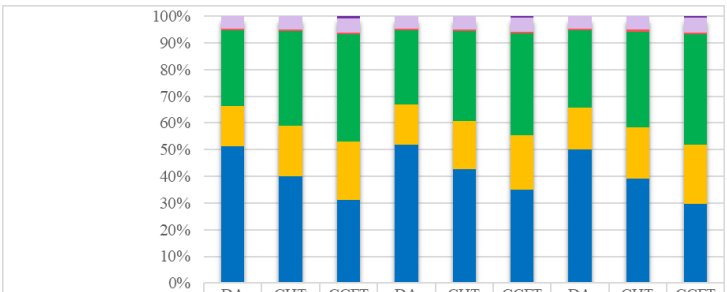

	DA	CHT	CCFT	DA	CHT	CCFT	DA	CHT	CCFT
	PRATT			HOWE			WARREN		
CONCRETE FILLING	0.0%	0.0%	0.7%	0.0%	0.0%	0.5%	0.0%	0.0%	0.7%
REINFORCING MESH	4.9%	5.2%	5.5%	4.8%	5.1%	5.4%	4.9%	5.2%	5.5%
SHEAR CONNECTOR	0.6%	0.6%	0.7%	0.6%	0.6%	0.6%	0.6%	0.6%	0.7%
STEEL FORMWORK	28.8%	35.8%	41.1%	28.4%	34.3%	38.6%	29.5%	36.5%	41.9%
CONCRETE SLAB	15.5%	19.2%	22.1%	15.3%	18.4%	20.8%	15.9%	19.6%	22.6%
STEEL PROFILE	52.4%	40.8%	31.9%	53.1%	43.3%	35.6%	51.2%	39.6%	29.9%

Figure 8. CO_2 Emission Composition of a 24-m span.

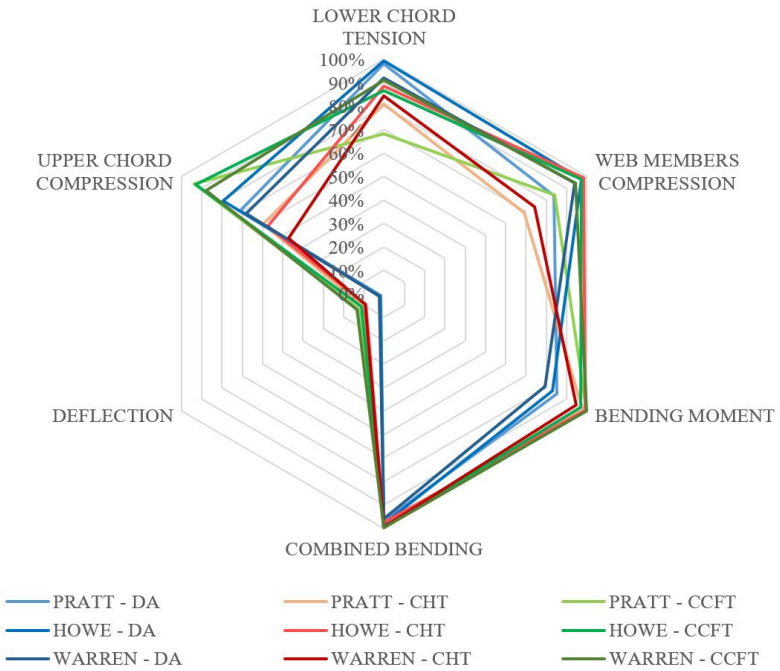

Figure 9. Constraints analysis provided to the 24 meters truss.

Table 7. Relation between design and resistant efforts of the solutions.

Truss Model	Profile Shape	Upper Chord Compression	Lower Chord Tension	Web Members Compression	Bending Moment	Combined Bending	Deflection
Pratt	DA	74.56%	**99.01%**	90.72%	94.37%	94.53%	17.28%
	CHT	61.88%	87.88%	85.68%	**99.11%**	93.55%	15.80%
	CCFT	95.98%	76.33%	98.44%	97.03%	**99.92%**	16.47%
Howe	DA	80.50%	**98.56%**	96.53%	91.89%	96.28%	20.72%
	CHT	53.20%	89.59%	95.89%	**98.95%**	97.83%	13.44%
	CCFT	88.58%	86.05%	94.92%	97.79%	**98.31%**	15.46%
Warren	DA	67.23%	94.56%	92.69%	89.08%	**99.38%**	15.23%
	CHT	61.14%	90.41%	**99.07%**	98.94%	92.81%	15.80%
	CCFT	92.62%	87.70%	**99.91%**	97.25%	98.76%	17.00%

As can be observed, the lower chord tension criterion was more relevant in trusses using DA, being the critical for the Pratt and Howe models. The bending moment criterion, on the other hand, was more expressive for tubular profiles, being critical in Pratt and Howe trusses using CHT. In the case of Warren trusses using CHT and CCFT, the stress criterion in the diagonals and amounts was critical and, in the others, it was the combined bending criterion. As in the previous case, the constraints referring the serviceability limit state, the maximum deflection, is the one that least impacts on the final solution of the optimization problem for all analyzed solutions.

3.3 Truss with 40 meters

For the third example, a truss with 40 meters of span with the same slab characteristics of the previous examples was analyzed. Similarly, the same slab concrete, steel formwork and reinforcement mesh strength solutions were indicated, each of them emitting 952.34, 1770.63 and 186.24 $kgCO_2$, respectively. 84 connectors were required, generating 21.91 $kgCO_2$ and totaling 2931.12 $kgCO_2$. The emissions related to the steel profile and the concrete filling are presented in Table 8.

Table 8. Geometric parameters of solutions provided to the 40-m truss.

Truss Model	Profile Shape	Algorithm	CO_2 Emission ($kgCO_2$)		
			Profile	Concrete	Total*
Pratt	DA	GA	6335.49	-	9266.61
		PSO	6335.49	-	9266.61
	CHT	GA	3503.90	-	6435.01
		PSO	3490.92	-	6422.04
	CCFT	GA	2294.48	69.12	5294.71
		PSO	2294.48	69.12	5294.71
Howe	DA	GA	6346.21	-	9277.33
		PSO	6346.21	-	9277.33
	CHT	GA	3962.27	-	6893.39
		PSO	4000.82	-	6931.94
	CCFT	GA	2922.01	69.12	5922.25
		PSO	2912.22	64.66	5908.00
Warren	DA	GA	5961.09	-	8892.21
		PSO	5961.09	-	8892.21
	CHT	GA	3422.31	-	6353.43
		PSO	3407.94	-	6339.06
	CCFT	GA	2243.29	54.92	5229.33
		PSO	2267.68	60.97	5259.76

*The total emission is the sum of the emission from the profiles, filling, and slab.

Table 8 shows that algorithms diverged in most cases, but again for solutions with total emissions that differ by less than 1%. Of the five cases where there was no convergence, GA provided more efficient solutions in two cases and PSO in three, representing a slight advantage for this algorithm in this example. Table 9 shows the geometric parameters of the provided trusses and Figure 10 presents the geometry of the best solutions to each truss model, as well as the best solution using DA.

Table 9. Geometric parameters of solutions provided to the 40-m truss.

Truss Model	Profile Shape	Alg.	Lower Chord	Upper Chord	Web Members	N° Panels	Height [mm]	f_{ck} [MPa]
Pratt	DA	GA	2L 101.6 x 14.6	2L 152.4 x 29.2	2L 127.0 x 12.3	12	2800	-
		PSO	2L 101.6 x 14.6	2L 152.4 x 29.2	2L 127.0 x 12.3	12	2800	-
	CHT	GA	TC 114.3 x 7.1	TC 219.1 x 6.4	TC 101.6 x 4.5	8	4700	-
		PSO	TC 114.3 x 8.0	TC 168.3 x 7.1	TC 101.6 x 4.0	12	4250	-
	CCFT	GA	TC 101.6 x 8.0	TC 114.3 x 4.0	TC 114.3 x 4.0	6	4600	45
		PSO	TC 101.6 x 8.0	TC 114.3 x 4.0	TC 114.3 x 4.0	6	4600	45
Howe	DA	GA	2L 101.6 x 12.2	2L 127.0 x 23.5	2L 127.0 x 12.3	16	3300	-
		PSO	2L 101.6 x 12.2	2L 127.0 x 23.5	2L 127.0 x 12.3	16	3300	-
	CHT	GA	TC 101.6 x 10.0	TC 168.3 x 7.1	TC 114.3 x 4.5	12	4450	-
		PSO	TC 141.3 x 7.1	TC 168.3 x 7.1	TC 114.3 x 4.5	12	4450	-
	CCFT	GA	TC 101.6 x 8.8	TC 114.3 x 4.0	TC 141.3 x 5.0	6	4700	45
		PSO	TC 101.6 x 8.8	TC 114.3 x 4.0	TC 141.3 x 5.0	6	4650	40
Warren	DA	GA	2L 127.0 x 15.3	2L 152.4 x 29.2	2L 101.6 x 9.8	13	2700	-
		PSO	2L 127.0 x 15.3	2L 152.4 x 29.2	2L 101.6 x 9.8	13	2700	-
	CHT	GA	TC 114.3 x 7.1	TC 168.3 x 7.1	TC 101.6 x 4.0	11	4750	-
		PSO	TC 114.3 x 7.1	TC 168.3 x 6.4	TC 101.6 x 4.0	12	4800	-
	CCFT	GA	TC 114.3 x 6.4	TC 114.3 x 4.5	TC 114.3 x 4.0	5	5000	30
		PSO	TC 114.3 x 6.4	TC 114.3 x 4.0	TC 101.6 x 4.5	6	5000	35

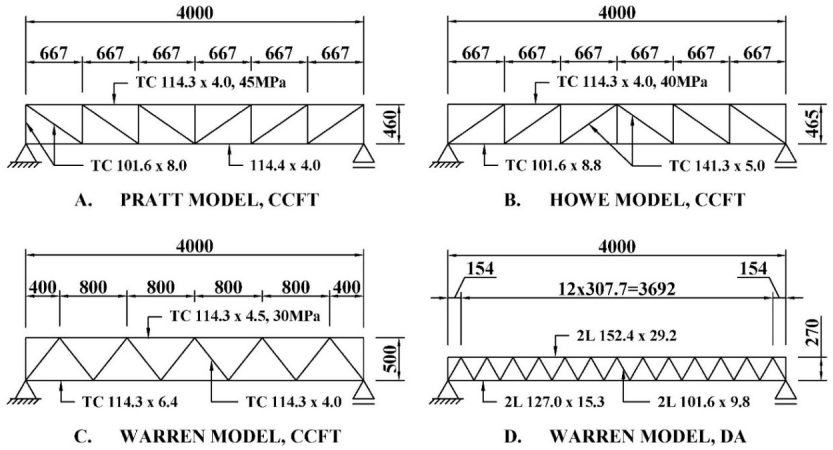

Figure 10. Final geometry to the best solutions to the 40-m truss.

It is possible to notice, as in the previous examples, that there is a clear tendency of solutions using DA to use more panels and lower heights, in order to minimize the size of the elements. Three of the 6 solutions using DA reached the lower bound of the search interval considered, while two of the solutions for CCFT reached the upper bound. Figure 11 shows the best solutions between GA and PSO for each case, in relation to the best solution.

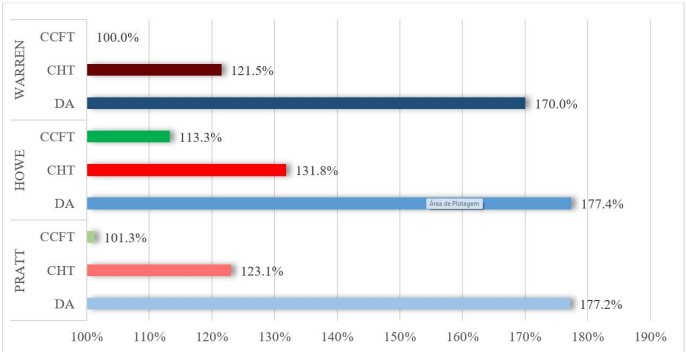

Figure 11 - Comparison between solutions provided to the 40-m truss.

Once again following the tendency, the Warren truss using CCFT was the most efficient solution and the Howe truss using DA the least efficient, a difference even greater than the one found in previous examples, reaching 77.4%. It was found that the trusses using CHT emits, on average, 19.81% more CO_2 than the ones using CCFT, a value that is even higher for trusses using DA, where the average emission is 67.24% higher. Figure 12 shows the reduction of total CO_2 emission obtained by substituting DA profiles by CHT and CCFT in each example.

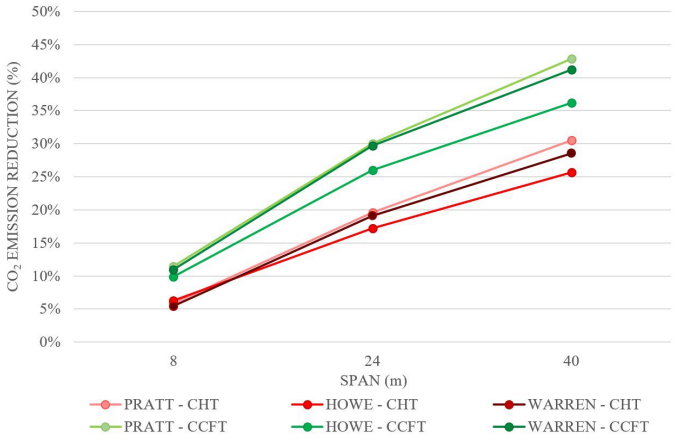

Figure 12 - CO_2 Emission reduction in relation to the DA solution.

It is possible to conclude that, the greater the span, the greater the reduction obtained by using CCFT instead of DA. That can be better explained by Figure 13, which shows the detailed emission caused by each element of the truss. In it, profiles are shown to be the largest responsible for the total emission of the beam, in contrast to the previous examples, where its representativeness was quite inferior.

In this case it is possible to notice that steel profiles are the largest responsible for the CO_2 emission of all solutions, reaching more than two thirds of the entire emission, in the case of DA trusses. The steel shape follows as the second largest emitter and the concrete slab the next. As the dimensions of the profiles of the upper chord increased, the emission due to the filling concrete now exceeds the emission of the connectors, with more than 1%, but with a value still derisory when compared to the substantial savings caused by the reduction in the steel weight of profiles. Table 10 shows the relation between design and resistant efforts to each of the safety criteria analyzed and Figure 14 presents an analysis of the constraints.

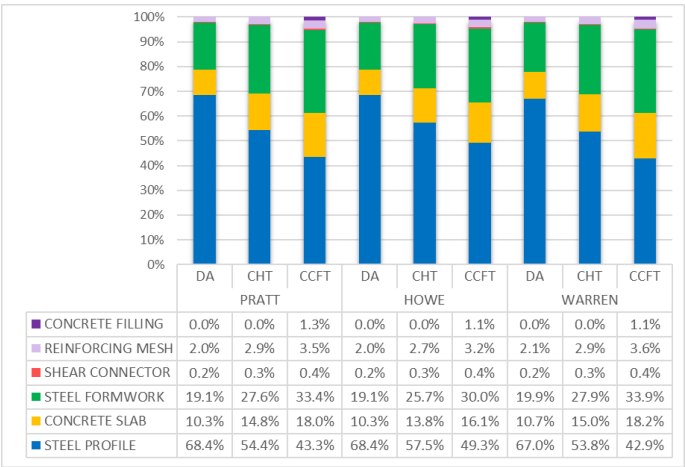

	DA	CHT	CCFT	DA	CHT	CCFT	DA	CHT	CCFT
	PRATT			HOWE			WARREN		
CONCRETE FILLING	0.0%	0.0%	1.3%	0.0%	0.0%	1.1%	0.0%	0.0%	1.1%
REINFORCING MESH	2.0%	2.9%	3.5%	2.0%	2.7%	3.2%	2.1%	2.9%	3.6%
SHEAR CONNECTOR	0.2%	0.3%	0.4%	0.2%	0.3%	0.4%	0.2%	0.3%	0.4%
STEEL FORMWORK	19.1%	27.6%	33.4%	19.1%	25.7%	30.0%	19.9%	27.9%	33.9%
CONCRETE SLAB	10.3%	14.8%	18.0%	10.3%	13.8%	16.1%	10.7%	15.0%	18.2%
STEEL PROFILE	68.4%	54.4%	43.3%	68.4%	57.5%	49.3%	67.0%	53.8%	42.9%

Figure 13. CO_2 Emission Composition of a 40-m span truss.

Table 10 - Relation between design and resistant efforts of the solutions.

Truss Model	Profile Shape	Upper Chord Compression	Lower Chord Tension	Web Members Compression	Bending Moment	Combined Bending	Deflection
Pratt	DA	74.09%	99.55%	88.79%	98.05%	**99.67%**	41.76%
	CHT	67.35%	86.04%	98.09%	**99.84%**	98.66%	21.45%
	CCFT	95.67%	80.69%	97.47%	99.85%	**99.90%**	22.10%
Howe	DA	75.44%	98.45%	97.55%	94.95%	**99.22%**	31.39%
	CHT	68.55%	85.90%	94.91%	95.10%	**99.87%**	18.92%
	CCFT	95.35%	89.17%	89.82%	98.26%	**99.62%**	20.34%
Warren	DA	78.42%	95.80%	97.53%	92.59%	**99.39%**	38.16%
	CHT	65.21%	86.67%	97.21%	97.12%	**99.70%**	18.94%
	CCFT	85.85%	90.11%	99.24%	**99.88%**	91.52%	20.36%

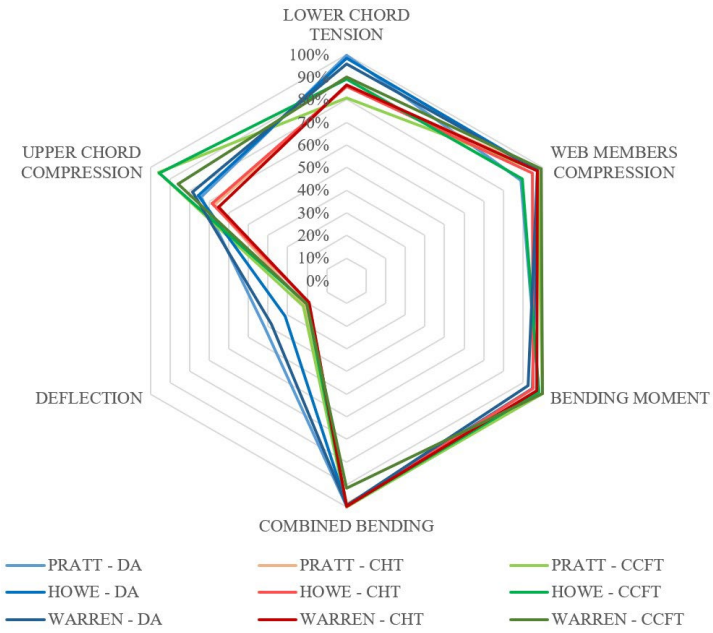

Figure 14. Constraints analysis provided to the 40-m truss.

By analyzing Table 10 and Figure 14, it is noted that the bending moment and combined bending were the determinant criteria in the dimensioning of all solutions. It is also noticed that the lower chord tension was more critical for trusses using DA, while the compression in the upper chord approached closer to the resistance limit in the trusses using CCFT, indicating a better exploitation of the elements when using concrete filling.

4. CONCLUSIONS

By analyzing the results obtained for each algorithm in the three examples studied, it was possible to notice that both converged to equal or similar solutions. For the first case, where the span was smaller, all the solutions provided were the same for both algorithms. For the other case, where the spans were larger, most results diverged. The divergence between the algorithms tested, however, did not exceed 2% in any case, confirming the effectiveness of the solutions. In general, the PSO was more efficient than the GA in obtaining the best solutions to the problems analyzed.

As for the models of truss, it was concluded that the most effective model for the cases analyzed was Warren, followed by Pratt and, finally, Howe. Among the profile shapes, the trusses using DA were the least efficient, followed by trusses using CHT and CCFT being the most efficient. The overall emission saving varied, being even more significant for longer span lengths, much because the use of this type of section reduced the weight of the profiles, which are the major responsible for the general emission of the truss in these cases. The saving provided by filling the upper chord was 5.4% in the 8-meter span example and reached almost 20% for the 40-meter span. Comparing the

solutions using CHT and CCFT, it was concluded that the increase in emission caused by the filling concrete is much lower than the emission avoided by the reduction of profiles weight.

In all examples, the best solutions were to concrete with f_{ck} equal 20MPa for the slab, but the same did not happen for the concrete fillings of the CCFT profiles. The choice of concrete used in the slab, as well as steel formwork and reinforcement mesh, did not vary, indicating that these parameters are not influenced by the span size. The strength of the filling concrete, on the other hand, varied between span lengths and truss models, but all the best solutions were found for concretes with compressive strength equal to or greater than 25 MPa. These results reinforce that, although concretes with higher resistances generate a higher CO_2 emission, their use allowed for a general gain in resistance that helped minimize the use of steel and, consequently, the total emission of the truss.

Regarding the constraints that governed the analyzed problems, the combined bending criterion was critical in the optimum design of all examples, generating a design-resistant relation greater than 90% in all cases. Another critical criterion in many cases, especially in solutions using tubular profiles, was the bending moment. In the trusses of the solutions using DA, in general, the criterion of lower chord tension was more relevant, while the upper chord compression was more relevant in the solutions using CCFT. In all the solutions, the governing criterion reached more than 96% in the relation between design and resistant efforts, confirming the efficiency of the optimization algorithm.

5. ACKNOWLEDGEMENTS

The authors are thankful to the Brazilian Federal Government Agency CAPES for the financial support provided during the development of this research. The second author thanks the Brazilian Federal Government Agency CNPq for the productivity research grant number 309741/2020-3.

6. REFERENCES

[1] Intergovernmental Panel on Climate Change, *Contribution of Working Groups I, II and III to the Fourth Assessment Report on Intergovernmental Panel on Climate Change: Climate Change 2007: Synthesis Report*, Geneva, IPCC, 2007.

[2] Intergovernmental Panel on Climate Change, *Contribution of Working Group II to the Sixth Assessment Report of the Intergovernmental Panel on Climate Change: Climate Change 2022: Impacts, Adaptation, and Vulnerability*, Cambridge, Cambridge University Press, 2022.

[3] UN Environment and International Energy Agency, *2020 Global Status Report for Buildings and Construction: Towards a Zero-Emission, Efficient, and Resilient Buildings and Construction Sector*, Nairobi, United Nations Environment Programme, 2021.

[4] I. Payá-Zaforteza, V. Yepes, A. Hospitaler, and F. González-Vidosa, "CO2-optimization of reinforced concrete frames by simulated annealing," *Eng. Struct.*, vol. 31, no. 7, pp. 1501–1508, 2009, http://dx.doi.org/10.1016/j.engstruct.2009.02.034.

[5] D. Yeo and R. D. Gabbai, "Sustainable design of reinforced concrete structures through embodied energy optimization," *Energy Build.*, vol. 43, pp. 2028–2033, 2011, http://dx.doi.org/10.1016/j.enbuild.2011.04.014.

[6] V. Yepes, F. Gonzalez-Vidosa, J. Alcala, and P. Villalba, "CO2-optimization design of reinforced concrete retaining walls based on a VNS-threshold acceptance strategy," *J. Comput. Civ. Eng.*, vol. 26, no. 3, pp. 378–386, 2012, http://dx.doi.org/10.1061/(asce)cp.1943-5487.0000140.

[7] C. V. Camp and F. Huq, "CO2 and cost optimization of reinforced concrete frames using a big bang-big crunch algorithm," *Eng. Struct.*, vol. 48, pp. 363–372, 2013, http://dx.doi.org/10.1016/j.engstruct.2012.09.004.

[8] G. F. de Medeiros and M. Kripka, "Optimization of reinforced concrete columns according to different environmental impact assessment parameters," *Eng. Struct.*, vol. 59, pp. 185–194, 2014, http://dx.doi.org/10.1016/j.engstruct.2013.10.045.

[9] S. W. Choi, B. K. Oh, J. S. Park, and H. S. Park, "Sustainable design model to reduce environmental impact of building construction with composite structures," *J. Clean. Prod.*, vol. 137, pp. 823–832, 2016, http://dx.doi.org/10.1016/j.jclepro.2016.07.174.

[10] T. Dede, M. Kripka, V. Togan, V. Yepes, and R. V. Rao, "Usage of optimization techniques in civil engineering during the last two decades," *Curr. Trends Civ. Struct. Eng*, vol. 2, no. 1, 2019, http://dx.doi.org/10.33552/ctcse.2019.02.000529.

[11] A. F. Tormen, Z. M. C. Pravia, F. B. Ramires, and M. Kripka, "Optimization of steel concrete composite beams considering cost and environmental impact," *Steel Compos. Struct.*, vol. 34, no. 3, pp. 409–421, 2020, http://dx.doi.org/10.12989/scs.2020.34.3.409.

[12] N. D. Lagaros, "The environmental and economic impact of structural optimization," *Struct. Multidiscipl. Optim.*, vol. 58, no. 4, pp. 1751–1768, 2018, http://dx.doi.org/10.1007/s00158-018-1998-z.

[13] B. K. Oh, S. W. Choi, and H. S. Park, "Influence of variations in CO2 emission data upon environmental impact of building construction," *J. Clean. Prod.*, vol. 140, pp. 1194–1203, 2017, http://dx.doi.org/10.1016/j.jclepro.2016.10.041.

[14] M. M. Khasreen, P. F. G. Banfill, and G. F. Menzies, "Life-cycle assessment and the environmental impact of buildings: a review," *Sustainability*, vol. 1, no. 3, pp. 674–701, 2009, http://dx.doi.org/10.3390/su1030674.

[15] T. García Segura and V. Yepes, "Multiobjective optimization of post-tensioned concrete box-girder road bridges considering cost, CO2 emissions, and safety," *Eng. Struct.*, vol. 125, pp. 325–336, 2016, http://dx.doi.org/10.1016/j.engstruct.2016.07.012.

[16] J. F. Santoro and M. Kripka, "Minimizing environmental impact from optimized sizing of reinforced concrete elements," *Comput. Concr.*, vol. 25, no. 2, pp. 111–118, 2020, http://dx.doi.org/10.12989/cac.2020.25.2.111.

[17] A. A. A. Esmin, R. A. Coelho, and S. Matwin, "A review on particle swarm optimization algorithm and its variants to clustering high-dimensional data," *Artif. Intell. Rev.*, vol. 44, no. 1, pp. 23–45, 2015, http://dx.doi.org/10.1007/s10462-013-9400-4.

[18] V. Govindaraj and J. V. Ramasamy, "Optimum detailed design of reinforced concrete continuous beams using Genetic Algorithms," *Comput. Struc.*, vol. 84, no. 1–2, pp. 34–48, 2005, http://dx.doi.org/10.1016/j.compstruc.2005.09.001.

[19] C. A. C. Coello, A. D. Christiansen, and F. S. Hernández, "A simple genetic algorithm for the design of reinforced concrete beams," *Eng. Comput.*, vol. 13, no. 4, pp. 185–196, 1997, http://dx.doi.org/10.1007/bf01200046.

[20] V. K. Koumousis and S. J. Arsenis, "Genetic algorithms in optimal detailed design of reinforced concrete members," *Comput. Civ. Infrastruct. Eng*, vol. 13, no. 1, pp. 43–52, 1998, http://dx.doi.org/10.1111/0885-9507.00084.

[21] B. D. Breda, T. C. Pietralonga, and E. C. Alves, "Optimization of the structural system with composite beam and composite slab using Genetic Algorithm," *IBRACON Struct. Mater. J.*, vol. 13, no. 6, pp. 1–14, 2020, http://dx.doi.org/10.1590/s1983-41952020000600002.

[22] A. H. Whitworth and K. D. Tsavdaridis, "Genetic algorithm for embodied energy optimisation of steel-concrete composite beams," *Sustainability*, vol. 12, no. 8, pp. 1–17, 2020, http://dx.doi.org/10.3390/SU12083102.

[23] A. B. Senouci and M. S. Al-Ansari, "Cost optimization of composite beams using genetic algorithms," *Adv. Eng. Softw.*, vol. 40, no. 11, pp. 1112–1118, 2009, http://dx.doi.org/10.1016/j.advengsoft.2009.06.001.

[24] F. Erdal, E. Doan, and M. P. Saka, "Optimum design of cellular beams using harmony search and particle swarm optimizers," *J. Construct. Steel Res.*, vol. 67, no. 2, pp. 237–247, 2011, http://dx.doi.org/10.1016/j.jcsr.2010.07.014.

[25] G. Erlacher and E. C. Alves, "Optimal design of composite cellular beams with partial interaction and its environmental impacts", in *ABMEC-IACM*, Rio de Janeiro, 2021.

[26] R. E. Perez and K. Behdinan, "Particle swarm optimization in structural design," in *Swarm Intelligence, Focus on Ant and Particle Swarm Optimization*, F. T. Chan, M. K. Tiwari, Eds., London, United Kingdom: IntechOpen, 2007, pp. 373-394.

[27] A. C. C. Lemonge and H. J. C. Barbosa, "An adaptive penalty scheme for genetic algorithms in structural optimization," *Int. J. Numer. Methods Eng.*, vol. 59, no. 5, pp. 703–736, 2004, http://dx.doi.org/10.1002/nme.899.

[28] A. Baghlani and M. H. Makiabadi, "An enhanced particle swarm optimization for design of pin connected structures," *Sci. Iran.*, vol. 20, no. 5, pp. 1415–1432, 2013.

[29] F. B. Ramires, S. A. L. Andrade, P. C. G. S. Vallasco, and L. R. O. Lima, "Genetic algorithm optimisation of composite and steel endplate semi-rigid joints," *Eng. Struct.*, vol. 45, pp. 177–191, 2012, http://dx.doi.org/10.1016/j.engstruct.2012.05.051.

[30] J. Wardenier, Y. Kurobane, J. A. Packer, D. Dutta, and N. Yeomans, *Design Guide for Circular Hollow Section (CHT) Joints Under Predominantly Static Loading*. Germany: *Comité International pour le Développemente et l'Étude de la Construction Tubulaire*, 1991.

[31] S. A. Raji, K. K. Abdulraheem, R. O. Rahmon, and A. A. Adelowo, "Design of a composite truss system in a multistorey building," *J. Multidiscip. Eng. Sci. Technol.*, vol. 4, no. 3, pp. 6863–6870, 2017.

[32] J. Bujnak, P. Michalek, and W. Baran, "Experimental and theoretical investigation of composite truss beams", in *MATEC Web Conference*, 2018, vol. 174, pp. 6-13, https://doi.org/10.1051/matecconf/201817404001.

[33] J. D. Martins, S. E. Pereira, E. M. Jr., Xavier, L. H. A. Neiva, and A. M. C. Sarmanho, "Experimental and numerical analysis of composite steel and concrete trusses," *IBRACON Estructures Mater. J.*, vol. 14, pp. 1–14, 2021, http://dx.doi.org/10.1590/s1983-41952021000200001.

[34] A. Kaveh and B. Ahmadi, "Sizing, geometry and topology optimization of trusses using force method and supervised charged system search," *Struct. Eng. Mech.*, vol. 50, 2014, http://dx.doi.org/10.12989/sem.2014.50.3.365.

[35] M. A. K. Tarabay and L.S. Lima, "Otimização topológica, geométrica e dimensional de estruturas metálicas treliçadas, dimensionadas conforme a norma ABNT NBR 8800: 2008," *REA*, vol. 11, pp. 21–38, 2022.

[36] T. E. Müller and E. van der Klashorst, "A quantitative comparison between size, shape, topology and simultaneous optimization for truss structures," *Lat. Am. J. Solids Struct.*, vol. 14, no. 12, pp. 2221–2242, 2017, http://dx.doi.org/10.1590/1679-78253900.

[37] Gerdau. "Perfis estruturais Gerdau: tabela de bitolas." https://mais.gerdau.com.br/catalogos-e-manuais/ (accessed Apr. 26, 2022).

[38] Vallourec Tubos do Brasil. "Tubos estruturais de seção circular, quadrada e retangular." https://www.aecweb.com.br/empresa/vallourec/20437/downloads/1 (accessed Apr. 26, 2022).

[39] METFORM. "Catálogo de Fôrmas." www.aecweb.com.br (accessed Apr. 26, 2022).

[40] Worldsteel Association. "LCI data for steel products." https://worldsteel.org (accessed May 27, 2022).

[41] Associação Brasileira de Normas Técnicas, *Design of steel and composite steel and concrete structures for buildings*, ABNT NBR 8800, 2008.

[42] Associação Brasileira de Normas Técnicas, *Design of steel and composite structures for buildings using hollow sections,* ABNT NBR 16239, 2013.

[43] Associação Brasileira de Normas Técnicas, *Cargas para o cálculo de estruturas de edificações,* ABNT NBR 6120, 2019.

[44] S. A. Guimarães, D. Klein, A. F. G. Calenzani, and E. C. Alves, "Optimum design of steel columns filled with concrete via genetic algorithm: environmental impact and cost analysis," *REM Int. Eng. J.*, vol. 75, no. 1, pp. 117–128, 2022, http://dx.doi.org/10.1590/0370-44672021750034.

[45] J. S. Lourenção, P. A. T. Arpini, G. Erlacher, and E. C. Alves, "Optimized design of concrete-filled steel columns," *IBRACON Struct. Mater. J.*, vol. 15, no. 1, pp. e15102, 2022, http://dx.doi.org/10.1590/s1983-41952022000100002.

Author contributions: GE: formal analysis, data curation, writing; AFGC: formal analysis, data curation, writing, supervision; ECA: methodology, formal analysis, data curation, conceptualization, writing, supervision.

Editors: Edna Possan, Guilherme Aris Parsekian.

IBRACON Structures and Materials Journal
Revista IBRACON de Estruturas e Materiais
ISSN 1983-4195 ismj.org

ORIGINAL ARTICLE

On the mechanical behavior of a hybrid reinforced concrete for industrial floors

Sobre o comportamento mecânico de um concreto com reforço híbrido para pisos industriais

Igor Nogueira Lima[a]
Victor Nogueira Lima[b]
Felipe Rodrigues de Souza[b]
Felipe Pinheiro Teixeira[c]
Maria Isabel Brasileiro Rodrigues[d]
Flávio de Andrade Silva[b]

[a]Pontifícia Universidade Católica do Rio de Janeiro – PUC-Rio, Department of Chemical and Materials Engineering, Rio de Janeiro, RJ, Brasil
[b]Pontifícia Universidade Católica do Rio de Janeiro – PUC-Rio, Department of Civil and Environmental Engineering, Rio de Janeiro, RJ, Brasil
[c]Universidade Estadual do Norte Fluminense Darcy Ribeiro – UENF, Postgraduate Program in Civil Engineering, Campos dos Goytacazes, RJ, Brasil
[d]Universidade Federal do Cariri – UFCA, Science and Technology Center, Juazeiro do Norte, CE, Brasil

Received 23 September 2022
Accepted 09 February 2023

Abstract: Civil construction is an industry sector that has been used as an outlet for the reuse of industrial waste. The present work aims to use the residue of Ethylene Vinyl Acetate (EVA) from the footwear industry as a partial substitute for a granulometric range of aggregates, aiming at the production of structural concrete and application to industrial floors. The proposed mixing ratios were evaluated from uniaxial compression, three-point bending, and drying shrinkage tests. The results of the uniaxial compression tests showed that the concrete with EVA addition still has enough strength to be considered structural concrete. In addition, the EVA and polypropylene fiber particles act as stress transfer bridges in the cracked zone, resulting in an increase in residual stresses and, consequently, in the toughness of the concrete in the three-point bending test. Finally, Technical Report 34 was used as a procedure to design an industrial floor based on the compressive strength, Young's modulus, and flexural behavior of the tested composites. The final result showed that even with lower compressive strength, fiber-reinforced concrete with EVA achieves greater structural efficiency for an industrial floor with the same cross-sectional height as ordinary fiber-reinforced concrete.

Keywords: EVA, concrete, fiber reinforced concrete, industry waste, toughness.

Resumo: A construção civil é um setor da indústria que tem sido utilizado como uma saída para o reaproveitamento de muitos resíduos. O presente trabalho visa utilizar o resíduo de Etileno Vinil Acetato (EVA) da indústria calçadista como substituto parcial de uma faixa granulométrica de agregados, visando produção de concreto estrutural e aplicação a concretagem de pisos industriais. As proporções de mistura propostas foram avaliadas a partir de ensaios de compressão uniaxial, flexão em três pontos e retração por secagem. Os resultados dos testes de compressão uniaxial mostraram que o concreto com substituição ainda apresenta resistência suficiente para ser considerado concreto estrutural. Além disso, as partículas de EVA e da fibra de polipropileno funcionam como pontes de transferência de tensões na zona fissurada, resultando em um aumento das tensões residuais e, consequentemente, da tenacidade do concreto no teste de flexão em três pontos. Por fim, o Technical Report 34 foi utilizado como procedimento para dimensionar um piso industrial a partir da resistência a compressão, módulo de Young e comportamento a flexão dos compósitos ensaiados. O resultado final mostrou que mesmo com menor resistência à compressão, o concreto reforçado com fibras e substituição parcial de EVA consegue maior eficiência estrutural para um piso industrial de mesma altura de seção transversal que o concreto reforçado com fibras comum.

Palavras-chave: EVA, concreto, concreto reforçado com fibra, resíduos da indústria, tenacidade.

How to cite: I. N. Lima, V. N. Lima, F. R. Souza, F. P. Teixeira, M. I. B. Rodrigues, and F. A. Silva, "On the mechanical behavior of a hybrid reinforced concrete for industrial floors," *Rev. IBRACON Estrut. Mater.*, vol. 16, no. 6, e16607, 2023, https://doi.org/10.1590/S1983-41952023000600007

Corresponding author: Victor Nogueira Lima. E-mail: eng.vnl@gmail.com
Financial support: This study was financed in part by the Coordenação de Aperfeiçoamento de Pessoal de Nível Superior (CAPES) – Brasil – Finance Code 001, by Brazilian funding agencies FAPERJ and CNPq, and by Lafarge Holcim, with the donation of cement.
Conflict of interest: Nothing to declare.
Data Availability: The data that support the findings of this study are available from the corresponding author, [VNL], upon reasonable request.

1 INTRODUCTION

The industrialization process along with demographic and technological growth brought, in addition to the benefits, an increase in the generation of solid waste, causing environmental problems [1]–[3]. Because of this, many industry sectors are valuing the search for eco-friendly solutions to dispose of their waste. In the construction industry, for example, many researchers are concerned about how to reuse demolition waste as inert materials in the mixture of mortar and concrete [4]–[6].

In addition to the demolition waste, advances can be seen in the production of lightweight concrete using other types of waste as lightweight aggregate, which can lead to a decrease in compressive strength, a parameter that directly influences the quality of the cementitious material [7]–[11]. In this case, Ethylene Vinyl Acetate (EVA) is a residue that has been widely proposed for research focused on lightweight concrete formulations with permeable characteristics [12], [13] or for bituminous concretes [14], [15]. Most applications for this type of material are focused on paving [16], [17], and its use as an addition in structural concrete is a gap in the literature.

The use of plastic materials, such as the EVA mentioned above, has aroused much interest due to the difficulties encountered in disposing of the waste. As highlighted by Lima et al. [2], storage or disposal in landfills implies the availability of large surfaces, and incineration can emit potentially harmful gases and ashes. Because of this, the use of thermoplastic materials has become widespread in various sectors of the industry, as they can be melted in the recycling process [18]. However, EVA is not characterized as a thermoplastic material, but as a thermosetting material and, therefore, cannot be melted by heat due to its molecular chains.

In addition to EVA, some other plastic wastes have been destined for use as inert materials in concrete, i.e. polyethylene and polystyrene [19], [20], high-density polyethylene [21], polyethylene terephthalate (PET) [22], polyvinyl chloride (PVC) [23]. In general, the increase in the plastic content added to the mixture is inversely proportional to the density and strength of the cementitious material [24]–[27]. Li et al. [28] evaluated the variation of the apparent density and the incorporated air content of the cement paste and mortar samples with EVA additions. They noticed that when increasing the EVA content in the cement mixtures by up to 6%, there was a decrease in the apparent density and a significant increase in the content of incorporated air. Furthermore, Li et al. [28] pointed out a direct correlation between the EVA content and the compressive strength, showing that there is a reduction in the compressive strength with the increase of the amount of EVA in the mixture. Plastic aggregates reduce the strength of concrete when compared to ordinary concrete, mainly due to the low Young's modulus of plastic materials [26]. Therefore, the deformability of the material prevents the aggregate from functioning as a rigid core, not restricting displacement in its vicinity [27]. The impact of this substitution on Young's modulus is significant, ranging from 21 to 42% at levels of substitution up to 100% [27], [29].

On the other hand, some studies point out that the presence of plastic particulates can serve as bridges in cracks, mitigating the propagation of micro cracks and contributing to the toughness of the material [2], [30]. The EVA-modified concrete, using addition of EVA powder to the concrete mix, increases the flexural and tensile strength by incorporating up to 16% of EVA powder by weight of cement [31]. Thus, despite the impact on the strength of concrete, this material can have suitable applications, such as in situations where crack opening must be controlled or in cases where the structure is subject to impact loads [30].

Brovelli et al. [32] studied the influence of EVA on the rheology of bituminous concrete, comparing it with reference cases (without EVA addition). For all investigated samples, the addition of EVA increased the yield point and the plastic viscosity of the mixture. Furthermore, Ben Fraj et al. [33] performed slump tests comparing samples of ordinary concrete and concrete with partial replacement of aggregates by polyurethane. The results showed that the increase in rheological parameters observed by Brovelli et al. [32] was translated into a significant reduction in a slump test. They attributed this behavior to the fact that polymeric aggregates are quite porous, which facilitates the process of absorbing water from the mixture and cement paste, directly affecting workability. In addition to this mechanism, Alqahtani and Zafar [1] attribute the reduction in a slump to the increase in friction between the plastic particles, which leads to less fluidity. The large surface area of the particles coupled with the lack of uniformity in the geometry of the particles causes this friction [19], [34], [35].

Finally, aiming at the use of concrete with plastic aggregate for structures supported on an elastic base, i.e. industrial floors, it is important to understand the impact of replacement on the abrasion resistance and drying shrinkage of the material. In general, most studies highlight a significant increase in drying shrinkage for replacements of up to 80% [23], [36], [37]. This increase is attributed to the low rigidity and compressibility of the plastic material, which results in a low restriction to the shrinkage deformations induced by the cement paste [36], [37]. On the other hand, in the case of abrasion, Alqahtani et al. [24] showed that the abrasion resistance of concrete with indirect replacement of aggregates showed an increase of more than 50%. Alqahtani and Zafar [1] highlighted that the low strength and roughness of the plastic aggregate, when compared to the common aggregate, was the main responsible for this increase in abrasion resistance.

Moreover, discrete synthetic fiber addition, such as polypropylene (PP), has been used primarily to reduce shrinkage effects [38]. Fibers also mitigate crack propagation and improve impact resistance, flexural and tensile strengths [39]–[41], toughness [41], [42], and abrasion resistance [43]. For use in concrete pavements, where high flexural strength is required, PP fibers contribute to reducing the concrete design thickness, and the pavement integrity remains even after the crack formation [44]–[46].

Hybrid EVA particle and PP fiber-reinforced concretes have been also addressed in the literature [47], [48]. The flexural performance of PP-EVA hybrid reinforced concrete is improved as the maximum and residual flexural strength increase up to 11% when compared to ordinary concrete, and up to 4% when compared to polypropylene fiber reinforced concrete (PP-FRC) [47]. Besides, an improvement of around 40% in the toughness can be seen in the PP-EVA hybrid reinforced concretes compared to a PP-FRC with the same fiber content [47].

Although several studies have already addressed the basic properties of concrete with the replacement of aggregates by recycled plastic aggregates and also the fiber inclusion, few works have sought to replace an existing granulometric range, and none clearly addressed the use in industrial floors, adding a fiber content consistent with the proposed field application. Knowing that the replacement directly affects the strength and elastic properties of the cementitious material, this work proposes the use of polypropylene plastic fibers as a way to improve the control of crack propagation, directly impacting the ability to absorb energy. In addition, a comparison between an industrial floor calculated using the properties of ordinary concrete is compared to the proposed material.

2 MATERIAL AND METHODS

2.1 Materials

The cement used was a Portland cement CP V ARI from the manufacturer Lafarge Holcim, which is equivalent to ASTM type III according to Natalli et al. [49]. This cement type, according to the Brazilian standard NBR 16697/18 [50], has a minimum compressive strength of 34 MPa at 7 days when mixed in a standard 1:3 mortar, and the results for the used cement batch are presented in Table 1. In addition to the mechanical characteristics, chemical tests were carried out on this batch of cement, and the results are shown in Table 2.

Table 1. Compressive tests for the batch of cement used in the research.

Tests	Mean [SD]*	Requirement**
Compressive strength 1 day (MPa)	24.5 [1.45]	≥ 14
Compressive strength 3 days (MPa)	34.4 [1.35]	≥ 24
Compressive strength 7 days (MPa)	40.5 [1.05]	≥ 34
Compressive strength 28 days (MPa)	48.8 [1.11]	not applicable

*Standard deviation. **According to NBR 16697/18

Table 2. Chemical tests for the cement batch used in the research.

Tests	Standards	Unit	Mean	Requirement*
SO_3	NM 16/12	%	3.17	≤ 4.5
IR	NM 22/04	%	1.58	≤ 1
CaO_{free}	NM 13/13	%	1.97	not applicable
MgO	NM 14/14	%	1.71	≤ 6.5

SO_3 - determination of the sulfur trioxide content in the composition. IR - the percentage of insoluble residue in the composition. CaO_{free} - determination of the free calcium oxide content in the composition. MgO - determination of the magnesium oxide content in the composition. *According to NBR 16697/18

Two coarse granite aggregates were included in the mix design: one with a maximum diameter of 9 mm and the other with 19 mm. In addition, natural quartz sand and mineral stone sand were used as fine aggregates. Natural quartz sand has a maximum characteristic dimension of 4.75 mm and a fineness modulus of 2.74, and mineral stone sand has a maximum dimension of 2.40 mm and a fineness modulus of 2.02. Therefore, both are classified as fine aggregates in the optimal zone according to NBR 7211 [51]. In addition, EVA was also used as a mixing material. The EVA used is a waste from the footwear industry in the countryside of the state of Ceará in Brazil, and it is found in a carved condition with a granulometry close to the 9 mm diameter coarse aggregate mentioned above. The granulometry of the aggregates and EVA are shown in Figure 1.

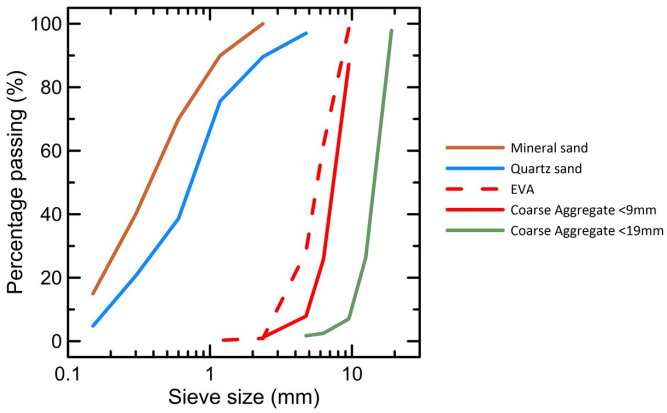

Figure 1. Aggregates granulometric distribution curve.

Although the EVA particles present a granulometric curve similar to the 9 mm coarse aggregate, their shape is quite irregular and predominantly two-dimensional, as seen in Figure 2. Therefore, evaluation of the shape of the particles with the aid of a Nikon microscope model SMZ800N and through image processing using the Image J software was done. Figure 2 shows the segmentation performed and the binary images generated for the total area of the particles analyzed, with a resolution of 1596x1064 pixels. Then, data related to the analysis of particles was obtained through the segmented image. The data obtained are summarized in Table 3.

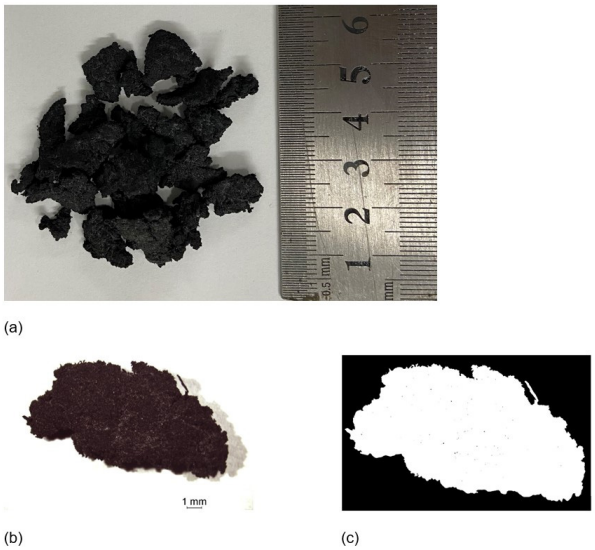

Figure 2. EVA carved particles and microscopic analysis of one EVA particle. (a) EVA carved samples, (b) image of the EVA particle obtained through a Nikon microscope model SMZ800N, and (c) binary image resulting from the segmentation.

Table 3. Summary of geometric measurements of EVA particles accessed by microscopy technique.

Particle	Total Area (mm^2)	Perimeter (mm)	Circularity
EVA 1	75.54	15.81	0.77
EVA 2	84.33	54.29	0.36
EVA 3	81.54	53.06	0.36
EVA 4	80.08	47.75	0.44
EVA 5	68.51	25.91	0.66
Mean	78.00	39.36	0.52
Standard Deviation (SD)	6.18	17.44	0.19

The results obtained from five EVA particle samples show that the EVA particles have a total area of 78 ± 6.18 mm^2, which means 46.01 ± 3.61% of the total area considering the image background. Due to the irregularity of the particles, it can be noted that the perimeter varies considerably concerning the calculated average, with values of 39.36 ± 17.44 mm, different from the low standard deviation found for the particle area values. This consideration becomes even clearer when the circularity of the particles is evaluated, which resulted in 0.52. The circularity parameter is a dimensionless measure obtained through a metric used in image processing and analysis techniques, defined by $C=4\pi \times (A/P2)$, where A is the area of the particle and P is the perimeter of the particle. The reference value of the circularity parameter is 1, representing the perfect circle. Therefore, as the value approaches 0, an increasingly elongated shape is indicated. Furthermore, an X-ray Fluorescence analysis (XRF) was performed on the EVA, and the elements and their respective amounts found are presented in Table 4.

Table 4. Composition of the EVA generated by the XRF analysis.

Composition	Content	Unit
Si	3060	ppm
Si	71.2	ppm
Cl	779.9	ppm
Ca	2.58 x 10^5	ppm
Ti	2.85 x 10^4	ppm
V	105.1	ppm
Mn	44.0	ppm
Fe	573.2	ppm
Cu	251.1	ppm
Zn	4 x 10^4	ppm
Sr	81.1	ppm
Zr	55.1	ppm
Sm	54.5	ppm

The polypropylene (PP) fibers used in this work were the 51 mm length Viapol TUF-Strand SF® with an aspect ratio of 74. The main characteristics and properties of these macro fibers are presented in Table 5. The fibers have twisted geometry, which aims to facilitate the mixing procedure, as well as improve the mechanical anchorage at the fiber-matrix interface. In addition, each fiber is the result of the union of about 3 strands grouped, giving the fiber irregular cross-sections along its length, as seen in Figure 3.

Table 5. Polypropylene fiber properties provided by the manufacturer.

Density (g/cm^3)	0.92
Length (mm)	0.51
Aspect ratio (l/d)	74
Tensile strength (MPa)	625
Modulus of elasticity (Gpa)	9.5
Fusion point (ºC)	160
Thermal and electrical conductivity	Low
Water absorption	Negligible
Resistance to alkali and acids	Excellent

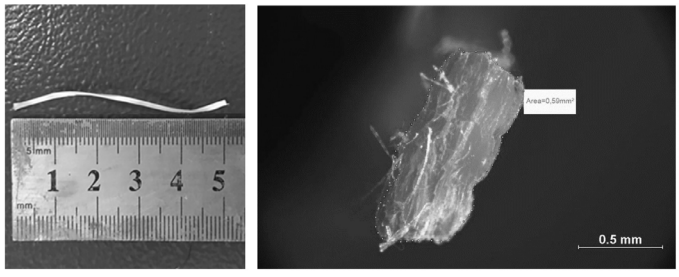

(a) (b)

Figure 3. Polypropylene fiber with 51 mm length. (a) Image presenting the PP twisted geometry and (b) Image of the PP fiber cross section obtained through a Nikon microscope model SMZ800N.

2.2 Mixing design

The dosage of the structural concrete matrix used is shown in Table 6, considering the mixture proportion of ordinary concrete (OC), concrete with the volume replacement of coarse aggregate by EVA (EVA-C), PP fiber reinforced concrete (FRC), and the concrete with replacement of coarse aggregate by EVA reinforced with PP fiber (EVA-FRC). The mixing procedure was started by adding the aggregates (quartz sand, mineral sand, coarse aggregates, and EVA) which were mixed with 70% water for one minute. Then, cement was added to the mixture and allowed to mix for another minute. The remaining water was added to the mixture with the superplasticizer chemical admixtures, which was used to give better workability to the concrete. The superplasticizer admixture used was PLASTOL® 4100, produced by the manufacturer VIAPOL, characterized as type SP-II N by the NBR 11768 standard [52]. The superplasticizer content was adjusted from the slump test following NBR NM 67 [53] before starting the specimens molding process. For the mixtures containing polypropylene (PP) fibers, a final step was added to the procedure to throw and let the fiber disperse, following the time target stated by Lima et al. [41].

Table 6. Mixture compositions of the concretes used, considering the ordinary concrete (OC), the concrete with replacement of coarse aggregate by EVA (EVA-C), PP fiber reinforced concrete (FRC), and the concrete with replacement of coarse aggregate by EVA reinforced with PP fiber.

Material type	OC	EVA-C	FRC	EVA-FRC
	kg/m³			
Cement (CPV ARI)	380	380	380	380
Quartz sand	675	675	675	675
Mineral sand	136	136	136	136
Coarse aggregate (maximum diameter 9 mm)	250	-	250	-
EVA	-	51	-	51
Coarse aggregate (maximum diameter 19 mm)	650	650	650	650
Water	190	190	190	190
Superplasticizer	1.52	1.52	1.52	1.52
Polypropylene fiber	0	0	5	5

All samples were cured in a room with controlled temperature and humidity (23°C and 100%) for 28 days before mechanical testing. On the twenty-eighth day, the specimens were removed from the curing room and taken to the specimen preparation room. Finally, on the twenty-ninth day, the mechanical tests commenced.

2.3 Density measurements

The variation of concrete density was measured by weighing cylindrical specimens measuring 10 x 20 cm. For this test, the samples destined for the compressive strength test were weighed before the destructive test. Knowing the weight and volume of the sample, the approximate apparent density of the materials was calculated. It can be seen in Table 7 that the density variation was not so significant, and this is since only the coarse aggregate with a 9 mm maximum particle size was completely replaced by the EVA aggregate. Thus, the coarse aggregate with a maximum particle size of 19 mm and the natural and mineral sands remained as constituent materials of the mixture. Therefore, in terms of weight, there is a 10% weight relief of concrete with EVA (EVA-C) compared to ordinary concrete (OC).

Table 7. Approximate apparent density for the two analyzed concretes (OC and EVA-C).

Specimen	Volume (m³)	Weight (Kg)	Density (Kg/m³)
EVA-C	0.0015	3.374 ± 0.152	2249 ± 114
OC	0.0015	3.682 ± 0.197	2455 ± 125

2.4 Mechanical tests

The experimental mechanical characterization and testing of concretes evaluated include measurement of uniaxial compressive strength and a 3-point bending test controlled by the crack mouth opening displacement. From the mechanical results obtained, it is possible to verify the application of the material developed for industrial floors, drawing a comparison between the OC and the EVA-C.

2.4.1 Uniaxial compressive strength

Uniaxial compressive strength test and Young's modulus estimation were done at 28 days, according to NBR 5739 [54] and NBR 8522 [55] standards. Cylinders of 100 mm in diameter and 200 mm in height were cast. Before this process, the molds were prepared with a release oil coat for then the concrete to be poured. Its densification was done by external vibration, initially with a rubber hammer and then on a vibrating table. After 24 hours, the specimens were demolded and taken to an environment of controlled temperature and humidity (humid chamber). Approximately 24 hours before the test, the specimens went through the process of gridding the base and the top to ensure the regularity of the surface and parallelism between the faces. It ensures that the transfer of stresses during loading is uniform.

The tests were carried out in a servo-controlled Controls testing machine model MCC8, with a load capacity of 2000 kN and a loading speed of 0.35 MPa/s. For higher precision of Young's modulus, two vertical displacement transducers (LVDT) attached to cylindrical rings were fixed around the specimen to measure the deformation, as can be seen in the scheme of Figure 4. In this way, the value of the specimen's deformation was obtained by the relation between the average value of the measured relative displacement and the initial length of reference given by the distance between the rings. Stress was calculated as the ratio between the applied load and the cross-sectional area of the specimen. Young's modulus corresponds to the slope of the initial region of the stress versus strain curve, up to approximately 30% of the maximum stress.

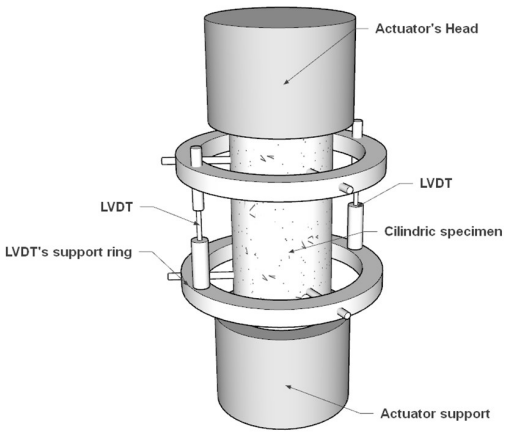

Figure 4. Uniaxial compressive strength setup detailing the cylindrical rings and LVDTs positions.

2.4.2 Three-point bending test

Three-point bending tests were performed on prismatic elements of rectangular sections, following the standard EN 14651 [56]. The dimensions of the specimens were 150 x 150 x 550 mm, with a 25 mm high notch in the central region of the lateral face of the prisms made with a 3 mm thick diamond saw. For molding the concrete samples, the mixture was carried out in a concrete mixer with a capacity of 400 l, following the procedure described in section 2.2.

To assemble the test apparatus, support rollers were first positioned. The rollers were 37 mm in diameter, with a 500 mm span, and 25 mm from the edges of the prisms. The rollers had freedom of horizontal movement, however, the left roller had also freedom of transverse movement. This freedom for horizontal displacements prevents the induction of horizontal reactions in the supports and, consequently, the appearance of an eccentric normal force in the structural element, which would cause a change in the stress distribution.

The load application roller was free to move in the transverse direction and had the same diameter as the support rollers. The load application was centered on the top face of the prism. The test equipment used was an MTS model 244.41 servo-hydraulic actuator with a 500 kN loading capacity. To control the piston displacement, a clip gauge and a flex-test 60 controller were used, resulting in a closed-loop system.

The Crack Mouth Opening Displacement (CMOD) values were obtained using an MTS clip gauge model 632.02B-20, fitted to metallic plates fixed to the specimen in the region of the notch Figure 5. The CMOD was adopted as control parameter of the test, carried out at a displacement rate of 0.05 mm/min, to a crack width of 0.1 mm, and then at a rate

of 0.2 mm/min to a crack width of 4 mm. Data were acquired at a frequency of 5 Hz. The geometry of the prismatic specimen and the test setup is shown in Figure 5.

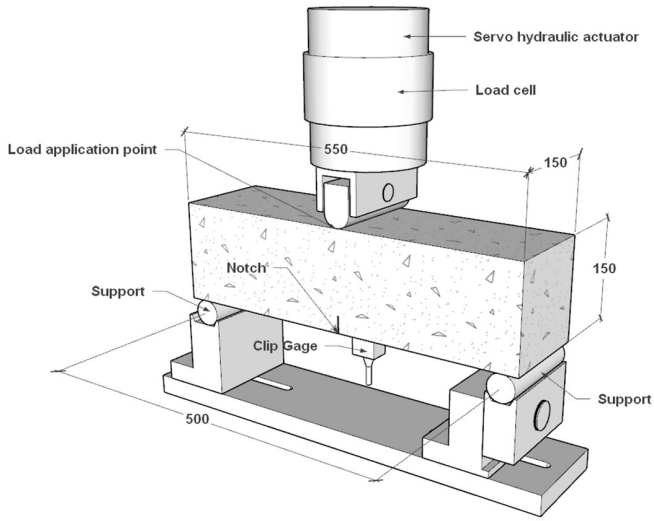

Figure 5. Flexural specimens' geometry, setup of the three-point bending test, and positioning of the clip gauge to measure the crack mouth opening displacement (CMOD).

From the test results, it is possible to plot the stress versus CMOD curves, considering the stress values obtained from Equation 1. The term P refers to the load, S to the test span, b to the width of the specimen, and h_{sp} is the distance between the top of the notch and the top face of the prism.

$$\sigma = \frac{3PS}{2bh_{sp}^{\ 2}} \tag{1}$$

The advantage of this kind of test is that, due to the presence of the notch in the central region of the specimen, the crack formation is induced to occur in an orientated way, propagating itself along cross-section. In this way, the deformation is always localized, which minimizes energy dissipation throughout the test specimen. Therefore, all the energy absorbed can be directly associated with the fracture along the notch plane and all the energy dissipated can be correlated with the response of the evaluated concrete.

Furthermore, the fib Model Code [57] recommends the determination of residual stresses $f_{R,1}$ and $f_{R,3}$. The stress $f_{R,1}$ corresponds to a crack width of 0.5 mm and is related to the serviceability limit state. On the other hand, the stress $f_{R,3}$ corresponds to a crack width of 2.5 mm and is related to the ultimate limit state. It should also be noted that, according to EN 14651 [56], two other residual stresses refer to the crack openings of 1.5 and 3.5 mm, respectively called $f_{R,2}$ and $f_{R,4}$. The last important parameter that must be obtained through the three-point bending tests is the toughness at the 4 mm crack opening ($T_{4,0}$), calculated as the area under force per CMOD curve. This parameter indicates the material's ability to absorb energy.

2.4 Drying shrinkage test

Drying shrinkage tests were performed according to ASTM C157 [58] and ASTM C490 [59] standards, in order to estimate the magnitude of the stress independent strain in the two types of concrete studied (Figure 6). Three prisms measuring 75 x 75 x 285 mm were molded for each of the mixtures. The molding was performed in the same test room, with controlled temperature and relative humidity (20 ± 1◦C and 50 ± 5%). Strain readings were taken once a day from the first measurement to 28 days of age. From then on, measurements were taken weekly.

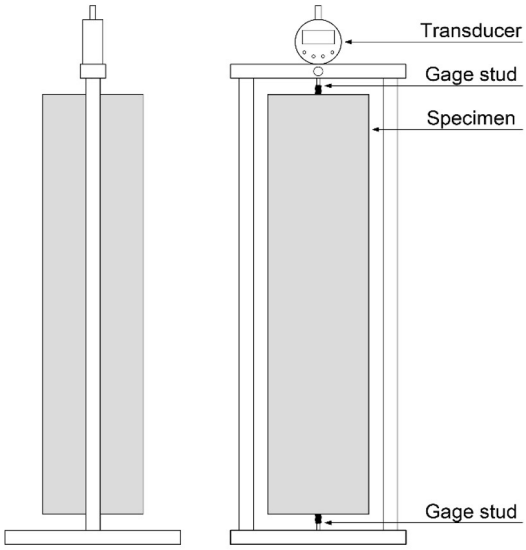

Figure 6. Drying shrinkage test setup.

2.4 Considerations for numerical approach

Since the main application of fiber-reinforced concrete is aimed at ground-supported industrial floors, we decided to make a comparison between an industrial floor designed for the conventional FRC concrete and another designed for the EVA-FRC. For this analysis, Technical Report 34 [60] was used, and only the case of internal loading was considered, not taking into account the case of loading at the borders of the floor (Figure 7).

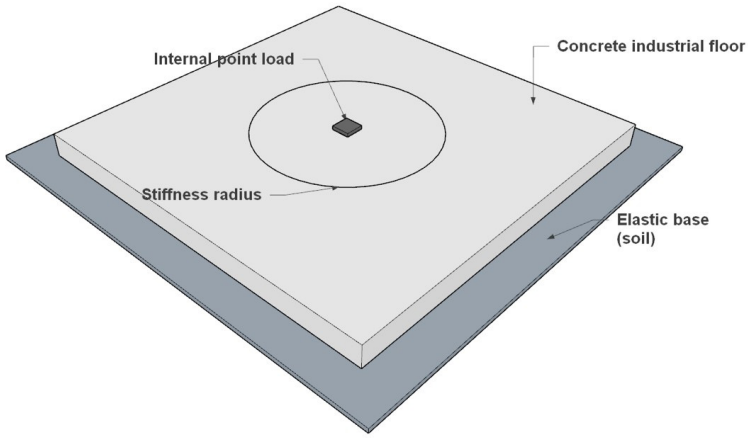

Figure 7. Schematic drawing of the type of loading used to calculate the industrial floor (internal loading) according to [60].

3 RESULTS AND DISCUSSIONS

3.1 Uniaxial compressive strength

According to the test procedure described in Section 3, uniaxial compressive strength tests were performed for ordinary concrete (OC) and concrete with total replacement of the coarse aggregate of smaller diameter by EVA (EVA-C). In addition, the inclusion of fibers was considered in this test stage, evaluating the behavior of the two concretes with the inclusion of 5 kg/m^3 of polypropylene fiber (FRC and EVA-FRC). The results of compressive strength and Young's modulus are shown in Figure 8. It is noteworthy that the results obtained correspond to the average of the results of 5 tests for each specimen group.

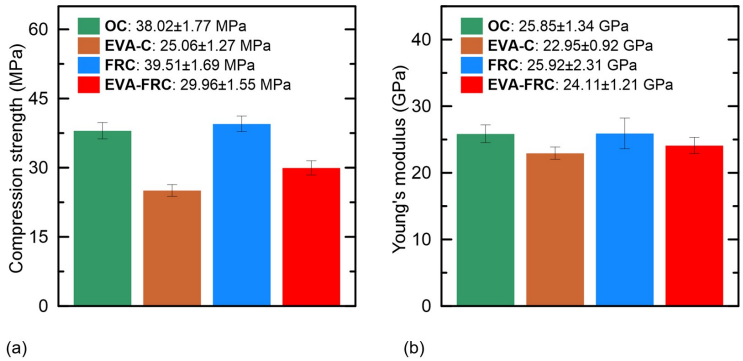

Figure 8. Uniaxial compressive strength results for the four types of concrete evaluated. (a) Maximum compressive strength and (b) Young's modulus.

In the cases of concrete with aggregate replacement by EVA (EVA-C and EVA-FRC), a drop in compressive strength was noticed when compared to the results of ordinary concrete (OC and FRC). This difference may have been caused by the reduction in the compacity of the aggregates, generating critical areas with stress concentrations in the vicinity of the EVA particles that are significantly more deformable than the conventional aggregate [2], [61]. It is known that rock aggregates help in the compaction of the material, improving cohesion and friction angle, and in cases where there are shear stresses, the aggregate helps in interlocking [62], [63]. In the case of EVA, meshing and interlocking are impaired, but an improvement in material toughness can be expected, a property that will be evaluated with bending tests.

Yang et al. [64] performed compressive strength tests on cement modified with EVA for underground gas storage, varying the percentage of EVA particle inclusion by volume (1%, 2%, 3%, and 4% EVA). The results showed that there is a decrease in the compressive strength of the samples from 3% for the addition of 1% EVA to 14% for the addition of 4% EVA. Li et al. [65] and Lima et al. [2] addressed in their studies a greater inclusion of EVA by volume, considering 10% addition and 50% replacement of aggregate respectively. Consequently, this level of inclusion of EVA in the mixture resulted in a more significant reduction in the compressive strength of the samples, reaching values about 40% and 70% lower than the reference case. In the present work, as the total replacement of only one granulometric range was carried out, the reduction of the compressive strength did not reach the same magnitude found by Lima et al. [2] for the replacement of 50% of the aggregates. Comparing OC and EVA-C the reduction of compressive strength was 33% and comparing FRC and EVA-FRC this reduction was less significant reaching 20%.

As for the fiber-reinforced concrete (FRC) specimen, the compressive strength result was higher than the conventional concrete (OC) strength, and this may have happened due to the contribution of the fibers acting as a confinement agent for the concrete, resulting in a better distribution of the applied stresses [66]. However, it is known that the fibers have little influence on the compressive and tensile strength of concrete, being quite effective in the post-peak [67]. Therefore, it is likely that this difference of 1 MPa is more correlated to the variability of the results since concrete is a heterogeneous material than to an improvement in strength.

Finally, when comparing only the EVA-FRC and EVA-C concretes, it can be seen that the fibers may be contributing to the improvement of uniaxial compressive strength. It is known that concrete with aggregates with lower Young's modulus, such as EVA, can lose the ability to mesh and interlock, starting to concentrate stress in the vicinity of the EVA [68]. Thus, the inclusion of fibers in the mixture can improve the interlocking capacity of the material, serving as a bridge for the stress transfer to the microcracks that may arise.

3.2 Three-point bending test

The efficiency of fibers as reinforcement depends mainly on interactions at the interface and includes chemical, frictional adhesion, and mechanical anchoring. Chemical adhesion corresponds to the primary adhesion of the interface, which is the result of chemical reactions from the composition of both the fibers and the matrix [38]. To evaluate the efficiency of the reinforcements with polypropylene fiber and the addition of EVA, bending tests were performed with monotonic loading as established in Section 3.

Table 8 and Table 9 present the results of the three-point bending test. For each type of concrete evaluated, three tests were carried out, with the values expressed as the final result corresponding to the average of the results obtained, followed by its standard deviation.

Table 8. Summary of three-point bending test parameters.

Specimen	P_{LOP} (KN)	σ_{LOP} (MPa)	$CMOD_{LOP}$	$f_{R,1}$ (MPa)	$f_{R,2}$ (MPa)	$f_{R,3}$ (MPa)	$f_{R,4}$ (MPa)
OC	13.07 [1.14]	4.18 [0.11]	0.034 [0.017]	-	-	-	-
EVA-C	12.65 [0.80]	4.05 [0.26]	0.049 [0.001]	1.04 [0.09]	0.34 [0.05]	0.19 [0.03]	0.12 [0.02]
FRC	14.66 [1.09]	4.22 [0.31]	0.046 [0.003]	1.47 [0.07]	1.49 [0.09]	1.49 [0.09]	1.38 [0.09]
EVA-FRC	13.88 [0.94]	4.00 [0.27]	0.044 [0.006]	1.97 [0.16]	1.94 [0.16]	1.99 [0.29]	1.98 [0.30]

P_{LOP} = load corresponding to the limit of proportionality; σ_{LOP} = stress corresponding to the limit of proportionality; $CMOD_{LOP}$ = crack opening corresponding to the limit of proportionality; $f_{R,1}$ = residual flexural strength corresponding to 0.5 mm CMOD; $f_{R,2}$ = residual flexural strength corresponding to 1.5 mm CMOD; $f_{R,3}$ = residual flexural strength corresponding to 2.5 mm CMOD; $f_{R,4}$ = residual flexural strength corresponding to 3.5 mm CMOD;

Table 9. Peak stress maintenance and toughness results.

Sample	$f_{R,1}/\sigma_{LOP}$	$f_{R,2}/\sigma_{LOP}$	$f_{R,3}/\sigma_{LOP}$	$f_{R,4}/\sigma_{LOP}$	$f_{R,3}/f_{R,1}$	$T_{4,0}$ (J)
EVA-C	0.25 [0.02]	0.08 [0.01]	0.05 [0.01]	0.03 [0.01]	0.18 [0.02]	6.63 [0.56]
FRC	0.35 [0.04]	0.35 [0.04]	0.35 [0.04]	0.33 [0.04]	1.01 [0.01]	21.5 [1.18]
EVA-FRC	0.52 [0.08]	0.53 [0.08]	0.55 [0.07]	0.55 [0.06]	1.05 [0.02]	30.24 [1.04]

$f_{R,i}/\sigma_{LOP}$ = peak stress maintenance; $T_{4,0}$ = toughness up to 4.0 mm CMOD.

As recommended by standard EN 14651 [56], the characteristic parameters of concrete were obtained from the tests carried out. Among them, proportionality limit (σ_{LOP}), that is defined as the stress corresponding to the maximum load within the crack width range from 0 to 0.05 mm. The value of the ultimate load (P_U) was also determined, being the point where the slope of the load versus the CMOD curve is null. In addition, residual stresses were obtained at pre-defined CMOD values, 0.5, 1.5, 2.5, and 3.5 mm, and toughness values were defined as the area under the load versus CMOD curves. For the toughness, the limit point considered for the calculation was the end of the test, that is, a crack opening of 4 mm.

Figure 9 and Figure 10 show the stress per CMOD and toughness per CMOD curves, respectively, of all composites evaluated. It is observed that all curves displayed a linear behavior until the appearance of the first crack, followed by a decrease in stress with increasing CMOD. This behavior is called deflection softening and is characterized by the appearance of a single crack, common in composites reinforced with discrete fibers [69]–[71]. Therefore, in all cases, the ultimate load value corresponds to the load at the proportionality limit (P_{LOP}).

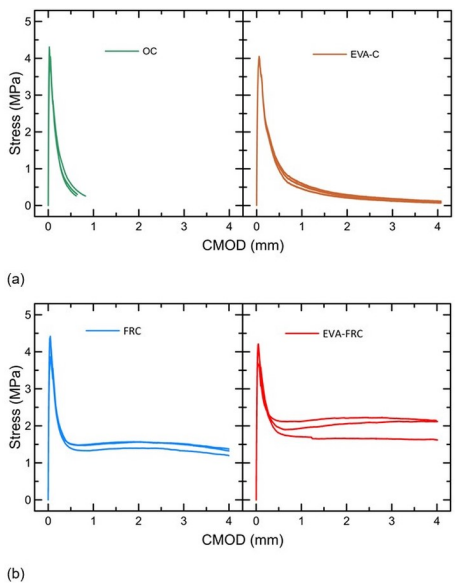

Figure 9. Stress versus CMOD graphs of the 3-point bending test for the four concretes evaluated (OC, EVA-C, FRC, and EVA-FRC). (a) Ordinary concrete and EVA concrete and (b) Fiber reinforced concretes considering the OC based and EVA based concretes as matrices.

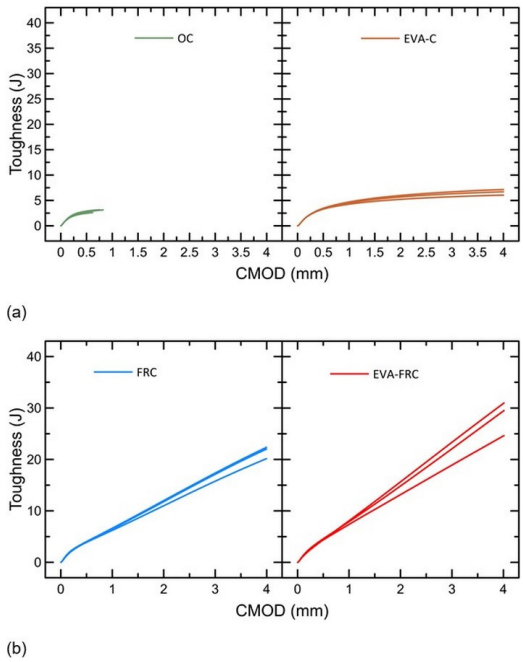

Figure 10. Toughness versus CMOD graphs of the 3-point bending test for the four concretes evaluated (OC, EVA-C, FRC, and EVA-FRC). (a) Ordinary concrete and EVA concrete and (b) Fiber reinforced concretes considering the OC based and EVA based concretes as matrices.

For all composites, the appearance of the first crack is related to the strength of the matrix and, therefore, it can be verified for OC the typical behavior of brittle material with immediate loss of strength after cracking. For FRC, after cracking, the fibers begin to absorb the tensile stresses in the cracked region, making the material behave in a pseudo-ductile manner. In the case of the three-point bending test, and considering the combinations investigated, the ultimate strength presented an average variation of 5.32% when comparing the fiber-reinforced plain concrete (FRC) and the EVA fiber-reinforced concrete (EVA-FRC).

Although the pre-cracking behavior was similar, the post-cracking behavior varied. The use of fibers improves the mechanical behavior of concrete, especially toughness and post-cracking residual strength. Table 9 presents the relationship between the residual stresses and the ultimate composite stress ($f_{R,i}/\sigma_{LOP}$), defined as relative residual strength. It is considered that the greater the value of this ratio, the greater the ability of the composite to maintain its strength after the appearance of the first crack. The evaluation of these values allows us to characterize the efficiency of the reinforcement in absorbing the stresses to which they are submitted. In the case of EVA-C, the strength capacity at serviceability state was maintained at approximately 25%. For the case of the FRC, the strength capacity observed was 35% while in the EVA-FRC it resulted in an average strength capacity of 52%. These results indicate that the addition of EVA hybridized with the addition of fibers improves the maintenance of the post-peak strength capacity for the concrete evaluated.

Another way of evaluating the influence of fibers on concrete is through the toughness, which reflects the energy absorption capacity of the material. Thus, it can be seen that both composites resulted in toughness greater than 20 J. The EVA-FRC reached a toughness resultant of about 30 J, which shows that not only the fiber but also the EVA is somehow bridging the crack opened.

4 NUMERICAL APPROACH

4.1 Fib Model Code simplified model

Using the simplified model of the fib Model Code (Figure 11) and considering that the ultimate tensile strength is defined by the residual stress $f_{R,3}$, assuming that the compressive stress resultant is applied on the extrados chord and that the tensile behavior is rigid-linear, it is possible to estimate the moment associated with this ultimate stress and calculate the contribution of EVA in terms of the resistant moment of the section. Thus, calculating the moment equivalent to the CMOD 2.5 mm ($CMOD_3$), the FRC resulted in a resistant moment of 53.90 kN.cm and the EVA-FRC

resulted in a resistant moment of 77.34 kN.cm. Therefore, EVA-FRC has a moment resistance of approximately 43.5% higher than conventional FRC, presenting by constitutive law that the EVA plays a role in bridging the fractured section.

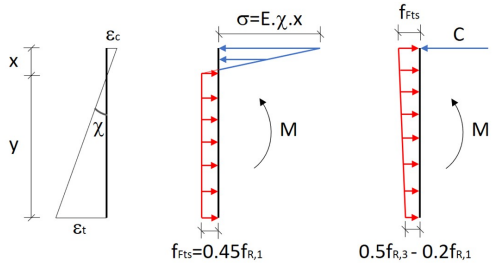

Figure 11. Fib Model Code simplified model to compute the ultimate tensile strength in uniaxial tension f_{FTu} by means of the residual nominal bending strength $f_{R,3}$ [57].

4.2 Industrial floor design based on Technical Report 34

It should be noted that the constitutive law of the material for this application differs from that described by the fib Model Code since, in this case, the structural element is supported on an elastic media (soil). In this way, Figure 12 presents the constitutive law of the material that now depends on $f_{R,1}$ and $f_{R,4}$ and no longer on $f_{R,3}$. Hence, the conservatively calculated ultimate moment can be estimated according to Equation 2.

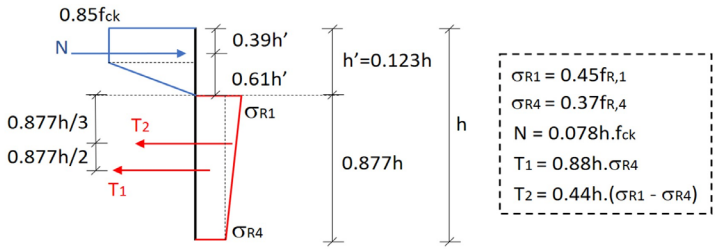

Figure 12. Fiber reinforced concrete constitutive law for ground supported floors according to Technical Report 34 [60].

$$M_u = \frac{h^2}{\gamma_m}(0.29\sigma_{r4} + 0.16\sigma_{r1}) \quad (2)$$

From the data obtained through the compressive test (compressive strength and Young's modulus) and the three-point bending test (matrix flexural strength, residual stresses, and toughness), the necessary dimension for an industrial floor was calculated using the two FRCs and considering an elastic base of 0.048 N/mm^3. As well, it should be noted that the partial safety factor for materials was applied for the ultimate limit state case ($\gamma_{m,uls}$=1.5). An isolated point load of 5 tf/pallet end support and 6 tf/axle for forklift traffic were adopted for calculation. The summary of the dimensions and degree of use (M_{calc}/M_{adm}) considering the loads adopted are shown in Table 10. The design results showed that even with lower compressive strength and a not so significant decrease in the tensile strength of the matrix in bending, the EVA-FRC achieves greater structural efficiency for an industrial floor of the same cross-sectional height (13 cm).

Table 10. Summary **table of** the efficiency of FRC and EVA-FRC applied in the design of industrial floors.

Material	Cross section height (cm)	Mcalc/Madm (pallet support)	Mcalc/Madm (forklift)
FRC	13	97%	90%
EVA-FRC	13	91%	84%

Therefore, the carved EVA is functioning as a support to the fibers in the crack bridge. This hypothesis makes sense, as the aggregates that intercept a crack tend to rupture or be completely pulled out at the moment of the matrix rupture.

In the case of carved EVA, as it is a flexible material, it may be stretched and pulled out after the appearance of the crack in the cement matrix, and thus the bending behavior of the concrete with EVA has a certain ductility, further improving the pseudo ductile behavior of fiber-reinforced concrete.

Industrial floors are subject to the stress of loads and potentially from restraint to drying shrinkage, and this combination can cause cracking [44], [45], [72]. A realistic evaluation of the combined effects of stresses induced by load and shrinkage is problematic and can produce conservative designs without significantly reducing the risk of cracking. Hence, Technical Report 34 [60] recommends an approach that does not take into account the effect of stresses induced by shrinkage, minimizing shrinkage by focusing on the design of the concrete mix, and constraining shrinkage with careful attention to the design and construction of the sub-base. In addition, Technical Report 34 [60] sets average drying shrinkage of the order of 300 μm/m – 450 μm/m. Thus, although the concrete with aggregate replacement by EVA residue presents a significant efficiency for the application on industrial floors, it must be ensured that the concrete drying shrinkage does not exceed recommendations limits.

From a drying shrinkage point of view, the main effect of the aggregate is to restrict the contraction of the cement paste, thus helping to reduce the likelihood of cracking. In general, aggregates with a higher Young's modulus, cubic shape, and rough particle surface textures tend to offer more restraint to concrete shrinkage [73]–[76]. However, the EVA used in this work has a low modulus of elasticity and an approximately two-dimensional shape, which can result in a significant increase in drying shrinkage even considering only partial replacement of the aggregates.

Therefore, drying shrinkage tests were performed according to ASTM C157 [58] and ASTM C490 [59] standards. Figure 13 shows the results of the drying shrinkage test for ordinary concrete and concrete with aggregate replacement by EVA, considering three specimens for each group tested. It can be seen from the analysis of the curves that the granular skeleton of the concrete with replacement still considerably restricts the shrinkage and, therefore, even with the presence of EVA in the composition, which is a flexible and easily deformable material, the coarse aggregate 19 mm in diameter and the fine aggregates can contain the deformation of the bulk cement paste.

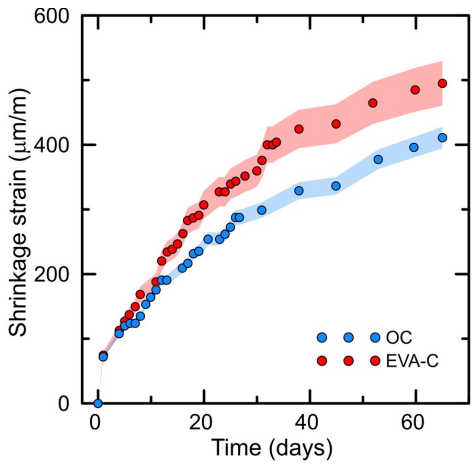

Figure 13. Schematic drawing of the type of loading used to calculate the industrial floor (internal loading) according to Technical Report 34 [60].

However, considering the shrinkage limit imposed by Technical Report 34 [60], the average shrinkage of EVA-C around 500 μm/m exceeds this limit. Therefore, aiming at the application of this material for industrial floors, chemical expander admixtures must be used in addition to the already widespread wet curing and/or chemical curing processes.

5 CURRENT STUDY LIMITATIONS AND UNCERTAINTY

From a material point of view, the residue substitution limits need to be addressed, carrying out tests with various residue contents and verifying the design of the mixture. In addition, one should seek to understand the effect of EVA replacement on the rheological properties of concrete and the possible impacts on durability, from a chemical to a mechanical point of view with creep and fatigue tests. In the case of the composite, the work presented only one type of reinforcing fiber and only one fiber volumetric fraction. These points need to be variables for future studies to

characterize the contribution of EVA particles to different fibers and different fiber contents. Finally, experimental analysis on a structural scale needs to be carried out to validate the use of this material and verify if the industrial floor design proposed in this work is valid in practice.

6 CONCLUSIONS

This paper presents valuable information on the influence of EVA particles on the mechanical properties of plain and fiber-reinforced concrete. Density, drying shrinkage, uniaxial compressive strength, and three-point bending tests were performed to draw the following conclusions:

- EVA particles have dimensions and granulometric distribution of approximately 9 mm coarse aggregates with 23% lower density.
- With the total replacement of the 9 mm stone aggregate by the EVA particles residue, lighter weight concretes (EVA-C and EVA-FRC) were produced, which showed a drop of up to 34% in compressive strength when compared to concretes without replacement of stone aggregates (OC and FRC).
- In the three-point bending tests, it can be verified that the appearance of the first crack occurred at similar strength values for all the concretes investigated. After the formation of the first crack, the concrete with the replacement of coarse aggregate by EVA (EVA-C), the fiber-reinforced plain concrete (FRC), and the EVA fiber-reinforced concrete (EVA-FRC) maintained a residual strength of about 25%, 35%, and 52% respectively indicating that the hybridization of EVA with the addition of fibers improves the maintenance of post-peak strength in the investigated concretes. Besides, the toughness values for the FRC were approximately 20 J while the toughness for the EVAFRC was approximately 30 J indicating that the addition of EVA is playing a role in bridging the crack opened.
- Applying the results obtained in the three-point bending tests for the FRC and the EVA-FRC in the design of industrial floors according to TR-34 showed that the EVAFRC presented greater structural efficiency than the FRC for a cross-section of the same height (13 cm), considering the application of internal loads. Finally, the EVA particles play an important role in supporting the fiber to bridge the cracks, as could be seen by the constitutive analysis and by the three-point bending tests. Therefore, a pullout mechanism takes place in each EVA particle from the matrix before propagating the crack, improving the behavior of the fiber-reinforced 635 plain concrete.

ACKNOWLEDGEMENTS

This study was financed in part by the Coordenação de Aperfeiçoamento de Pessoal de Nível Superior (CAPES) – Brasil – Finance Code 001, by Brazilian funding agencies FAPERJ and 640 CNPq, and by Lafarge Holcim, with the donation of cement.

CITATIONS

[1] F. K. Alqahtani and I. Zafar, "Plastic-based sustainable synthetic aggregate in Green Lightweight concrete: a review," *Constr. Build. Mater.*, vol. 292, pp. 123321, Jul 2021, http://dx.doi.org/10.1016/j.conbuildmat.2021.123321.

[2] P. R. L. Lima, M. B. Leite, and E. Q. R. Santiago, "Recycled lightweight concrete made from footwear industry waste and CDW," *Waste Manag.*, vol. 30, no. 6, pp. 1107–1113, Jun 2010, http://dx.doi.org/10.1016/j.wasman.2010.02.007.

[3] F. A. Salgado and F. A. Silva, "Recycled aggregates from construction and demolition waste towards an application on structural concrete: a review," *J. Build. Eng.*, vol. 52, pp. 104452, Jul 2022, http://dx.doi.org/10.1016/j.jobe.2022.104452.

[4] H. P. Nguyen, A. Mueller, V. T. Nguyen, and C. T. Nguyen, "Development and characterization of lightweight aggregate recycled from construction and demolition waste mixed with other industrial by-products," *Constr. Build. Mater.*, vol. 313, pp. 125472, Dec 2021, http://dx.doi.org/10.1016/j.conbuildmat.2021.125472.

[5] M. Contreras Llanes, M. Romero Pérez, M. J. Gázquez González, and J. P. Bolívar Raya, "Construction and demolition waste as recycled aggregate for environmentally friendly concrete paving," *Environ. Sci. Pollut. Res. Int.*, vol. 29, no. 7, pp. 9826–9840, Feb 2022, http://dx.doi.org/10.1007/s11356-021-15849-4.

[6] J. A. Ferriz-Papi, E. Weekes, N. Whitehead, and A. Lee, "A cost-effective recycled aggregates classification procedure for construction and demolition waste evaluation," *Constr. Build. Mater.*, vol. 324, pp. 126642, Mar 2022, http://dx.doi.org/10.1016/j.conbuildmat.2022.126642.

[7] F. G. Cunha, Z. L. M. Sampaio, and A. E. Martinelli, "Fiber-reinforced lightweight concrete formulated using multiple residues," *Constr. Build. Mater.*, vol. 308, pp. 125035, Nov 2021, http://dx.doi.org/10.1016/j.conbuildmat.2021.125035.

[8] R. Ahmmad, M. Z. Jumaat, U. J. Alengaram, S. Bahri, M. A. Rehman, and H. Hashim, "Performance evaluation of palm oil clinker as coarse aggregate in high strength lightweight concrete," *J. Clean. Prod.*, vol. 112, pp. 566–574, Jan 2016, http://dx.doi.org/10.1016/j.jclepro.2015.08.043.

[9] K. Piszcz-Karaś, M. Klein, J. Hupka, and J. Łuczak, "Utilization of shale cuttings in production of lightweight aggregates," *J. Environ. Manage.*, vol. 231, pp. 232–240, Feb 2019, http://dx.doi.org/10.1016/j.jenvman.2018.09.101.

[10] N. Dulsang, P. Kasemsiri, P. Posi, S. Hiziroglu, and P. Chindaprasirt, "Characterization of an environment friendly lightweight concrete containing ethyl vinyl acetate waste," *Mater. Des.*, vol. 96, pp. 350–356, Apr 2016, http://dx.doi.org/10.1016/j.matdes.2016.02.037.

[11] Z. L. M. Sampaio, A. E. Martinelli, and T. S. Gomes, "Formulation and characterization of structural lightweight concrete containing residues of porcelain tile polishing, tire rubber and limestone," *Ceramica*, vol. 63, no. 368, pp. 530–535, Oct 2017, http://dx.doi.org/10.1590/0366-69132017633682139.

[12] X. Yang, J. Liu, H. Li, and Q. Ren, "Performance and ITZ of pervious concrete modified by vinyl acetate and ethylene copolymer dispersible powder," *Constr. Build. Mater.*, vol. 235, pp. 117532, Feb 2020, http://dx.doi.org/10.1016/j.conbuildmat.2019.117532.

[13] A. Singh, P. V. Sampath, and K. P. Biligiri, "A review of sustainable pervious concrete systems: emphasis on clogging, material characterization, and environmental aspects," *Constr. Build. Mater.*, vol. 261, pp. 120491, Nov 2020, http://dx.doi.org/10.1016/j.conbuildmat.2020.120491.

[14] S. Saoula, K. Ait Mokhtar, S. Haddadi, and E. Ghorbel, "Improvement of the performances of modified bituminous concrete with EVA and EVA-waste," *Phys. Procedia*, vol. 2, no. 3, pp. 1319–1326, Nov 2009, http://dx.doi.org/10.1016/j.phpro.2009.11.098.

[15] S. Haddadi, E. Ghorbel, and N. Laradi, "Effects of the manufacturing process on the performances of the bituminous binders modified with EVA," *Constr. Build. Mater.*, vol. 22, no. 6, pp. 1212–1219, Jun 2008, http://dx.doi.org/10.1016/j.conbuildmat.2007.01.028.

[16] A. Noor and M. A. U. Rehman, "A mini-review on the use of plastic waste as a modifier of the bituminous mix for flexible pavement," *Clean. Mater.*, vol. 4, pp. 100059, Jun 2022, http://dx.doi.org/10.1016/j.clema.2022.100059.

[17] A. Chegenizadeh, L. Tokoni, H. Nikraz, and E. Dadras, "Effect of ethylene-vinyl acetate (EVA) on stone mastic asphalt (SMA) behaviour," *Constr. Build. Mater.*, vol. 272, pp. 121628, Feb 2021, http://dx.doi.org/10.1016/j.conbuildmat.2020.121628.

[18] P. Panyakapo and M. Panyakapo, "Reuse of thermosetting plastic waste for lightweight concrete," *Waste Manag.*, vol. 28, no. 9, pp. 1581–1588, Jan 2008, http://dx.doi.org/10.1016/j.wasman.2007.08.006.

[19] Z. Z. Ismail and E. A. AL-Hashmi, "Use of waste plastic in concrete mixture as aggregate replacement," *Waste Manag.*, vol. 28, no. 11, pp. 2041–2047, Nov 2008, http://dx.doi.org/10.1016/j.wasman.2007.08.023.

[20] A. Kan and R. Demirboğa, "A novel material for lightweight concrete production," *Cement Concr. Compos.*, vol. 31, no. 7, pp. 489–495, Aug 2009, http://dx.doi.org/10.1016/j.cemconcomp.2009.05.002.

[21] T. R. Naik, S. S. Singh, C. O. Huber, and B. S. Brodersen, "Use of post-consumer waste plastics in cement-based composites," *Cement Concr. Res.*, vol. 26, no. 10, pp. 1489–1492, Oct 1996, http://dx.doi.org/10.1016/0008-8846(96)00135-4.

[22] B. W. Jo, S. K. Park, and J. C. Park, "Mechanical properties of polymer concrete made with recycled PET and recycled concrete aggregates," *Constr. Build. Mater.*, vol. 22, no. 12, pp. 2281–2291, Dec 2008, http://dx.doi.org/10.1016/j.conbuildmat.2007.10.009.

[23] S. C. Kou, G. Lee, C. S. Poon, and W. L. Lai, "Properties of lightweight aggregate concrete prepared with PVC granules derived from scraped PVC pipes," *Waste Manag.*, vol. 29, no. 2, pp. 621–628, Feb 2009, http://dx.doi.org/10.1016/j.wasman.2008.06.014.

[24] F. K. Alqahtani, G. Ghataora, S. Dirar, M. I. Khan, and I. Zafar, "Experimental study to investigate the engineering and durability performance of concrete using synthetic aggregates," *Constr. Build. Mater.*, vol. 173, pp. 350–358, Jun 2018, http://dx.doi.org/10.1016/j.conbuildmat.2018.04.018.

[25] F. K. Alqahtani, G. Ghataora, M. I. Khan, and S. Dirar, "Novel lightweight concrete containing manufactured plastic aggregate," *Constr. Build. Mater.*, vol. 148, pp. 386–397, Sep 2017, http://dx.doi.org/10.1016/j.conbuildmat.2017.05.011.

[26] Y. W. Choi, D. J. Moon, J. S. Chung, and S. K. Cho, "Effects of waste PET bottles aggregate on the properties of concrete," *Cement Concr. Res.*, vol. 35, no. 4, pp. 776–781, Apr 2005, http://dx.doi.org/10.1016/j.cemconres.2004.05.014.

[27] D. C. Jansen et al., "Lightweight fly ash-plastic aggregates in concrete," *Transp. Res. Rec.*, vol. 1775, no. 1, pp. 44–52, Jan 2001, http://dx.doi.org/10.3141/1775-07.

[28] H. Li et al., "Improvements in setting behavior and strengths of cement paste/mortar with EVA redispersible powder using C-S-Hs-PCE," *Constr. Build. Mater.*, vol. 262, pp. 120097, Nov 2020, http://dx.doi.org/10.1016/j.conbuildmat.2020.120097.

[29] Y. W. Choi, D. J. Moon, Y. J. Kim, and M. Lachemi, "Characteristics of mortar and concrete containing fine aggregate manufactured from recycled waste polyethylene terephthalate bottles," *Constr. Build. Mater.*, vol. 23, no. 8, pp. 2829–2835, Aug 2009, http://dx.doi.org/10.1016/j.conbuildmat.2009.02.036.

[30] G. Sang, Y. Zhu, and G. Yang, "Mechanical properties of high porosity cement-based foam materials modified by EVA," *Constr. Build. Mater.*, vol. 112, pp. 648–653, Jun 2016, http://dx.doi.org/10.1016/j.conbuildmat.2016.02.145.

[31] K. A. Khan, I. Ahmad, and M. Alam, "Effect of Ethylene Vinyl Acetate (EVA) on the setting time of cement at different temperatures as well as on the mechanical strength of concrete," *Arab. J. Sci. Eng.*, vol. 44, no. 5, pp. 4075–4084, 2019, http://dx.doi.org/10.1007/s13369-018-3249-4.

[32] C. Brovelli, L. Hilliou, Y. Hemar, J. Pais, P. Pereira, and M. Crispino, "Rheological characteristics of EVA modified bitumen and their correlations with bitumen concrete properties," *Constr. Build. Mater.*, vol. 48, pp. 1202–1208, Nov 2013, http://dx.doi.org/10.1016/j.conbuildmat.2013.07.032.

[33] A. Ben Fraj, M. Kismi, and P. Mounanga, "Valorization of coarse rigid polyurethane foam waste in lightweight aggregate concrete," *Constr. Build. Mater.*, vol. 24, no. 6, pp. 1069–1077, Jun 2010, http://dx.doi.org/10.1016/j.conbuildmat.2009.11.010.

[34] E. Rahmani, M. Dehestani, M. H. A. Beygi, H. Allahyari, and I. M. Nikbin, "On the mechanical properties of concrete containing waste PET particles," *Constr. Build. Mater.*, vol. 47, pp. 1302–1308, Oct 2013, http://dx.doi.org/10.1016/j.conbuildmat.2013.06.041.

[35] M. Batayneh, I. Marie, and I. Asi, "Use of selected waste materials in concrete mixes," *Waste Manag.*, vol. 27, no. 12, pp. 1870–1876, Jan 2007, http://dx.doi.org/10.1016/j.wasman.2006.07.026.

[36] W. C. Tang, Y. Lo, and A. Nadeem, "Mechanical and drying shrinkage properties of structural-graded polystyrene aggregate concrete," *Cement Concr. Compos.*, vol. 30, no. 5, pp. 403–409, May 2008, http://dx.doi.org/10.1016/j.cemconcomp.2008.01.002.

[37] B. Chen and J. Liu, "Properties of lightweight expanded polystyrene concrete reinforced with steel fiber," *Cement Concr. Res.*, vol. 34, no. 7, pp. 1259–1263, Jul 2004, http://dx.doi.org/10.1016/j.cemconres.2003.12.014.

[38] A. Bentur and S. Mindess, *Fibre Reinforced Cementitious Composites.* London: Taylor & Francis, 2007.

[39] R. Jain, R. Gupta, M. Khare, and D. Ashish, "Use of polypropylene fiber reinforced concrete as a construction material for rigid pavements," *Indian Concr. J.*, vol. 85, pp. 45–53, Mar 2011.

[40] J. Roesler, S. Altoubat, D. Lange, K.-A. Rieder, and G. Ulreich, "Effect of synthetic fibers on structural behavior of concrete slabs on ground," *ACI Mater. J.*, vol. 103, pp. 3, Jan 2006.

[41] V. N. Lima, D. C. T. Cardoso, and F. A. Silva, “Creep mechanisms in precracked polypropylene and steel fiber–reinforced concrete,” *J. Mater. Civ. Eng.*, vol. 33, no. 8, pp. 04021187, May 2021, http://dx.doi.org/10.1061/(ASCE)MT.1943-5533.0003775.

[42] D. T. C. Madhavi, L. S. Raju, and D. Mathur, "Polypropylene fiber reinforced concrete," *RE:view*, 2014.

[43] O. Ozturk and N. Ozyurt, "Sustainability and cost-effectiveness of steel and polypropylene fiber reinforced concrete pavement mixtures," *J. Clean. Prod.*, vol. 363, pp. 132582, Aug 2022, http://dx.doi.org/10.1016/j.jclepro.2022.132582.

[44] F. R. Souza, “Concreto reforçado com fibras de PVA aplicado a pavimentos aeroportuários: propriedades mecânicas e dimensionamento,” Ph.D. dissertation, Pontif. Univ. Catol. Rio de Janeiro, Rio de Janeiro, 2021.

[45] R. P. Manfredi, “Dimensionamento de compósitos cimentícios reforçados com fibras de aço,” M.S. thesis, Pontif. Univ. Catol. Rio de Janeiro, Rio de Janeiro, 2020.

[46] B. Ali, L. A. Qureshi, and R. Kurda, "Environmental and economic benefits of steel, glass, and polypropylene fiber reinforced cement composite application in jointed plain concrete pavement," *Compos. Commun.*, vol. 22, pp. 100437, 2020, http://dx.doi.org/10.1016/j.coco.2020.100437.

[47] C. Y. Sung and K. S. Nam, "Flexural performance of polypropylene fiber reinforced EVA concrete," *J. Korean Soc. Agric. Eng.*, vol. 58, no. 2, pp. 83–90, Mar 2016, http://dx.doi.org/10.5389/KSAE.2016.58.2.083.

[48] K. S. Nam and C. Y. Sung, "The compressive strength and durability properties of polypropylene fiber reinforced EVA concrete," *J. Korean Soc. Agric. Eng.*, vol. 57, no. 4, pp. 11–19, Jul 2015, http://dx.doi.org/10.5389/KSAE.2015.57.4.011.

[49] J. F. Natalli, E. C. S. Thomaz, J. C. Mendes, and R. A. F. Peixoto, "A review on the evolution of Portland cement and chemical admixtures in Brazil," *Rev. IBRACON Estrut. Mater.*, vol. 14, no. 6, pp. 14603, 2021, http://dx.doi.org/10.1590/s1983-41952021000600003.

[50] Associação Brasileira de Normas Técnicas, *Cimento Portland – Requisitos*, ABNT NBR 16697, 2018.

[51] Associação Brasileira de Normas Técnicas, *Agregados para Concreto*, ABNT NBR 7211, 2005.

[52] Associação Brasileira de Normas Técnicas, *Aditivos para Concreto de Cimento Portland*, ABNT NBR 11768, 1992.

[53] Associação Brasileira de Normas Técnicas, *Concreto – Determinação da Consistência pelo Abatimento do Tronco de Cone*, ABNT NBR NM 67, 1998.

[54] Associação Brasileira de Normas Técnicas, *Concreto – Ensaio de Compressão de Corpos de Prova Cilíndricos, ABNT NBR 5739*, 2007.

[55] Associação Brasileira de Normas Técnicas, *Concreto – Determinação do Módulo Estático de Elasticidade à Compressão*, ABNT NBR 8522, 2008.

[56] European Standard, *Test Method for Metallic Fibered Concrete – Measuring the Flexural Tensile Strength (Limit of Proportionality (LOP), Residual)*, EN 14651, 2005.

[57] fib, *fib Model Code.* Switzerland, 2010.

[58] American Society for Testing and Materials, *Standard Test Method for Length Change of Hardened Hydraulic-Cement Mortar and Concrete*, ASTM C157, 2017.

[59] American Society for Testing and Materials, *Standard Practice for Use of Apparatus for the Determination of Length Change of Hardened Cement Paste, Mortar, and Concrete BT - Standard Practice for Use of Apparatus for the Determination of Length Change of Hardened Cement Paste, Mortar, and Concrete*, ASTM C490, 2017.

[60] The Concrete Society, *Concrete Industrial Ground Floor Slabs: a Guide to Their Design and Construction* (Technical Report 34). Berkshire, 2013.

[61] L. R. Brancher, M. Nunes, A. Grisa, D. Pagnussat, and M. Zeni, "Acoustic behavior of subfloor lightweight mortars containing micronized poly (Ethylene Vinyl Acetate) (EVA)," *Materials*, vol. 9, no. 1, pp. 51, Jan 2016, http://dx.doi.org/10.3390/ma9010051.

[62] W. Shen, R. Dong, J. Li, M. Zhou, W. Ma, and J. Zha, "Experimental investigation on aggregate interlocking concrete prepared with scattering–filling coarse aggregate process," *Constr. Build. Mater.*, vol. 24, no. 11, pp. 2312–2316, Nov 2010, http://dx.doi.org/10.1016/j.conbuildmat.2010.04.023.

[63] M. Pundir, M. Tirassa, M. Fernández Ruiz, A. Muttoni, and G. Anciaux, "Review of fundamental assumptions of the Two-Phase model for aggregate interlocking in cracked concrete using numerical methods and experimental evidence," *Cement Concr. Res.*, vol. 125, pp. 105855, Nov 2019, http://dx.doi.org/10.1016/j.cemconres.2019.105855.

[64] Y. Yang, B. Yuan, Q. Sun, X. Tang, and X. Yingquan, "Mechanical properties of EVA-modified cement for underground gas storage," *J. Nat. Gas Sci. Eng.*, vol. 27, pp. 1846–1851, Nov 2015, http://dx.doi.org/10.1016/j.jngse.2015.11.013.

[65] H. Li et al., "Influence of defoaming agents on mechanical performances and pore characteristics of Portland cement paste/mortar in presence of EVA dispersible powder," *J. Build. Eng.*, vol. 41, pp. 102780, Sep 2021, http://dx.doi.org/10.1016/j.jobe.2021.102780.

[66] V. N. Lima, “Fluência e propriedades mecânicas de compósitos cimentícios reforçados com fibra de aço e polipropileno,” Ph.D. dissertation, Pontif. Univ. Catol. Rio de Janeiro, Rio de Janeiro, 2019.

[67] P. D. Nieuwoudt, “Time-dependent behaviour of cracked steel fibre reinforced concrete: from single fibre level to macroscopic level,” M.S. thesis, Stellenbosch Univ., Stellenbosch, 2016.

[68] J. Brito and N. Saikia, "Recycled aggregate in concrete: use of industrial, construction and demolition waste," *Green Energy Technol.*, vol. 54, 2013, http://dx.doi.org/10.1007/978-1-4471-4540-0.

[69] S. Yin, R. Tuladhar, T. Collister, M. Combe, N. Sivakugan, and Z. Deng, "Post-cracking performance of recycled polypropylene fibre in concrete," *Constr. Build. Mater.*, vol. 101, pp. 1069–1077, Dec 2015, http://dx.doi.org/10.1016/j.conbuildmat.2015.10.056.

[70] R. S. Castoldi, L. M. S. Souza, and F. A. Silva, "Comparative study on the mechanical behavior and durability of polypropylene and sisal fiber reinforced concretes," *Constr. Build. Mater.*, vol. 211, pp. 617–628, Jun 2019, http://dx.doi.org/10.1016/j.conbuildmat.2019.03.282.

[71] V. N. Lima, D. C. T. Cardoso, and F. A. Silva, “Flexural creep behavior of steel and polypropylene fiber reinforced concrete,” in *Proc. 10th Int. Conf. Fract. Mech. Concr. Concr. Struct.*, 2019, http://dx.doi.org/10.21012/FC10.234778.

[72] R. P. Manfredi, F. A. Silva, and D. C. T. Cardoso, "On punching shear strength of steel fiber-reinforced concrete slabs-on-ground," *ACI Struct. J.*, vol. 119, no. 4, pp. 185–196, Jul 2022, http://dx.doi.org/10.14359/51734520.

[73] T. Fujiwara, "Effect of aggregate on drying shrinkage of concrete," *J. Adv. Concr. Technol.*, vol. 6, no. 1, pp. 31–44, Feb 2008, http://dx.doi.org/10.3151/jact.6.31.

[74] A. K. H. Kwan, W. W. S. Fung, and H. H. C. Wong, "Reducing drying shrinkage of concrete by treatment of aggregate," *Mag. Concr. Res.*, vol. 62, no. 6, pp. 435–442, May 2010, http://dx.doi.org/10.1680/macr.2010.62.6.435.

[75] S. Ismail and M. Ramli, "Mechanical strength and drying shrinkage properties of concrete containing treated coarse recycled concrete aggregates," *Constr. Build. Mater.*, vol. 68, pp. 726–739, Oct 2014, http://dx.doi.org/10.1016/j.conbuildmat.2014.06.058.

[76] M. E. Karaguler and M. S. Yatagan, "Effect of aggregate size on the restrained shrinkage of the concrete and mortar," *MOJ Civ. Eng.*, vol. 4, no. 1, pp. 15–21, Jan 2018, http://dx.doi.org/10.15406/mojce.2018.04.00092.

Author contributions: INL, FRS, FPT: data curation, methodology, formal analysis; VNL: conceptualization, data curation, formal analysis, methodology, writing original draft; MIBR, FAS: conceptualization, funding acquisition, supervision.

Editors: Diogo Ribeiro, Guilherme Aris Parsekian.

IBRACON Structures and Materials Journal
Revista IBRACON de Estruturas e Materiais
ISSN 1983-4195 ismj.org

ORIGINAL ARTICLE

Ultrasound monitoring of setting behavior of concrete mixtures

Monitoramento do período de pega de misturas de concreto com ultrassom

Hella Fernanda Giehl Bressan[a]
Felipe Carraro[a]
Roberto Caldas de Andrade Pinto[a]

[a]Universidade Federal de Santa Catarina, Departamento de Engenharia Civil, Florianópolis, SC, Brasil

Received 12 September 2022
Accepted 15 February 2023

Abstract: The setting behavior of concrete mixtures can be indirectly monitored by the penetration resistance test given by ASTM C 403. Arbitrary values of penetration resistance are associated to the initial and final set times. This test is carried out on the previously sieved mortar portion of the concrete mixture, which makes its practical use rare. Alternatively, ultrasound testing can be used to characterize this transition period, since the propagation of ultrasonic waves is greatly affected by the formation of cement hydration products and the extent of microstructure development. In this research, the propagation of ultrasonic waves in fresh concrete during the setting period was studied. In addition to the ultrasonic pulse velocity (UPV), other ultrasonic parameters such as group velocity, parameters related to ultrasonic energy and frequency were monitored during the setting period of various concrete mixes. It was observed that as setting progressed, there was a greater ease of ultrasonic transmission with a continuous increase of wave amplitudes. The results indicated that a combined analysis of the time domain parameters of UPV, group velocity and the time that 10% of energy has propagated (t_{10}) could be used to improve the characterization of the microstructure development regarding the setting behavior of concrete mixtures.

Keywords: fresh concrete, setting time, ultrasonic wave propagation, ultrasonic waveform parameters, equivalent ages.

Resumo: O período de pega do concreto pode ser monitorado indiretamente pelo teste de resistência à penetração fornecido pela ASTM C 403. Valores arbitrários de resistência à penetração são associados aos tempos de início e fim de pega. Este ensaio é realizado na porção de argamassa previamente peneirada da mistura de concreto, o que torna rara sua utilização prática. Alternativamente, o teste de ultrassom pode ser empregado para caracterizar esse período de transição, uma vez que a propagação das ondas ultrassônicas é grandemente afetada pela formação dos produtos de hidratação do cimento e pela extensão do desenvolvimento da microestrutura. Nesta pesquisa, estudou-se a propagação de ondas ultrassônicas no concreto fresco durante o período de pega. Além da velocidade do pulso ultrassônico (UPV), outros parâmetros ultrassônicos, como velocidade de grupo, parâmetros relacionados à energia ultrassônica e frequência, foram monitorados durante o período de pega de várias misturas de concreto. Observou-se uma maior facilidade de transmissão ultrassônica com aumento contínuo das amplitudes das ondas durante o período de pega. Os resultados indicaram que uma análise combinada dos parâmetros no domínio de tempo como UPV, velocidade de grupo e tempo de propagação de 10% da energia (t_{10}) poderia ser utilizada para melhorar a caracterização do desenvolvimento da microestrutura em relação ao comportamento de pega de misturas de concreto.

Palavras-chave: concreto fresco, tempo de pega, propagação de ondas ultrassônicas, parâmetros do formato de ondas ultrassônicas, idade equivalente.

How to cite: H. F. G. Bressan, F. Carraro, and R. C. A. Pinto, "Ultrasound monitoring of setting behavior of concrete mixtures," *Rev. IBRACON Estrut. Mater.*, vol. 16, no. 6, e16608, 2023, https://doi.org/10.1590/S1983-41952023000600008

Corresponding author: Roberto Caldas de Andrade Pinto. E-mail: r.pinto@ufsc.br
Financial support: This study was financed in part by the Coordenação de Aperfeiçoamento de Pessoal de Nível Superior – Brasil (CAPES) – Finance Code 001.
Conflict of interest: Nothing to declare.
Data Availability: the data that support the findings of this study are openly available in Repositório Institucional - UFSC at https://repositorio.ufsc.br/handle/123456789/211574.

1 INTRODUCTION

Concrete, like other cement-based products, is a material that undergoes a gradual and progressive transformation over time. Cementitious compositions in their initial stages are plastic and workable while at later stages they become rigid structures. Concrete´s transition period from a liquid to a brittle solid is commonly called as the setting period. This stiffening process depends on the development of the concrete microstructure, which will be the main agent responsible for the desirable mechanical properties required in civil engineering projects.

The setting phase begins with the total loss of plasticity and workability of the material; setting ends with the beginning of the C_3S hydration, one of the principal chemical compounds of cement. The method to determine initial and final setting times of a concrete mixture is based on the penetration resistance of its mortar portion. ASTM C403 [1] indicates the initial setting time of concrete as the time required for the sieved mortar to reach a penetration resistance of 3.5 MPa, while final setting time is established when the penetration resistance reaches 27.6 MPa. However, the initial and final setting times obtained using this method are considered purely reference points, since it is not possible to correlate the results of penetration resistance measurements with the development of the material's microstructure. These times do not represent a specific change in the physical-chemical characteristics of the cement paste.

Instead, as shown by Abel et al. [2], the setting times given by the penetration resistance method are related to the time when the concrete mixture becomes unworkable (achieves zero-slump), and to the time at which carefully handled concrete specimens can be broken in compression. Reaching final set, as indicated by the ASTM method, does not indicate that concrete has become a solid material, but simply that concrete can no longer be evaluated by this test. Moreover, in order to determine the setting times by means of this method, it is necessary to sieve the concrete in order to remove the mortar portion, which makes this method unusual in practice.

On the other hand, changes in the concrete microstructure during setting of the concrete also alter other properties of the material, in addition to its penetration resistance. The use of a non-destructive test method, such as the ultrasound directly on the concrete mixture, and not on its mortar portion, allows for real-time monitoring of the development of the microstructure.

Changes in the ultrasonic waveforms are associated with physical changes in the material's microstructure [3]. Although the main parameter obtained in the ultrasonic test is the Ultrasonic Pulse Velocity (UPV), other parameters associated with the waveform can be determined by considering the entire behavior of the ultrasonic pulse. These parameters may be more sensitive and efficient in the characterization of the tested material.

The stiffening of the mixture not only allows stress waves to propagate more quickly, but also that less wave attenuation occurs. A typically ultrasonic waveform is shown in Figure 1. The UPV is obtained by measuring the elapsed propagation time between two transducers placed at a known distance. Alternatively, one could calculate the group velocity as the velocity with which the major part of the energy propagates. It can be calculated from the waveform signal by recording the time at maximum amplitude [4].

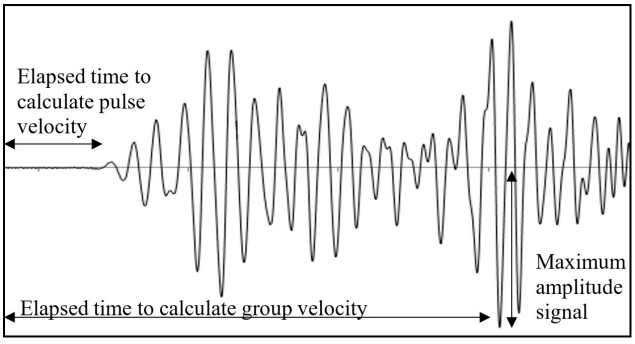

Figure 1. Typical ultrasonic waveform

The quantification of the energy of the ultrasonic signal can be adopted as the area under the rectified signal of the wave envelope according to Equation 1, with t_f being the end of the time window defined in the experiment and $A(t)$ the amplitudes of the signal as a function of time [5].

$$E = \int_0^{t_f} |A(t)|\, dt \tag{1}$$

Shiotani and Aggelis [4] using Equation 1, showed that the accumulated energy curve underwent a decrease in its initial inclination with an increase of small plastic inclusions in mortar specimens. Contents of 1%, 5% and 10% in total mortar volume were used to simulate materials with different levels of internal damage. Even though this finding was related to damaged materials, this approach can also be applied to different levels of homogeneity achieved during setting.

This potential delay of energy arrivals can be described by the time that a certain small percentage of the accumulated energy arrived. In this study, the time at which 10% and 25% of total energy has propagated (t_{10} and t_{25}, respectively) was explored, as given by Equation 2 and Equation 3.

$$10\% = \frac{\int_0^{t_{10}} |A(t)| dt}{\int_0^{t_f} |A(t)| dt} \tag{2}$$

$$25\% = \frac{\int_0^{t_{25}} |A(t)| dt}{\int_0^{t_f} |A(t)| dt} \tag{3}$$

In addition, the ultrasonic signal can also be analyzed in the frequency domain, through a Fast Fourier Transform (FFT) yielding frequency-related parameters, such as the peak frequency and center frequency. The former is defined as the frequency value corresponding to the largest amplitude in the frequency spectrum, while the latter is defined as the centroid of the frequency spectrum, according to Equation 4.

$$C = \frac{\int_0^y f\, M(f) df}{\int_0^y M(f) df} \tag{4}$$

where C = center frequency (kHz); f = frequency (kHz); $M(f)$ = frequency magnitude; y = frequency limit.

This research explores other stress wave parameters besides UPV, such as group velocity, energy and frequency associated parameters to characterize setting of concrete mixtures. Concrete mixtures with varying water-cement ratios were produced in laboratory. Their initial and final setting times were determined by ASTM C403 [1]. The evolution of ultrasonic parameters during these early ages was monitored. The results indicate a clear sensibility between wave parameters and the development of setting of concrete mixtures.

2 MATERIALS AND METHODS

Six concrete mixtures were produced in the laboratory. Concrete mixture proportions are presented in Table 1. The paste content and the mortar content were kept constant at 32% and at 55% for all mixtures, respectively. The fine aggregates consisted of a mixture of 70% of granite rock crushing sand with a fineness modulus of 2.84, and 30% natural sand with fineness modulus of 0.58. A granite coarse aggregate with maximum aggregate size of 19 mm, and a Brazilian early-strength cement CPV-ARI, similar to ASTM Type III cement, were used. The addition of a polycarboxylate-based superplasticizer was necessary in different amounts to achieve a slump of 150 ± 10 mm for all concrete mixtures.

Table 1. Concrete mixtures proportions (kg/m^3)

Mixture	w/c	Cement	Manufactured sand	Natural sand	Coarse aggregate	Water	Admixture
C40	0.40	445	575	243	980	178	1.65
C45	0.45	416	583	246	969	187	1.28
C50	0.50	391	590	249	959	195	0.98
C55	0.55	368	596	251	951	203	0.61
C60	0.60	348	601	254	943	209	0.21
C65	0.65	330	606	256	936	215	-

For each concrete mixture, three mortar cylinder samples of 150 mm x 150 mm and one concrete cube sample of 200 mm x 200 mm x 200 mm were cast. The mortar samples were used to evaluate the penetration resistance according to ASTM C403 [1], while the concrete sample was employed for ultrasound testing.

Thus, freshly prepared concrete was sieved with a 4.75 mm opening sieve and the resulting mortar placed in the cylindrical molds. Penetration resistance readings were performed using a Proctor equipment, with standard needles of different cross section areas. The penetration resistance was determined by the pressure required to penetrate 25 mm over 10 seconds. The initial and final setting times were determined as the times when the penetration resistance reached 3.5 MPa and 27.6 MPa, respectively. Mortar temperatures were monitored by thermocouples immersed in the samples.

The ultrasound measurements were performed with a commercially available equipment using 54 kHz frequency transducers at an acquisition frequency of 2 MHz. A layer of an acoustic coupler was applied between the transducers and the concrete sample. For each mixture, ultrasonic monitoring started immediately after the concrete cubic sample has been cast and ended two hours after final set given by the penetration resistance test. Mortar penetration resistance and concrete ultrasonic measurements were performed simultaneously.

The apparatus used for ultrasonic testing in fresh concrete was developed by Irrigaray [6]. It consists of an external structure in plywood with circular openings, centered on opposite faces that serve as a guide for placing the transducers. The apparatus was filled with fresh concrete in two layers of equal height (approximately 100 mm). Each layer was manually consolidated by applying 20 strokes with a metallic rod. Any internal void was eliminated with light strokes on the external face of the apparatus. Thermocouples at mid-height were embedded in the sample in order to monitor concrete temperature during ultrasonic monitoring.

Ultrasonic waveforms were acquired at a five-minute interval. Initially, ultrasonic signal de-noising was performed by a filtering algorithm developed in the Matlab® software. A low-pass filter was applied to the frequency-domain data. Then, from the filtered ultrasonic signals, UPV, group velocity, t_{10} and t_{25} were determined, as well as the peak frequency and the central frequency, for each acquired waveform.

The concrete mixtures were prepared on different days, at different environmental temperature conditions. Although they were placed in a controlled temperature environment, the specimens underwent different temperature evolutions. Therefore, the maturity method was used to take into account the influence of the different concrete and mortar temperatures.

The Freiesleben-Hansen and Pedersen Maturity Function (FHP) was used, as indicated by ASTM C1074 [7]. Regarding the apparent activation energy value, a value of 30 kJ/mol was applied. This value lies between the values presented by Pinto and Schindler [8] and Carette and Staquet [9] for the activation energy during the setting period. Equation 5 presents the FHP function for calculating the equivalent age at a reference temperature of 20ºC.

$$t_e = \sum_0^t exp\left[\frac{-E_a}{R}\left(\frac{1}{T+273} - \frac{1}{293}\right)\right]\Delta t \tag{5}$$

where t_e – equivalent age at a 20ºC; E_a – apparent activation energy (30000 J/mol); R – universal gas constant (8.314 J/mol/K); T – concrete or mortar temperature (ºC); Δt – time interval.

Thus, the initial and final setting times obtained by the penetration resistance test, as well as the elapsed times of each waveform acquired in the concrete cube, were transformed into equivalent ages according to Equation 5, using the temperature values given by the thermocouples.

3 RESULTS AND DISCUSSION

3.1 Penetrations Resistance Test

Table 2 shows the initial and final setting times for each concrete mixture. The results represent the average of the values obtained at each cylinder specimen. Figure 2 shows the temperature history, as well as the initial and final setting times for each mixture.

Table 2. Initial setting time, final setting time and setting duration per mixture

Mixture	Initial setting (min.)	Final setting (min.)	Setting duration (min.)
C40	286	378	92
C45	270	355	85
C50	326	420	94
C55	294	378	84
C60	288	363	75
C65	295	380	85

Although there were observed differences in setting times, it can be noticed, from Figure 2, that the initial set generally occurred when the generation of hydration heat began, and the mortar temperature started to increase. The temperatures continued to increase after final set for all mixtures.

The temperature of the concrete cubes was always higher than that of the mortar cylinders. Thus, the evolution of the concrete cube microstructure could not be directly related to the setting times obtained in the mortar cylinders. Temperature influences the rate of cement hydration; a higher rate of cement hydration is expected at high temperatures. Therefore, the initial and final setting times obtained by the mortar penetration resistance test did not correspond directly to the setting times of the concrete sample. Setting in the concrete sample should have occurred earlier than setting given by the penetration resistance test, due to higher concrete temperatures.

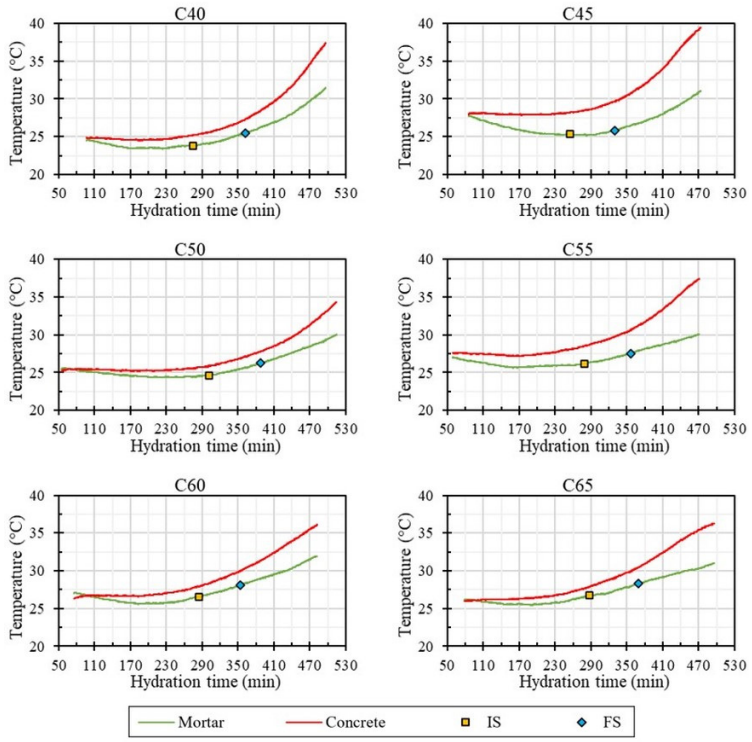

Figure 2. Temperature evolution of all mixtures

In order to account for such differences in temperatures, the maturity method was used to correlate the behavior of the concrete ultrasonic parameters during setting with the times given by the mortar penetration resistance method. Initially, Equation 5 was applied together with the temperature history of the mortar specimens (Figure 2) to transform actual initial and final setting times given in Table 2 in equivalent ages. The resultant equivalent ages at initial and final setting times are presented in Table 3. With the equivalent ages calculated, Equation 5 was again applied considering the concrete temperature history. The actual times of the concrete samples corresponding to the equivalent ages in Table 3 were obtained. Such values are presented in Table 4.

Table 3. Initial and Final setting times in equivalent ages

Mixture	Initial setting (min. at 20ºC)	Final setting (min. at 20ºC)	Setting duration (min. at 20ºC)
C40	334	446	112
C45	354	461	107
C50	399	519	120
C55	380	493	113
C60	374	476	102
C65	376	493	117

Table 4. Actual times of concrete samples when setting in the mortar samples occurred.

Mixture	Initial setting (min.)	Final setting (min.)
C40	274	362
C45	255	330
C50	302	387
C55	279	356
C60	284	354
C65	288	369

Table 3 does not show any trend regarding setting times and the w/c ratio of the mixtures studied here. One would expect that, as the w/c ratio decreased, the setting times for the concrete mixtures would also decrease. However, Table 3 shows a small variation in the final and initial setting times, and similar duration of the setting period. Different amounts of superplasticizer were used in each mix, as can be seen in Table 1, mixtures with lower w/c ratio required greater amount of superplasticizer to maintain similar workability. Therefore, any possible acceleration effect expected for low w/c mixes may have been overcome by the greater superplasticizer amount employed in such mixtures.

Since the temperature of the concrete samples were always higher than that of the mortar samples, when final setting occurred, as given by the mortar penetration resistance, the corresponding concrete sample has already set. The observed difference between final setting in mortar and in the concrete specimens, as given in Tables 2 and 4 varied from 9 to 33 minutes depending on the mixture and temperature histories. For instance, the equivalent age at final set for mixture C45 was 461 minutes at 20ºC, which was achieved in the mortar specimen at 355 minutes and in the concrete sample at 330 minutes. Thus, final set in the concrete sample occurred 25 minutes before final set in the mortar sample for that particular mixture.

3.2 ULTRASONIC WAVEFORMS

Several ultrasonic waveforms were acquired for each mixture. For each waveform, UPV, group velocity, as well as the frequency spectrum and the normalized accumulated energy curve were calculated. The frequency spectrum would yield the peak frequency and the center frequency while the normalized accumulated energy would give the t_{10} and t_{25} energy parameters.

As an example, Figure 3 shows the acquired waveforms, and corresponding frequency spectra and normalized accumulated energy curves for mixture C40 at three different times. One close to initial set (275 min), another during the setting period (315 minutes), and the last at a time close to final set (360 minutes).

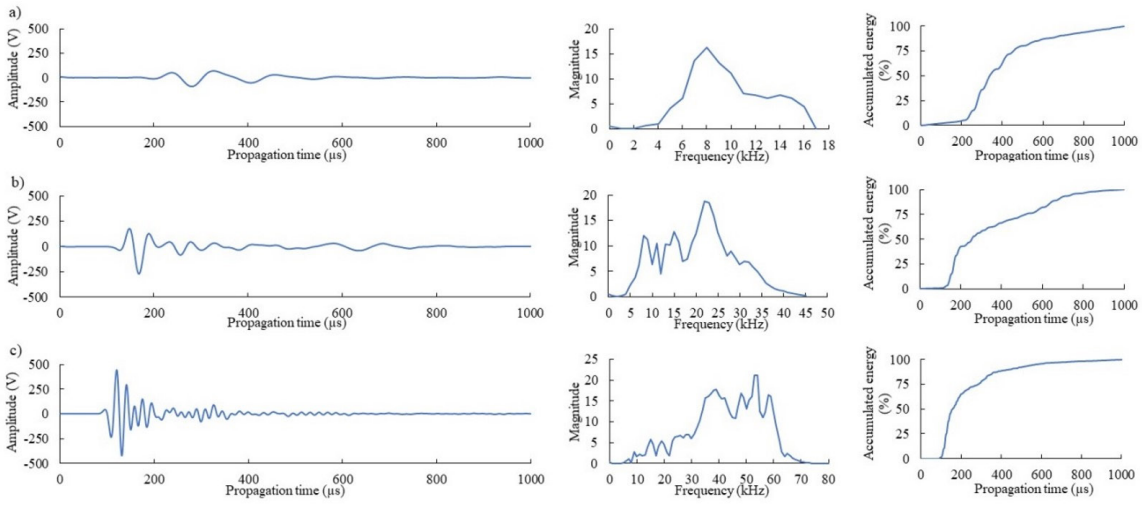

Figure 3. Ultrasonic waveforms, frequency spectrum and accumulated energy curves for C40: a) close to initial setting; (b) between initial and final setting (c) close to the final setting.

During monitoring, it was necessary to modify the amplitude gain of the ultrasonic signal in order to better visualize the waveform. Amplitude gains of 1000, 200 and 10 were used to acquire the waveforms presented in Figure 3. This variation in the amplitude gain did not alter the UPV, the group velocity, and any frequency-based parameters obtained from the waveform. Moreover, the energy related parameters used in this study were based on normalized amplitude values, as depicted in Equation 2 and Equation 3, and thus were also not affected by differences in amplitude gain of the ultrasonic signal.

Figure 3 shows that as setting progressed, a much more significant wave transmission occurred through the C40 specimen since a continuous increase of the stress wave amplitudes, as given by the ordinate magnitudes of Figure 3a-3c, could be observed. There was an observed shift of transmitted energy at earlier times. Also, the frequency spectra show that the dominant frequency component also changed as setting progressed. The dominant frequency was close to the center frequency of the transducers (54 kHz) at final setting.

Since waveforms were acquired at a five-minute interval, it was possible to obtain the development with time of the UPV, group velocity, peak and center frequencies, and the energy related parameters of t_{10} and t_{25} for each mixture. Figure 4 presents the development of these ultrasonic parameters at early ages for all mixtures. The time of initial and final setting, as given in Table 4 are also depicted in Figure 4.

From Figure 4, one could state that as concrete aged, cement hydration increased, since the values of the UPV and group velocity also increased with age. This behavior would continue to occur, albeit in a less accentuated way, even after the end of the setting period, as also seen by Chávez-García et al. [10] and Pellegrino et al. [11].

Table 5 presents the values of the ultrasonic parameters here investigated of the concrete samples obtained from the waveforms acquired when initial and final setting of the mortar samples occurred (Table 4).

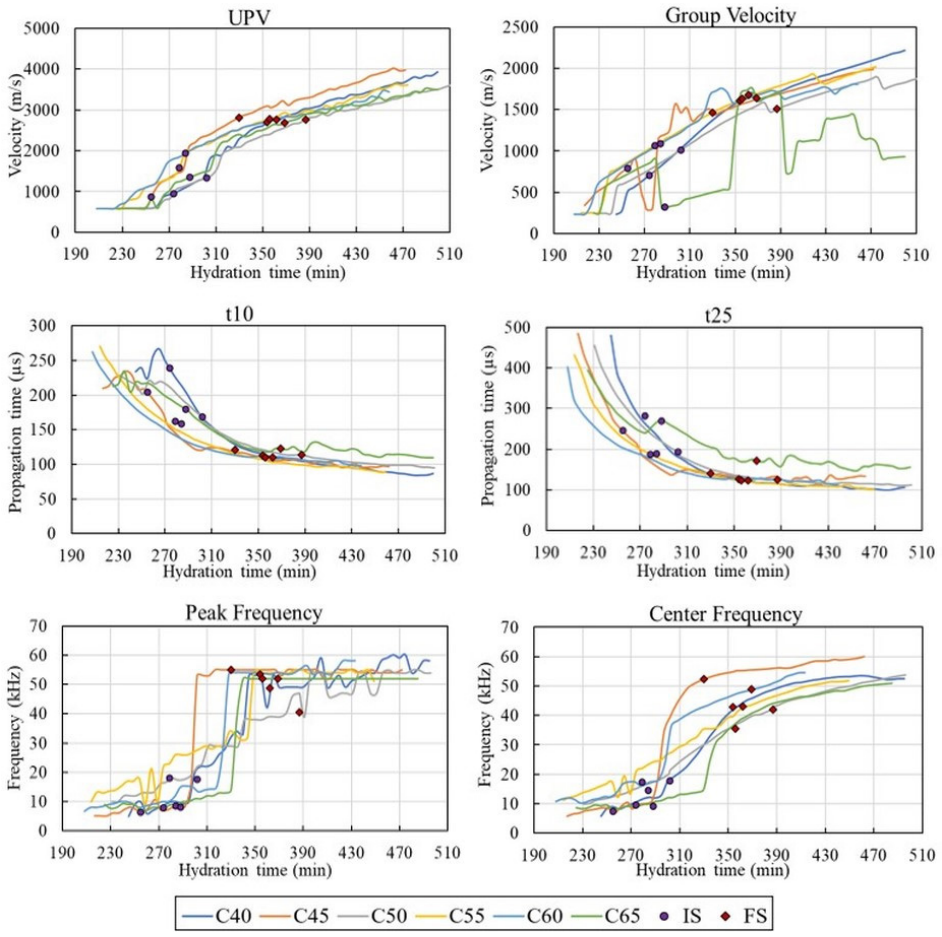

Figure 4. Development of ultrasonic parameters at early ages.

In order to better show the behavior of the ultrasound parameters during the setting period, and also to be able to correlate them with the results of the penetration resistance, the abscissa axis of Figure 4 was transformed to reflect the development of UPV during the setting period given by the penetration resistance method, as shown in Figure 5. The axis was divided in regular intervals depending on the percentage of the setting duration, with 0% corresponding to initial setting time and 100% corresponding to the final setting time.

Table 5. UPV, group velocity, t_{10}, t_{25}, peak frequency and center frequency values at initial and final setting times

Mixture	UPV (m/s)	Group Velocity (m/s)	t_{10} (µs)	t_{25} (µs)	Peak Frequency (kHz)	Central Frequency (kHz)
			Initial set			
C40	946	704	238	281	7.8	9.6
C45	866	790	204	245	6.4	7.5
C50	1338	1011	168	192	17.6	17.7
C55	1586	1066	162	187	18.0	17.4
C60	1937	1090	158	188	8.5	14.5
C65	1343	1022	179	269	8.0	9.15
			Final set			
C40	2762	1680	110	123	48.6	43
C45	2816	1435	120	140	55.0	52.3
C50	2763	1509	113	125	40.4	40.3
C55	2781	1630	109	122	32.8	35.4
C60	2698	1610	112	126	53.5	42.9
C65	2681	1642	122	172	52.0	36.5

As far as UPV is concerned, Figure 4 shows an increase in UPV during setting for all mixtures. This behavior has been previously observed by several researchers [3], [9], [12]-[17]. At very early-ages, ultrasonic waves propagate into a viscous suspension, at low UPV values. After the dormant period has ended, cement hydration products start to be formed, and to be interconnected. Consequently, there is a sharper increase on the rate of UPV development with time. UPV continues to increase as hydration progresses. Mixtures C50 e C65 showed UPV close to 1430 m/s at initial setting, which is close to UPV in water. By contrast, mixtures C55 e C60 showed UPV greater than 1430 m/s, (1586 m/s e 1937 m/s, respectively), while mixtures C40 e C45 showed much smaller UPV values (946 m/s e 866 m/s) at initial setting.

Very low UPV values, as in C40 and C45, can be attributed to the elongation in the wave path, given the suspension of cement grains in the fresh concrete [18] or the possibility of the low w/c ratio having generated an insufficient union between the cement and water [19].

Even though there was not a direct correspondence between initial setting time and UPV, similar final setting times were observed for the concrete samples, as shown in Table 5. For the mixtures studied here, UPV at final set varied between 2681 m/s to 2816 m/s, with a mean value of 2750 m/s and a coefficient of variation of 1.9%. This UPV value at final set lies between the ones indicated by Lee and Lee [20] (1900 to 2900 m/s at final set).

The group velocity also increased, indicating that there was an earlier shift of the most part of the energy. This behavior can also be seen in the waveforms presented in Figure 3 and in the observed decreasing values of the energy-related parameters of t_{10} and t_{25}. There was a greater ease of ultrasonic transmission as setting progressed. Even though, the group velocity development with setting time of mixture C65 showed a different behavior than the other mixtures, as shown in Figure 5, the group velocity values at final setting time were close for all mixtures, with an average value of 1585 m/s and a small coefficient of variation of 5.9%.

Figure 5 shows a significant decrease in t_{10} and t_{25} with increasing time of setting, as a consequence of an increase on the initial inclination of the accumulated energy curve, as can be seen in Figure 6, obtained for mixture C65. As the microstructure is being formed, most of the ultrasonic energy is able to propagate faster, resulting in a greater accumulation of energy at the beginning of the ultrasonic signal. Similarly to UPV and group velocity, there was not a unique value at initial setting, with t_{10} values ranging from 158 μs to 238 μs, and t_{25} values ranging from 187 μs to 281 μs. However, at final setting times, an average t_{10} value of 114 μs (coefficient of variation of 5.4%) and t_{25} values ranging from 122 μs s to 172 μs were obtained.

The peak and central frequencies of the ultrasonic waveform increased as setting progressed, as shown in Figure 5. The increase in the magnitude values indicates more significant wave transmission through the specimen. As stated by Lee et al. [14], when concrete is changing from a viscous suspension into a porous solid, low-frequency components of

the ultrasonic waveform begin to propagate before the high-frequency components. With continuing hydration, and consequently establishment of the porous solid structure, there is an easier transmission of all frequency components.

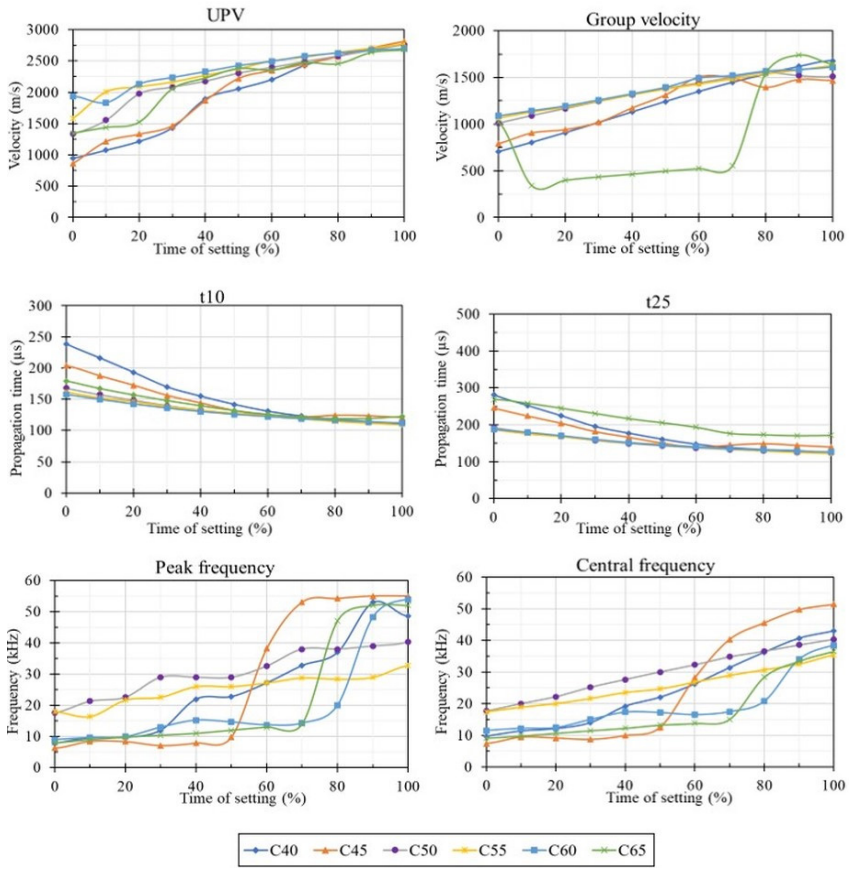

Figure 5. UPV, group velocity, t_{10}, t_{25}, peak frequency and center frequency development during setting.

Shiotani and Aggelis [4] observed decay in the central frequency for mixtures with higher amounts of plastic inclusions, indicating that frequency is related to homogeneity. This frequency-domain phenomenon only occurred during this early stage of microstructure development since at setting progressed, both the central frequency and the peak frequency tended to reach 54 kHz, the center frequency of the transducer. However, despite this continuous and similar increasing behavior, these frequency parameters seemed to be mixture dependent. It was not possible to indicate a central frequency value neither a peak frequency value at initial nor final setting for all mixtures.

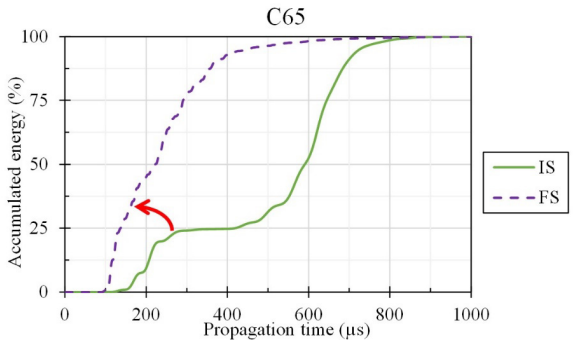

Figure 6. Accumulated energy curves at initial setting (IS) and final setting (FS) to mixture C65.

4 CONCLUSIONS

Nondestructive tests have been widely used in the quality control of concrete structures. The propagation of stress waves is affected by changes in the microstructure of the material, making it possible to use ultrasound to monitor the development of the concrete microstructure. At early stages, due to high rates of cement hydration, the microstructure is in continuous development. The quality of the microstructure formed greatly influences the mechanical properties and durability of the concrete structure.

In this research, the propagation of ultrasonic waves in fresh concrete during the setting period was studied. As concrete moved from a plastic stage to a rigid solid, the ultrasonic wave format changed. Regarding the ultrasonic parameters investigated here, the following conclusions can be drawn:

- As setting progressed, there was an observed increase of wave amplitudes, as a result of a more significant wave transmission through concrete.
- None of the ultrasonic parameters investigated here was able to be correlated uniquely to initial set times as given by the penetration resistance method, since significant variations were observed in their values at initial set time.
- The UPV and group velocity values increased during setting for all mixtures, with mean values of 2750 m/s and 1585 m/s at final setting, respectively.
- An earlier shift of the accumulated energy occurred, and as a consequence, the energy-related parameters of t_{10} and t_{25} decreased as setting progressed. At final setting times, an average t_{10} value of 114 μs, and t_{25} values ranging from 122 μs to 172 μs were obtained.
- The frequency parameters seemed to be mixture dependent. It was not possible to indicate a central frequency value neither a peak frequency value at initial setting for all mixtures.
- The peak and center frequencies was close to the frequency of the transducers (54 kHz) at final setting.

Although the initial and final setting times, as given by ASTM C403, are related to the concrete stiffening process, they do not represent when specific changes in the physical-chemical characteristics of the cement paste occur. Setting of concrete is a continuous phase in which the material's microstructure is constantly developing, as shown by the wide changes of the various ultrasonic parameters here investigated.

A combined analysis of the time domain parameters of UPV, group velocity and t_{10} can be used to improve the characterization of the microstructure development regarding the setting behavior of concrete mixtures.

ACKNOWLEDGEMENTS

The authors would like to thank the Universidade Federal de Santa Catarina, as well as Supremo Cimentos and Engemix for supplying the cement and aggregates for this research.

REFERENCES

[1] American Society for Testing and Materials, *Standard Test Method for Time of Setting of Concrete Mixtures by Penetration Resistance*, ASTM C403, 2008.

[2] J. Abel, R. C. A. Pinto, and K. C. Hover, “Monitoring the liquid to solid transition in concrete with conventional tests,” in *Transition from Fluid to Solid: Re-Examining the Behavior of Concrete at Early Ages*, K. Riding, Ed., Farmington Hills, United States: American Concrete Institute, 2009, pp. 139–154.

[3] G. Ye, P. Lura, K. Van Breugel, and A. L. A. Fraaij, “Study on the development of the microstructure in cement-based materials by means of numerical simulation and ultrasonic pulse velocity measurement,” *Cement Concr. Compos.*, vol. 26, no. 5, pp. 491–497, Jul. 2004.

[4] T. Shiotani and D. G. Aggelis, “Wave propagation in cementitious material containing artificial distributed damage,” *Mater. Struct.*, vol. 42, no. 3, pp. 377–384, May 2009.

[5] A. V. Hauwert, F. Delannay, and J. F. Thimus, “Cracking behavior of steel fiber reinforced concrete revealed by means of acoustic emission and ultrasonic wave propagation,” *ACI Mater. J.*, vol. 96, no. 3, pp. 291–296, May 1999.

[6] M. A. P. Irrigaray, “Estimativa da resistência do concreto à compressão por meio da velocidade de pulsos ultrassônicos na pasta do concreto,” Doctoral dissertation, Univ. Federal Santa Catarina, Florianópolis, 2012.

[7] American Society for Testing and Materials, *Standard Practice for Estimating Concrete Strength by the Maturity Method*, ASTM C1074, 2016.

[8] R. C. A. Pinto and A. K. Schindler, “Unified modeling of setting and strength development,” *Cement Concr. Res.*, vol. 40, no. 1, pp. 58–65, Jan. 2010.

[9] J. Carette and S. Staquet, “Monitoring the setting process of mortars by ultrasonic P and S-wave transmission velocity measurement,” *Constr. Build. Mater.*, vol. 94, pp. 196–208, Sep. 2015.

[10] H. L. Chávez-García, E. M. Alonso-Guzmán, W. Martínez-Molina, M. Graff, and J. C. Arteaga-Arcos, "Prediction of the static modulus of elasticity using four non destructive testing," *Rev. Constr.*, vol. 13, no. 1, pp. 33–40, 2014.

[11] F. Pellegrino et al., "Continuous monitoring of early-age properties of sprayed mortars by in situ ultrasound measurements," *Constr. Build. Mater.*, vol. 292, p. 123389, Jul. 2021.

[12] H. J. Yim, Y. H. Bae, and Y. Jun, "Hydration and microstructural characterization of early-age cement paste with ultrasonic wave velocity and electrical resistivity measurements," *Constr. Build. Mater.*, vol. 303, p. 124508, Oct. 2022.

[13] G. Karaiskos, A. Deraemaeker, D. G. Aggelis, and D. Van Hemelrijck, "Monitoring of concrete structures using the ultrasonic pulse velocity method," *Smart Mater. Struct.*, vol. 24, no. 11, p. 113001, Oct. 2015.

[14] H. K. Lee, K. M. Lee, Y. H. Kim, H. Yim, and D. B. Bae, "Ultrasonic in-situ monitoring of setting process of high-performance concrete," *Cement Concr. Res.*, vol. 34, no. 4, pp. 631–640, Apr. 2004.

[15] H. W. Reinhardt, C. U. Große, and A. T. Herb, "Ultrasonic monitoring of setting and hardening of cement mortar—a new device," *Mater. Struct.*, vol. 33, no. 9, pp. 581–583, Nov. 2000.

[16] Y. Zhang, W. Zhang, W. She, L. Ma, and W. Zhu, "Ultrasound monitoring of setting and hardening process of ultra-high performance cementitious materials," *NDT & E Int.*, vol. 47, pp. 177–184, Apr. 2016.

[17] D. Y. Yoo, H. O. Shin, and Y. S. Yoon, "Ultrasonic monitoring of setting and strength development of ultra-high-performance concrete," *Materials*, vol. 9, no. 4, p. 294, Apr. 2016.

[18] J. R. Rapoport, J. S. Popovics, S. V. Kolluru, and S. P. Shah, "Using ultrasound to monitor stiffening process of concrete with admixtures," *ACI Struct. J.*, vol. 97, no. 6, pp. 675–683, Jan. 2000.

[19] A. Feylessoufi, F. C. Tenoudji, V. Morin, and P. Richard, "Early ages shrinkage mechanisms of ultra-high-performance cement-based materials," *Cement Concr. Res.*, vol. 31, no. 11, pp. 1573–1579, Nov. 2001.

[20] T. Lee and J. Lee, "Setting time and compressive strength prediction model of concrete by nondestructive ultrasonic pulse velocity testing at early age," *Constr. Build. Mater.*, vol. 252, p. 119027, Aug. 2020.

Author contributions: HFGB: conceptualization, methodology, writing, data analysis; FC: data analysis; RCAP: funding acquisition, supervision, writing.

Editors: Vladimir Haach, Guilherme Aris Parsekian.

IBRACON Structures and Materials Journal
Revista IBRACON de Estruturas e Materiais
ISSN 1983-4195 ismj.org

REVIEW ARTICLE

Dataset construction and data science analysis of physicochemical characterization of ordinary Portland cement

Construção e análise de banco de dados das propriedades do cimento Portland comum

Jéssica Fall Nogueira Chaves[a]
Francisco Evangelista Junior[a]
João Henrique da Silva Rêgo[a]
Lucas de Paula Vasques[a]

[a]University of Brasilia, Department of Civil and Environmental Engineering, Brasilia, Federal District, Brazil

Received 15 October 2022
Accepted 16 February 2023

Abstract: This paper presents a dataset construction and data science analysis from the literature results of physicochemical characterization of ordinary Portland cement (OPC). The physicochemical variables included the percentage by mass of calcium oxide (CaO), silicon dioxide (SiO_2), aluminum oxide (Al_2O_3), iron oxide (Fe_2O_3), magnesium oxide (MgO), sulfuric oxide (SO_3), sodium oxide (Na_2O), potassium oxide (K_2O), titanium oxide (TiO_2), free lime (CaO_{free}), equivalent alkaline (Na_2O_{eq}), loss on ignition, specific surface, density, water-cement ratio, and compressive strength of cement at 28 days. The searching, collection, and assembly of the dataset aimed to evaluate the information related to those variables through exploratory data analysis, enabling a basic understanding of characterization results of OPCs obtained in publications from different types, sources, years, and countries. The dataset provides a useful source of physicochemical characterization of ordinary cement, and the exploratory data analysis provided an understanding of central, dispersion, and data distribution with statistical metrics of each variable and their pair-wise correlations in the assembled dataset. The constructed dataset and its analysis are a starting point to further data, studies, and artificial intelligence models to provide a broader global view of the production and properties of ordinary Portland cement.

Keywords: Portland cement, oxides, data science, physicochemical properties, compressive strength.

Resumo: Este artigo apresenta a construção de um conjunto de dados e a análise exploratória de dados a partir dos resultados da literatura de caracterização físico-química do cimento Portland comum (CPC). As variáveis físico-químicas incluíram a porcentagem em massa de óxido de cálcio (CaO), dióxido de silício (SiO_2), óxido de alumínio (Al_2O_3), óxido de ferro (Fe_2O_3), óxido de magnésio (MgO), óxido sulfúrico (SO_3), óxido de sódio (Na_2O), óxido de potássio (K_2O), óxido de titânio (TiO_2), cal livre (CaO_{free}), equivalente alcalino (Na_2O_{eq}), perda ao fogo, superfície específica, densidade, relação água-cimento e resistência à compressão do cimento aos 28 dias. A busca, coleta e montagem do conjunto de dados teve como objetivo avaliar as informações relacionadas a essas variáveis por meio de análise exploratória de dados, permitindo uma compreensão básica dos resultados de caracterização de CPCs obtidos em publicações de diferentes tipos, fontes, anos e países. O conjunto de dados fornece uma fonte útil de caracterização físico-química de cimento comum, e a análise exploratória de dados forneceu uma compreensão da distribuição central, de dispersão e de dados com métricas estatísticas de cada variável e suas correlações de pares no conjunto de dados montado. O conjunto de dados construído e sua análise são um ponto de partida para novos dados, estudos e modelos de inteligência artificial para fornecer uma visão global mais ampla da produção e propriedades do cimento Portland comum.

Palavras-chave: cimento Portland comum, óxidos, análise exploratória dos dados, propriedades físico-químicas, resistência à compressão.

How to cite: J. F. N. Chaves, F. Evangelista Junior, J. H. S. Rêgo, and L. P. Vasques, "Dataset construction and data science analysis of physicochemical characterization of ordinary Portland cement," *Rev. IBRACON Estrut. Mater.*, vol. 16, no. 6, e16609, 2023, https://doi.org/10.1590/S1983-41952023000600009

Corresponding author: Jéssica Fall Nogueira Chaves. E-mail: jessicafall@live.com
Financial support: Coordenação de aperfeiçoamento de Pessoal de Nível Superior (CAPES) - Financial Code 001, Conselho Nacional de Desenvolvimento Científico e Tecnológico (CNPq), Fundação Universidade de Brasília (FUB) and Decanato de Pós-Graduação (DPG) of the University of Brasília, Brazil.
Conflict of interest: Nothing to declare.
Data Availability: Due to the nature of this research, participants of this study did not agree for their data to be shared publicly, so supporting data are not available.

1 INTRODUCTION

Portland cement is one of the most used materials worldwide and its compressive strength after 28 days of age is the most used measure concerning engineering and performance properties. This strength is a critical input in the technological control of the material and structural design. At 28 days, it is considered the end of the curing process of cement, and it is expected that the strength specified by the manufacturer will be reached, making the compressive strength a fundamental parameter for comparison, and it is still the most used requirement in the choice of cementitious materials [1], [2]. Therefore, this property is an important criterion for standard compliance and is frequently used in the field of civil construction and scientific research. It is well known that this 28-day compressive strength is influenced by its constituent materials [2], [3].

Ordinary Portland cement (OPC) consists of clinker, which has as raw materials limestone, clay or siliceous materials, and materials containing iron and aluminum oxide, and a small percentage of gypsum to regularize the setting. The cement manufacturing process essentially consists of grinding the raw material, mixing it intimately in certain proportions, and burning (at temperatures of up to around 1.450 °C) in large rotary kilns, where the material is sintered and partially melted. The chemical reaction that takes place between the raw materials of clinker in the rotary kiln generates its four main compounds which are tricalcium silicate or alite (C_3S), dicalcium silicate, or belite (C_2S), tricalcium aluminate (C_3A), and tetracalcium ferroaluminate (C_4AF) [4]–[6]. The proportions of the phases present in the cement influence the physical properties of cementitious materials, such as strength, setting time, among other factors.

It is important to point out that silicates in cement are not pure compounds as they contain secondary oxides in solid solution. Both invariably contain small amounts of magnesium, aluminum, iron, potassium, sodium, and sulfur ions. These oxides exert significant effects on the atomic arrangement, crystal shape and hydraulic properties of silicates. Similar to calcium silicates, Mehta and Monteiro [4] mention that in industrial clinkers both C_3A and C_4AF contain significant amounts of magnesium, sodium, potassium and silica in their crystalline structure [4], [7].

The alkalis, potassium oxide (K_2O) and sodium oxide (Na_2O), because they are soluble and reactive, are among the most common elements in nature and are found in small amounts in all raw materials used in the manufacture of cement, especially in clay compounds. Alkalis are of interest in concrete technology due to their reaction with reactive aggregates, originating the alkali-aggregate reaction that causes disintegration of concrete [8]. However, Neville and Brooks [9] mentions that they influence the speed of development of cement strength.

The Portland Cement manufacturing process has undergone changes to improve the environmental aspect of production. The co-processing technique, for example, is the reusing waste as raw material, or as a source of energy, or both to replace natural mineral resources and fossil fuels such as coal, petroleum, and gas in industrial processes [10]. Although this practice can improve the efficiency of material resources, most waste contains contaminants that can be inserted into some of the secondary oxides in the structure of the 4 main cement compounds and interfere with the products formed. In this way, cleaner production through co-processing therefore requires a good understanding of the impacts of these contaminants on the cement manufacturing process, cement quality and the environment [11], [12].

As much as the present research deals with OPC, commercial cements usually incorporate some type of supplementary cementitious materials (SCM). Some materials such as calcined clay, limestone, silica fume, rice hush ash with controlled burning and metacaulim are studied and increasingly used in the sector as SCM, having different influences on the final product. Limestone, for example, contributes to the process of hydration of cement and during the hydration process there is the formation of carbonamine compounds in the presence of finely ground carbonate material, decreasing the porosity of the cementitious system. In addition, the mechanical strength of cementitious materials is greatly influenced by the presence of SCM, in which the strength gain is slower, being lower in the initial ages and increasing with advancing time [13], [14].

Since the chemical composition of Portland cement and its hydrates have a direct influence on the characteristics of cementitious matrices, its characterization and quantification are of fundamental importance. Quantitative analysis of the concentrations of cement elements is a step widely applied in research that uses it in their experimental programs. Although Portland cement consists essentially of various calcium compounds, the results of routine chemical analyzes are expressed in terms of the elemental oxides present [4].

In research that uses and investigate the OPC, parameters such as its chemical composition, specific surface, density, water-cement ratio, among other properties, are usually investigated together with the results of 28-day compressive strength, since scientific works around the world have already proven the influence between physicochemical properties with the development of mechanical resistance of cementitious materials. The change in the chemical composition of the cement, for example, influences the compressive strength, since the proportions of the different compounds vary significantly from one cement to another. The main oxides, expressed in percentage by mass, investigated in scientific research are calcium oxide (CaO), silicon dioxide (SiO_2), aluminum oxide (Al_2O_3), iron oxide (Fe_2O_3), magnesium oxide (MgO), sulfuric oxide (SO_3), sodium oxide (Na_2O), potassium oxide (K_2O), titanium oxide (TiO_2), free lime (CaO_{free}), and alkaline equivalent (Na_2O_{eq}). The oxide content

of each cement influences the proportion of the main compounds (C_3S, C_2S, C_3A, C_4AF). Because each compound has a different reactivity and forms different products, they influence the mechanical strength in different ways [15]. Several techniques are applied to determine the composition of OPC; however, X-ray fluorescence spectroscopy (XRF) is widely used to characterize the oxides present in Portland cement samples. In addition, X-ray diffraction (XRD) with the Rietveld method and X-ray fluorescence spectroscopy combined with the Bogue Potential calculation are used in studies with ordinary Portland cement to quantify its 4 main compounds (C_3S, C_2S, C_3A, C_4AF).

Regarding the physical characterization, fineness is a parameter used by several researchers that use cementitious matrices, as it is a property that is directly related to the speed of the hydration reaction, having a proven influence on its mechanical behavior. The fineness of the cement is related to the specific surface of the grains and its determination serves mainly to check the uniformity of the material's grinding process. Normally, this property can be measured by using nitrogen adsorption technique (BET), based on a mathematical theory that has the measurement of the specific surface area of a material through the physical adsorption of hydrogen gas molecules on the surface [16], and Blaine air-permeability apparatus, which the specific surface is expressed as area total surface area in square centimeters per gram, or square meters per kilogram, of cement [17]. Since the reaction of Portland cement with water is an effect from the outer surface to the inner surface of the grain, that is, the degree of grinding of the cement will influence the hydration speed and the development of compressive strength [1], [6], [11].

The determination of the compressive strength of Portland cement is standardized worldwide, using cement mortar specimens. The standards of each country establish factors such as dimensions of the specimens, water-cement and sand-cement ratios, type of sand, consistency, among others, to provide uniformity in the process of producing mortars. The American standard C 109/C109M [18] and the British BS EN 196-1 [19], serve as a theoretical basis for the development of standards in different countries. In Brazil, the test method is established by ABNT NBR 7215 [20]. The characterization and mechanical behavior of OPC have been investigated by researchers all over the world with several different goals and results, like Malami et al. [21], Felekoğlu et al. [22], Parande et al. [23], Yao and Sun [24], Dhandapani et al. [25] and Yun et al. [26], however, there is an absolute lack of statistical studies of its oxide components and standard properties. Furthermore, no paper in literature collected and statistically quantified physicochemical characteristics of OPC's composition considering different sources, years, and countries.

This paper aims the collection and analysis of a dataset from the literature on the physicochemical characterization of OPC considering as variables the mass percentage of its oxides: CaO, SiO_2, Al_2O_3, Fe_2O_3, MgO, SO_3, Na_2O, K_2O, TiO_2, CaO_{free}, Na_2O_{eq}, loss on ignition; and the commonly reported physical properties: specific surface, density, water-cement ratio, compressive strength at 28 days. From the collected data, the present work also performs a data science exploratory assessment of each variable, as well as their correlations, through an exploratory data analysis to investigate their statistical moments, distribution characteristics, outlier identification, and statistical correlations among variables that make up the dataset. A bibliometric study of the papers was also carried out, showing the scenario in which, these publications are found, as the most frequently used keyword, year and type of publication, main sources. The main contribution of this paper is the collection and assembly of a novel dataset on which the variables are the commonly reported physical properties and chemical composition of OPCs. Furthermore, the exploratory data analysis provided a basic understanding of central, dispersion, and data distribution with statistical metrics of each variable and their pair-wise correlations in the assembled dataset. This set is crucial to statistical regression, machine learning, and artificial intelligence applications to develop predictive models for the compressive strength based on the physicochemical characteristics of OPC.

2 METHODOLOGY, BIBLIOMETRIC REVIEW, AND DATASET COLLECTION AND ASSEMBLY

The data set was formed from the reading of more than 3.000 scientific productions between March and June 2021 through the Scopus database. To standardize during the entire search, the string "Ordinary Portland Cement" was inserted to limit the results in searches that contained the OPC in the titles, abstracts, and keywords. From the results of the research, the titles, abstracts, and especially the topics of materials and methods were read in all works. The selection of a publication was based on the availability of the results of the OPC characterization tests. In other words, to be selected, the research needed to explicitly provide the mass percentage of, at least, the main four OPC oxides CaO, SiO2, Al2O, FeO2, and the 28-day strength characterization. By having the results of these five variables, especially the compressive strength, the results were collected and added to the dataset collecting, when applicable. After the final screening, the dataset was finally formed from 102 publications.

An initial bibliometric review was carried out to analyze selected scientific productions that used the OPC, using the VOSviewer tool, which provides an interface for viewing and analyzing bibliometric and sociometric networks. The analysis in the software was performed regarding the terms of occurrence of the keywords, applying the full counting method to scan the titles, abstracts, and keywords. This tool employs a visualization method based on the

distance between the nodes of the analyzed network, in which the distance between two nodes approximately indicates the intensity of the relationship between them, thus, the smaller the distance, the greater the intensity of this relationship. Figure 1 presents the bibliometric network extracted from the VOSviewer software, which presents all the terms used in the titles, abstracts, and keywords. The network shows that the most used word is "compressive strength", having 17 occurrences, 66 links, meaning that this term has 66 connections with other words, and a link strength of 76, which indicates the number of publications in which it appears linked to other keywords.

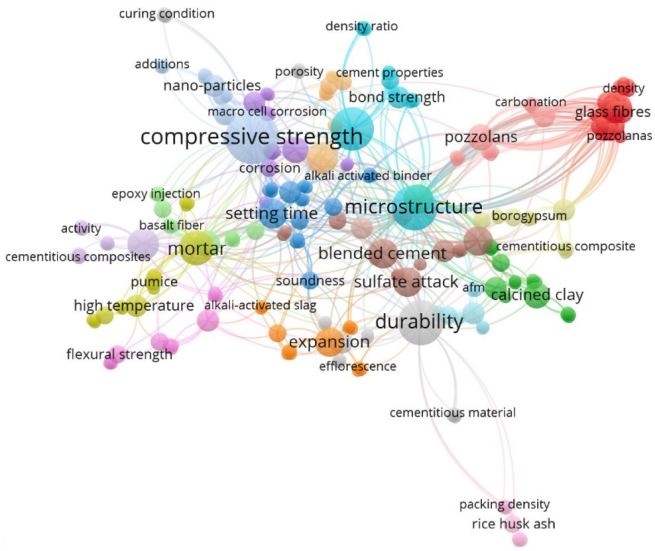

Figure 1. Network of co-occurrence words.

The development of the dataset consisted in the search and collection of the mass percentage values of the main OPC oxides (*CaO*, *SiO₂*, *Al₂O*, *FeO₂*, *MgO*, *SO₃*, *Na₂O*, *K₂O*, *TiO₂*, *CaO$_{free}$*, *Na₂O$_{eq}$*), loss on ignition, specific surface, density, water-cement ratio, and compressive strength at 28 days of the OPCs used in scientific articles published in literature including high-impact journals, books, thesis, and dissertations.

Table 1 presents the physicochemical variables (oxides or properties) considered in this study. Note that the table also specifies how each variable is labeled in all tables and graphs in this manuscript.

Table 1. Physicochemical variables used on the dataset: oxides and test properties.

	Variable	Unity	Label
Oxides	CaO	%	*CaO*
	SiO_2	%	*SiO2*
	Al_2O_3	%	*Al2O3*
	Fe_2O_3	%	*Fe2O3*
	MgO	%	*MgO*
	SO_3	%	*SO3*
	Na_2O	%	*Na2O*
	K_2O	%	*K2O*
	TiO_2	%	*TiO2*
	CaO_{free}	%	*Caofree*
	Na_2O_{eq}	%	*Na2Oeq*
Properties	Loss on Ignition	%	*loss*
	Specific Surface	m^2/kg	*surface*
	Density	g/cm^3	*dens*
	Water-cement ratio	-	*wc*
	28-day compressive strength	MPa	*strength*

Figure 2 presents the evolution of the number of scientific productions published per year among the selected 102 publications. It is possible to notice that from the year 2015 up to 2020 the number of publications increases. The only exceptions are 2019 and 2021, in which this last one was only partially elapsed by the data this paper was written.

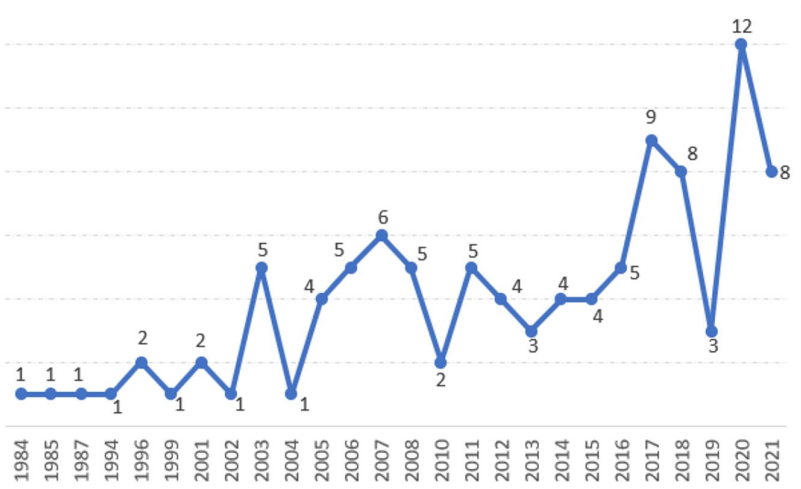

Figure 2. Number of scientific productions per year.

The 102 scientific productions consisted of 92 journal papers (11 international journals), 2 book results (Calcined Clay for Sustainable Concrete), and 8 thesis/dissertations. Figure 3 contains the main sources with their respective numbers of selected publications that characterized the physicochemical properties of OPC. Construction and Building Materials (CBM) stands out with 33 publications, followed by Cement and Concrete Research (CCR) and Cement and Concrete Composites (CCC), with 22 and 17 papers, respectively.

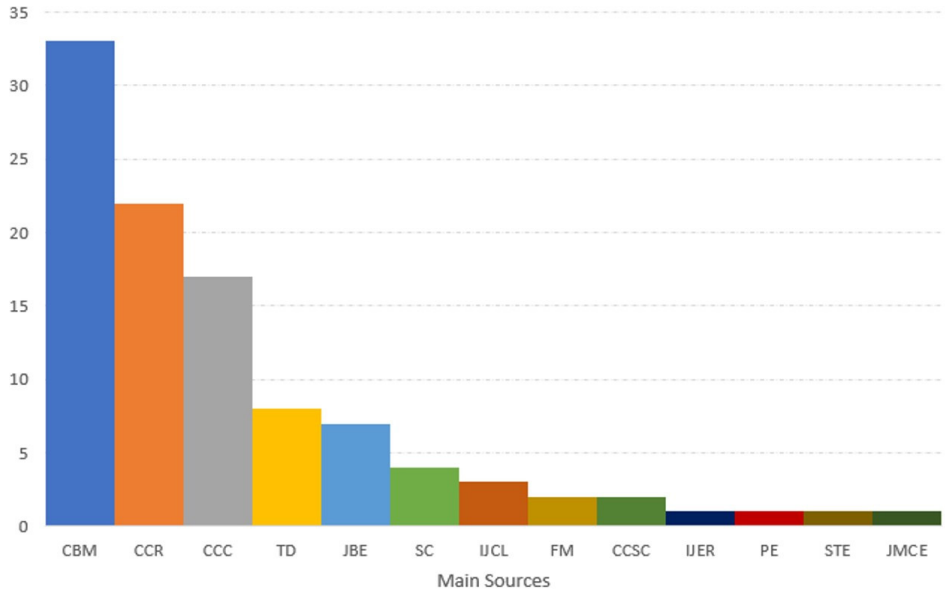

Figure 3. Number of papers per source. Legend: Construction and Building Materials (CBM), Cement and Concrete Research (CCR), Cement and Concrete Composites (CCC), Thesis/Dissertation (TD), Journal of Building Engineering (JBE), Structural Concrete (SC), The International Journal of Cement Composites and Lightweight Concrete (IJCL), Fire and Materials (FM), Calcined clay for Sustainable Concrete (CCSC), International Journal of Energy Research (IJER), Procedia Engineering (PE), Science of the Total Environment (STE) and Journal of Materials in Civil Engineering (JMCE).

The graph plotted in Figure 4 shows the data-filling matrix of the assembled dataset, in which the white blanks represent the lack of data for a given variable, and the blue color represents the presence of data. It is possible to observe that TiO_2 is the parameter that was least provided in the literature, either because it was not investigated in the respective publication or because it was not identified in the chemical characterization test, followed by alkalis (Na_2O and K_2O)

and CaO_{free}. In addition, the sample preparation process for chemical characterization tests, such as XRF, for example, can influence the accuracy of the determination of the percentage of alkalis. The strength was the only parameter that had results shown in all publications. The oxides CaO, SiO_2, Al_2O_3 e Fe_2O_3, which give rise to the four main compounds of Portland cement, are also factors that the researchers sought to investigate and that were described in the characterization of OPC. Likewise, the determination of the specific surface (*surface*) was present in the works and the water-cement ratio (*wc*) was indicated through the standard of the respective country of the publication.

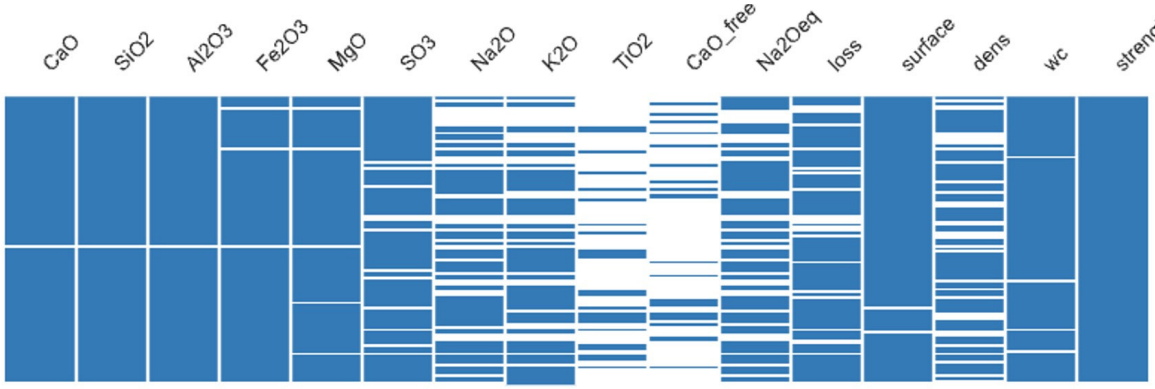

Figure 4. Data-filling matrix.

3 DATA SCIENCE ANALYSIS

From the assembled dataset, an exploratory analysis was performed, which consisted primarily of data preparation, exploratory data analysis of each variable, and the relationships between them. Statistical metrics such as maximum, minimum, mean, and median; metrics of dispersion/variability such as standard deviation, coefficient of variation, range, and outliers detection; and metrics of data distribution such as interquartile range and skewness were also performed. An in-house software Tyche [27] with its data science module Datum was used for those metrics.

The analysis starts with Figure 5 showing a data matrix with pair-wise scatter plots and individual histograms for the 16 variables. The main diagonal shows the individual histograms for each variable, whereas the off-diagonal components, shows the dispersion plot for a combination of two variables. For example, the plot in the first row and the third column is the scatter plot of CaO versus Al_2O_3 oxide variables. Note that the histogram for the water-cement ratio (*wc*) almost represents a categorical variable with only three valid bins: 0.40-0.41, 0.48-0.49, and 0.49-0.50, in which the latter is significatively dominant. This is because almost all standards used the 0.50 water-cement ratio. Fewer exceptions used slightly different values which were counted in the other bins. The Indian standard for determining compressive strength IS 4031 (Part 6) [28], for example, considers that the water-cement ratio is acquired through another standard of the slump measurements IS 4031(Part 4) [29].

Although the water-cement ratio (*wc*) presented this extreme concentration, at the 0.5 ratios, almost as a deterministic variable for this dataset, the authors decided to keep it for completeness of the analysis. The oxides TiO_2 and CaO_{free} also presented a dominant value, but to a lesser degree than *wc*, as showed in the histograms. This is also observed on the scatter plots of those variables (rows 9, 10, and 15) that tend to form horizontal lines on the plots. Figure 5 only allows an initial qualitative assessment of data, therefore, the following paragraphs present an in-depth quantitative analysis of variables. Levels of heading establish the hierarchy of sections by the format or appearance. The section and subsection headings must be preceded by progressive numbering, presented in Arabic numerals, starting at 1.

The histogram of the compressive strength does not suggest any conventional probability distribution. Goodness of fit tests were performed for the main known distributions: normal, log normal, uniform, exponential, extreme value, and they all failed the null-hypothesis showing that there is significant difference between the observed strength values and the expected distributions. The determination of a possible probability distribution will be further investigated in future papers.

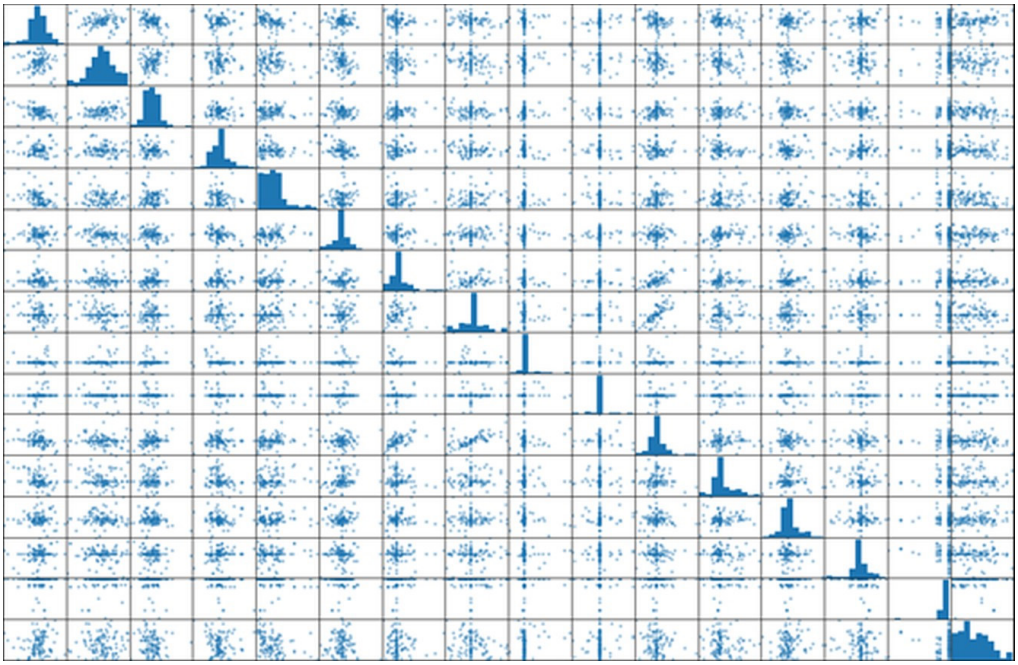

Figure 5. Matrix with histograms and pair-wise scatter plots of the variables.

Table 2 presents the summary of the main statistical parameters for the samples of each variable of the dataset: minimum (min), maximum (max), mean, standard deviation (SD), and coefficient of variation (CV), median, skewness, and interquartile range (IQR).

Table 2. Summary of statistical parameters of each variable.

Variables	Min	Max	Range	Mean	SD	CV	Median	Skewness	IQR
CaO	56.00	68.97	12.97	63.27	2.04	3%	63.44	-0.68	1.90
SiO_2	16.51	23.70	7.19	20.60	1.48	7%	20.65	-0.27	1.88
Al_2O_3	2.45	9.82	7.37	5.06	0.98	19%	5.10	1.02	1.20
Fe_2O3	0.30	7.69	7.39	3.43	1.08	31%	3.34	0.95	1.05
MgO	0.60	6.51	5.91	2.08	1.15	55%	1.93	1.55	1.36
SO_3	0.59	6.24	5.65	2.58	0.80	31%	2.62	0.71	0.77
Na_2O	0.01	0.98	0.97	0.27	0.18	65%	0.22	1.69	0.16
K_2O	0.10	1.32	1.22	0.63	0.30	48%	0.59	0.35	0.43
TiO_2	0.14	0.56	0.42	0.29	0.10	35%	0.24	1.32	0.11
CaO_{free}	0.15	2.41	2.26	1.23	0.66	53%	1.16	0.19	1.03
Na_2O_{eq}	0.08	1.71	1.63	0.65	0.27	42%	0.63	1.00	0.34
Loss	0.00	4.50	4.50	1.79	0.91	51%	1.55	0.70	1.09
Surface	175.00	582.00	407	352.83	59.66	17%	347.00	0.76	51.30
Dens	3.00	3.22	0.22	3.13	0.04	1%	3.13	-0.74	0.05
wc	0.40	0.50	0.10	0.49	0.02	4%	0.50	-3.31	0.01
Strength	38.23	71.00	32.77	50.74	7.90	16%	50.00	0.38	11.83

From the values of the percentage by mass of the oxides from the collected dataset, the mean values of the main components of ordinary Portland cement, C_3S (53,98%), C_2S (17,87%), C_3A (6,92%) e C_4AF (10,15%) were calculated, in percentage, using Bogue's equations [21] considering the addition of gypsum. It is noteworthy that the remainder of the sum of the percentage values of those four compounds was adopted as the content of incorporated calcium sulfate and impurities, determining a mean value of 11.08%.

For the calculation using Bogue, it is necessary to consider that the composition of the four main components of Portland cement are C_3S, C_2S, C_3A and C_4AF with theoretical stoichiometries; all Fe_2O_3 present reacts with Al_2O_3 and CaO to turn into C_4AF; the remaining Al_2O_3 reacts with the CaO to produce C_3A; the remaining CaO reacts with SiO_2

and becomes C_3S and C_2S. The method also considers non-real clinker temperatures close to 2,000 °C, perfect combination of oxides, the existence of balance between C_3S, C_2S and liquid phase [30], [31]. According to Gobbo [30] the calculation restricts the constitution of the cement clinkers to C_3S, C_2S, C_3A e C_4AF, being that it despises the existence of minor elements, such as the TiO_2, MgO, K_2O e Na_2O, among others. It is important to emphasize that some impurities, instead of being present in the cement material, may be incorporated into the structures of main compounds.

3.1 Analysis of sample dispersion, distribution properties, and outliers

The coefficient of variation (CV) conveys the data dispersion (variability of sample data) in terms of the ratio of the standard deviation (SD) and the sample mean values. The CV is a suitable quantity because it expresses the variability of the data excluding the influence of different scales allowing direct comparison among variables of different units or order of magnitude. Figure 6 shows the CV, in percentage, for the 16 variables in descending order. The graph shows that two oxides (*CaO* and SiO_2), *dens*, and *wc* has CV below 8% meaning that their values used around the world to manufacture OPC have very low variability. This was already mentioned for the water-cement ratio since the histogram already showed almost exclusivity of values within the range 0.49-0.50 because of uniformity of compressive strength standards used the 0.5 ratios as discussed before. Another important factor is that *CaO* and SiO_2 are the first and second most dominant components of OPC's mass with means 63.27% and 20.60%, respectively, according to Table 2, which both account for approximately 84% (mean) in OPC's mass. This further showed that those two components mostly related to the manufacturing and extraction process of cement raw materials showed very low variability in their percentage composition in OPCs in the reported literature. However, the CV for the strength was 16%, which is almost double the CV for the most dominant components (in mass). The dashed line in Figure 6 allows a visual comparison of the compressive strength's coefficient of variation with the other variables. Furthermore, the compressive strength samples had a standard deviation of 7.9 Mpa and its mean was 50.74 Mpa, since the values obtained for strength in the research range mainly from 40 to 60 Mpa, having only 9 out of 102 that had resistance below 40 Mpa and only 1 out of 102 above 70 Mpa.

The majority of the other oxides presented high CV, such as SO_3 (31%), Fe_2O (31%), TiO_2 (35%), Na_2O_{eq} (42%), K_2O (48%), CaO_{free} (53%), MgO (55%) e Na_2O (65%). This greater variability in the mass percentage values of these oxides can be explained by the influence of impurities present in the raw materials extracted and used for cement manufacturing, as well as by adjustments made in the chemical composition of the material in each country due to some specific standard. Among the test properties variables, the loss on ignition (*loss*) presented a high CV value (51%) demonstrating the high variability of these test results in the literature.

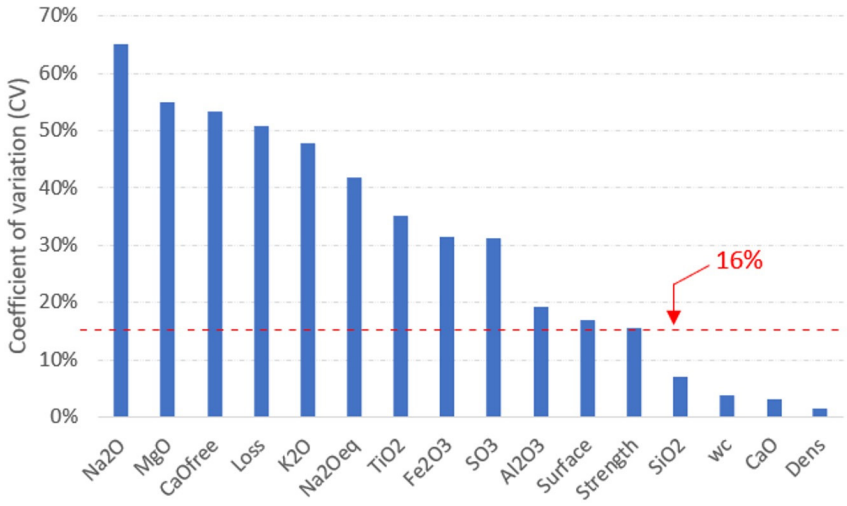

Figure 6. Coefficient of variation (CV) of each variable.

The interquartile range (IQR) measures the data sample distribution in-between the first (Q1) and third (Q3) quartiles (between 25th and 75th percentile). Therefore, IQR shows the range of values around the median (second quartile Q2) corresponding to the 50% central samples. Smaller IQR values imply more sample values toward the left and right tails: lowest and highest 25% values. The IQR and total range (max – min) values for each variable are presented in Table 2.

Figure 7a shows the IQR/Range ratio, in percentage, for each variable. The component CaO_{free} presented the highest ratio showing that 46% of the range amplitude correspond to 50% of the data samples. The K_2O and strength presented slightly more than one-third of range amplitude as IQR. This shows those three variables had quantitatively compacted data distribution around the median as shown in Figure 5. However, the oxides CaO, Fe_2O_3, SO_3; and the property specific surface (*surface*) had less than 15 of their respective total amplitude as IQR which shows that more than 85% of their samples are below the first quartile (25% lowest values) and above the third quartile (25% highest values). The water-cement ratio (*wc*) presented the lowest IQR/Range percentage due to the concentration of values on the right-hand side of the data distribution as shown and explained before in Figure 5.

Based on each IQR, a systematic method of identifying outliers can be used to establish limit values outside Q1 and Q3. The lower limit is 1.5IQR – Q1, while the upper limit is 1.5IQR + Q3, and any sample value outside those limits is considered an outlier. Figure 7b shows the percentage of outliers identified for each variable showing the specific surface, TiO_2, CaO, Fe_2O_3, SO_3 had more than 5% of each respective sample data as outliers. This agrees with the results of Figure 7a, which indicate higher percentages of the range of those variables toward the tails. The only exception is the TiO_2 that although presented a reasonable IQR/Range, had 8% of its data as outliers which demonstrated the use of very discrepant content of TiO_2 in the composition of ordinary cement. One possible explanation is that this oxide is not commonly used as a component of OPC. The high amount of 10% outliers of the surface showed a reasonable percentage of extreme results of those tests to characterize the specific surface presented by the literature for similar cement compositions. This property is related to cement grinding, the greater scatter and outlier percentage identified from collected data shows that this process is carried out in different ways in different countries and can influence the speed of hydration reactions and strength gain in the early ages of the final product.

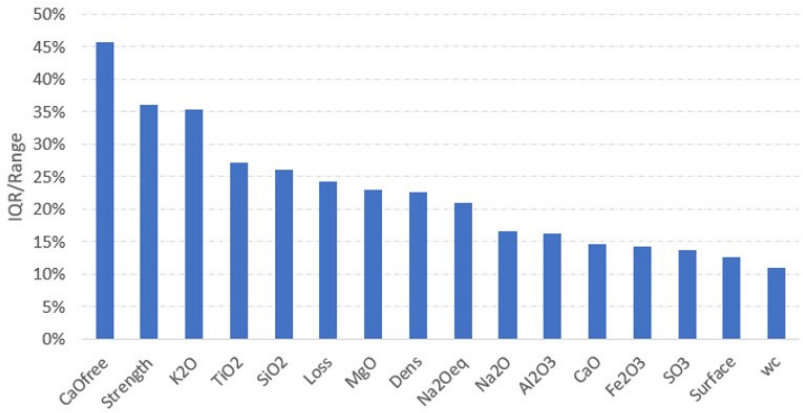

(a) IQR/Range

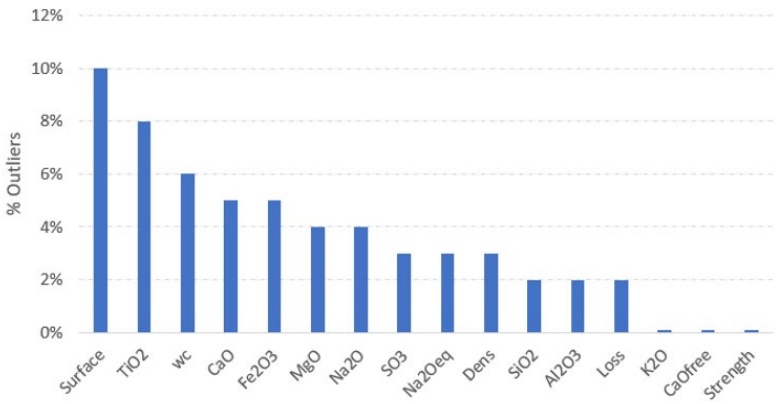

(b) Percentage of outliers

Figure 7. Interquartile range (IQR) and outlier quantification: a) IQR/Range and b) the percentage of outliers for each variable.

Regarding the data distribution of each variable, the sample skewness was determined to quantitatively assess the level of asymmetry of the data distribution around its mean. Figure 8 shows the skewness values of each variable and presents the schematic representation of symmetry or asymmetries, in which negative skewness indicates that the tail is on the left side of data distribution, and positive skewness indicates the distribution tail is on the right. Approximately null-value skewness indicates symmetric data distribution as shown in the figure. The oxides K_2O, SiO_2, CaO_{free}, and the compressive strength property had symmetric data distribution due to their very small skewness values (< 0.4). However, the three oxides Na_2O, MgO, and TiO_2 had significant skewness to the right side (skewness > 1.0), quantitatively confirming them to have an asymmetric data distribution. All the other variables showed a moderate to low skewness. The only exception is the water-cement ratio (*wc*) that presented -3.2 skewness due to the data concentration at 0.5 of the uniform standards.

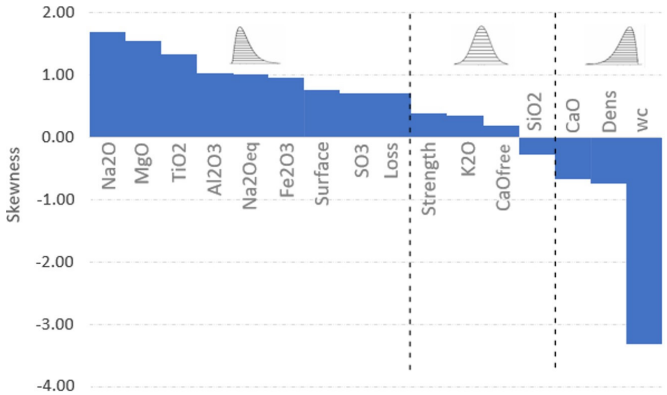

Figure 8. Skewness of data distribution of each variable.

3.2 Correlation between OPC physicochemical properties

The Pearson correlation matrix for the 16 variables is plotted in Figure 9. Due to the symmetry of the matrix, only the lower triangular part is plotted. Each coefficient (ρ) is a measure of linear correlation between two sets of data, and the color intensity means the magnitude of correlation coefficients for pair-wise combinations. Among the oxides, only the correlation between Na_2O_{eq} with Na_2O and K_2O, presented significant positive values of 0.72 and 0.68, respectively. This is somewhat expected since Na_2O_{eq} is derived from the other two oxides. A moderate negative correlation of -0.45 can be observed between CaO and MgO meaning that, when the percentage in the mass of one of these components tends to increase in the cement composition, the other oxide tends to decrease its percentage.

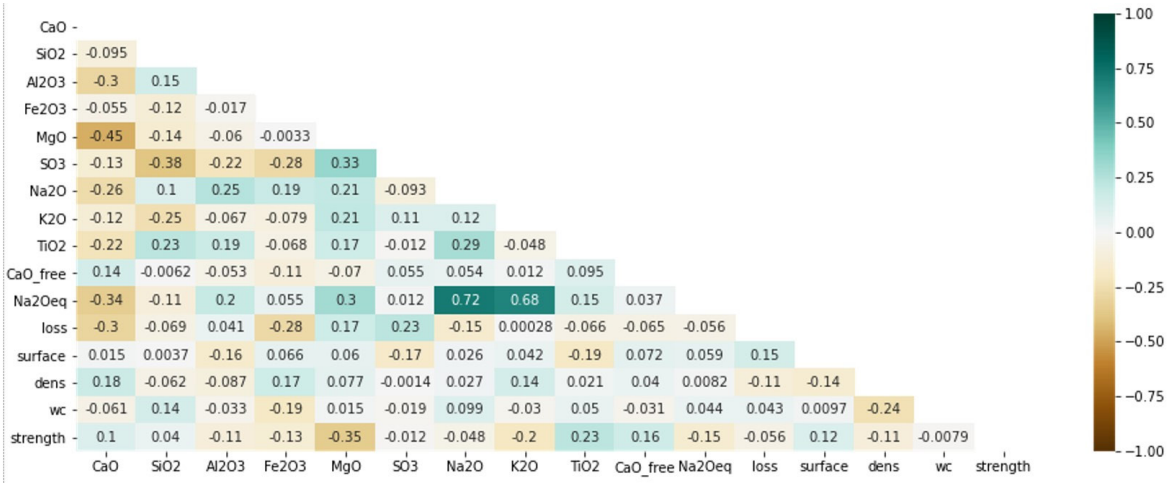

Figure 9. Pearson correlation matrix.

The last row of the Pearson correlation matrix, which corresponds to ρ-values between the compressive strength and all other variables, is plotted in Figure 10. The highest positive correlation (ρ=0.23) was found to be with TiO_2, whereas the highest negative correlation of ρ=-0.35 was with *MgO*. Nevertheless, those magnitudes can be considered moderate to low correlation values. According to Moreno [8], the addition of titanium dioxide to cement aims to adjust the raw material, and *MgO* is derived from the magnesium carbonate present in the original limestone in the form of dolomite, present only in small amounts depending on the specificity of the cement to be produced. Thus, the presence of these two compounds has no evidence of direct influence on compressive strength. It is important to note that the approximately null correlation between the water-cement ratio and compressive strength is due to the very low variability of the collected data set with almost all *wc* values being in 0.50 as already discussed.

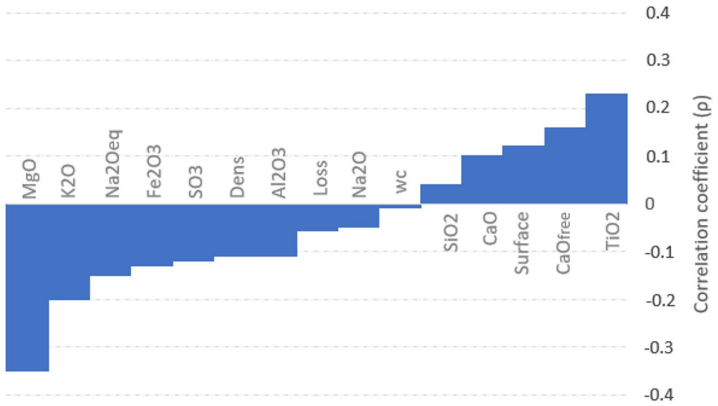

Figure 10. Pearson correlation coefficients between physicochemical variables and OPC's compressive strength.

4 CONCLUSIONS

This paper presented the methodology to construct and analyze a dataset, collected from the literature of different sources, types, and dates with the main thirteen physicochemical properties of Ordinary Portland Cement (OPC) as variables. It was searched the eleven most used oxides components of OPC and five commonly reported properties including the 28-day compressive strength. The dataset was analyzed through an exploratory statistical to quantify the main statistical properties and parameters for each variable and their correlations. The exploratory analysis provided a basic understanding of the data collected and the relationships between the analyzed OPC variables. The constructed dataset is a starting point to further studies with the addition of more data to complement and provide a broader global view of the production and properties of ordinary Portland cement.

The more specific conclusions from the analysis are:

- The main oxides *CaO* and SiO_2 that compose approximately 85% in mass of OPC presented very small data dispersion through their small coefficients of variation (< 7%). Therefore, the composition of OPC produced worldwide has low variability of *CaO* and SiO_2, which had the lowest coefficients of variation and are responsible for 2 of the 4 main components of cement, C_3S, and C_2S, indicating a certain standardization of these compounds. However, the 28-day compressive strength presented a much higher coefficient of variation reaching 16%. Most of the remaining oxides (Na_2O, *MgO*, CaO_{free}, K_2O, Na_2O_{eq}) presented higher dispersion values among the literature in which they had a coefficient of variation greater than 40%. Concerning the C_3A and C_4AF, moderate coefficients of variation were noticed for the oxides Al_2O_3 and Fe_2O_3.
- Compressive strength at 28 days presented a mean value of 50.7 MPa, and the data range for this property is mostly in-between 40 to 60 MPa, but some publications found more scattered values with a minimum value of 38.2 MPa and a maximum of 71.0 MPa. However, the 28-day strength presented symmetric data distribution and 36% of the data were within the IQR. Furthermore, no outlier was detected for the strength data. All these statistical measurements show a compact assemble of the strength for the OPC among the literature, despite the variability and high skewness of the main oxides that compose OPCs.
- Most of the oxides that compose the minority of the OPC in mass had non-symmetric data distribution, especially the Na_2O, *MgO*, TiO_2, and Al_2O_3 presented high skewness to the left (mean greater than the median). Among those

oxides, TiO_2 showed a high value of 8% of the outlier. The specific surface property was the variable that presented the most amount of outliers (10%) showing extreme values for this characterization reported by the literature.

- The ratio between the interquartile range (Q3 – Q1) and the total range (max – min) demonstrated to have a good agreement to the number of outliers detected by each variable, especially variables with higher values for that ratio presented very low or null percentage of outliers on their data samples.
- The correlations showed moderate negative correlation (-0.45) between *MgO* and the main oxide *CaO*, which indicates compositions with higher percentages of MgO had lower percentages of *CaO*. Moreover, the increase in the percentages of *MgO* on the OPC composition, moderately decrease the 28-day compressive strength as indicated by the negative correlation of -0.35 between those variables. The strength did not present any other relevant correlation with other variables.

ACKNOWLEDGEMENTS

This study was partially funded by the Coordenação de aperfeiçoamento de Pessoal de Nível Superior (CAPES) - Financial Code 001, Conselho Nacional de Desenvolvimento Científico e Tecnológico (CNPq), Fundação Universidade de Brasília (FUB) and Decanato de Pós-Graduação (DPG) of the University of Brasília, Brazil.

REFERENCES

[1] D. D. S. Mindess and J. F. Young, *Concrete*, 2nd ed. Upper Saddle River: Prentice Hall, 2003.

[2] B. A. Young, A. Hall, L. Pilon, P. Gupta, and G. Sant, "Can the compressive strength of concrete be estimated from knowledge of the mixture proportions?: New insights from statistical analysis and machine learning methods," *Cement Concr. Res.*, vol. 115, pp. 379–388, 2019, http://dx.doi.org/10.1016/j.cemconres.2018.09.006.

[3] T. Oey, S. Jones, J. W. Bullard, and G. Sant, "Machine learning can predict setting behavior and strength evolution of hydrating cement systems," *J. Am. Ceram. Soc.*, vol. 103, no. 1, pp. 480–490, 2020, http://dx.doi.org/10.1111/jace.16706.

[4] P. K. Mehta and P. J. M. Monteiro, *Concrete: Microstructure, Properties, and Materials*, 4th ed. New York: McGraw-Hill Education, 2014. Accessed: Oct. 15, 2022. [Online]. Available: https://www.accessengineeringlibrary.com/content/book/9780071797870

[5] W. C. Kosmatka, S. H. Kerkhoff, and B. Panarese, *Design and Control of Concrete Mixtures*, 14th ed. Illinois, USA: Skokie, 2002.

[6] J. W. Bullard et al., "Mechanisms of cement hydration," *Cement Concr. Res.*, vol. 41, no. 12, pp. 1208–1223, 2011, http://dx.doi.org/10.1016/j.cemconres.2010.09.011.

[7] A. M. Neville, *Propriedades do Concreto* [Concrete properties]. Porto Alegre: Bookman, 2016.

[8] F. A. C. Moreno, "Predição da resistência à compressão de um cimento industrial utilizando técnicas de redes neurais artificias" [Prediction of the compressive strength of an industrial cement using artificial neural network techniques], M.S. thesis, Fac. Chem. Eng., State Univ. Campinas, Campinas, 2001.

[9] J. J. Neville and A. M. Brooks, *Tecnologia do Concreto* [Concrete technology], 2ª ed. Porto Alegre: Bookman, 2013.

[10] W. de Q. Lamas, J. C. F. Palau, and J. R. de Camargo, "Waste materials co-processing in cement industry: ecological efficiency of waste reuse," *Renew. Sustain. Energy Rev.*, vol. 19, pp. 200–207, 2013, http://dx.doi.org/10.1016/j.rser.2012.11.015.

[11] A. A. Bogush et al., "Co-processing of raw and washed air pollution control residues from energy-from-waste facilities in the cement kiln," *J. Clean. Prod.*, vol. 254, pp. 119924, 2020, http://dx.doi.org/10.1016/j.jclepro.2019.119924.

[12] M. Achternbosch, K.-R. Bräutigam, N. Hartlieb, C. Kupsch, U. Richers, and P. Stemmermann, "Impact of the use of waste on trace element concentrations in cement and concrete," *Waste Manag. Res.*, vol. 23, no. 4, pp. 328–337, 2005, http://dx.doi.org/10.1177/0734242X05056075.

[13] B. Lothenbach, K. Scrivener, and R. D. Hooton, "Supplementary cementitious materials," *Cement Concr. Res.*, vol. 41, no. 12, pp. 1244–1256, 2011, http://dx.doi.org/10.1016/j.cemconres.2010.12.001.

[14] J. F. N. Chaves, D. L. Nascimento, E. Fonseca, and J. H. S. Rêgo, "Estado da arte sobre o Cimento LC^3," [State of the art about the LC^3 Cement], *Brazilian Congress of Concrete*, 2017.

[15] R. H. Bogue, *The Chemistry of Portland Cement*, 2nd ed. Washington: Reinhold Publishing, 1955.

[16] D. S. Andrade, "Microestrutura de pastas de cimento Portland com nanossílica coloidal e adições minerais altamente reativas [Microstructure of Portland cement pastes with colloidal nanosilica and highly reactive mineral additions]," Ph.D. dissertation, Univ. Brasília, Brasília, 2017.

[17] P. Palacios, M. Hadi, K-K. Mantellato, and S. Bowen, "Laser diffraction and gas adsorption techniques," in *Practical Guide to Microstructural Analysis of Cementitious Materials*, K. L. Scrivener, R. Snellings and B. Lothenbach, Eds., Boca Raton: CRC Press, 2016, pp. 446–472.

[18] American Society for Testing and Materials, *Standard Test Method for Compressive Strength of Hydraulic Cement Mortars*, ASTM C109/C109M-21, 2021.

[19] European Standard, *Methods of Testing Cement - Part 1: Determination of Strength*, EN 196-1, 2016.

[20] Associação Brasileira de Normas Técnicas, *Cimento Portland - Determinação da Resistência à Compressão de Corpos de Prova Cilíndricos*, NBR 7215, 2019.

[21] C. Malami, V. Kaloidas, G. Batis, and N. Kouloumbi, "Carbonation and porosity of mortar specimens with pozzolanic and hydraulic cement admixtures," *Cement Concr. Res.*, vol. 24, no. 8, pp. 1444–1454, 1994, http://dx.doi.org/10.1016/0008-8846(94)90158-9.

[22] B. Felekoğlu, K. Ramyar, K. Tosun, and B. Musal, "Sulfate resistances of different types of Turkish Portland cements by selecting the appropriate test methods," *Constr. Build. Mater.*, vol. 20, no. 9, pp. 819–823, 2006, http://dx.doi.org/10.1016/j.conbuildmat.2005.01.048.

[23] A. K. Parande, B. Ramesh Babu, M. Aswin Karthik, K. K. Deepak Kumaar, and N. Palaniswamy, "Study on strength and corrosion performance for steel embedded in metakaolin blended concrete/mortar," *Constr. Build. Mater.*, vol. 22, no. 3, pp. 127–134, 2008, http://dx.doi.org/10.1016/j.conbuildmat.2006.10.003.

[24] Y. Yao and H. Sun, "Durability and leaching analysis of a cementitious material composed of high volume coal combustion byproducts," *Constr. Build. Mater.*, vol. 36, pp. 97–103, 2012, http://dx.doi.org/10.1016/j.conbuildmat.2012.04.100.

[25] Y. Dhandapani, T. Sakthivel, M. Santhanam, R. Gettu, and R. G. Pillai, "Mechanical properties and durability performance of concretes with Limestone Calcined Clay Cement (LC3)," *Cement Concr. Res.*, vol. 107, pp. 136–151, 2018, http://dx.doi.org/10.1016/j.cemconres.2018.02.005.

[26] C. M. Yun, M. R. Rahman, C. Y. W. Phing, A. W. M. Chie, and M. K. Bin Bakri, "The curing times effect on the strength of ground granulated blast furnace slag (GGBFS) mortar," *Constr. Build. Mater.*, vol. 260, pp. 120622, 2020, http://dx.doi.org/10.1016/j.conbuildmat.2020.120622.

[27] Tyche, *Data Science and Artificial Intelligence Software*. 2020.

[28] Bureau of Indian Standards, *Methods of Physical Tests for Hydraulic Cement Part 6 Determination of Compressive Strength of Hydraulic Cement Other Than Masonry Cement (First Revision)*, IS 4031 (Part 6), 2005, pp. 1–3. Accessed: Oct. 15, 2022. [Online]. Available: https://ia800400.us.archive.org/0/items/gov.in.is.4031.6.1988/is.4031.6.1988.pdf

[29] Bureau of Indian Standards, *Methods of Physical Tests for Hydraulic Cement. Part IV- Determination of Consistency of Standard Cement Paste*, IS 4031 (Part 4), 1988.

[30] L. A. Gobbo, "Aplicação da difração de raios-X e método de Rietveld no estudo de Cimento Portland" [Application of X-ray diffraction and Rietveld Method in the study of Portland cement], M.S. thesis, Inst. Geosci., Univ. São Paulo, São Paulo, 2009.

[31] S. H. Shim, T. H. Lee, S. J. Yang, N. B. M. Noor, and J. H. J. Kim, "Calculation of cement composition using a new model compared to the bogue model," *Materials*, vol. 14, no. 16, pp. 4663, 2021, http://dx.doi.org/10.3390/ma14164663.

Author contributions: J.F.N.C conceptualization, experimental procedure, methodology, analysis, and writing; F.E.J experimental procedure, data curation, supervision and revising; J.H.S.R supervision and revising; L.P.V supervision.

Editors: Fernando Pelisser, Guilherme Aris Parsekian.

IBRACON Structures and Materials Journal
Revista IBRACON de Estruturas e Materiais
ISSN 1983-4195 ismj.org

ORIGINAL ARTICLE

Dynamic identification of a cable-stayed footbridge using a low-cost data acquisition system

Identificação dinâmica de uma passarela estaiada utilizando um sistema de aquisição de dados de baixo custo

Danilo de Santana Nunes[a]
José Luis Vital de Brito[b]
Graciela Nora Doz[b]

[a]Universidade Estadual de Santa Cruz - UESC, Departamento de Engenharias e Computação, Ilhéus, BA, Brasil
[b]Universidade de Brasília - UnB, Programa de Pós-graduação em Estruturas e Construção Civil, Brasília, DF, Brasil

Received 19 October 2022
Accepted 23 February 2023

Abstract: This study describes the dynamic identification of a cable-stayed footbridge using an alternative data acquisition system and output-only modal identification methods. Data were collected during dynamic tests performed using an acquisition system based on the Arduino platform, consisting of low-cost devices with on-board Micro-Electro-Mechanical System (MEMS) accelerometers. The Peak-Picking (PP) method was used for the stay cables. The Frequency Domain Decomposition (FDD) and Stochastic Subspace Identification – Unweighted Principal Components (SSI-UPC) methods were used for the complete structure. The proposed data acquisition system efficiently recorded the time series required for Operational Modal Analysis and the acceleration acquisition process provided stable results. At least four mode shapes were identified in all tests. A minimum of four high energy peaks in the 0 – 24 Hz frequency range of the spectrum were obtained by the acquisition system in all of the cable tests and selected by the method. In the complete structure tests, the low-cost data acquisition system and the identification methods provided the first four flexural mode shapes, within the 0 – 9 Hz frequency range. Results for the frequency domain method showed a maximum difference of 2.37% in the first experimental frequency when compared to a 3D finite element numerical model, while in the other frequencies the difference was between 1 and 2%. For the time domain method, the maximum difference was 1.74% in the fourth frequency, with differences of between 0.1 and 0.7% in the other frequencies. The mode shapes were evaluated using the Modal Assurance Criterion (MAC) index, and the results varied between 0.8513 and 0.9990.

Keywords: cable-stayed footbridge, data acquisition system, modal identification, dynamic tests, low-cost devices.

Resumo: Este trabalho apresenta a identificação dinâmica de uma passarela estaiada a partir da aplicação de um sistema de aquisição de dados alternativo e métodos de identificação modal que se baseiam apenas na resposta. Os dados foram coletados durante ensaios dinâmicos realizados com um sistema de aquisição baseado na plataforma Arduino, composto por dispositivos de baixo custo com acelerômetros microeletromecânicos embarcados. Para os estais, foi utilizado o método *Peak-Picking*. Para a estrutura completa, foram utilizados os métodos *Frequency Domain Decomposition* e o *Stochastic Subspace Identification – Unweighted Principal Components*. O sistema de aquisição de dados proposto registrou as séries temporais necessárias para a Análise Modal Operacional de forma eficiente e o processo de aquisição das acelerações proporcionou resultados estáveis. Pelo menos quatro formas modais foram identificadas em todos os testes. Em todos os ensaios dos estais, um mínimo de quatro picos de alta energia na faixa de frequência entre 0 – 24 Hz do espectro foram obtidos com o sistema de aquisição e selecionados pelo método. Nos ensaios da estrutura completa, o sistema de aquisição de dados de baixo custo e os métodos de identificação forneceram os quatro primeiros modos de flexão, dentro da faixa de frequência entre 0 – 9 Hz. Os resultados do método no domínio da frequência mostraram uma diferença máxima, quando comparados aos de um modelo numérico 3D em elementos finitos, de 2,37% na primeira frequência experimental, enquanto que nas demais frequências a diferença ficou entre 1 e 2%. Para o método no domínio do tempo, a diferença máxima foi de 1,74% na quarta frequência, enquanto que nas demais, a diferença ficou entre 0,1 e

Corresponding author: Danilo de Santana Nunes. E-mail: dsnunes@uesc.br
Financial support: None.
Conflict of interest: Nothing to declare.
Data Availability: The data that support the findings of this study are available from the corresponding author, [D. de S.], upon reasonable request.

0,7%. As formas modais foram avaliadas através do índice *Modal Assurance Criterion*, e os resultados variaram entre 0,8513 e 0,9990.

Palavras-chave: passarela estaiada, sistema de aquisição de dados, identificação modal, ensaios dinâmicos, dispositivos de baixo custo.

How to cite: D. S. Nunes, J. L. V. Brito, and G. N. Doz, "Dynamic identification of a cable-stayed footbridge using a low-cost data acquisition system," *Rev. IBRACON Estrut. Mater.*, vol. 16, no. 6, e16610, 2023, https://doi.org/10.1590/S1983-41952023000600010

1 INTRODUCTION

Bridge maintenance, safeguarding, and health monitoring are important topics in the prevention of potentially catastrophic events [1]. Analysis generally involves accurate numerical modeling of the structure, which must be calibrated, usually for the material parameters and boundary conditions, according to the on-site response to the dynamic loads [2]. Modal parameters estimated from the data obtained via nondestructive tests, usually ambient vibration tests, can be used in the structural model updating and Structural Health Monitoring (SHM) processes. The dynamic properties are also useful for model updating [3] and provide a good evaluation tool for non-destructive damage assessment [4]. As such, buildings and other structures (e.g., bridges, highways, etc.) have been equipped with monitoring systems that provide continuous control, thus minimizing the possibility of structural hazards [5]. The usual sensing techniques used in SHM include piezoelectric transducers, Macro Fiber Composites, optic Fiber Bragg Grating sensors, accelerometers, strain gauges, acoustic emission sensors, etc. [6], but new ideas have been proposed for recording the dynamic response of structures [7]. Novel sensing technologies, high-speed computing, and communication technologies could enable the engineering community to measure and evaluate ambient structural vibrations quickly and accurately [8].

Both the traditional and innovative systems have advantages and disadvantages. The traditional systems are composed of acquisition boards and signal conditioners that offer the best performance to date, using analog sensors that offer high sensitivity and low signal noise. The most recent systems mainly pursue wireless solutions in order to eliminate interruptions to the structures' operations, as well as provide continuous and remote monitoring of the structure, as described in [9], [10]. It would be much less expensive to use low-cost sensors for this purpose that can remain fixed to or embedded in the structure (not recovered), as long as they offer acceptable performance and robustness. The digital sensors known as Micro-Electro-Mechanical Systems (MEMS) display these characteristics. The benefits of these sensors include their small size, low weight, high performance, easy mass production, low cost [11], and low power consumption, which is an important advantage of battery-powered wireless systems. Their main disadvantage is that they lack the high sensitivity of an analog sensor [5], as well as presenting more output noise. However, despite this, research groups working in a range of fields have obtained promising results with their low-cost systems [12]-[16]. The civil engineering area could also benefit from this technology, which has become increasingly accessible with the growth of electronic prototyping platforms such as the Arduino platform. The Arduino devices, boards, and sensors providing interesting commercial alternatives for these types of applications [17].

Arduino boards can read inputs and turn them into an output. The board can be controlled via a set of instructions sent to its microcontroller, using the Arduino programming language [18] and the Arduino Integrated Development Environment (IDE) [19], [20]. This enables the creation of tools capable of high-resolution environmental monitoring without a large financial investment and with minimal development effort or experience. Additionally, the Arduino boards have demonstrated that they are capable of withstanding a large amount of physical abuse [21]. This physical resistance demonstrates their capacity for use in the application of continuous health monitoring of civil structures [17]. The option selected for this research was the Arduino/Genuino 101 board (a low-cost device), equipped with the Bosch BMI160 3-axis accelerometer and gyroscope, and the open software Realterm [22] to capture and register the acceleration time series. This paper focuses on the dynamic properties identification of a cable-stayed footbridge via the application of output-only modal identification methods, using the data collected with a low-cost data acquisition system. This is the first step in the integrity evaluation process of cable-stayed structures, which would follow these steps: *i*) dynamic testing of the stay cables and complete structure using a low-cost data acquisition system; *ii*) identification of the natural frequencies of the stays using a dynamic identification method, in order to determine the prestressing forces through the Mersenne/Taylor Law; *iii*) identification of the dynamic properties (natural frequencies and modes of vibration) of the structure using stochastic modal identification methods, given the difficulty of using deterministic excitations and even interrupting the operation of infrastructure constructions, as is the case with cable-stayed structures (bridges and footbridges); *iv*) design and updating of the numerical model of the structure by inserting the experimental prestressing forces of the stays into the numerical model and optimization of the materials properties

process; *v*) analysis of the current efforts of the structure, provided by the updated numerical model, in comparison with the structural design, so as to identify overloaded regions; *vi*) new testing and updating stages at pre-defined age intervals, using the updated numerical model as a reference, in order to identify any variations in the dynamic properties and stay forces that could characterize a change in the stiffness and equilibrium condition of the structure, indicating structural problems in service. The methods and computational systems used in the first three steps, which were the objective of this research, are presented below in detail.

2 DYNAMIC STRUCTURAL IDENTIFICATION

Three methods were used for dynamic identification, two in the frequency domain and one in the time domain. The cable tests used one sensor to determine only the natural frequencies of the system, using the frequency domain Peak-Picking (PP) Method. The complete structure tests used three sensors and 17 setups, which enabled the mode shapes to be obtained using the Frequency Domain Decomposition (FDD) and the Stochastic Subspace Identification – Unweighted Principal Components (SSI-UPC) methods.

2.1 Peak-Picking Method (PP)

The structure's natural frequencies are associated with the values of frequency peaks, where the amplitude tends to infinity in the Frequency Response Function (FRF) and in the power spectrum estimated using the Fast Fourier Transform (FFT). Equation 1 shows the FFT applied to the signal $R(\tau)$, resulting in the power spectrum $S(f)$.

$$S(f) = \int_{-\infty}^{\infty} R(\tau) e^{-i2\pi f\tau}\, d\tau \tag{1}$$

For multiple degrees of freedom, the spectral information can be organized into matrices as shown in Equation 2:

$$S_q(f) = H(f)\, S_p(f)\, H^H(f) \tag{2}$$

where $S_q(f)$ = Power Spectral Density (PSD) functions matrix of response; $H(f)$ = FRFs matrix; $H^H(f)$ = transposed conjugate of matrix $H(f)$; and $S_p(f)$ = PSD functions matrix of excitation.

2.2 Frequency Domain Decomposition Method (FDD)

The FDD also uses the PSD functions of the response and adopts the following steps:

i) Calculation and evaluation of the normalized PSD functions of the response: Normalization is an artifice used to overcome certain drawbacks when working with several measurement setups, such as the greatest number of degrees of freedom. This provides a higher number of frequency peaks of each auto-spectrum to be identified, and the variation in excitation intensity during the test, which leads to different energy contents for the measured time series. Thus, it is sought to normalize the energy content of each spectrum, which can be performed by dividing each ordinate of the $PSD_i(\omega)$ function by summation of all ordinates N, resulting in a normalized function ($NPSD_i(\omega)$), as follows:

$$NPSD_i(\omega) = \frac{PSD_i(\omega)}{\sum_{k=1}^{N} PSD_i(\omega_k)} \tag{3}$$

Through Equation 3, we achieve equality between the areas under each spectrum. The next step is to determinate the average $NPSD_i(\omega)$, the $ANPSD$ functions, by Equation 4:

$$ANPSD = \frac{1}{setups} \sum_{i=1}^{setups} NPSD_i\,(\omega) \tag{4}$$

ii) Singular Value Decomposition (SVD) of the average normalized PSD functions matrix;

iii) Peak selection of the average normalized PSD decomposed in singular values, which correspond to the structure's natural frequencies;
iv) Evaluation of mode shapes through the singular vectors related to the singular values (natural frequencies) obtained at the degrees of freedom (measurement points).

2.3 Stochastic Subspace Identification – Unweighted Principal Components Method (SSI-UPC)

Subspace methods identify state-space models from (input and) output data by applying numerical techniques, such as QR factorization and SVD. The discrete-time deterministic state-space model is obtained by Equations 5 and 6:

$$x_{k+1} = Ax_k + Bp_k \tag{5}$$

$$y_k = Cx_k + Dp_k \tag{6}$$

where x_k = discrete-time state vector; p_k = input samples; y_k = output samples; A = discrete system state matrix; B = discrete input matrix; C = output matrix; D = direct transmission matrix.

The SSI-UPC follows these steps:

i) Kalman filter application: The aim of the Kalman filter is to produce an optimal prediction, $\hat{X}_i$, for the state vector x_k by making use of observations of the outputs up to time k-1 and the available system matrices, together with noise and others uncertainties.
ii) Organization of response time series by the Hankel matrix: Reduction of the matrices is performed in the Data-Driven Stochastic Subspace by projecting the row space of the future outputs into the row space of the past reference sensors (outputs). This projection is computed from the QR factorization of a big data Hankel matrix. In addition, this also aims to cancel out the noise.
iii) Projection matrix weighting: The data matrices are weighted before the application of the SVD. This weighting determines the state-space basis in which the identified model will be identified. In SSI-UPC, as the term "unweighted" suggests, the weighting matrices W_1 and W_2 applied to the projection matrix P_i^{ref} are equal to identity matrices I with the same order, as follows (Equation 7):

$$P_{i,w}^{ref} = W_1 P_i^{ref} W_2 \tag{7}$$

where $P_{i,w}^{ref}$ = weighted projection matrix.

Influencing the state vector prediction:

$$\hat{X}_i = O_i^* P_{i,w}^{ref} \tag{8}$$

where $\hat{X}_i$ = optimal state vector prediction; O_i^* = conjugate transpose of the observability matrix.
iv) SVD: The decomposition reveals the order of the system and the column space of the observability matrix O_i (Equation 8).
v) Identification of system matrices: After applying the numerical techniques described above, the stochastic state-space model representation for multiple degrees of freedom results in Equation 9:

$$\begin{bmatrix} \hat{X}_{i+1} \\ Y_{i/i} \end{bmatrix} = \begin{bmatrix} A \\ C \end{bmatrix} \hat{X}_i + \begin{bmatrix} W_i \\ V_i \end{bmatrix} \tag{9}$$

where $\hat{X}_{i+1}$ = Kalman filter state sequence; $Y_{i/i}$ = Hankel matrix with only one block row; W_i = process noise; and V_i = measurement noise, which is considered as white noise can be excluded from the process because of its constant energy content, resulting in Equation 10:

$$\begin{bmatrix} A \\ C \end{bmatrix} = \begin{bmatrix} \hat{X}_{i+1} \\ Y_{i/i} \end{bmatrix} \hat{X}_i^* \tag{10}$$

where $\hat{X}_i^*$ = conjugate transpose of the $\hat{X}_i$ vector.

The modal parameters of the dynamical system can then be extracted from the state matrix A, which contains the matrices of the structure (M, C_1 and K), based on solving an eigenvalues and eigenvectors problem. Equation 11 shows the system matrices:

$$A = \begin{bmatrix} 0 & I \\ -M^{-1}K & -M^{-1}C_1 \end{bmatrix} \tag{11}$$

where M = mass matrix; C_1 = damping matrix; and K = stiffness matrix of the structure.

vi) Stabilization diagram: Selects stable, unstable and noise modes, thus determining the dimension of the ideal state space. For modes to be classified as stable they must meet certain requirements, e.g., valid range of damping rates. By adjusting this range, harmonic components and non-physical modes can be filtered out, with only true modes of vibration highlighted as stable modes.

More details about the methods presented above can be found in [23] and [24].

3 MATERIALS AND EXPERIMENTAL PROGRAM

3.1 Data Acquisition System

The acquisition system assembled to perform the dynamic tests of the complete structure consisted of a computer with data acquisition software, three 5.0m-long USB A/B cables, three 15.0m-long USB A/B extension cables equipped with signal amplifiers, and three Arduino/Genuino 101 boards. For the stay cable tests, the acceleration time series were obtained using one Arduino/Genuino 101 board connected to the computer by a 3.0m-long USB A/B cable. Figure 1 shows the components of the data acquisition system.

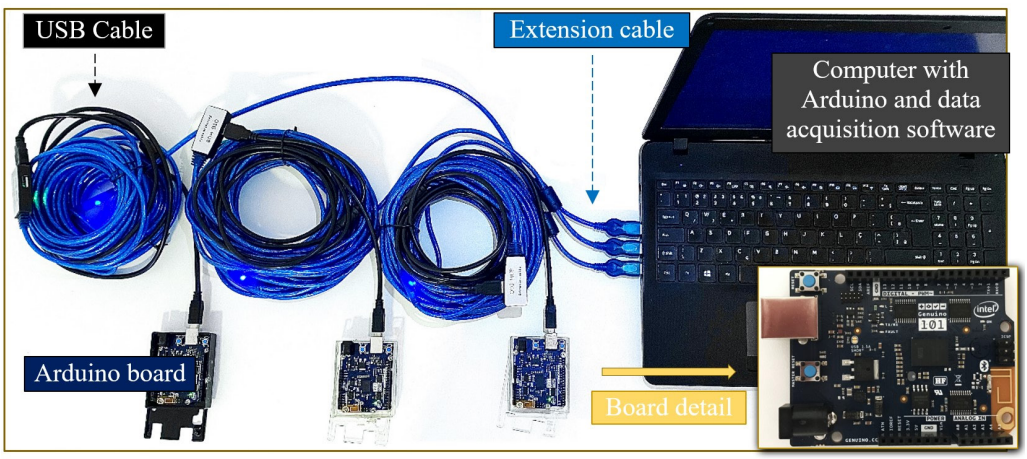

Figure 1. Data acquisition system - Arduino boards, cables, extension cables and computer.

The Arduino/Genuino 101 board comes preprogrammed with a Real Time Operating System (RTOS) that handles USB connection and allows new code to be uploaded without the use of an external hardware programmer. It communicates using the device firmware update protocol. It contains the Intel® Curie™ Module, designed to integrate the core's low power consumption and high performance with the Arduino boards. It maintains the same robust form factor and peripheral list as the Arduino UNO basic board version, with the addition of on-board Bluetooth LE capabilities and a 6-axis accelerometer/gyroscope. The RTOS and framework developed by Intel is open sourced. The

board has 14 digital input/output pins, six analog inputs, a USB connector for serial communication and uploading of sketches (which can also be used as a power supply), a power jack, an ICSP header with SPI signals, and I2C dedicated pins [25]. It can be supplied with the following specifications: 7 – 12V (via DC power jack), 7 – 12V (via VIN pin), or 5V (via USB connector), with the latter used in this research. In addition, the board can be powered by an external power supply, which represents an important feature for large structure applications.

To work with the acceleration data it is necessary to implement the "CurieIMU.h" library, which gives access to all the parameters, features and readings of the Arduino/Genuino 101 board's Inertial Measurement Units (IMU) chip. This library is part of the board core and it is loaded together with the core files [25]. Each board was programmed during this research, using the open-source Arduino IDE, to read accelerations at the desired sampling frequency (above 200 Hz) by using the loop function, which repeats the implemented code at the desired time, and with enough output data to obtain the time series (time, accelerations in x, y, and z-axis directions). The Bosch BMI160 3-axis accelerometer and gyroscope contained in the board's IMU chip has ±2 g sensitivity at 16384 LSB/g and 180 μg/√Hz typical output noise. The Arduino/Genuino 101 was chosen for this research because of its practicality for use in real structures. Its compact shape and sturdiness are attractive for applications in the structural engineering field.

Open-source RealTerm software was used to capture and record the accelerations measured by the on-board Bosch BMI160 accelerometer. This serial terminal program is designed for capturing, controlling and debugging binary and other difficult data streams. It automatically identifies and registers any device programmed to perform measurements, simply by selecting the desired USB port. For example, for the tests with three Arduino boards, three USB ports were selected and used simultaneously through three different RealTerm software windows.

The proposed data acquisition system was tested in advance by the research team in the laboratory. Three different structural models were used–a three-story shear building reduced model, a fixed-free bar reduced model, and a concrete slab (6.1 m long, 4.9 m wide and 0.1 m thick)–in four different tests, with one sensor applied in each model (three tests) and two sensors applied with the slab (the fourth test), in order to also identify mode shapes. In the shear building and fixed-free bar tests, which used manually imposed initial displacements to put the models in free vibration, the proposed system's results were compared to a professional system consisting of an accelerometer made by Endevco (model 7754-A), a signal conditioner made by Endveco (model 4416BM1), and a data acquisition module made by Linx (model ADS2000). In the concrete slab tests with one and two sensors, which used the heel drop test, the results were compared to a professional system consisting of accelerometers made by PCB Piezotronics (model 353B33), a signal conditioner made by PCB Piezotronics (model 482A22), and a data acquisition module made by Linx (model ADS2000). The tests were used to evaluate the capacity of the data acquisition system in a specific frequency range (≈ 1.00 Hz – 37.83 Hz) equivalent to that of real structures, especially cable-stayed structures, which present structural problems due to excessive oscillations. In addition, it was possible to use usual sampling frequency values for testing civil engineering structures (around 200 Hz). All experiments presented promising results. For the tests with one sensor, the maximum difference in the natural frequencies identified compared to a professional accelerometer was 2.41%. The test using two sensors also enabled the identification of three mode shapes, and a maximum difference in the natural frequencies of 4.30% was obtained (related to the third mode shape). More details about the validation of the proposed data acquisition system can be found in [17].

3.2 The footbridge

The cable-stayed footbridge crosses the BR101 highway at km 88, in the city of Nossa Senhora do Socorro, Sergipe State, Brazil. The deck is 58.0 m long and 2.0 m wide, divided into two parts by a single central mast 22.4 m tall. The semi-fan cable arrangement of the bridge is distributed spatially in two inclined planes on each side of the deck. Each plane has eight stay cables. Half of the 16 cables are backstays, anchored externally to a foundation block (see Figure 2a). All of the stays use 32 mm-diameter Dywidag bars and the superstructure concrete has fck = 30 MPa (design value). Problems with the foundations of the structure resulted in unexpected deformation of the mast and deck. This problem was resolved, but the footbridge displays excessive oscillations in service under usual loads (pedestrians crossing and wind). These were factors that encouraged this research to be undertaken.

A 3D finite element model of the footbridge was created for this study using SAP2000 software [26] (see Figure 2b). Six-degree-of-freedom single beam elements at each end were used for the deck and tower, and cable elements were used for the stay cables, totaling 349 beam elements, 16 cable elements, 468 nodes, and 2808 degrees of freedom. Specifically, four 3D beam elements with equivalent stiffness were used for the deck. The cross-section was divided into four parts; the moment of inertia and the centroid showing the longitudinal equivalent element positions were calculated for each part. The stiffness of transverse elements was calculated for the 0.5 m half-widths between them (3D beam elements were also used). For the tower, 3D beam elements considering the design cross-section were used

and, for the stay cables, cable elements with undeformed lengths. The concrete weight per unit volume was assumed to be 25.0 kN/m^3 and the modulus of elasticity to be 30 GPa. The cable (Dywidag bar) weight per unit volume provided by the manufacturer was 76.9415 kN/m^3 and the modulus of elasticity was 205 GPa. The boundary conditions between the deck and tower, the deck and anchorage block, and the tower and foundation were considered fixed for rotations and displacements. The pylon support was assumed to be fixed for displacements only, as well as the connection between the stay cables and the anchorage block. The numerical model, used here only to define the test setups through the theoretical mode shapes and to evaluate the experimental results, presented perfect contact and sliding boundary conditions, which can be calibrated using the dynamic properties extracted experimentally.

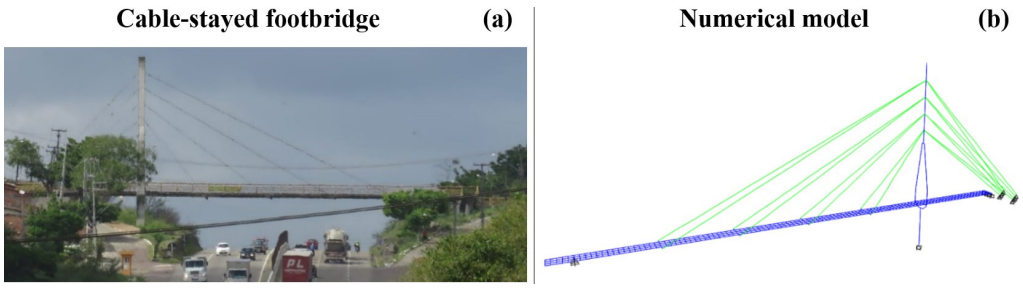

Figure 2. (a) Cable-stayed footbridge, Sergipe, Brazil; **(b)** Numerical model.

3.3 Field test routine

The excitation types cited in the literature for the various tests conducted on footbridges during experimental analysis result from shock, slow sine sweep testing, ambient vibration (normal operating conditions), and pedestrian walking and jumping [27]-[29]. Although there are several modal test techniques available for footbridges, those that require investigation are generally lightweight, with natural frequencies of less than 5 Hz, and can be excited with high energy for the designed load, such as pedestrians crossing. Consequently, the response generated by pedestrians walking or jumping is widely used in footbridge dynamic testing [28]. For stay cables, a range of techniques with different sensors have been used, i.e., lift-off test, electromagnetic sensor method, and vibration method (using accelerometers, laser interferometry, Ground-based Microwave Interferometer, etc.) [30]-[32].

In addition to people crossing, the main excitation factors during the tests were wind and air displacement caused by trucks driving by under the footbridge, which remained quite stable during the testing period. Additionally, during the complete structure tests two people ran and jumped along the footbridge deck to increase the excitation energy. The 205 Hz sampling frequency lasted for 30 s, with a total of 6150 acceleration samples in g scale measured by three sensors fixed to the structure with scotch tape. The same procedure was used as in the acquisition system validation tests (surface cleaning and sensors protected by acrylic case, fixed directly to the structure). Despite the rule of thumb presented in the dynamic testing literature, the 30 s time window was adopted as a result of a limitation detected in the data acquisition system. The number of recorded samples varied for intervals longer than 30 seconds, even while using the same codes for the three boards, which affected the synchronization of the obtained data. In a previous evaluation, a relationship was identified between the measured data volume (sampling frequency), number of connected boards, and the computer processing power. This problem was not crucial to the case study but will be thoroughly investigated in the future.

The tests of the complete structure were conducted using 17 setups along the deck and mast. For each test setup, one board was used as a stationary sensor and two boards as mobile sensors. The stationary sensor (Arduino board 1) was positioned in the connection region of the deck with the stay cable 3 at left (S3-L). It was defined as a reference measurement point for all test setups for calibrating energy content and normalizing signals. Based on analysis of the mode shapes provided by the numerical model of the footbridge), the position proved to be promising as it presents significant coordinates in almost all theoretical mode shapes. The pair of mobile sensors (Arduino boards 2 and 3) moved through 34 other measurement points, resulting in 17 test setups. The Arduino boards were synchronized by recording the computer operating system time in the board output. Although the accelerations were recorded in three directions, significant energy content was only generated perpendicularly to the structural elements. Therefore, only the z-direction in the deck and y-direction in the mast were considered in the system identification process. Figure 3 shows the test setups used in the Operational Modal Analysis (OMA).

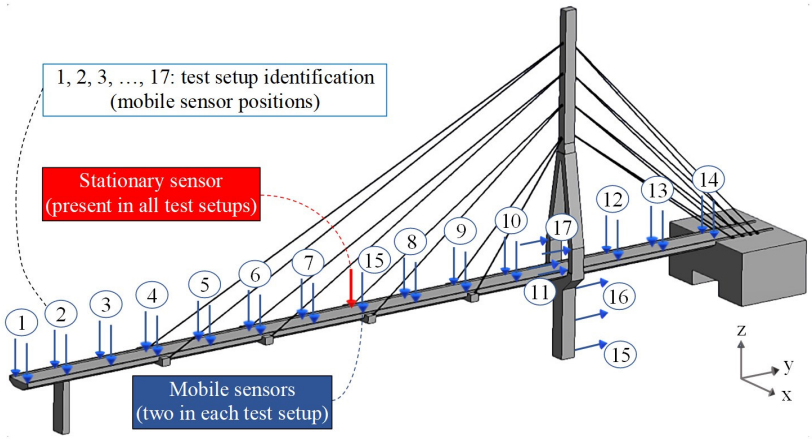

Figure 3. Test setups.

The excitation energy in the stay cables was increased by manually-imposed random initial displacements, while an Arduino board placed 2.0 m from the deck and fixed to the stay with a clamp measured the accelerations. The position chosen permitted identification of a minimum of four mode shapes. The 210 Hz sampling frequency lasted 30 s, with a total of 6300 acceleration samples on g scale. Figure 4 shows the test scheme and the proposed data acquisition system installed on-site, these examples are from Test setup 9 (global tests) and stay cable 2 at left (S2-L).

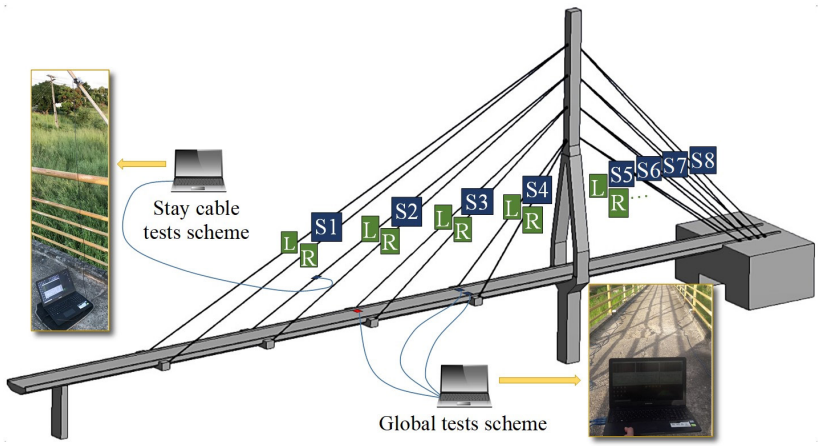

Figure 4. Data acquisition system installed on the footbridge – Global and stay cable tests.

4 RESULTS AND DISCUSSIONS

The experimental results of this research are presented below. The proposed data acquisition system was used in the dynamic tests described above, with three dynamic identification methods applied. The dynamic properties identified using the system are compared with those obtained with a 3D finite element model.

4.1 Stay cables

Stay cables are one of the most critical structural components in cable-stayed structures, since cable tension plays an important role in the construction, control, and monitoring of these structures [33]. The cable's natural frequencies were identified using the PP method. The spectral information presented below was obtained through the equations described in section 2.1, which were implemented in this research using the Matlab software [34]. Figure 5a shows the acceleration time series of the stay cable 2 at left (S2-L) (see Figure 4) obtained with the Arduino board, and Figure 5b shows the signal power spectrum.

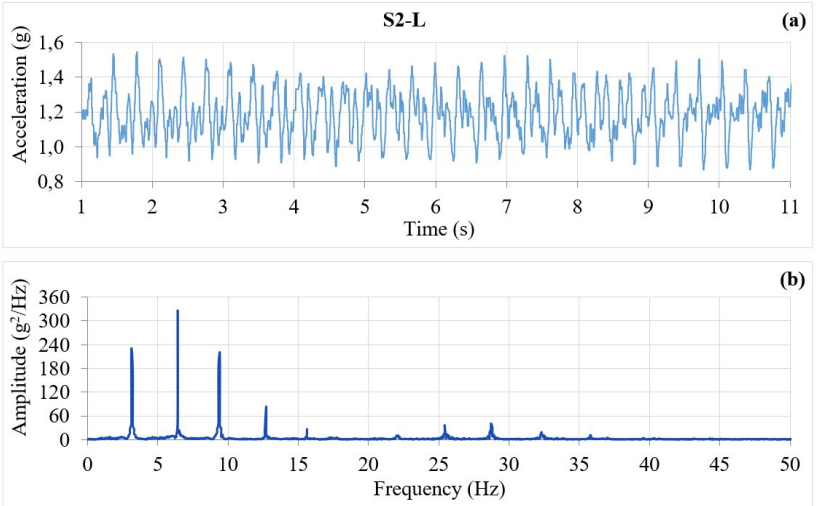

Figure 5. (a) Acceleration time series of the S2-L stay; **(b)** signal power spectrum.

It is interesting to note the high energy of the second peak, which can be explained by the position of the sensor. For the stays S2 (at left and right), the region where the board was positioned has the highest coordinates of the second theoretical mode shape. The cable's natural frequencies were used to determine the on-site axial forces of the stays. A simple way to estimate the cable forces in terms of natural vibration frequencies is to use the Vibrating String Mersenne/Taylor Law, considering that the cable is pinned at both ends, given by Equation 12:

$$f_n = \frac{n}{2L}\sqrt{\frac{T}{m}} \tag{12}$$

where n = mode shape number; L = cable span; T = cable force; m = mass per unit cable length; and f_n = natural frequency of the n mode shape.

The cable length was obtained from the solid drawing, i.e., it is the length between the concrete element faces. Table 1 shows, for example, the stay cable axial forces related to the 1st, 2nd, 3rd and 4th natural frequencies obtained for the stays 1, 2 and 3 (at left and right) through the PP Method.

Table 1. Stay cable forces related to the first four natural frequencies (S1, S2 and S3).

Stay cable	1st frequency (Hz) [related force (kN)]	2nd frequency (Hz) [related force (kN)]	3rd frequency (Hz) [related force (kN)]	4th frequency (Hz) [related force (kN)]	Average force (kN)
S1-L	2.733 [226.935]	5.465 [226.852]	8.397 [238.028]	11.030 [231.022]	**230.710**
S1-R	2.799 [238.028]	5.564 [235.146]	8.530 [245.628]	11.230 [239.476]	**239.570**
S2-L	3.125 [174.954]	6.383 [182.479]	9.376 [174.991]	12.670 [179.745]	**178.042**
S2-R	3.128 [175.290]	6.323 [179.064]	9.284 [171.574]	12.550 [176.356]	**175.571**
S3-L	4.420 [173.207]	8.807 [171.916]	13.560 [181.133]	17.850 [176.554]	**175.703**
S3-R	4.504 [179.853]	8.976 [178.578]	13.810 [187.874]	18.150 [182.539]	**182.211**
⋮	⋮	⋮	⋮	⋮	⋮

4.2 Complete structure

The dynamic properties, natural frequencies, and mode shapes were identified from ambient vibration data using the FDD and SSI-UPC methods. These are available in the ARTeMIS Modal 4.0 software [35], which was used in this section of the research. The accelerations were recorded and it was observed that the system's 0.01g limitation interfered with the acquisition of intervals with low variation of acceleration, resulting in levels in the time series. This problem was overcome by applying the moving average concept. In the case of the signals from the monitored footbridge, a moving average time frame of seven samples was sufficient. Figure 6a shows the recorded and "improved" acceleration

time series, using the example of Test Setup 9, and Figure 6b shows the moving average applied to the Mobile sensor 1 signal, between 11 and 22 seconds. The raw signal is in black and "improved" signal is in blue.

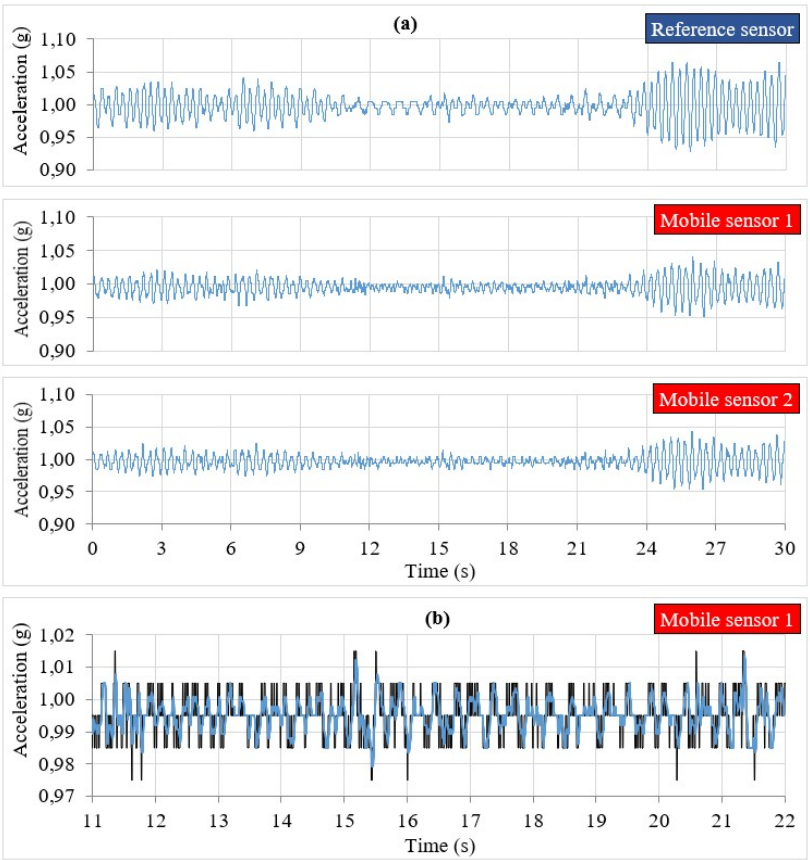

Figure 6. (a) Acceleration time-series captured by the data acquisition system in Test Setup 9; **(b)** Detail of the moving average applied to the signal.

Figure 7 shows the average normalized PSD function of the signals shown in Figure 6 decomposed into three singular values (SVD 1, SVD 2 and SVD 3) using the FDD method.

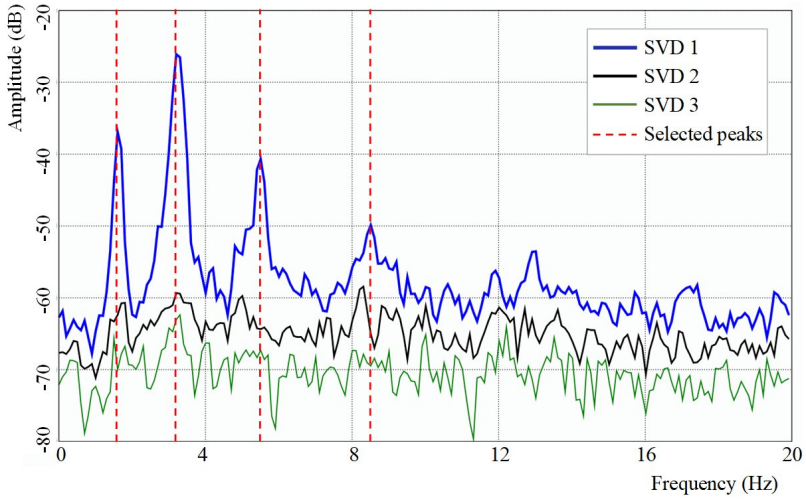

Figure 7. Average normalized PSD function decomposed into three singular values, using the FDD (Test setup 9).

The spectrum shows four well-defined peaks, highlighted in Figure 7. These peaks represent the first four natural frequencies related to the footbridge's first four flexural mode shapes. Table 2 shows the natural frequencies identified by the FDD method and compares the values and mode shapes with the numerical model using the Modal Assurance Criterion (MAC). The MAC index shows the correlation between mode shapes. It can vary between 0 and 1, where values close to 0 correspond to a lack of correlation, while values close to 1 indicate consistent correlation between the mode shapes. In the case of this research, the index was calculated to show the correlation between the experimental and numerical (reference) mode shapes, using Equation 13 below:

$$MAC = \frac{|\varphi_{exp}^{T}\varphi_{num}|^{2}}{(\varphi_{exp}^{T}\varphi_{exp})(\varphi_{num}^{T}\varphi_{num})} \tag{13}$$

where φ_{exp} = experimental modal vector; φ_{num} = numerical modal vector; "^{T}" = vector transpose.

Table 2. First four flexural natural frequencies identified by the FDD.

Flexural mode shape	f_{FDD}	$f_{numerical\ model}$	Difference	MAC
1st	1.6016 Hz	1.6404 Hz	↓ 2.37%	0.9990
2nd	3.2031 Hz	3.2423 Hz	↓ 1.21%	0.9915
3rd	5.5054 Hz	5.4472 Hz	↑ 1.07%	0.8554
4th	8.5083 Hz	8.3444 Hz	↑ 1.96%	0.9068

The experimental process identified natural frequency values very close to those provided by the numerical model. The greatest difference between these values, of 2.37%, was observed in the first frequency, while in the other frequencies the difference was between 1 and 2%.

Figure 8 shows the stabilization diagram of the signals shown in Figure 6 for the estimated state-space mode, using the SSI-UPC method.

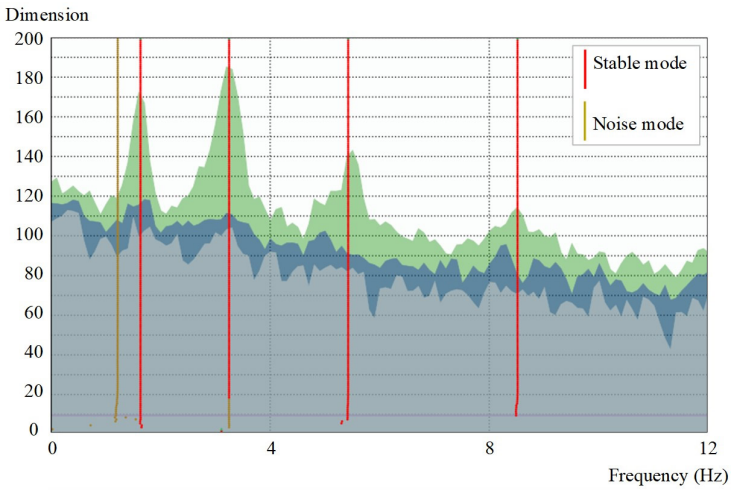

Figure 8. Mode shapes identified by the SSI-UPC (Test setup 9).

The SSI-UPC method highlighted five frequencies in the PSD function of the signals obtained in Test setup 9, decomposed into three singular values (SVD 1, SVD 2 and SVD 3). Four were classified as natural frequencies related to stable modes of vibration. The other, close to the first spectrum peak, was classified as related to a noise mode, probably resulting from the noisy signal of the acquisition system. Table 3 shows the natural frequencies related to the stable modes–in this case flexural mode shapes–identified by the method, and compares the results with the frequencies and mode shapes (MAC) provided by the numerical model.

Table 3. First four flexural natural frequencies identified by the SSI-UPC.

Flexural mode shape	$f_{SSI\text{-}UPC}$	$f_{numerical\ model}$	Difference	MAC
1st	1.6315 Hz	1.6404 Hz	↓ 0.54%	0.9971
2nd	3.2479 Hz	3.2423 Hz	↑ 0.17%	0.9895
3rd	5.4139 Hz	5.4472 Hz	↓ 0.61%	0.8513
4th	8.4900 Hz	8.3444 Hz	↑ 1.74%	0.9017

The experimental process identified natural frequency values very close to those provided by the numerical model. The greatest difference between them, of 1.74%, was observed in the fourth frequency, while in the other frequencies the difference was between 0.1 and 0.7%.

In general, the flexural modes identified presented excellent shapes. However, the third and fourth flexural mode shapes indicated problems in some coordinates (highlighted in Figure 9). Consequently, these presented the lowest MAC indexes among the identified mode shapes. The FDD method identified mode shapes with ≈ 0.86 and 0.91 MAC indexes, and the SSI-UPC method identified mode shapes with ≈ 0.85 and 0.90 MAC indexes, respectively. Analysis of all the measurement points and mode shapes obtained in previous tests [17] and in this case study suggests that this is due to the accuracy of the Arduino board (0.01g). The problem regions have the largest modal coordinates of the third and fourth theoretical modes of vibration. Experimentally, the acceleration variations in the adopted sampling frequency may not have been detected by the sensors, resulting in the signal saturation. On the other hand, the discontinuity of the third and fourth experimental modal vectors could be a warning of the existence of damage. This is an interesting possibility and will be part of a future study. Figure 9 shows the first four flexural mode shapes provided by the numerical model (Figure 9a) and experimentally identified by the proposed data acquisition system and FDD method (Figure 9b), and SSI-UPC method (Figure 9c).

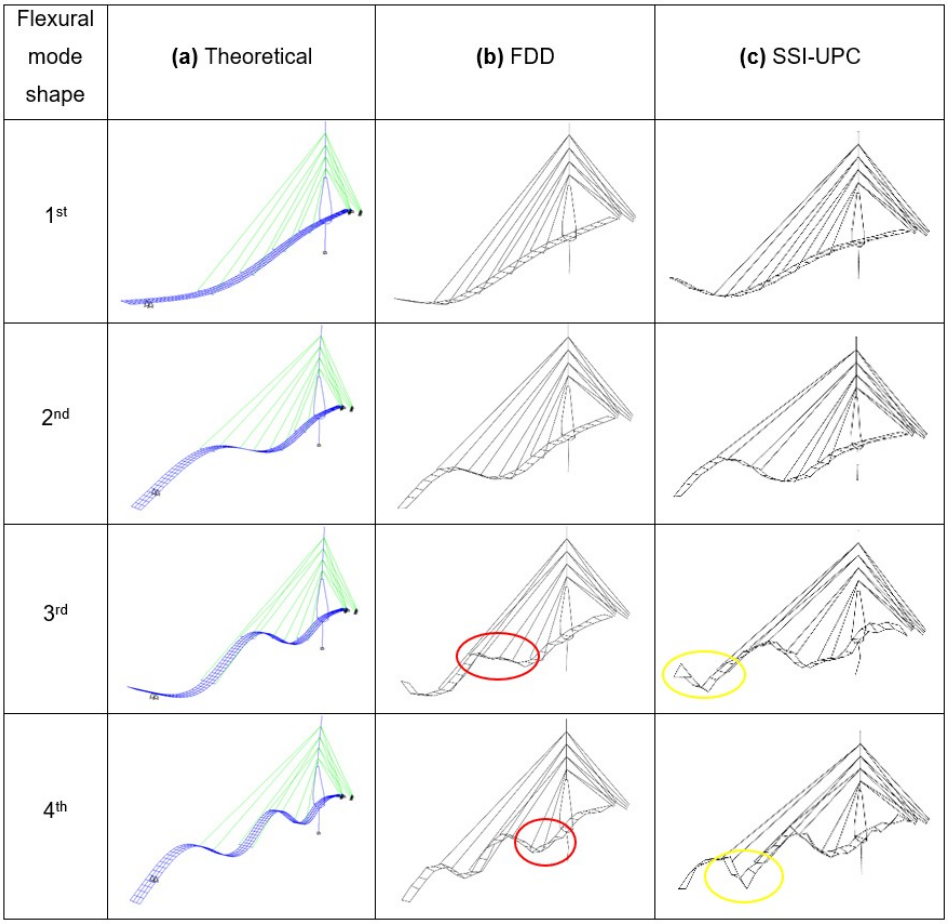

Figure 9. First four flexural mode shapes: **(a)** provided by the numerical model; **(b)** experimentally identified by FDD; **(c)** experimentally identified by SSI-UPC.

No transverse and torsional mode shapes were identified. Either it was difficult to generate enough energy in the corresponding directions during the tests or the respective vibrations were not noticeable, which explains the absence of these vibration modes in the system identification process.

5 CONCLUSIONS

The proposed system efficiently recorded the time series necessary for the OMA, with the acceleration acquisition process providing stable results in both the cable and complete structure tests. Despite the level of noise in the output signal revealed by the spectral density functions and the limited precision that made it difficult to capture low variations of accelerations, at least four mode shapes were identified in all tests. It was demonstrated that even with limited resources it is possible to obtain data for the evaluation of real structures.

The acceleration time series and the PSD functions were well-defined in all cable tests. At least four high energy peaks in the 0 – 24 Hz frequency range were generated by the data acquisition system and the PP method. These were used to determine the cable forces on-site. The procedure was effective, since the deck shape resulting from the numerical model resembled that observed visually on-site, which directly depends on the set forces of the stay cables.

In the tests of the complete structure, the data acquisition system and the identification methods were good tools for obtaining the first four flexural stable mode shapes, within the 0 – 9 Hz frequency range. Comparing the results to a 3D finite element model, the experimental natural frequencies presented a good correlation with the theoretical frequencies. When using the FDD method, the greatest difference, of 2.37%, was observed in the first frequency, while in the other frequencies the difference was between 1 and 2%. When using the SSI-UPC method, the greatest difference was 1.74% in the fourth frequency, while in the other frequencies the difference was between 0.1 and 0.7%. Despite the excellent shapes of the first and second experimental modes of vibration (MAC indexes above 0.99), the third and fourth flexural mode shapes indicated a continuity problem in some coordinates. The region has the largest modal coordinates in the respective theoretical mode shape. The acceleration variations may not have been detected by the sensors experimentally, resulting in signal saturation, or the discontinuity of the third and fourth experimental modal vectors may be indicating damage. A future study based on a damage detection routine will clarify this uncertainty and warn of any structural problems, if applicable.

In general, the proposed data acquisition system demonstrates the capacity to acquire the response time series used in the dynamic identification of civil engineering structures, but some improvements are necessary. Future research will seek to increase the accuracy of the system, if possible, to enable it to deal with structures that have low variations in acceleration (less than 0.01g). This would rule out the need to use the moving average. Another aspect is the synchronization of the devices. The number of records varies considerably for recording intervals longer than 30 seconds when using acquisition systems with multiple devices. Therefore, longer measurement time windows were avoided, despite the rule of thumb presented in the dynamic testing literature. It is very likely that other mode shapes will be identified if this problem can be overcome. Additionally, low-cost systems and sensors that have acceptable performance and close-to-optimal parameters for micro vibration detection, such as the one developed in this research, enable continuous and remote monitoring of the structure. This eliminates the need to interrupt the structure's operations and travel to the location. The Arduino boards were chosen for their portability, resistance, and cost. They could be fixed to and/or embedded in the structure (not recovered) to remotely record accelerations via wireless, especially with larger structures such as bridges, buildings, etc.

ACKNOWLEDGEMENTS

The authors wish to thank DNIT for authorizing the tests, B. de Almeida for the photos of the footbridge, and A. Araujo and E. Nunes for their assistance in conducting the tests.

REFERENCES

[1] W.-X. Ren and X.-L. Peng, "Baseline finite element modeling of a large span cable-stayed bridge through field ambient vibration tests," *Comput. Struc.*, vol. 83, no. 8-9, pp. 536–550, Mar 2005, http://dx.doi.org/10.1016/j.compstruc.2004.11.013.

[2] C. Chisari, C. Bedon, and C. Amadio, "Dynamic and static identification of base-isolated bridges using genetic algorithms," *Eng. Struct.*, vol. 102, no. 1, pp. 80–92, Nov 2015, http://dx.doi.org/10.1016/j.engstruct.2015.07.043.

[3] K.-V. Yuen, "Updating large models for mechanical systems using incomplete modal measurement," *Mech. Syst. Signal Process.*, vol. 28, pp. 297–308, Apr 2012, http://dx.doi.org/10.1016/j.ymssp.2011.08.005.

[4] A. Malekjafarian and E. J. Obrien, "Identification of bridge mode shapes using short time frequency domain decomposition of the responses measured in a passing vehicle," *Eng. Struct.*, vol. 81, no. 15, pp. 386–397, Dec 2014, http://dx.doi.org/10.1016/j.engstruct.2014.10.007.

[5] F. P. Pentaris, J. Stonham, and J. P. Makris, "A review of the state-of–the-art of wireless SHM systems and an experimental set-up towards an improved design," in *Proc. Eurocon 2013*, 2013, pp. 275-282, https://doi.org/10.1109/EUROCON.2013.6624997.

[6] Y. Liu and S. Nayak, "Structural health monitoring: state of the art and perspectives," *J. Miner. Met. Mater. Soc.*, vol. 64, no. 7, pp. 789–792, Jul 2012, http://dx.doi.org/10.1007/s11837-012-0370-9.

[7] C. Negulescu et al., "Comparison of seismometer and radar measurements for the modal identification of civil engineering structures," *Eng. Struct.*, vol. 51, pp. 10–22, Jun 2013, http://dx.doi.org/10.1016/j.engstruct.2013.01.005.

[8] J.-H. Weng, C.-H. Loh, J. P. Lynch, K.-C. Lu, P.-Y. Lin, and Y. Wang, "Output-only modal identification of a cable-stayed bridge using wireless monitoring systems," *Eng. Struct.*, vol. 30, no. 7, pp. 1820–1830, Jul 2008, http://dx.doi.org/10.1016/j.engstruct.2007.12.002.

[9] E. Toledo Júnior, A. Cury, and J. Landre Júnior, "Assessment of low-cost wireless sensors for structural health monitoring applications," *Rev. IBRACON Estrut. Mater.*, vol. 14, no. 2, pp. e14213, 2021, http://dx.doi.org/ 10.1590/S1983-41952021000200013.

[10] J. D. Braido and Z. M. C. Pravia, "Application of MEMS accelerometer of smartphones to define natural frequencies and damping ratios obtained from concrete viaducts and footbridge," *Rev. IBRACON Estrut. Mater.*, vol. 15, no. 2, pp. e15206, 2022, http://dx.doi.org/10.1590/S1983-41952022000200006.

[11] F. Khoshnoud and C. W. de Silva, "Recent advances in MEMS sensor technology – mechanical applications," *IEEE Instrum. Meas. Mag.*, vol. 15, no. 2, pp. 14–24, Apr 2012, http://dx.doi.org/10.1109/MIM.2012.6174574.

[12] M. Moradi and S. Sivoththaman, "MEMS multisensor intelligent damage detection for wind turbines," *IEEE Sens. J.*, vol. 15, no. 3, pp. 1437–1444, Mar 2015, http://dx.doi.org/10.1109/JSEN.2014.2362411.

[13] G. S. Maruthi and V. Hedge, "Application of MEMS accelerometer for detection and diagnosis of multiple faults in the roller element bearings of three phase induction motor," *IEEE Sens. J.*, vol. 16, no. 1, pp. 145–152, Jan 2016, http://dx.doi.org/10.1109/JSEN.2015.2476561.

[14] L. A. S. Pedotti, R. M. Zago and F. Fruett, "Fault diagnostics in rotary machines through spectral vibration analysis using low-cost MEMS devices," *IEEE Instrum. Meas. Mag.*, vol. 20, no. 6, pp. 39–44, Dec 2017, http://dx.doi.org/10.1109/MIM.2017.8121950.

[15] A. Vidal-Pardo and S. Pindado, "Design and development of a 5-channel arduino-based data acquisition system (ABDAS) for experimental aerodynamics research," *Sensors (Basel)*, vol. 18, no. 7, pp. 2382–2402, Jul 2018, http://dx.doi.org/10.3390/s18072382.

[16] A. González, J. L. Olazagoitia, and J. Vinolas, "A low-cost data acquisition system for automobile dynamics applications," *Sensors (Basel)*, vol. 18, no. 2, pp. 366–386, Jan 2018, http://dx.doi.org/10.3390/s18020366.

[17] D. S. Nunes, J.L.V. Brito and G.N. Doz, "A low-cost data acquisition system for dynamic structural identification," *IEEE Instrumen. Meas. Mag.*, vol. 22, no. 5, pp. 64-72, Oct. 2019, http://dx.doi.org/10.1109/IMM.2019.8868280.

[18] Arduino.CC, "Language Reference." Arduino.CC. https://www.arduino.cc/reference/en/ (accessed Jan. 8, 2022).

[19] Arduino IDE, "Arduino 1.8.5." Arduino IDE. https://www.arduino.cc/en/software (accessed Jan. 8, 2022).

[20] Arduino.CC., "What is Arduino?." Arduino.CC. http://www.arduino.cc/en/Guide/Introduction (accessed Jan. 8, 2022).

[21] G. Lockridge, B. Dzwonkowski, R. Nelson, and S. Powers, "Development of a low-cost arduino-based sonde for coastal applications," *Sensors (Basel)*, vol. 16, no. 4, pp. 528–544, Apr 2016, http://dx.doi.org/10.3390/s16040528.

[22] RealTerm software, "Realterm: serial and TCP terminal for engineering and debugging 3.0.1.44." http://realterm.sourceforge.io (accessed Jan. 8, 2022).

[23] B. Peeters, "System identification and damage detection in civil engineering," Ph.D. Thesis, Kath. Univ. Leuven, Belgium, 2000.

[24] J. Rodrigues, "Identificação modal estocástica – Métodos de análise e aplicações em estruturas de engenharia civil," Ph.D. Thesis, Fac. de Eng. da Univ. do Porto, Portugal, 2004.

[25] Arduino.CC., "Arduino 101." Arduino.CC. https://docs.arduino.cc/retired/boards/arduino-101-619 (accessed Jan. 8, 2022).

[26] Computers and Structures Inc., *SAP2000 Integrated Software for Structural Analysis and Design*. Berkeley, California: CSI – Computers and Structures Inc., 2000.

[27] R. Cantieni, "Cable-stayed footbridge: investigation into superstructure and cable dynamics," *Top. Dyn. Bridges*, vol. 3, pp. 11–25, Mar 2013, http://dx.doi.org/10.1007/978-1-4614-6519-5_2.

[28] J. M. W. Brownjohn et al., "Footbridge system identification using wireless inertial measurements units for force and response measurements," *J. Sound Vibrat.*, vol. 384, no. 8, pp. 339–355, Dec 2016, http://dx.doi.org/10.1016/j.jsv.2016.08.008.

[29] I. J. Drygala and J. M. Dulinska, "A theoretical and experimental evaluation of the modal properties of a cable-stayed footbridge," *Procedia Eng.*, vol. 199, pp. 2937–2942, 2017, http://dx.doi.org/10.1016/j.proeng.2017.09.347.

[30] L. O. Santos and X. Min, "Load Tests of a cable-stayed bridge in Coimbra, Portugal," *Struct. Eng. Int.*, vol. 17, no. 4, pp. 337–341, Nov 2007, http://dx.doi.org/10.2749/101686607782359146.

[31] S. Cho, J. Yim, S. W. Shin, H.-J. Jung, C.-B. Yun, and M. L. Wang, "Comparative field study of cable tension measurement for a cable-stayed bridge," *J. Bridge Eng.*, vol. 18, no. 8, pp. 748–757, Aug 2013, http://dx.doi.org/10.1061/(ASCE)BE.1943-5592.0000421.

[32] G. Piniotis, V. Gikas, T. Mpimis, and H. Perakis, "Deck and cable dynamic testing of a single-span bridge using radar interferometry and videometry measurements," *J. Appl. Geod.*, vol. 10, no. 1, pp. 87–94, Jan 2016, http://dx.doi.org/10.1515/jag-2015-0030.

[33] J. Lardies and M.-N. Ta, "Modal parameter identification of stay cables from output-only measurements," *Mech. Syst. Signal Process.*, vol. 25, no. 1, pp. 133–150, Jan 2011, http://dx.doi.org/10.1016/j.ymssp.2010.05.020.

[34] Matlab, *Version R2017a. The MathWorks*, Inc – MATLAB and Simulink for Technical Computing.

[35] Structural Vibration Solution A/S, *ARTeMIS Modal 4.0. Ambient Response Testing and Modal Identification Software ARTeMIS Extractor Pro 4.0*. Aalborg East, Denmark: Structural Vibration Solution A/S.

Author contributions: DSN: conceptualization, methodology, data curation, writing; JLVB: data curation, formal analysis; GND: data curation, formal analysis.

Editors: Sergio Hampshire C. Santos, Guilherme Aris Parsekian.